

# Mechanistic Studies on the Decomposition of Photoactive Nitrosyl Hydride (HNO) Precursors

Ruth B. Cink

A thesis submitted to  
Auckland University of Technology  
in fulfilment of the requirements for the degree of  
Doctorate of Philosophy (PhD)

School of Science  
Department of Chemistry

2018

# ABSTRACT

---

Nitroxyl hydride (HNO) is a biologically relevant, highly reactive molecule and is a redox cousin of NO. HNO shows extremely promising pharmacological properties, including treating congestive heart failure. The overarching motivation for this research is to facilitate kinetic and mechanistic studies of HNO with biologically relevant molecules. As HNO rapidly dimerizes in aqueous solution, HNO studies require compounds that release HNO upon demand. However, the release of HNO from thermally decomposing molecules is slow (typically minutes to hours), making kinetic and mechanistic studies challenging.

There is increasing interest in the development of photoactive HNO donor molecules because the use of light to activate HNO release enables a high degree of temporal and spatial control. In an effort to meet this need, a Piloty's acid derivative comprising an HNO-generating trifluoromethanesulfonamidoxy moiety tethered to the (6-hydroxynaphthalene-2-yl)methyl (6,2-HNM) photocage (**4**) is evaluated in order to establish if it can rapidly and cleanly generate HNO upon light activation. The photodecomposition of **4** was probed under a range of solvent conditions using a combination of characterization techniques, including  $^1\text{H}$  NMR spectroscopy,  $^{19}\text{F}$  NMR spectroscopy, high resolution mass spectrometry (HRMS), steady state fluorescence spectroscopy, and time-resolved transient absorption spectroscopy.

Photodecomposition of donor **4** occurred via two pathways: via concerted C-O and N-S bond cleavages to release  $^1\text{HNO}$ , the 6,2-HNM carbocation, and trifluorosulfinate,  $\text{CF}_3\text{SO}_2^-$ ; or via heterolytic N-O bond cleavage to generate the sulfonamide  $\text{CF}_3\text{SO}_2\text{NH}_2$ , and 6-hydroxynaphthalene-2-carbaldehyde. The selectivity between the two pathways is highly responsive to solvent. Donor **4** is shown to decompose to selectively release HNO upon excitation in a solvent mixture of 80:20 v/v MeCN to 5 mM phosphate buffer (pH 7.0). HNO characterization was achieved using two trapping molecules, aquacobalamin and glutathione, and from observation of its dimerization product,  $\text{N}_2\text{O}$ . Evidence for concerted heterolytic C-O and N-S bond cleavages versus elimination of  $\text{CF}_3\text{SO}_2\text{NHOH}$  was obtained by  $^{19}\text{F}$  NMR spectroscopy under pH conditions where  $\text{CF}_3\text{SO}_2\text{NHOH}$  is stable.

$^1\text{H}$  NMR and UV-vis spectroscopic titration experiments showed that donor **4** exists in three protonation states ( $\text{p}K_{\text{a}(\text{NH})} = 4.39 \pm 0.06$  and  $\text{p}K_{\text{a}(\text{OH})} = 9.73 \pm 0.01$ ,  $25.0\text{ }^\circ\text{C}$ , aqueous solution). Importantly, HNO photorelease occurs from donor **4** under conditions where the naphtholic OH is protonated and the nitrogen atom is deprotonated. Despite exhibiting both photoacidity and photobasicity, release of HNO from donor **4** does not require water and hence does not involve excited state proton transfer(s). Indeed, deprotonation of the photoacidic site of donor **4** decreases pathway selectivity for the generation of HNO following photolysis. The time-resolved spectroscopic studies indicate that HNO release may occur on the picosecond timescale following excitation of donor **4** and occurs via the short-lived  $^1\text{NO}^-$  species ( $^1\text{HNO}/^1\text{NO}^-$   $\text{p}K_{\text{a}} \sim 23$ ).

Studies were also completed towards determining the rate constant for the reaction between HNO and hydroxycobalamin. A thermally decomposing HNO donor (Piloty's acid) was used; this HNO donor releases HNO in alkaline conditions. Under alkaline conditions, a pH-dependent mixture of  $^1\text{HNO}$  and  $^3\text{NO}^-$  was formed from the decomposition of Piloty's acid.  $^3\text{NO}^-$  itself is a good reductant, and a reaction of  $^3\text{NO}^-$  and hydroxycobalamin was observed. Furthermore,  $^3\text{NO}^-$  reacts with the product of the reaction between hydroxycobalamin and  $^1\text{HNO}/^3\text{NO}^-$  namely nitroxylcobalamin.

# TABLE OF CONTENTS

---

Abstract .....	i
List of Figures .....	vi
List of Schemes .....	xxvi
List of Tables .....	xxviii
Attestation of Authorship .....	xxx
Acknowledgements .....	xxxii
Chapter 1: Introduction .....	1
1.1    Fundamental Chemistry of HNO .....	4
1.2    Biological and Therapeutic Significance of HNO .....	5
1.3    Kinetic and Mechanistic Studies on the Reactions of Biologically Relevant Molecules with HNO .....	8
1.4    HNO Donating Molecules .....	10
1.5    Photochemistry of Hydroxyarenes .....	20
Chapter 2: Methods and Instrumentation .....	33
2.1    Instrumentation .....	33
2.2    Materials .....	35
2.3    Steady State Spectroscopy .....	38
2.4    Photoproduct Characterizations .....	40
2.5    Transient Absorption Spectroscopy (TrA) .....	44
Chapter 3: Stoichiometric HNO Release from a Photocaged (6-Hydroxynaphthalen-2-yl)methyl Analogue of Piloty's Acid .....	50
3.1    Introduction .....	50
3.2    Thermal Stability of Donor 4 .....	52
3.3    The Acid-Base Chemistry of Donor 4 .....	52
3.4    Photodecomposition of Donor 4 in Aqueous Conditions .....	56

## Table of Contents

---

3.5	Origin of 6-[( <i>E</i> )-(hydroxyimino)methyl]naphthalen-2-ol.....	73	
3.6	Evidence for Concerted Release of HNO and CF <sub>3</sub> SO <sub>2</sub> <sup>-</sup> .....	78	
3.7	Photoproduct Quantum Yield of HNO Photorelease.....	79	
3.8	Conclusions.....	80	
Chapter 4: Ultrafast Generation of HNO from Photolysis of Photocaged (6-Hydroxynaphthalen-2-yl)methyl Analogue of Piloty's Acid .....			82
4.1	Introduction.....	82	
4.2	The Role Ionization of 4 in Pathway Selectivity .....	84	
4.3	Investigation of Excited State Proton Transfers to and from Solvent using Fluorescence Spectroscopy .....	86	
4.4	The Ability of Donor 4 to Undergo Excited State Proton Transfer to Solvent in Partially Aqueous Conditions .....	93	
4.5	Investigation of the Release of <sup>1</sup> HNO versus <sup>1</sup> NO <sup>-</sup> from Excitation of Donor 4 .....	98	
4.6	Investigation of the Rate of <sup>1</sup> NO <sup>-</sup> Release from Excitation of 4a Using Femtosecond Transient Absorption (fs-TA).....	108	
4.7	Characterization of Unique Triplet Species Observed in Photolysis of 4 using Nanosecond Laser Flash Photolysis.....	110	
4.8	Investigation of the Reaction between <sup>1</sup> HNO and Carbocation 9 using Time Resolved Absorption Spectroscopy .....	123	
4.9	Conclusions.....	125	
Chapter 5: Mechanistic Studies of N-O Bond Cleavage from Photocaged (Hydroxynaphthalenyl)methyl Analogues of Piloty's Acid .....			128
5.1	Introduction.....	128	
5.2	Influence of Acid Sites for Possible Deprotonation on Pathway Selectivity for N-O Bond Cleavage.....	130	
5.3	Studies on N-O Bond Cleavage from Excitation of the Neutral Form of Donor 4 .....	131	

## Table of Contents

---

5.4	Studies on N-O Bond Cleavage from Excitation of the Naphtholate Analogue of Donor 4 .....	140
5.5	The Influence of Excited State Intramolecular Proton Transfer on Pathway Selectivity .....	143
5.6	Conclusions.....	153
Chapter 6: Studies on the reactions of Hydroxycobalamin and Nitroxylcobalamin with Piloty's Acid .....		154
6.1	Introduction.....	154
6.2	Methods.....	155
6.3	Studies on the Reactions between $^1\text{HNO}/^3\text{NO}^-$ and Hydroxycob(III)alamin.....	156
6.4	Studies on the Reactions between $^1\text{HNO}/^3\text{NO}^-$ and Nitroxylcobalamin.....	161
6.5	Discussion and Conclusions .....	167
Chapter 7: Summary and Future Directions .....		170
References.....		177
Glossary .....		189
Appendices.....		191

# LIST OF FIGURES

---

Figure 1.1. (a) 3,2-HNM-photocaging of <i>N</i> -hydroxysulfonamides. (b) 6,2-HNM-photocaging of <i>N</i> -hydroxysulfonamides.....	2
Figure 1.2. Above: General design of the photoactive HNO donor molecules ((hydroxynaphthalenyl)methyl (HNM) photocaged <i>N</i> -hydroxysulfonamides), where the reactant decomposes to generate one mol. equiv. of HNO, a non-reactive by-product (pink), and a chemical marker (green). Below: Outline of photochemical and photophysical exploration and mechanistic studies to be addressed in this thesis. The reactant has been synthesized by collaborators at Kent State University and preliminary characterization completed of the chemical marker of HNO generation. The remaining points are addressed individually in Chapters 3-5. Chapter 6 highlights the difficulties associated with the use of currently available thermally decomposing HNO donors. ....	3
Figure 1.3. Structure of Angeli's Salt. ....	8
Figure 1.4. Structure of <i>N</i> -alkoxysulfonamide compounds. ....	12
Figure 1.5. Structures of <i>N</i> -substituted hydroxylamines. ....	13
Figure 1.6. Toscano's <i>N</i> -substituted hydroxylamines. ....	13
Figure 1.7. Structure of diazeniumdiolates. ....	17
Figure 1.8. <i>o</i> -Nitrobenzyl chromophore tethered with benzohydroxamic acid. ....	19
Figure 1.9. Example of concerted biprotonic transfer for 7-azaindole to form 7-H-tautomer monohydrate. ....	25
Figure 1.10. Example of stepwise ESPT for lumichrome in the presence of acetic acid to form a flavin tautomer. ....	25
Figure 1.11. Example of ESPT occurring via proton-relays for 7-hydroxyquinoline.....	25
Figure 1.12. Example of intrinsic intramolecular proton transfer in 3-hydroxyflavone to form the pyrylium tautomer. ....	29
Figure 1.13. 2-Phenylnaphthalen-1-ol and its methylated analogue.....	30
Figure 2.1. Correlation between $p_{aH}$ and $p_{HD}$ for solvent mixtures in 80:20 v/v MeCN to aqueous solution. The data point at 11.0 (gray triangle) was excluded from the analysis due to the alkaline error associated with the measurement.....	34
Figure 2.2. Examples of averaged laser excitation of ruthenium trisbipyridine dichloride [Ru(bipy) <sub>3</sub> ] in aqueous solution. The data were collected at 370 nm after photoexcitation	

at 355 nm. Green trace: 1.0 mm slit width, primary monochromator; secondary monochromator not installed. Blue trace: 1.0 mm slit width after sample, primary monochromator; 2.5 mm slit width, secondary monochromator. Red trace: 1.0 mm slit width after sample; primary monochromator; 1.5 mm slit width, secondary monochromator. ....	44
Figure 2.3. (a) Absorbance change seen at 320 nm for the laser flash photolysis of donor <b>4</b> (150 $\mu$ M) in 80:20 v/v MeCN to 5.0 mM phosphate buffer, pH 7.0 using a Nd:YAG laser fitted with 2 <sup>nd</sup> and 4 <sup>th</sup> harmonic generators operating at 60 mJ/pulse, 44 mJ/pulse, and 28 mJ/pulse. (b) Plot of pulse energy (mJ/pulse) to absorbance change seen at 320 nm (0 to 180 $\mu$ s) for the laser flash photolysis of <b>4</b> ( $\sim\mu$ M); $R^2 = 0.99597$ . Linearity indicates that the absorbance changes seen are due to excitation energy and not another process (concentration issues, photobleaching). ....	45
Figure 2.4. Flow set-up of cuvette. (a) NO <sup>-</sup> -Cbl(III) solution flowed into anaerobic water (t = 0 min); (b) successful transfusion of NO <sup>-</sup> -Cbl(III) into cuvette (t = 1 min); (c) preservation of oxygen-sensitive NO <sup>-</sup> -Cbl(III) through continuous circulation into and out of an argon in solution reservoir (t = 30 min). ....	46
Figure 2.5. (a) Example of unprocessed spectral kinetic data. Laser flash photolysis of 2-naphthol in anaerobic MeCN. (b) Example of processed spectral kinetic data. Laser flash photolysis of 2-naphthol in anaerobic MeCN. ....	47
Figure 3.1. Structures of photoactive HNO donors <b>1-4</b> . ....	51
Figure 3.2. <sup>19</sup> F NMR spectra of donor <b>4</b> (4.0 mM) in 50:50 v/v MeCN to D <sub>2</sub> O immediately, 24, 48, 72, 96, 120, and 144 hr following sample preparation (Spectrum 1-7, respectively). ....	52
Figure 3.3. <sup>19</sup> F NMR spectra of donor <b>4</b> (1.00 mM) in aerobic 20% v/v aqueous MeCN, where the aqueous component is 0.1 M HCl, 0.1 M NaOH, 5.0 mM phosphate buffer (pH 3.0, 7.0), 5.0 mM acetate buffer (pH 5.0), 5.0 mM borate buffer (pH 9.0), or 5.0 mM carbonate buffer (pH 11.0). ....	53
Figure 3.4. <sup>1</sup> H NMR spectra of donor <b>4</b> (1.00 mM) in aerobic 20% v/v aqueous MeCN, where the aqueous component is 0.1 M HCl, 0.1 M NaOH, 5.0 mM phosphate buffer (pH 3.0, 7.0), 5.0 mM acetate buffer (pH 5.0), 5.0 mM borate buffer (pH 9.0), or 5.0 mM carbonate buffer (pH 11.0). Residual chloroform is observed at 7.77 ppm. ....	53
Figure 3.5. <sup>1</sup> H NMR spectrum of donor <b>4</b> in CD <sub>3</sub> CN. <sup>1</sup> H NMR peaks are assigned as depicted in the inset. The peak at $\delta$ 5.07 ppm corresponds to the methylene protons. ....	54

## List of Figures

---

- Figure 3.6. (a) UV-Vis spectra of **4** ( $3.0 \times 10^{-5}$  M) as a function of pH (aqueous solution, 25.0 °C). Inset: Absorbance at 230 nm plotted as a function of pH. Data were fitted to equation (4.1), giving  $pK_a = 4.4 \pm 0.1$ . (b) UV-Vis spectra of **4** ( $2.0 \times 10^{-5}$  M) as a function of pH (aqueous solution, 25.0 °C). Inset: Absorbance at 228 nm plotted as a function of pH. Data were fitted to equation (4.1), giving  $pK_a = 9.7 \pm 0.1$ .....55
- Figure 3.7. (a)  $^{19}\text{F}$  NMR spectra as a function of irradiation time (Rayonet photoreactor, 8 x 350 nm bulbs, 4 W; 0.5, 1, 2, 5, 8, and 13 min;  $\pm 5$  s) for the photodecomposition of HNO donor **4** (0.500 mM) in an anaerobic mixture of 80:20 v/v  $\text{CD}_3\text{CN}$  to 5.0 mM phosphate buffer solution, pH 7.0. (b) Plot of observed species as a function of irradiation time. Final composition:  $\text{CF}_3\text{SO}_2^-$  ( $\delta$  -88.7 ppm; 98%);  $\text{CF}_3\text{SO}_2\text{NH}_2$  ( $\delta$  -81.2 ppm; 2%). (c) Best fit of the peak area of donor **4** ( $-\text{CF}_3$ ) to a first-order rate equation, giving  $k_{\text{obs}} = 0.29 \pm 0.02 \text{ min}^{-1}$ .....56
- Figure 3.8.  $^{19}\text{F}$  NMR spectra of photolyzed solutions of **4** (Spectrum 1: 0.100 mM, Spectrum 2: 1.00 mM, Spectrum 3: 5.00 mM, and Spectrum 4: 15.0 mM) upon complete decomposition of **4** in 80:20 v/v  $\text{CD}_3\text{CN}$  to 0.1 M phosphate buffer, pH 7.0 using a Rayonet photoreactor, 8 x 350 nm bulbs, 4 W.  $\text{CF}_3\text{SO}_2^-$ :  $\delta$  -88.8 ppm.  $\text{CF}_3\text{SO}_2\text{NH}_2$ :  $\delta$  -81.2 ppm. Unknown an additional species:  $\delta$  -74.45 ppm. **4**:  $\delta$  -76.4 ppm. ....57
- Figure 3.9. N-O bond cleavage pathway selectivity (indicated by % $\text{CF}_3\text{SO}_2\text{NH}_2$ , by total integration) as a function of concentration of **4**. Photolysis performed in solvent mixtures of 80:20 v/v  $\text{CD}_3\text{CN}$  to 5.0 mM phosphate buffer, pH 7.0.....57
- Figure 3.10. UV-vis spectra for  $\text{H}_2\text{OCbl(III)}^+$  (0.200 mM) in an anaerobic mixture of 40:60 v/v MeCN to 5.0 mM phosphate buffer (pH 7.0) after 5, 20, and 50 min sample preparation, following 50 min irradiation (Xe lamp, monochromator slit width = 5.0 mm, 331 nm), and following addition of Angeli's salt (1.2 mol equiv). ....59
- Figure 3.11. UV-vis spectra for  $\text{H}_2\text{OCbl(III)}^+$  (0.300 mM) before and after irradiation from a Xe lamp (150 W, monochromator slit width = 3.0 mm, full spectrum) in a mixture 40:60 v/v MeCN to 5 mM phosphate buffer (pH 7.0) at 25 °C for 1, 4, 9 and 19 min...59
- Figure 3.12.  $^1\text{H}$  NMR spectra of 2-naphthol (1.00 mM) and  $\text{H}_2\text{OCbl(III)}^+$  (1.20 mM) in anaerobic 40:60 MeCN to 0.1 M phosphate buffer (pD 7.0) upon sample preparation (a) and after 5 minutes irradiation (b). 2-Naphthol:  $\delta$  7.87, 7.85, 7.79, 7.77, 7.50, 7.37, 7.27, 7.26 ppm.  $\text{H}_2\text{OCbl(III)}^+$ :  $\delta$  7.18, 6.54, 6.46, 6.23, and 6.19 ppm..... 60
- Figure 3.13. (a)  $^{31}\text{P}$  NMR spectra of  $\text{NO}^-$ -Cbl(III) (mM) in 60:40 v/v MeCN to 5.0 mM phosphate buffer (pH 7.0); (b) following irradiation for 20 min (Rayonet photoreactor, 8

## List of Figures

---

x 350 nm bulbs, 4 W). H <sub>3</sub> PO <sub>4</sub> external standard in capillary insert: $\delta$ -0.24 ppm. Phosphate buffer: $\delta$ 2.01 ppm. NO <sup>-</sup> -Cbl(III): $\delta$ 0.18 ppm. ....	61
Figure 3.14. UV-vis spectra for NO <sup>-</sup> -Cbl(III) (~25 $\mu$ M) before and after irradiation using a Xe lamp (150 W, monochromator slit width = 3.0 mm, full spectrum) in a mixture of phosphate buffer (pH 7.0, 5.0 mM) and MeCN (40:60, v/v) at 25 °C for 0, 5, and 10 min. The sample was then irradiated using a Nd:YAG laser fitted with 2 <sup>nd</sup> and 4 <sup>th</sup> harmonic generators (1 Hz, 120 pulses, ~60 mJ/pulse, ~5 ns pulse width). ....	61
Figure 3.15. <sup>19</sup> F NMR spectra of donor <b>4</b> (1.00 mM) and H <sub>2</sub> OCbl(III) <sup>+</sup> (0.900 mM) in an anaerobic mixture of 40:60 v/v MeCN to 0.1 M phosphate buffer (pD 7.0) upon after 5 min irradiation (Rayonet photoreactor, 8 x 350 nm bulbs, 4 W). Donor <b>4</b> : $\delta$ -77.17 ppm. CF <sub>3</sub> SO <sub>2</sub> <sup>-</sup> : $\delta$ -88.35 ppm. ....	62
Figure 3.16. <sup>1</sup> H NMR spectra of donor <b>4</b> (1.00 mM) and H <sub>2</sub> OCbl(III) <sup>+</sup> (0.900-1.00 mM) in an anaerobic mixture of 40:60 v/v MeCN : 0.10 M deuterated phosphate buffer (pD 7.0) immediately after sample preparation (A) and after 5 min irradiation (B, C, D; Rayonet photoreactor, 8 x 350 nm bulbs, 4 W). Donor <b>4</b> : 7.85, 7.82, 7.80, 7.75, 7.73, 7.50, 7.48, 7.24, 7.19 ppm. H <sub>2</sub> OCbl(III) <sup>+</sup> : $\delta$ 7.16, 6.52, 6.43, 6.21, and 6.17 ppm. NO <sup>-</sup> -Cbl(III): 7.83 (overlapping), 7.29 (overlapping), 7.11, 6.48 (overlapping), 6.27 ppm; confirmed by recording authentic NO <sup>-</sup> -Cbl(III) in the same solvent system. The peak positions vary by up to 0.02 ppm (within experimental error). ....	63
Figure 3.17. <sup>1</sup> H NMR spectra of donor <b>4</b> (1.00 mM) and H <sub>2</sub> OCbl(III) <sup>+</sup> (1.00 mM) in an anaerobic mixture of 40:60 MeCN to 0.1 M phosphate buffer (pD 7.0) after 8 min irradiation (Rayonet photoreactor, 8 x 350 nm bulbs, 4 W); Spectrum (a): Sample B and spectrum (b): Sample C). Donor <b>4</b> : $\delta$ 7.85, 7.82, 7.80, 7.75, 7.73, 7.50, 7.48, 7.24, 7.19 ppm. H <sub>2</sub> OCbl(III) <sup>+</sup> : $\delta$ 7.16, 6.52, 6.43, 6.21, and 6.17 ppm. NO <sup>-</sup> -Cbl(III): 7.83 (overlapping), 7.29 (overlapping), 7.11, 6.48 (overlapping), 6.27 ppm. ....	64
Figure 3.18. Concentration of NO <sup>-</sup> -Cbl(III) and CF <sub>3</sub> SO <sub>2</sub> <sup>-</sup> as a function of irradiation time from a reaction mixture of donor <b>4</b> (1.00 mM) and H <sub>2</sub> OCbl(III) <sup>+</sup> (1.00 mM) in an anaerobic mixture of 40:60 MeCN to 0.1 M phosphate buffer (pD 7.0). Plot (a) shows the analysis of Sample B and plot (b) shows the analysis of Sample C. ....	65
Figure 3.19. Calibration curve of Angeli's salt ( $\mu$ M) versus abundance of N <sub>2</sub> O (44.01 <i>m/z</i> , retention time 1.7 min).....	66
Figure 3.20. Concentration of Angeli's salt in 5.0 mM phosphate buffer (pH 7.0) solutions (total volume of 5.000 mL) with 5% by vol. of MeCN plotted against GC-MS headspace	

## List of Figures

---

- analysis of  $\text{N}_2\text{O}$  ( $m/z$  44.0). Photolysis of 2-naphthol (1.04 mM) and Angeli's salt (0.820 mM; Rayonet photoreactor, 8 x 350 nm bulbs, 4 W) decreased  $\text{N}_2\text{O}$  counts by ~35% (green). ..... 67
- Figure 3.21.  $^{19}\text{F}$  NMR spectra for the photodecomposition of **4** (0.500 mM) in an aerobic mixture of 80:20 v/v  $\text{d}_6$ -DMSO to 5.0 mM phosphate buffer solution, pH 7.0, as a function of the total irradiation time (Rayonet photoreactor, 8 x 350 nm bulbs, 4 W; 0.50, 1.0, 1.5, 2.0, 4.0, 6.0, and 10.0 min). Complete decomposition of **4** produced a mixture of  $\text{CF}_3\text{SO}_2^-$  ( $\delta$  -86.55 ppm: 94%) and  $\text{CF}_3\text{SO}_2\text{NH}_2$  ( $\delta$  -79.82 ppm: 5%). ..... 70
- Figure 3.22.  $^1\text{H}$  NMR spectra for the photodecomposition of **4** (0.500 mM) in an aerobic 80:20 v/v  $\text{d}_6$ -DMSO to 5.0 mM phosphate buffer solution, pH 7.0, as a function of the total irradiation time (Rayonet photoreactor, 8 x 350 nm bulbs, 4 W; 0.50, 1.0, 1.5, 2.0, 4.0, 6.0, and 10.0 min). ..... 70
- Figure 3.23. Comparison of the  $^1\text{H}$  NMR spectrum of the photolytic products derived from HNO donor **4** (0.500 mM) following 50% photodecomposition (95%  $\text{CF}_3\text{SO}_2^-$  in product mixture) with authentic samples of **4**, diol **7**, oxime **10**, and aldehyde **8** (in aerobic 80:20 v/v  $\text{d}_6$ -DMSO to 5.0 mM phosphate buffer solution, pH 7.0). ..... 71
- Figure 3.24. The photodecomposition of **4** (1.00 mM) in aerobic 80:20 v/v  $\text{d}_6$ -DMSO to 5.0 mM phosphate buffer solution, pH 7.0, as a function of the total irradiation time (Rayonet photoreactor, 8 x 350 nm bulbs, 4 W;  $\pm$  5 s) by  $^1\text{H}$  NMR ( $\delta$  7.35 ppm; overlapping with diol **7**) and  $^{19}\text{F}$  NMR ( $\delta$  -77.25 ppm) spectroscopy. Photolysis was 94% selective for the desired pathway. ..... 72
- Figure 3.25. Total integration and observed photoproducts as a function of time (Rayonet photoreactor, 8 x 350 nm bulbs, 4 W) from the photodecomposition of **4** (1.00 mM) in aerobic 80:20 v/v  $\text{d}_6$ -DMSO to 5.0 mM phosphate buffer solution, pH 7.0. The integrations of the listed peaks were calculated relative to an external standard. .... 72
- Figure 3.26.  $^1\text{H}$  NMR spectrum from the reaction of diol **7** (5.00 mM) and Angeli's salt (1.5 equiv) in an anaerobic mixture of 5:95 v/v MeCN to 0.1 M phosphate buffer, pH 7.0. Reaction was left to proceed for three hr, taken down to dryness, and dissolved in  $\text{CD}_3\text{CN}$ .  $^1\text{H}$  NMR shifts of diol **7** are observed at  $\delta$  = 7.75, 7.73, 7.71, 7.68, 7.66, 7.41, 7.39, 7.15, 7.10, 7.08, 5.45 ppm (compared with authentic sample). ..... 73
- Figure 3.27. UV/Vis spectrum of  $\text{CF}_3\text{SO}_2\text{NHOH}$  (0.02 M) in anhydrous methanol. .... 74
- Figure 3.28.  $^1\text{H}$  NMR spectrum of the steady state photolysis product mixture from diol **7** and  $\text{CF}_3\text{SO}_2\text{NHOH}$  (1.5 equiv.) in an anaerobic mixture of 5:95 v/v MeCN to 0.1 M

## List of Figures

---

phosphate buffer, pH 7.0 (Rayonet photoreactor, 8 x 350 nm bulbs, 4 W). Product was taken to dryness and dissolved in CD <sub>3</sub> CN. <sup>1</sup> H NMR shifts of diol <b>7</b> were assigned to δ 7.75, 7.73, 7.71, 7.68, 7.66, 7.41, 7.39, 7.15, 7.10, 7.08, 5.45 ppm from comparison to authentic sample.....	75
Figure 3.29. <sup>1</sup> H NMR spectra of an authentic sample of diol <b>7</b> in 1:1 MeOH to 5.0 mM phosphate buffer (pD 7.0) (a) before and (b) after irradiation (35 minutes irradiation, Rayonet photoreactor, 8 x 350 nm bulbs, 4 W); referenced to solvent residual peak. ...	75
Figure 3.30. (a) <sup>1</sup> H NMR spectrum of oxime <b>10</b> (6.00 mM) in 60:40 v/v CD <sub>3</sub> CN and 0.1 M phosphate buffer solution (pH 7.0) following irradiation for 15 min (~30% decomposition, Rayonet photoreactor, 8 x 350 nm bulbs, 4 W). (b) Authentic sample of oxime <b>10</b> (6.00 mM) in the same solvent. (c) Aldehyde <b>8</b> in the same solvent.....	78
Figure 3.31. (a) <sup>19</sup> F NMR spectra as a function of irradiation time (Rayonet photoreactor, 8 x 350 nm bulbs, 4 W; 0, 0.5, 1, 2, 5, 8, 13, 23, 38, and 53 min) for the photodecomposition of donor <b>4</b> (1.0 mM) in an anaerobic mixture of 80:20 v/v CD <sub>3</sub> CN to 5.0 mM phosphate buffer (pH 3.0). (b) Plot of observed species as a function of irradiation time. (c) Best fit of the peak area of donor <b>4</b> (-CF <sub>3</sub> ) to a first-order rate equation, giving $k_{\text{obs}} = 0.09 \pm 0.01 \text{ min}^{-1}$ . ....	79
Figure 4.1. Selectivity for HNO photorelease (from <sup>19</sup> F NMR total integration) according to pH of aqueous solution and concentration of aqueous component in CD <sub>3</sub> CN, where the aqueous component is 0.1 M HCl, 0.1 M NaOH, 5.0 mM phosphate buffer (pH 3.0, 7.0), 5.0 mM acetate buffer (pH 5.0), 5.0 mM borate buffer (pH 9.0), or 5.0 mM carbonate buffer (pH 11.0). Steady state photolysis samples of <b>4</b> (0.500-1.00 mM) were prepared in anaerobic solutions and irradiated using a Rayonet photoreactor (8 x 350 nm bulbs, 4 W) until completely degraded.....	84
Figure 4.2. (a) Emission spectra of donor <b>4</b> (~μM) in 80:20 v/v MeCN to aqueous conditions, 20 by vol aqueous in MeCN, where the aqueous component is 0.1 M HCl, 0.1 M NaOH, 5.0 mM phosphate buffer (pH 3.0, 7.0), 5.0 mM acetate buffer (pH 5.0), 5.0 mM borate buffer (pH 9.0), or 5.0 mM carbonate buffer (pH 11.0). Excitation wavelength is at an isosbestic point between <b>4a</b> and <b>4c</b> ( $\lambda_{\text{exc}} = 315 \text{ nm}$ ). (b) Integrated intensity as a function of pH. ....	85
Figure 4.3. Emission spectra of donor <b>4</b> (~μM) in 95% by vol. of 5.0 mM phosphate buffer pH 7.0 (5% MeCN), 95% by vol. of 0.1 M NaOH (5% MeCN), and in MeCN. ( $\lambda_{\text{exc}} = 315 \text{ nm}$ ).....	87

## List of Figures

---

Figure 4.4. Absorption and fluorescence spectra of 2-naphthol in (a) 0.1 M HCl, (b) 0.1 M NaOH, (c) 80:20 v/v MeCN to 0.1 M HCl, and (d) 80:20 v/v MeCN to 0.1 M NaOH ( $\lambda_{exc} = 315$ nm).....	89
Figure 4.5. Absorption and fluorescence spectra of <b>4</b> in (a) MeCN and (b) 0.1 M NaOH ( $\lambda_{exc} = 315$ nm).....	89
Figure 4.6. (a) Emission spectra of 2-naphthol and <b>4</b> in DMSO ( $\lambda_{exc} = 315$ nm). (b) Emission spectra of 2-naphthol and <b>4</b> in MeCN ( $\lambda_{exc} = 315$ nm).....	91
Figure 4.7. (a) Emission spectra of 2-naphthol and donor <b>4b</b> in 0.1 M HCl (5% MeCN by vol.; $\lambda_{exc} = 315$ nm). (b) Emission spectra of donor <b>4b</b> (~25 $\mu$ M) in MeCN with increasing concentrations of aqueous acid (0.1 M HCl) in MeCN ( $\lambda_{exc} = 315$ nm). ....	92
Figure 4.8. Emission spectra of donor <b>4b</b> ( $\mu$ M) and 2-naphthol ( $\mu$ M) in TFE ( $\lambda_{exc} = 315$ nm).....	93
Figure 4.9. Effect of solvent composition on the percentage of HNO generated upon irradiation of HNO donor <b>4</b> (0.50-2.00 mM; Rayonet photoreactor, 8 x 350 nm bulbs, 4 W) in a mixture of phosphate buffer (5 mM, pH 7.00) and CD <sub>3</sub> CN (v/v).....	94
Figure 4.10. Emission spectra of 2-naphthol (~ $\mu$ M) in (a) ~100% aqueous conditions and (b) 80:20 v/v MeCN to aqueous solution, where the aqueous component is 0.1 M HCl, 0.1 M NaOH, 5.0 mM phosphate buffer (pH 3.0, 7.0), 5.0 mM acetate buffer (pH 5.0), 5.0 mM borate buffer (pH 9.0), or 5.0 mM carbonate buffer (pH 11.0). To avoid selective excitation of 2-naphthol or 2-naphtholate, the samples were excited at the isosbestic point between the two species ((a) $\lambda_{exc} = 303$ nm; (b) $\lambda_{exc} = 308$ nm).....	95
Figure 4.11. fs-TA of 2-naphthol in aerobic MeCN following excitation (a, b, and c; $\lambda_{exc} = 267$ nm). Kinetics at 340, 560, and 440 nm are shown in (d).....	96
Figure 4.12. fs-TA of 2-naphthol in aerobic 5:95 v/v MeCN to 5.0 mM phosphate buffer solution (pH 7.0) following excitation (a, b, and c; $\lambda_{exc} = 267$ nm). Kinetics at 375, 560, and 435 nm are shown in (d).....	97
Figure 4.13. fs-TA of 2-naphthol in MeCN, 80:20 v/v, and 5:95 v/v MeCN to 5.0 mM phosphate buffer solution, pH 7.0 following (a) ~ 1 ps and (b) ~ 3 ns after excitation. .	97
Figure 4.14. fs-TA of 2-naphthol in aerobic 80:20 v/v MeCN to 5.0 mM phosphate buffer solution (pH 7.0) following excitation (a, b, and c; $\lambda_{exc} = 267$ nm). Kinetics at 340, 560, and 420 nm are shown in (d).....	98
Figure 4.15. (a) <sup>1</sup> H NMR spectra of donor <b>4</b> (1.00 mM) in aerobic 20% by vol. buffer in MeCN, where the aqueous component is 0.1 M HCl, 5.0 mM phosphate buffer (pH 7.0),	

or 0.1 M NaOH. Residual chloroform is observed at 7.63 ppm.(b) $^1\text{H}$ NMR spectrum of donor <b>4a</b> in $\text{CD}_3\text{CN}$ with peak assignments. $^1\text{H}$ NMR peaks are assigned as depicted in the inset. The peak at $\delta$ 5.07 ppm corresponds to the methylene protons. ....	99
Figure 4.16. $^1\text{H}$ NMR spectra of donor <b>4</b> (1.00 mM) upon approximate mol. Equiv. additions of potassium acetate in $\text{CD}_3\text{CN}$ . Spectra referenced to chloroform ( $\delta$ 7.58 ppm). Note: The solvent peak ( $\delta$ 1.94 ppm) overlapped with the acetate peak and the solubility of potassium acetate is poor; therefore, the mol. equiv. is approximated (approximately 0-10 mol. equiv.). The $^1\text{H}$ NMR spectra clearly show a shift in aromatic (H5 proton: $\delta$ 7.79 to 7.64 ppm) and methylene ( $\delta$ 5.07 to 4.65 ppm) protons. ....	100
Figure 4.17. $^1\text{H}$ NMR spectra of donor <b>4</b> (1.00 mM) upon additions of carboxylate salt (lithium acetate) in $d_6$ -DMSO (0.03% TMS by manufacturer). ....	101
Figure 4.18. $^1\text{H}$ NMR spectra of donor <b>4</b> (1.00 mM) upon additions of carboxylate salt (TSP) in $d_6$ -DMSO (0.03% TMS by manufacturer). ....	101
Figure 4.19. Molar equivalents of TSP and acetate to donor <b>4</b> (1.00 mM) in $d_6$ -DMSO (0.03% TMS by manufacturer) versus methylene carbon shift. ....	102
Figure 4.20. Transfer of electron density upon addition of acetate to naphtholic compounds as indicated by $^1\text{H}$ NMR upfield or downfield shifts. Green indicates a loss of electron density and red indicates a gain of electron density. ....	103
Figure 4.21. $^1\text{H}$ NMR spectra of 2-naphthol (1.00 mM) in $d_6$ -DMSO (Spectrum 1) and upon addition of lithium acetate (2 mol. equiv.) (Spectrum 2). $^1\text{H}$ NMR shifts: OH: $\delta$ 9.70 ppm (disappears upon acetate addition), H5: $\delta$ 7.77, 7.76 ppm, H4: $\delta$ 7.75, 7.74 ppm, H8: $\delta$ 7.68, 7.66 ppm, H7: 7.40-7.36 ppm, H6: $\delta$ 7.39-7.23 ppm, H1: $\delta$ 7.10 ppm, H3: $\delta$ 7.09 - 7.06 ppm. ....	103
Figure 4.22. $^1\text{H}$ NMR spectra of 1-naphthol (1.00 mM) in $d_6$ -DMSO (Spectrum 1) and upon addition of potassium acetate (2 mol. equiv.) (Spectrum 2). $^1\text{H}$ NMR shifts: H: $\delta$ 8.13, 8.11 ppm, H4: $\delta$ 7.81, 7.79 ppm, H8: $\delta$ 7.48-7.41 ppm, H3/H6: $\delta$ 7.33-7.27 ppm; H2: 6.87, 6.85 ppm. ....	103
Figure 4.23. $^1\text{H}$ NMR spectra of diol <b>5</b> (1.00 mM) in $d_6$ -DMSO (Spectrum 1) and upon addition of potassium acetate (2 mol. equiv.) (Spectrum 2). $^1\text{H}$ NMR shifts: H4: $\delta$ 7.79 ppm, H5: $\delta$ 7.76, 7.74 ppm; H8: $\delta$ 7.65, 7.63 ppm, H6/H7: $\delta$ 7.35-7.22 ppm, H1: $\delta$ 7.08 ppm, $\text{CH}_2$ : $\delta$ 4.63 ppm. ....	104
Figure 4.24. $^1\text{H}$ NMR spectra of diol <b>7</b> (1.00 mM) in $d_6$ -DMSO (Spectrum 1) and upon addition of potassium acetate (2 mol. equiv.) (Spectrum 2). $^1\text{H}$ NMR shifts: H8: $\delta$ 7.72,	

## List of Figures

---

7.70 ppm; H5: $\delta$ 7.66; H7: $\delta$ 7.64, 7.62 ppm, H4: $\delta$ 7.35, 7.33 ppm, H1: $\delta$ 7.08 ppm, H3: $\delta$ 7.06, 7.04 ppm, CH <sub>2</sub> : 4.58 ppm. ....	104
Figure 4.25. <sup>1</sup> H NMR spectra of donor <b>1</b> (1.00 mM) in CD <sub>3</sub> CN (Spectrum 1) and upon addition of TSP (1.6 mol. equiv.) (Spectrum 2). <sup>1</sup> H NMR shifts: H4: $\delta$ 7.84 ppm, H5: $\delta$ 7.83, 7.81 ppm; H8: $\delta$ 7.73, 7.71 ppm, H6/H7: $\delta$ 7.46-7.34 ppm, H1: $\delta$ 7.22 ppm, CH <sub>2</sub> : $\delta$ 5.15 ppm. ....	104
Figure 4.26. <sup>1</sup> H NMR spectra of donor <b>4</b> (1.00 mM) in d <sub>6</sub> -DMSO (Spectrum 1) and upon addition of lithium acetate (2 mol. equiv.) (Spectrum 2). <sup>1</sup> H NMR shifts: OH: 9.81 ppm (disappears upon acetate addition); H8: $\delta$ 7.80, 7.78 ppm; H5: $\delta$ 7.78 ppm; H7: $\delta$ 7.72, 7.70 ppm, H4: $\delta$ 7.39-7.37 ppm, H1: $\delta$ 7.13 ppm, H3: $\delta$ 7.11-7.09 ppm, CH <sub>2</sub> : $\delta$ 5.00 ppm. ....	105
Figure 4.27. (a) Emission of donor <b>4</b> ( $\mu$ M) and lithium acetate in DMSO. (b) Stern-Volmer quenching plot of <b>4</b> by lithium acetate in dry DMSO ( $\lambda_{\text{exc}} = 315$ nm).....	105
Figure 4.28. (a) Fluorescence of <b>4</b> ( $\mu$ M) and TSP in dry DMSO. (b) Stern-Volmer quenching plot of <b>4</b> by TSP in dry DMSO ( $\lambda_{\text{exc}} = 315$ nm).....	106
Figure 4.29. <sup>19</sup> F NMR spectra of <b>4</b> (1.00 mM) ) after photolysis for 5 min (Rayonet photoreactor, 8 x 350 nm bulbs, 4 W) in d <sub>6</sub> -DMSO (0.03% TMS by manufacturer) with 0-1.15 mol. equiv. of lithium acetate as determined by <sup>1</sup> H NMR integration. ....	107
Figure 4.30. <sup>19</sup> F NMR spectra of <b>4</b> (1.00 mM) after photolysis for 5 min (Rayonet photoreactor, 8 x 350 nm bulbs, 4 W) in d <sub>6</sub> -DMSO (0.03% TMS by manufacturer) with 0-1.00 mol. equiv of TSP as determined by <sup>1</sup> H NMR integration. ....	107
Figure 4.31. Mol. equiv. of acetate or TSP to <b>4</b> (1.00 mM) in d <sub>6</sub> -DMSO (0.03% TMS by manufacturer) versus HNO photorelease (indicated by %CF <sub>3</sub> SO <sub>2</sub> <sup>-</sup> ) to N-O bond cleavage (indicated by CF <sub>3</sub> SO <sub>2</sub> NH <sub>2</sub> ) after photolysis for 5 min (Rayonet photoreactor, 8 x 350 nm bulbs, 4 W).....	108
Figure 4.32. fs-TA of donor <b>4a</b> in aerobic 80:20 v/v MeCN to 5.0 mM phosphate buffer solution (pH 7.0) following excitation (a, b, and c; $\lambda_{\text{exc}} = 267$ nm). Kinetics at 390, 560, and 440 nm are shown in (d).....	109
Figure 4.33. fs-TA of donor <b>4b</b> in MeCN and donor <b>4a</b> in 80:20 v/v MeCN to 5.0 mM phosphate buffer solution, pH 7.0 following (a) $\sim 1$ ps and (b) $\sim 3$ ns after excitation. ....	110
Figure 4.34. Transient absorption spectral changes for 2-naphthol (150 $\mu$ M) in (a) anaerobic and (b) oxygenated 80:20 v/v MeCN to 5.0 mM phosphate buffer (pH 7.0; $\lambda_{\text{exc}}$	

## List of Figures

---

- = 266 nm). The vertical dashed line indicates the approximate wavelength above which the ground state species does not absorb; hence at longer wavelengths, ground state bleach is not a concern. .... 111
- Figure 4.35. Transient absorption spectral changes for diol **7** (150  $\mu\text{M}$ ) in anaerobic and oxygenated 80:20 v/v MeCN to 5.0 mM phosphate buffer (pH 7.0;  $\lambda_{\text{exc}} = 266 \text{ nm}$ ). The vertical dashed line indicates the approximate wavelength above which the ground state species does not absorb; hence at longer wavelengths, ground state bleach is not a concern. .... 111
- Figure 4.36. Transient absorption spectral changes for donor **4** (150  $\mu\text{M}$ ) in anaerobic and oxygenated 80:20 v/v MeCN to 5.0 mM phosphate buffer (pH 7.0;  $\lambda_{\text{exc}} = 266 \text{ nm}$ ). The vertical dashed line indicates the approximate wavelength above which the ground state species does not absorb; hence at longer wavelengths, ground state bleach is not a concern. .... 111
- Figure 4.37. ns-TA for donor **4** (100-150  $\mu\text{M}$ ) in (a) anaerobic and (b) oxygenated 80:20 v/v MeCN to 5.0 mM phosphate buffer solution, pH 7.0;  $\lambda_{\text{exc}} = 266 \text{ nm}$ . The vertical dashed line indicates the approximate wavelength above which the ground state species does not absorb; hence at longer wavelengths, ground state bleach is not a concern... 113
- Figure 4.38. (a) Transient absorption spectral changes of 2-naphthol (150  $\mu\text{M}$ ) after 1000 ns following excitation in anaerobic (dark gray) and oxygenated (light gray) 80:20 v/v MeCN to 5.0 mM phosphate buffer solution, pH 7.0. Probe wavelength is highlighted in green. The vertical dashed line indicates the approximate wavelength above which the ground state species does not absorb; hence at longer wavelengths, ground state bleach is not a concern. (b) Best fit of the kinetic trace at 440 nm observed in anaerobic conditions to a first-order rate equation giving  $k_{\text{obs}} = (4.2 \pm 0.1) \times 10^5 \text{ s}^{-1}$ . .... 114
- Figure 4.39. (a) Transient absorption spectral changes of diol **7** (150  $\mu\text{M}$ ) after 1000 ns following excitation in anaerobic (dark gray) and oxygenated (light gray) 80:20 v/v MeCN to 5.0 mM phosphate buffer solution, pH 7.0. Probe wavelength is highlighted in green. The vertical dashed line indicates the approximate wavelength above which the ground state species does not absorb; hence at longer wavelengths, ground state bleach is not a concern. (b) Best fit of the kinetic trace at 440 nm observed in anaerobic conditions to a first-order rate equation giving  $k_{\text{obs}} = (4.3 \pm 0.1) \times 10^5 \text{ s}^{-1}$ . .... 114
- Figure 4.40. (a) Transient absorption spectral changes of donor **4** (150  $\mu\text{M}$ ) after 1000 ns following excitation in anaerobic (dark gray) and oxygenated (light gray) 80:20 v/v

## List of Figures

---

- MeCN to 5.0 mM phosphate buffer solution, pH 7.0. The vertical dashed line indicates the approximate wavelength above which the ground state species does not absorb; hence at longer wavelengths, ground state bleach is not a concern. (b) Best fit of the kinetic trace at 440 nm observed in anaerobic conditions to a first-order rate equation giving  $k_{\text{obs}} = (4.3 \pm 0.1) \times 10^5 \text{ s}^{-1}$  (green) and at 300 nm giving  $k_{\text{obs}} = (2.6 \pm 0.1) \times 10^6 \text{ s}^{-1}$ . ..... 115
- Figure 4.41. Plot of transient absorption spectra for 2-naphthol, diol **7**, and donor **4** in anaerobic 80:20 v/v MeCN to 5.0 mM phosphate buffer solution (pH 7.0) (a) 200 ns and (b) 22  $\mu\text{s}$  after excitation;  $\lambda_{\text{exc}} = 266 \text{ nm}$ . The vertical dashed line indicates the approximate wavelength above which the ground state species does not absorb; hence at longer wavelengths, ground state bleach is not a concern. .... 116
- Figure 4.42. Laser flash photolysis of (a) 2-naphthol in anaerobic 80:20 v/v MeCN to 0.1 M NaOH, (b) 2-naphthol in oxygenated 80:20 v/v MeCN to 0.1 M NaOH, (c) **4** in anaerobic 80:20 v/v MeCN to 0.1 M NaOH, and (d) **4** in oxygenated 80:20 v/v MeCN to 0.1 M NaOH;  $\lambda_{\text{exc}} = 266 \text{ nm}$ . The vertical dashed line indicates the approximate wavelength above which the ground state species does not absorb; hence at longer wavelengths, ground state bleach is not a concern. .... 117
- Figure 4.43. (a) Transient absorption spectral changes for 2-naphthol and 2-naphtholate (150  $\mu\text{M}$ ) in oxygenated 80:20 v/v MeCN to 5 mM phosphate buffer, pH 7.0 or to 0.1 M NaOH, respectively, following 200 ns after excitation. The vertical dashed line indicates the approximate wavelength above which the ground state species does not absorb; hence at longer wavelengths, ground state bleach is not a concern. The decreased absorbance change at 360 nm for 2-naphtholate is attributed to ground state bleach. (b) UV-vis absorbance spectrum of 2-naphthol (in MeCN) and 2-naphtholate (in 80:20 v/v MeCN to 0.1 M NaOH);  $\lambda_{\text{exc}} = 266 \text{ nm}$ . .... 118
- Figure 4.44. (a) Transient absorption spectral changes for 2-naphthol (150  $\mu\text{M}$ ) in anaerobic and oxygenated 80:20 v/v MeCN to 0.1 M NaOH at 200 ns. The vertical dashed line indicates the approximate wavelength above which the ground state species does not absorb; hence at longer wavelengths, ground state bleach is not a concern. (b) Transient absorption spectral changes for donor **4** (150  $\mu\text{M}$ ) in anaerobic and oxygenated 80:20 v/v MeCN to 0.1 M NaOH at 200 ns;  $\lambda_{\text{exc}} = 266 \text{ nm}$ . .... 118
- Figure 4.45. Transient absorption spectral changes for **4** (150  $\mu\text{M}$ ) in oxygenated 80:20 v/v MeCN to 5.0 mM phosphate buffer (pH 7.0;  $\lambda_{\text{exc}} = 266 \text{ nm}$ ). The vertical dashed line

indicates the approximate wavelength above which the ground state species does not absorb; hence at longer wavelengths, ground state bleach is not a concern. ....	119
Figure 4.46. (a) Kinetic traces observed upon LFP of <b>4</b> (150 $\mu$ M) in listed solvent condition (oxygen purged; $\lambda_{\text{exc}} = 266$ nm). (b) Plot of observed pseudo-first order rate constant as a function of concentration of 5.0 mM phosphate buffer (pH 7.0) in MeCN; (c) Plot of amplitude of absorbance change as a function of concentration of 5.0 mM phosphate buffer (pH 7.0) in MeCN. ....	120
Figure 4.47. Absorbance change of <b>4</b> (150 $\mu$ M) at 300 nm following excitation in 50:50 v/v MeCN to 5.0 mM phosphate buffer, pH 7.0 with sodium azide concentrations of 0 mM (red), 5 mM (blue), and 15 mM (green); $\lambda_{\text{exc}} = 266$ nm.....	121
Figure 4.48. Kinetic traces observed upon LFP of <b>4</b> (150 $\mu$ M) in oxygenated (a) 80:20 v/v MeCN to 5.0 mM phosphate buffer, pH 7.0 and (b) 80:20 v/v MeCN to 5.0 mM phosphate buffer, pH 3.0; $\lambda_{\text{exc}} = 266$ nm. The decay traces were analyzed as pseudo-first order processes, giving $k_{\text{obs}} = (6.50 \pm 0.04) \times 10^6 \text{ s}^{-1}$ and $k_{\text{obs}} = (6.86 \pm 0.01) \times 10^6 \text{ s}^{-1}$ , respectively. ....	122
Figure 4.49. The reaction of (6-hydroxynaphthalen-2-yl)methyl cation and HNO to form 6-[( <i>E</i> )-(hydroxyimino)methyl]naphthalen-2-ol.....	123
Figure 4.50. LFP of donor <b>4</b> (150 $\mu$ M) and lithium acetate (~5 mol equiv) in (a) oxygenated and (b) Ar-purged MeCN; $\lambda_{\text{exc}} = 266$ nm. The vertical dashed line indicates the approximate wavelength above which the ground state species does not absorb; hence at longer wavelengths, ground state bleach is not a concern. ....	124
Figure 4.51. (a) Transient absorption spectral changes of donor <b>4</b> (150 $\mu$ M) and lithium acetate (~5 mol equiv) 1000 ns following excitation in anaerobic (dark gray) and oxygenated (light gray) in MeCN. Probe wavelengths are highlighted in green and pink. The vertical dashed line indicates the approximate wavelength above which the ground state species does not absorb; hence at longer wavelengths, ground state bleach is not a concern. (b) Best fit of the kinetic trace at 440 nm observed in anaerobic conditions to a first-order rate equation giving $k_{\text{obs}} = (4.5 \pm 0.3) \times 10^5 \text{ s}^{-1}$ (green) and best fit of the kinetic trace at 300 nm observed in anaerobic conditions to a first-order rate equation giving $k_{\text{obs}} = (3.1 \pm 0.1) \times 10^5 \text{ s}^{-1}$ (pink).....	124
Figure 4.52. (a)-(c) fs-TA of donor <b>4</b> in aerobic 80:20 v/v MeCN to 5.0 mM phosphate buffer solution (pD 7.0) achieved from 267 nm excitation. (d) Kinetics from 390 nm, 560 nm, and 440 nm in deuterated water (blue) and water (colored). ....	125

## List of Figures

---

Figure 5.1. Structures of photoactive HNO donors. ....	129
Figure 5.2. Selectivity for N-O bond cleavage (from $^{19}\text{F}$ NMR integration of $\text{CF}_3\text{SO}_2\text{NH}_2$ compared to other photoproducts). The concentration of aqueous component in $\text{CD}_3\text{CN}$ is 20% or 60% v/v aqueous MeCN, where the aqueous component is 0.1 M HCl, 0.1 M NaOH, 5.0 mM phosphate buffer (pH 3.0, 7.0), 5.0 mM acetate buffer (pH 5.0), 5.0 mM borate buffer (pH 9.0), or 5.0 mM carbonate buffer (pH 11.0). Steady state photolysis samples of <b>4</b> (0.500-1.00 mM) were prepared in anaerobic solutions and irradiated using a Rayonet photoreactor (8 x 350 nm bulbs, 4 W) until total degradation.....	131
Figure 5.3. (a) $^{19}\text{F}$ NMR spectra as a function of irradiation time (8 x 350 nm bulbs, 4 W; 0, 0.5, 1, 3, 7, 15, 31, and 61 min) for the photodecomposition of donor <b>4</b> (0.500 mM) in anaerobic $\text{CD}_3\text{CN}$ . (b) Plot of observed species as a function of irradiation time. Final composition: $\text{CF}_3\text{SO}_2\text{NH}_2$ ( $\delta$ -81.1 ppm; 88%); $\text{CF}_3\text{SO}_2\text{NH}^-$ ( $\delta$ -79.9 ppm; 10%). (c) Best fit of the peak area of donor <b>4</b> ( $-\text{CF}_3$ ) to a first-order rate equation, giving $k_{\text{obs}} = 0.075 \pm 0.003 \text{ min}^{-1}$ .....	132
Figure 5.4. $^1\text{H}$ NMR spectra as a function of irradiation time (8 x 350 nm bulbs, 4 W; 0, 0.5, 1, 3, 15, 31, and 61 min) for the photodecomposition of donor <b>4</b> (0.500 mM) in anaerobic $\text{CD}_3\text{CN}$ .....	132
Figure 5.5. (a) $^1\text{H}$ NMR spectrum of <b>4</b> in $\text{CD}_3\text{CN}$ after 3 min. irradiation (18% conversion to $\text{CF}_3\text{SO}_2\text{NH}_2$ by $^{19}\text{F}$ NMR spectroscopy); (b) $^1\text{H}$ NMR spectrum of an authentic sample of <b>4</b> in $\text{CD}_3\text{CN}$ ; (c) $^1\text{H}$ NMR spectrum of an authentic sample of aldehyde <b>8</b> in $\text{CD}_3\text{CN}$ . ....	133
Figure 5.6. Transient absorption spectral changes of 2-naphthol (150 $\mu\text{M}$ ) in (a) anaerobic and (b) oxygenated MeCN. The vertical dashed line indicates the approximate wavelength above which the ground state species does not absorb; hence at longer wavelengths, ground state bleach is not a concern. ....	135
Figure 5.7. Transient absorption spectral changes of donor <b>4</b> (150 $\mu\text{M}$ ) in (a) anaerobic and (b) oxygenated MeCN. The vertical dashed line indicates the approximate wavelength above which the ground state species does not absorb; hence at longer wavelengths, ground state bleach is not a concern. ....	135
Figure 5.8. (a) Transient absorption spectral changes of 2-naphthol (150 $\mu\text{M}$ ) after 1000 ns following excitation in anaerobic (dark gray) and oxygenated (light gray) MeCN. Probe wavelength is highlighted in green. The vertical dashed line indicates the approximate wavelength above which the ground state species does not absorb; hence at	

longer wavelengths, ground state bleach is not a concern. (b) Best fit of the kinetic trace at 440 nm observed in anaerobic conditions to a first-order rate equation giving $k_{\text{obs}} = (4.4 \pm 0.1) \times 10^5 \text{ s}^{-1}$ .....	136
Figure 5.9. (a) Transient absorption spectral changes of donor <b>4</b> (150 $\mu\text{M}$ ) after 1000 ns following excitation in anaerobic (dark gray) and oxygenated (light gray) MeCN. Probe wavelength is highlighted in green. The vertical dashed line indicates the approximate wavelength above which the ground state species does not absorb; hence at longer wavelengths, ground state bleach is not a concern. (b) Best fit of the kinetic trace at 440 nm observed in anaerobic conditions to a first-order rate equation giving $k_{\text{obs}} = (4.5 \pm 0.1) \times 10^5 \text{ s}^{-1}$ .....	136
Figure 5.10. ns-TA spectrum from excitation of donor <b>4b</b> in aerobic MeCN.....	137
Figure 5.11. (a) Transient absorption spectra for 2-naphthol and <b>4</b> in oxygenated MeCN at 900 ns. The vertical dashed line indicates the approximate wavelength above which the ground state species does not absorb; hence at longer wavelengths, ground state bleach is not a concern. (b) Single wavelength kinetics at 310 nm. (c) UV-vis spectra for aldehyde <b>8</b> (75 $\mu\text{M}$ ) and <b>4</b> (80 $\mu\text{M}$ ) in MeCN.....	138
Figure 5.12. fs-TA of donor <b>4b</b> in aerobic MeCN achieved from 267 nm excitation. .	139
Figure 5.13. (a) $^{19}\text{F}$ NMR spectra as a function of irradiation time (8 x 350 nm bulbs, 4 W; 0, 4, 8, 12, 16, and 24 min) for the photodecomposition of <b>4</b> (2.49 mM) in anaerobic 60:40 v/v $\text{CD}_3\text{CN}$ to 0.1 M NaOH. (b) Plot of observed species as a function of irradiation time. (c) Best fit of donor <b>4</b> ( $-\text{CF}_3$ ) to a first-order rate equation, giving $k_{\text{obs}} = 0.20 \pm 0.01 \text{ min}^{-1}$ .....	140
Figure 5.14. (a) $^1\text{H}$ NMR spectrum of <b>4</b> (2.49 mM) in 80:20 v/v $\text{CD}_3\text{CN}$ to 0.1 M NaOH upon total photolysis (50% conversion to $\text{CF}_3\text{SO}_2\text{NH}_2$ ). (b) $^1\text{H}$ NMR spectrum of an authentic sample of <b>4</b> in 80:20 v/v $\text{CD}_3\text{CN}$ to 0.1 M NaOH. $\delta = 7.63, 7.54, 7.33, 7.31, 7.00, 6.99, 6.97, 6.83 \text{ ppm}$ . (c) $^1\text{H}$ NMR spectrum of an authentic sample of aldehyde <b>8</b> in 80:20 v/v $\text{CD}_3\text{CN}$ to 0.1 M NaOH. Aldehyde <b>8</b> : $\delta = 8.22, 7.80, 7.78, 7.67, 7.65, 7.57, 7.54, 7.05, 7.03, \text{ and } 6.89 \text{ ppm}$ .....	141
Figure 5.15. (a) Emission spectra of donor <b>4</b> ( $\mu\text{M}$ ) in MeCN upon addition of 20-95% by vol. of 5.0 mM phosphate buffer solution, pH 7.0. (b) Emission spectra of 2-naphthol ( $\mu\text{M}$ ) in MeCN upon addition of 20-95% vol. of 5.0 mM phosphate buffer solution, pH 7.0.....	142

## List of Figures

---

- Figure 5.16. Effect of solvent composition on the percentage of N-O bond cleavage generated upon irradiation of HNO donor **4a** (0.500-2.00 mM; Rayonet photoreactor, 8 x 350 nm bulbs, 4 W) in mixtures of 5.0 mM phosphate buffer (pH 7.0) in CD<sub>3</sub>CN (v/v). ..... 143
- Figure 5.17. <sup>19</sup>F NMR of photolyzed donor **1** (1.00 mM; Rayonet photoreactor, 8 x 350 nm bulbs, 4 W) in (a) anaerobic CD<sub>3</sub>CN and (b) with addition of 20% by volume 5.0 mM phosphate buffer solution, pH 7.0. .... 144
- Figure 5.18. (a) <sup>1</sup>H NMR spectra of photolyzed donor **1** (1.00 mM; Rayonet photoreactor, 8 x 350 nm bulbs, 4 W) in anaerobic CD<sub>3</sub>CN (100% conversion to CF<sub>3</sub>SO<sub>2</sub>NH<sub>2</sub>). (b) <sup>1</sup>H NMR spectrum of authentic aldehyde **6** in CD<sub>3</sub>CN. Aldehyde **6**:  $\delta = 10.26, 10.12, 8.37, 7.99, 7.97, 7.78, 7.76, 7.63, 7.63, 7.61, 7.61, 7.59, 7.44, 7.42, 7.42, 7.40, 7.29$  ppm. (c) <sup>1</sup>H NMR spectrum of authentic diol **7** in CD<sub>3</sub>CN.  $\delta = 7.78, 7.76, 7.73, 7.70, 7.68, 7.42, 7.41, 7.40, 7.40, 7.38, 7.37, 7.32, 7.32, 7.30, 7.30, 7.30, 7.28, 7.16, 4.79$  ppm. Residual chloroform is observed at 7.68 ppm. .... 145
- Figure 5.19. (a) <sup>19</sup>F NMR spectra as a function of irradiation time (0, 0.5, 1.0, 2.0, 6.0, and 8.0 min) for the photodecomposition of HNO donor **1** (1.0 mM) in an anaerobic mixture of 60:40 v/v CD<sub>3</sub>CN to 5 mM phosphate buffer solution, pH 7.0. (b) Plot of observed species as a function of irradiation time. Final composition: CF<sub>3</sub>SO<sub>2</sub><sup>-</sup> ( $\delta -88.7$  ppm; 41%); CF<sub>3</sub>SO<sub>2</sub>NH<sub>2</sub> ( $\delta -81.2$  ppm; 59%). (c) Best fit of the peak area of donor **1** (-CF<sub>3</sub>) to a first-order rate equation, giving  $k_{\text{obs}} = 0.38 \pm 0.03 \text{ min}^{-1}$ . .... 146
- Figure 5.20. (a) <sup>31</sup>P NMR spectra for an anaerobic solution of TXPTS (2.30 mM) in 80:20 v/v CD<sub>3</sub>CN to phosphate buffer (5.0 mM, pH 7.0); (b) Sample (a) irradiated for 132 min (Rayonet photoreactor, 8 x 350 nm bulbs, 4 W). The peaks at  $\delta 1.75$  (a) and 2.07 ppm (b; note that the insufficient buffering capacity of the buffer is most likely responsible for the difference in chemical shift values) can be assigned to the phosphate buffer,  $\delta 0.00$  ppm to the external reference (phosphoric acid),  $\delta -35.12$  ppm to TXPTS, and  $\delta -38.2$  and  $-41.8$  ppm to two major products of TXPTS photodecomposition. (No attempt was made to characterize these latter species.) ..... 148
- Figure 5.21. Plot of the <sup>31</sup>P NMR peak area of TXPTS versus total irradiation time. The data has been fit to a first-order equation, giving  $k_{\text{obs}} = 0.029 \pm 0.002 \text{ min}^{-1}$ . .... 148
- Figure 5.22. (a) <sup>31</sup>P NMR spectra of a solution of TXPTS (5.00 mM) and CH<sub>3</sub>SO<sub>2</sub>NHOH (2.50 mM) in an anaerobic mixture of 80:20 v/v MeCN to 5 mM carbonate buffer (pH

10.3). (b) $^{31}\text{P}$ NMR spectra of the same sample upon irradiation (5 min, 8 x 350 nm bulbs, 4 W). .....	149
Figure 5.23. $^{31}\text{P}$ NMR spectra for (1) the photodecomposition of TXPTS (20 mM; 350 nm, 4 W, 12 min irradiation) in an anaerobic mixture of 20:80 v/v $\text{CD}_3\text{CN}$ to 5.0 mM phosphate buffer (pH 7.00), (2) solution 1 with addition of Angeli's salt (1 mM, no further irradiation), (3) a photolysis solution of donor <b>1</b> (5 mM) and TXPTS (20 mM) in an anaerobic mixture of 20:80 v/v $\text{CD}_3\text{CN}$ to 5.0 mM phosphate buffer (pH 7.00; 350 nm, 4 W, 12 min irradiation) and (4) solution 3 with addition of Angeli's salt (1 mM, no further irradiation).....	151
Figure 5.24. A proposed pathway for excited state intramolecular proton transfer to generate aldehyde <b>6</b> and the corresponding sulfonamide. <sup>23</sup> .....	152
Figure 6.1. The structure of vitamin B <sub>12</sub> : X = $\text{CN}^-$ , $\text{CH}_3$ , Ado, $\text{H}_2\text{O}$ , NO etc.....	155
Figure 6.2. (a) $^1\text{H}$ NMR spectra of an equilibrated solution of HOCbl (6.00 mM) with 1.0 molar equivalents of Piloty's acid in anaerobic 0.5 M carbonate buffer (pD 10.0). (b) $^1\text{H}$ NMR spectra of HOCbl (6.00 mM) with 1.5 mol. equiv. of Piloty's acid in anaerobic 0.5 M phosphate buffer (pD 12.5; Spectrum 2); (c) $^1\text{H}$ NMR spectra of HOCbl (6.00 mM) with 2.5 mol. equiv. on Piloty's acid in anaerobic 0.1 M NaOD (Spectrum 3). $\text{NO}^-$ -Cbl(III): $\delta \sim 7.42, 7.20, 6.80, 6.34, 6.25$ ppm. Piloty's acid: 8.43 ppm. $\text{PhSO}_2^-$ : 7.67-7.65, 7.55-7.54 ppm. ....	157
Figure 6.3. Percent $\text{NO}^-$ -Cbl(III) formed as a function of the rate constant of reaction ( $\text{HNO} + \text{HOCbl} \rightarrow \text{NO}^-$ -Cbl(III); $[\text{HOCbl}] = 8.5 \times 10^{-5}$ M) simulated from a model incorporating Eqn. 6.1, Eqn. 6.2, Eqn. 6.3, Eqn. 6.4, Eqn. 6.6, and Eqn. 6.7, at pH 10.2. ....	158
Figure 6.4. Percent product formed as a function of rate constant ( $\text{HNO} + \text{HOCbl} \rightarrow \text{NO}^-$ -Cbl(III); $[\text{HOCbl}] = 8.5 \times 10^{-5}$ M) simulated by a model incorporating Eqn. 6.1, Eqn. 6.4, and Eqn. 6.7 at pH 9.5.....	158
Figure 6.5. Overlaid best fit (solid line) of the reaction between HNO as generated by Piloty's acid (0.0128 M) and HOCbl ( $8.5 \times 10^{-5}$ M) monitored at 535 nm to the model described in Table 6.2 for data collected at pH 10.05 (a) and pH 10.12 (b) on the experimental data (dotted line). The rate constant between HNO and HOCbl was calculated to be $(2.46 \pm 0.01) \times 10^4 \text{ M}^{-1}\text{s}^{-1}$ .....	159
Figure 6.6. Absorbance at 535 nm for the reaction of Piloty's acid (0.0150 M) with HOCbl ( $\sim 1 \times 10^{-4}$ M) in anaerobic 0.2 M carbonate buffer (pH 10.0, 11.5, and 12.5)...	160

## List of Figures

---

- Figure 6.7. (a) UV-vis spectra of  $\text{NO}^-$ -Cbl(III) ( $7.2 \times 10^{-5}$  M) upon addition of Piloty's acid (0.015 M) in anaerobic 0.2 M phosphate buffer (final pH 12.5,  $I = 1.0$  M ( $\text{NaCF}_3\text{SO}_3$ )) monitored for 45 min. (b) Absorbance at 535 nm. .... 161
- Figure 6.8. (a) UV-vis spectra for  $\text{NO}^-$ -Cbl(III) ( $7.0 \times 10^{-5}$  M) upon addition of benzenesulfinate, sodium salt (0.015 M) in anaerobic 0.2 M phosphate buffer (pH 12.0,  $I = 1.0$  M ( $\text{NaCF}_3\text{SO}_3$ )) as monitored for 60 min. (b) Absorbance at 535 nm. .... 161
- Figure 6.9. (a) UV-vis spectra for  $\text{NO}^-$ -Cbl(III) ( $7.0 \times 10^{-5}$  M) upon the addition of Piloty's acid (0.015 M) in anaerobic 0.20 M phosphate buffer (pH 10.0,  $I = 1.0$  M ( $\text{NaCF}_3\text{SO}_3$ )). The reaction was monitored for 40 min. Inset: Plot of absorbance at 535 nm versus time. (b) UV-vis spectra of  $\text{NO}^-$ -Cbl(III) ( $7.8 \times 10^{-5}$  M) upon the addition of Piloty's acid (0.0150 M) in 0.15 M NaOH ( $I = 1.0$  M ( $\text{NaCF}_3\text{SO}_3$ )). Inset: Absorbance at 535 nm as a function of time.  $\text{NO}^-$ -Cbl(III) partially reacts with Piloty's acid, isosbestic points are observed at 375 and 499 nm. Inset: Plot of absorbance at 535 nm versus time. .... 162
- Figure 6.10. (a) UV-vis spectra of  $\text{NO}^-$ -Cbl(III) ( $\sim 7.0 \times 10^{-5}$  M) in anaerobic 0.1 M NaOH monitored every minute for 1 hr. (b) UV-vis absorption spectra of  $\text{HO}^+\text{Cbl}$  ( $8.5 \times 10^{-5}$  M) in anaerobic 0.2 M phosphate buffer (pH 12.5) monitored for 8 hr. .... 162
- Figure 6.11.  $^1\text{H}$  NMR spectra of  $\text{NO}^-$ -Cbl(III) ( $5.0 \times 10^{-4}$  M) in 0.15 M NaOD upon addition: (a) no Piloty's acid, (b) 0.3 mol. equiv. of Piloty's acid, (c) 1.0 mol. equiv. of Piloty's acid, (d) 1.5 mol. equiv. of Piloty's acid, and (e) 3.0 mol. equiv. of Piloty's acid. Spectra were recorded 2-3 hr after solution preparation. Decomposition of  $\text{NO}^-$ -Cbl(III) in 0.15 M NaOD is observed (10-20%; new peaks observed at  $\delta$  7.89, 7.14, 7.02, 6.46, 6.20 ppm).  $\text{NO}^-$ -Cbl(III):  $\delta$  7.47, 7.22, 6.84, 6.36, 6.26 ppm. Unreacted Piloty's acid: 8.43 ppm.  $\text{PhSO}_2^-$ : 7.67-7.65, 7.55-7.54 ppm. .... 164
- Figure 6.12.  $^1\text{H}$  NMR spectra of  $\text{NO}^-$ -Cbl(III) ( $5.0 \times 10^{-4}$  M) in anaerobic 0.15 M NaOD with the addition of sodium cyanide ( $\sim 10$  mol. equiv.) immediately upon sample preparation (Spectrum 1) and addition of sodium cyanide 2.5 hr following sample preparation (Spectrum 2). Dicyanocobalamin ( $\delta$  8.38, 7.51, 7.39, 6.35, 6.34, 5.87 ppm) highlighted with purple boxes. .... 165
- Figure 6.13. (a) Spectra taken after 20-30 min for the reaction between  $\text{NO}^-$ -Cbl(III) ( $\sim 7.0 \times 10^{-5}$ ) and Piloty's acid (0.015 M) in anaerobic 0.2 M buffered solutions (carbonate or phosphate,  $I = 1.0$  M ( $\text{NaCF}_3\text{SO}_3$ )) or sodium hydroxide solutions (0.15-0.35 M,  $I = 1.0$  M ( $\text{NaCF}_3\text{SO}_3$ )). (b) Plot of initial rate as a function of pH for the reaction between  $\text{NO}^-$

-Cbl(III) ( $\sim 7.0 \times 10^{-5}$ ) and Piloty's acid (0.015 M) in anaerobic 0.2 M buffered solutions (carbonate or phosphate, $I = 1.0$ M (NaCF <sub>3</sub> SO <sub>3</sub> )) or sodium hydroxide solutions (0.15-0.35 M, $I = 1.0$ M (NaCF <sub>3</sub> SO <sub>3</sub> )). Initial rates were calculated by determining the initial slope of plots of change in concentration versus time ( $\Delta c = \Delta \text{Abs} / (\epsilon(\text{HOCbl}) - \epsilon(\text{NO}^- \text{-Cbl(III)}))$ ); $\epsilon(\text{HOCbl}) = 8260 \text{ M}^{-1} \text{ cm}^{-1}$ and $\epsilon(\text{NO}^- \text{-Cbl(III)}) = 4430 \text{ M}^{-1} \text{ cm}^{-1}$ at 535 nm; determined by experiment.....	166
Figure 6.14. Change in absorbance at 535 nm as a function of pH for the reaction between NO <sup>-</sup> -Cbl(III) ( $\sim 7.0 \times 10^{-5}$ ) and Piloty's acid (0.015 M) in anaerobic 0.2 M buffered solutions (carbonate or phosphate, $I = 1.0$ M (NaCF <sub>3</sub> SO <sub>3</sub> )) or sodium hydroxide solutions (0.15-0.35 M, $I = 1.0$ M (NaCF <sub>3</sub> SO <sub>3</sub> ))......	166
Figure 6.15. (a) Plot of absorbance at 535 nm versus time upon the addition of a concentrated stock solution of NO <sup>-</sup> -Cbl(III) ( $\sim 7.0 \times 10^{-5}$ M) in anaerobic H <sub>2</sub> O to anaerobic 0.35 M NaOH. Inset: Final spectrum. (b) Plot of absorbance at 535 nm versus time upon the addition of a concentrated stock solution of HOCbl ( $\sim 7.0 \times 10^{-5}$ M) in anaerobic H <sub>2</sub> O to anaerobic 0.35 M NaOH. Inset: Final spectrum. ....	167
Figure 7.1. Simplified Jablonski diagram for donor <b>4</b> . S <sub>0</sub> : Ground state; S <sub>n</sub> (n≥1): excited singlet states; F: fluorescence; IC: internal conversion. Not depicted: intersystem crossing (ISC).....	171
Figure 7.2. The proposed reaction of (6-hydroxynaphthalen-2-yl)methyl cation and HNO to form 6-[(E)-(hydroxyimino)methyl]naphthalen-2-ol. ....	171
Figure 7.3. Photolysis of 6-[(E)-(hydroxyimino)methyl]naphthalen-2-ol. ....	172
Figure 7.4. Proposed modifications to the HNM-photocage. ....	173
Figure A1. <sup>1</sup> H NMR spectrum of Piloty's Acid in d <sub>6</sub> -acetone.....	191
Figure A2. <sup>1</sup> H NMR of MSHA-TBS in CDCl <sub>3</sub> .....	191
Figure A3. <sup>1</sup> H NMR spectrum of MSHA in DMSO.....	191
Figure A4. <sup>1</sup> H NMR spectrum of NO <sup>-</sup> -Cbl(III) in anaerobic D <sub>2</sub> O.....	192
Figure A5. <sup>1</sup> H NMR spectrum of diol <b>10</b> in d <sub>6</sub> -acetone.....	192
Figure A6. Example of method used to determine molar attenuation coefficients. a) Plot of donor <b>4</b> 's absorption (53, 104, 154, 203, and 251 μM) in 60:40 v/v MeCN to 5.0 mM phosphate buffer. (b) Plot of absorbance at 276 nm as a function of concentration. The molar extinction coefficient (slope) is $(5.54 \pm 0.06) \times 10^3 \text{ M}^{-1} \text{ cm}^{-1}$ .....	194
Figure A7. (a) Typical UV-vis spectra of solutions of azobenzene (67 μM, in MeOH) irradiated for 0 – 150 s using a Xe lamp ( $313 \pm 2$ nm, monochromator slit width = 2.0	

## List of Figures

---

mm). The initial absorbance at $A_{313} = 1.670$ a.u. The photon flux was $\phi = (1.08 \pm 0.12) \times 10^{-9}$ einsteins $s^{-1}$ . (b) Moles of <i>cis</i> -azobenzene photoproduct calculated from the absorbance change at 313 nm as a function of total irradiation time. Maximum conversion = 8.9%.....	195
Figure A8. (a) $^{19}\text{F}$ NMR spectra following photolysis of donor <b>4</b> (224 $\mu\text{M}$ ) in anaerobic 60:40 v/v MeCN : 5.0 mM phosphate buffer solution, pH 7.0, as of function of irradiation time (1: 0 min, 2: 3.00 min, 3: 6.00 min, and 4: 9.00 min; no more than 6.1% conversion). NMR samples were prepared as a 1:1 ratio of photolysis solution with MeOD, and $\alpha,\alpha,\alpha$ -trifluorotoluene was used as an internal standard ( $\alpha,\alpha,\alpha$ -trifluorotoluene impurity observed at $\delta$ -79.94 ppm). $A_{313} = 0.273$ a.u. (b) Plot of moles $\text{CF}_3\text{SO}_2^-$ generated from the photolysis of compound <b>4</b> as a function of time. Using azobenzene as the actinometer, $\Phi_{\text{PP}} = 0.51 \pm 0.07$ .....	195
Figure A9. Global analysis of 2-naphthol in oxygenated 80:20 v/v MeCN to 5.0 mM phosphate buffer solution (pH 7.0): (a) fitted data with two processes; (b) residual sum square progression of the fit; (c) component spectra; (d) lifetime of three components on a linear time scale.....	196
Figure A10. Global analysis of 2-naphthol in oxygenated MeCN: (a) fitted data with two processes; (b) residual sum square progression of the fit; (c) component spectra; (d) lifetime of three components on a linear time scale.....	197
Figure A11. Global analysis of 2-naphtholate in oxygenated 80:20 v/v MeCN to 0.1 M NaOH: (a) fitted data with two processes shown; (b) residual sum square progression of the fit; (c) component spectra; (d) lifetime of three components on a linear time scale. ....	198
Figure A12. Global analysis of diol <b>7</b> in oxygenated 80:20 v/v MeCN to 5.0 mM phosphate buffer solution (pH 7.0): (a) fitted data with two processes; (b) residual sum square progression of the fit; (c) component spectra; (d) lifetime of three components on a linear time scale.....	199
Figure A13. Global analysis of <b>4</b> in oxygenated 80:20 v/v MeCN to 0.1 M NaOH: (a) fitted data with two processes shown; (b) residual sum square progression of the fit; (c) component spectra; (d) lifetime of three components on a linear time scale.....	200
Figure A14. Global analysis of donor <b>4</b> in oxygenated 80:20 v/v MeCN to 5.0 mM phosphate buffer solution (pH 7.0): (a) fitted data with two processes; (b) residual sum	

## List of Figures

---

square progression of the fit; (c) component spectra; (d) lifetime of three components on a linear time scale.....	201
Figure A15. Global analysis of donor <b>4</b> in oxygenated MeCN: (a) fitted data with two processes; (b) residual sum square progression of the fit; (c) component spectra; (d) lifetime of three components on a linear time scale.....	202
Figure A16. Kinetic traces for the reaction between NO <sup>-</sup> -Cbl(III) ( $\sim 7.0 \times 10^{-5}$ M) and Piloty's acid (0.015 M) in anaerobic 0.2 M buffered solutions (carbonate or phosphate, $I = 1.0$ M (NaCF <sub>3</sub> SO <sub>3</sub> )) or sodium hydroxide solutions (0.15-0.35 M, $I = 1.0$ M (NaCF <sub>3</sub> SO <sub>3</sub> )) taken at 535 nm.....	204

# LIST OF SCHEMES

Scheme 1.1. Release of bioactive molecule (red circle) from photoprotecting group (blue-green). .....	2
Scheme 1.2. HNO release from cyanamide. ....	7
Scheme 1.3. HNO release from diazeniumdiolates. <sup>77</sup> .....	11
Scheme 1.4. Mechanism of Piloty's acid's decomposition and release of HNO.....	11
Scheme 1.5. Hydrolysis of acyloxy nitroso compounds to release HNO.....	12
Scheme 1.6. Release of HNO from acyl nitroso compounds. ....	14
Scheme 1.7. Release of acyl nitroso compounds from acyl nitroso-9,10-dimethylantracene cycloadducts. ....	14
Scheme 1.8. Jablonski diagram where valence electrons are excited by absorption of light to a singlet excited state ( $S_1$ , $S_2$ , etc.). Vibrational relaxation occurs rapidly via radiationless transitions to the lowest excited singlet state ( $S_1$ ). Fluorescence (re-emission of light) occurs from the lowest excited singlet state. Intersystem crossing may occur to a triplet state ( $T_1$ ), in which case phosphorescence may occur. Non-radiative decay may also occur to the electronic ground state. Photolytic pathways are discussed elsewhere. ....	16
Scheme 1.9. Photolysis of Angeli's salt.....	17
Scheme 1.10. Photorelease of HNO via hetero-Diels–Alder cycloadducts from acyl nitroso derivatives and 9,10-dimethylantracene. ....	18
Scheme 1.11. Photorelease of nitrosocarbonyls from 1,2,4-oxadiazole-4-oxides.....	19
Scheme 1.12. Photorelease the conjugate base of 2-nitro- <i>N</i> -hydroxybenzenesulfonamide from the (7-diethylaminocoumarin-4-yl)methyl photocage. 2-Nitro- <i>N</i> -hydroxybenzenesulfonamide subsequently thermally decomposes to then release HNO. ....	20
Scheme 1.13. Change in electronic density upon excitation of exemplar 2-naphthol in the $S_1$ state in $H_2O$ . <sup>126</sup> .....	21
Scheme 1.14. Traditional Jablonski diagram showing the Forster cycle.....	22
Scheme 1.15. Protolytic dissociation mechanism under neutral pH conditions where $k_R$ and $k_{-R}$ are the rate constants of forward and backward proton transfer along the hydrogen bond; $k_{sep}$ and $k_{rec}$ are the separation and formation of the ion-pair (typically separated by 2-3 hydrogen-bonded water molecules), $k_{NR}$ corresponds to non-radiative decay (fluorescence of this pair is not observed in typical experimental conditions).....	23

## List of Schemes

---

Scheme 1.16. Naphthalene's structure with the first two transition dipole moments with numbering system of naphthalene; carbon 4a and 8a are unmarked. ....	23
Scheme 1.17. Reaction scheme for the photohydration of 2-ethynylphenol. ....	26
Scheme 1.18. Reaction scheme for the photohydration of 2-ethenylphenol. ....	26
Scheme 1.19. Excitation of <i>o</i> -hydroxy- <i>t</i> -stilbene. ....	27
Scheme 1.20. Formation of a QM from excitation of 1,1'-(2,2'-dihydroxy-1,1'-binaphthyl-6,6'-diyl)bis(N,N,N-trimethylmethanaminium) bromide. ....	28
Scheme 1.21. QM formation from excitation of 4'-(1-phenylethenyl)[1,1'-biphenyl]-4-ol in aqueous MeCN. ....	29
Scheme 1.22. Excitation of 2-phenylphenol in MeCN and in H <sub>2</sub> O. ....	30
Scheme 3.1. Photolytic pathways accessible to donor <b>1-3</b> . ....	51
Scheme 3.2. Ground state ionization equilibria for donor <b>4</b> . ....	54
Scheme 3.3. Possible photodecomposition mechanisms leading to the release of leaving group (LG) from photolysis of a 6,2-HNM photocaged molecule. Bond homolysis is shown in pathway (a), heterolytic cleavage in pathway (b), and heterolytic cleavage resulting in QM formation in pathway (c). ....	68
Scheme 3.4. Pathway leading to HNO generation for donor <b>4</b> . ....	81
Scheme 4.1. Possible heterolytic bond cleavage pathways leading to HNO photorelease from donor <b>4</b> . ....	83
Scheme 4.2. Ground state acid-base equilibria for donor <b>4</b> . ....	84
Scheme 4.3. Proposed photolytic pathways accessible to donor <b>4</b> . ....	84
Scheme 4.4. Possible pathways to QM formation from 6,2-HNM-LG. ....	86
Scheme 5.1. The major decomposition pathways observed upon photolysis of HNO donors <b>1-3</b> . <sup>23</sup> ....	129
Scheme 5.2. Photolytic pathways accessible to donor <b>4</b> . ....	129
Scheme 5.3. Ground state ionization equilibria for donor <b>4</b> . ....	131
Scheme 5.4. Proposed decomposition pathways observed upon photolysis of HNO donors <b>1</b> in MeCN. ....	145
Scheme 5.5. HNO reacts with the phosphine TXPTS to give the corresponding phosphine oxide and aza-ylide. ....	147
A.6. Equilibrium constant calculation for spectrophotometric titration. ....	193

# LIST OF TABLES

Table 1.1. Examples of photophysical and photochemical processes. ....	16
Table 2.1. ESI-MS operating parameters.....	41
Table 2.2. Effect of monochromators' slit widths on probe signal amplitude and scatter from 355 nm excitation of ruthenium trisbipyridine dichloride in aerobic water.....	44
Table 2.3. Absorbance change seen at 320 nm for the laser flash photolysis of <b>4</b> (~ $\mu\text{M}$ ) in 80:20 v/v MeCN to 5.0 mM phosphate buffer, pH 7.0 using a Nd:YAG laser fitted with 2 <sup>nd</sup> and 4 <sup>th</sup> harmonic generators operating at 60 mJ/pulse, 44 mJ/pulse, and 28 mJ/pulse. Three trials at each power are averaged.....	45
Table 3.1. Comparison of the concentrations of $\text{CF}_3\text{SO}_2^-$ ( $\mu\text{M}$ ) and $\text{NO}^-$ -Cbl(III) ( $\mu\text{M}$ ) in the product solution upon partial irradiation of donor <b>4</b> in an anaerobic mixture of 40:60 v/v MeCN to 0.1 M phosphate buffer (pD 7.0). ....	64
Table 3.2. Abundance of $\text{N}_2\text{O}$ generated by Angeli's salt (AS) and from partial photolysis of <b>4</b> (0.500 mM) in an anaerobic mixture of 5:95 v/v MeCN to 0.1 M phosphate buffer, pH 7.0.....	66
Table 3.3. Mass assignments for the ion signals ( $m/z$ ) obtained from (A) a product mixture resulting from partial photolysis of donor <b>4</b> (1.00 mM; 25% conversion to $\text{CF}_3\text{SO}_2^-$ ) and (B) a product mixture (100 $\mu\text{M}$ maximum concentration) resulting from partial photolysis of donor <b>4</b> (1.00 mM; 33% conversion to 9:1 $\text{CF}_3\text{SO}_2^-$ : $\text{CF}_3\text{SO}_2\text{NH}_2$ ) and $\text{H}_2\text{OCbl}^+$ (3 mol. equiv.) in an anaerobic mixture of 60:40 v/v MeOH to 5.0 mM phosphate buffer (pH 7.0). ....	77
Table 4.1. Parameters used in Forster cycle $\text{p}K_{\text{a(OH)}}^*$ calculation for 2-naphthol and donor <b>4</b> .....	90
Table 4.2. Optical properties of 2-naphthol in water <sup>248</sup> and donor <b>4</b> measured in MeCN and DMSO. Absorbance maximum for $^1\text{L}_b \leftarrow \text{S}_0$ transitions = $\lambda\text{S1maxA}$ ; absorbance maximum for $^1\text{L}_a \leftarrow \text{S}_0$ = $\lambda\text{S2maxA}$ , nm; molar extinction coefficient = $\epsilon$ . ....	91
Table 4.3. Kamlet-Taft solvatochromatic parameters for solvents used in this thesis. <sup>249</sup> ....	93
Table 4.4. Decay of triplet states and $\text{ArO}^*$ generated upon laser flash photolysis of 2-naphthol, diol <b>7</b> and donor <b>4</b> in 80:20 v/v MeCN to 5.0 mM phosphate buffer (pH 7.0) or 0.1 M NaOH (discussed in Section 4.7.4). Triplet decay rates were analyzed at 420 or 440 nm; amplitude at 440 nm is reported. Naphthoxyl radical decay rates were analyzed	

## List of Tables

---

at 360 and 440 nm and global analysis (see Appendix D); amplitude at 360 nm is reported in 5.0 mM phosphate buffer (pH 7.0) and at 480 nm in 0.1 M NaOH. ....	112
Table 5.1. Observed pathway ratios for HNM-photocaged HNO donors in aqueous MeCN (pH 7.0). ....	129
Table 5.2. Photoproduct quantum yields for HNO photorelease (as indicated by chemical markers $\text{CF}_3\text{SO}_2^-$ or $\text{CF}_3\text{SO}_2\text{NH}_2$ ) in aqueous solutions. ....	134
Table 5.3. Decay of triplet states and naphthoxyl radicals generated upon laser flash photolysis of naphtholic compounds in MeCN. Triplet decay rates were analyzed as single decay kinetics at 420 or 440 nm; amplitude at 440 nm is reported. Naphthoxyl radical decay rates were analyzed at 360 and 440 nm and global analysis (see Appendix D); amplitude at 360 nm is reported. ....	136
Table 5.4. Photoproduct quantum yields for N-O bond cleavage (as indicated by chemical marker $\text{CF}_3\text{SO}_2\text{NH}_2$ ) in MeCN. ....	146
Table 5.5. Photoproduct quantum yields for HNO photorelease (as indicated by chemical marker $\text{CF}_3\text{SO}_2^-$ for HNO generation or $\text{CF}_3\text{SO}_2\text{NH}_2$ for N-O bond cleavage) in 60:40 v/v MeCN to 5.0 mM phosphate buffer solution (pH 7.0). ....	152
Table 6.1. Reactions observed upon addition of excess Piloty's acid to HOCbl. ....	157
Table 6.2. Reaction model with rate constants. ....	159
Table 7.1. Interfering pathways to HNO photorelease following excitation of donor <b>1</b> or <b>4</b> . ....	173
Table A2. Molar extinction coefficients at 313 nm. See Chapter 2, Section 2.3.1 for details. ....	194

# ATTESTATION OF AUTHORSHIP

---

I hereby declare that this submission is my own work and that, to the best of my knowledge and belief, it contains no material previously published or written by another person (except where explicitly defined), nor material which to a substantial extent has been submitted for the award of any other degree or diploma of a university or other institution of higher learning.



Ruth B. Cink

December 9, 2018

To the synthetic chemists involved in this project.

Thank you for giving me things to destroy.

# ACKNOWLEDGEMENTS

---

First of all, I must thank the person who invited me to New Zealand, my primary supervisor, Prof. Nicola Brasch. Thank you for giving me this opportunity to pursue a PhD and travel beyond my home country. I am very grateful for your support and dedication both to my education and this project.

I am also extremely thankful to my secondary and tertiary supervisors, Prof. Allan Blackman and Prof. Cather Simpson. Thank you to Prof. Allan Blackman for your humor and encouragement. Many thanks to Prof. Cather Simpson – you provided me with many opportunities to learn and grow as a scientist and for that I am truly thankful.

Several chemists directly assisted with this research over the past few years. My warmest praise to our collaborators from Kent State University: Prof. Paul Sampson, Prof. Alexander Seed, Dr. Yang Zhou, Dr. Sonya Adas, and Mr. Mohammad Rahman. Without your synthetic skills and your dedication, this thesis would not exist! Furthermore, your keen eyes and thought-provoking questions significantly elevated the level of research presented in this thesis. Thank you to two other research groups directly involved in this work: the groups of Prof. David Lee Phillips and Prof. Rudi van Eldik. Lili, Allison, and Justyna, it has been a pleasure working with you. I'm deeply indebted to the Spectroscopy Group at the Photon Factory – thank you for holding those weekly meetings so we could discuss current literature and our own research. I cannot begin to express my thanks to Dr. Christopher Pook, Mr. Adrian Owens, and Dr. Hannah Holtcamp for your technical support for key experiments in this thesis. And thank you for your help with the preliminary computational studies, Dr. Nina Novikova, Mr. Joshua Sutton, and Mr. Xindi Wang. My gratitude to Dr. Reece Whitby and Callaghan Innovation for assistance with preliminary fluorescence studies.

Thank you to Dr. Paul Sampson and Dr. Aaron Boyd Evans for assistance with editing this thesis and to Mr. Rod Cink for assistance with proof reading.

Of course, funding for this research should be acknowledged. Thanks to AUT for Doctoral Scholarship, the Dodd-Walls Centre for travel awards to the Gordon Research Conference in Photochemistry and also to the University of Hong Kong for a research

## Acknowledgements

---

visit, Kent State University for initially funding me, and the Photon Factory for the HRMS analyses and partial funding for the Hong Kong visit.

To past and present members of the Brasch Research Group, I am blessed to be part of this team and appreciate your support and encouragement. Special thanks to Joe, Harish, Sonya, Rohan, and Anthony for training me in numerous techniques at Kent State. To Lynn, Vinay, Dominique, Yue, and Marwa, thank you for your encouragement in the lab, especially on those difficult days. And Lynn, your fantastic sense of humor and positive attitude need special thanks.

I was very lucky to have support from two other research groups during my PhD: the Photon Factory and Prof. Penny Brother's research group. Andy, Nina, Michel, Reece, Margaux, and Rakesh, you all especially helped me so much. When I first arrived at AUT, I was the only PhD student in chemistry at AUT. These two groups at the neighboring university adopted me and helped me immensely with overcoming those unique challenges one faces during her first year in a PhD.

A huge thanks to the technicians and support staff in the School of Sciences. Without your quiet support, I would have been quite lost. Winnie, special thanks to you for your organization and patience that cannot be underestimated. Additionally, thank you to Premika at the University of Auckland for your help. Outside of AUT, special thanks to Dr. Peter Lachmann for training and technical assistance on the laser flash photolysis instrument.

I would like to express my deepest appreciation to my friends. I am a very fortunate person to have had so much support and encouragement during this PhD journey. I will not list everyone here by name as I'm sure you are anxious to start reading my thesis by now, but let me fully acknowledge my friends in the United States who cheered me on from halfway around the world and those friends travelled to New Zealand to visit me. Here in New Zealand, I express my heartfelt thanks to my flatmates who are charitable and patient people, my AUT friends who helped me navigate the academic world (especially the squid research team for including me in their shenanigans), my OGH buddies who are always supportive and always encouraging, and my rock climbing and hiking buddies who helped me re-center myself during stressful times.

## Acknowledgements

---

Finally, thank you to my family for putting up with me going on this adventure so far from home. It's been difficult, and I miss you. Mom and Dad, especially, I couldn't have done this without your support and encouragement.

# CHAPTER 1: INTRODUCTION

---

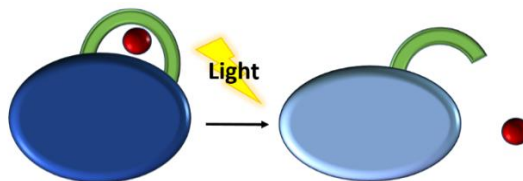
HNO (also called nitroxyl, nitrosyl hydride, hydrogen oxonitrate (IUPAC), nitroso hydrogen, and monomeric hyponitrous acid) is a biologically active, triatomic molecule. Despite being a small molecule, HNO exhibits unusual and complex acid-base chemistry. While the ground state of  ${}^1\text{HNO}$  is in a singlet state, the ground state of its conjugate base  ${}^3\text{NO}^-$  is in a triplet state.<sup>1</sup> The unusual change in spin states in the acid-base equilibrium of HNO was not realized until the early 2000's.<sup>1</sup> At that time, the reported  $\text{p}K_{\text{a}}$  value of HNO was revised from 4.7 to 11.4.<sup>1-4</sup> This revision led to a reexamination of the biological activity of HNO, as the dominant species at physiological pH would be  ${}^1\text{HNO}$ , not the nitroxyl anion as originally believed.<sup>1,2,5</sup> Excitingly, HNO pro-drugs appear to be a novel method of treatment for congestive heart failure. Furthermore, it has been hypothesized that HNO is generated endogenously and may be a biological signaling molecule.

The overall goal motivating this thesis is to assist with fundamental studies on the kinetics and mechanisms of HNO with relevant biomolecules. Unfortunately, these types of studies are challenging because HNO is unstable. HNO rapidly dimerizes and decomposes to form  $\text{N}_2\text{O}$  and  $\text{H}_2\text{O}$  ( $k = 8 \times 10^6 \text{ M}^{-1} \text{ s}^{-1}$ , 22 °C).<sup>6</sup> Hence, HNO donating molecules are commonly used to release HNO but these molecules generate HNO slowly ( $t_{1/2} \sim$  minutes to hours). The slow generation of HNO makes kinetic studies of HNO and relevant biomolecules particularly challenging,<sup>3,7,8</sup> as HNO reacts with biomolecules on the order of  $10^3 - 10^7 \text{ M}^{-1} \text{ s}^{-1}$ .<sup>9</sup>

One promising method to release HNO rapidly is the light excitation of photocages tethered to well-established HNO donors. Photocages (also called phototriggers) are photolabile protecting groups that release substituents upon photoactivation. Photocages are chemically tethered to other molecules of interest and release these molecules upon irradiation at appropriate wavelengths of excitation (Scheme 1.1). Biochemists use photocaged compounds as a tool to follow events in real time by this spatially and temporally controlled technique.<sup>10</sup> Photocages are also used in kinetic and mechanistic studies to control release of reactive substrates.<sup>11</sup> Photocages have been successfully applied for release of numerous biologically active molecules, such as ions,<sup>12</sup> acids,<sup>13</sup>

bases,<sup>14</sup> neurotransmitters,<sup>15</sup> fluorophores,<sup>16,17</sup> gene-inducers,<sup>18</sup> nucleic acids,<sup>19</sup> and proteins.<sup>10,20-22</sup>

Scheme 1.1. Release of bioactive molecule (red circle) from photoprotecting group (blue-green).



A promising class of (hydroxynaphthalenyl)methyl (HNM) photocaged *N*-hydroxysulfonamides was designed and synthesized in the research groups of Prof. Nicola Brasch (Auckland University of Technology, NZ), Prof. Paul Sampson (Kent State University, US), and Prof. Alexander Seed (Kent State University, US) (donors **1**-**4**; Figure 1.1).<sup>23,24</sup> Figure 1.2 shows a general scheme for the design of the molecules. The reactant molecule contains a photocage and an HNO donating moiety equipped with a chemical marker which should signify HNO generation. Upon photolysis, the reactant releases <sup>1</sup>HNO, a non-reactive byproduct, and the chemical marker of HNO generation. Preliminary studies completed by colleagues in Prof. Paul Sampson and Prof. Alexander Seed's research groups identified one very promising photoactive HNO donor (donor **4**) within the new class of HNM photocaged *N*-hydroxysulfonamides. My thesis research provides a detailed photochemical and photophysical exploration and mechanistic understanding of this exciting new photoactive HNO-releasing molecule. Special focus is paid to understanding donor **4**'s ability to selectively generate HNO under select solvent and pH conditions compared to its structural analogue donor **1**.

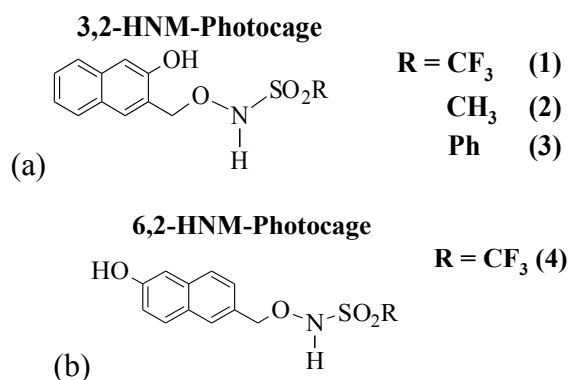


Figure 1.1. (a) 3,2-HNM-photocaging of *N*-hydroxysulfonamides. (b) 6,2-HNM-photocaging of *N*-hydroxysulfonamides.

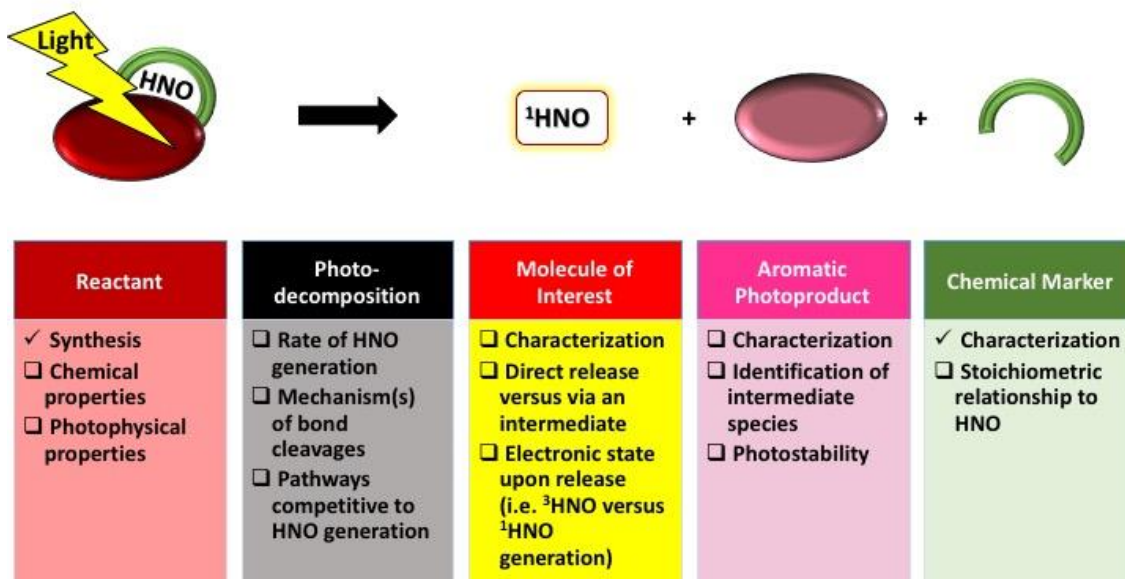


Figure 1.2. Above: General design of the photoactive HNO donor molecules ((hydroxynaphthalenyl)methyl (HNM) photocaged *N*-hydroxysulfonamides), where the reactant decomposes to generate one mol. equiv. of HNO, a non-reactive by-product (pink), and a chemical marker (green). Below: Outline of photochemical and photophysical exploration and mechanistic studies to be addressed in this thesis. The reactant has been synthesized by collaborators at Kent State University and preliminary characterization completed of the chemical marker of HNO generation. The remaining points are addressed individually in Chapters 3-5. Chapter 6 highlights the difficulties associated with the use of currently available thermally decomposing HNO donors.

This chapter will give a review of the chemistry of HNO and its implications in biology in order to establish the need for the investigation of HNO at physiological pH conditions. The chemistry of currently available thermally decomposing and photoactive HNO donors will also be discussed in detail. This section will clearly show that currently available HNO donor molecules are not adequate for kinetic and mechanistic studies of HNO with biologically relevant molecules. The HNM photocage used to protect the HNO donating moiety is a hydroxyarene (Figure 1.1); hence, an introduction to the photochemistry of hydroxyarenes will be described. Chapter 2 will describe the instruments and methods used throughout this thesis. In Chapter 3, experimental work will be presented on the chemical properties of donor **4** (Figure 1.2; column 1), and characterization data describing the photoproducts generated upon photolysis of donor **4** in aqueous MeCN conditions will be given (Figure 1.2; column 1, 3, 4, and 5). Evidence will be presented showing that donor **4** near stoichiometrically generates HNO upon excitation via concerted C-O and N-S heterolytic bond cleavage and that  $\text{CF}_3\text{SO}_2^-$  is a chemical marker of HNO production (Figure 1.2; column 3 and 5). In Chapter 4, a series

of photophysical studies and mechanistic studies of donor **4** will be presented, including data that suggests that HNO is generated on the picosecond timescale following photolysis of donor **4** (Figure 1.2; column 1 and 2). Careful attention is paid to characterizing the aromatic transient species generated upon C-O and N-S heterolytic bond cleavages upon photolysis of donor **4** (Figure 1.2; column 4). In Chapter 5, mechanisms of competing solvent and pH dependent photodecomposition pathways will be examined and methods of preventing these competitive pathways will be proposed (Figure 1.2; column 2). In Chapter 6, the rate of reaction between HNO and a biologically relevant molecule, hydroxycobalamin, will be estimated using a complex reaction system. The research presented in this chapter will highlight the need for HNO donor molecules to release  $^1\text{HNO}$  on the ultrafast scale in order to enable kinetic and mechanistic studies for the reactivity between  $^1\text{HNO}$  and relevant biomolecules.

## 1.1 FUNDAMENTAL CHEMISTRY OF HNO

### 1.1.1 Equilibrium between $^1\text{HNO}$ and $^3\text{NO}^-$

Despite being a triatomic molecule, the acid-base chemistry of HNO is unusual and complex.  $^1\text{HNO}$  exists in equilibrium with the nitroxyl anion,  $^3\text{NO}^-$  (eqn. 1.1).

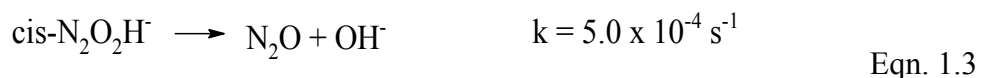
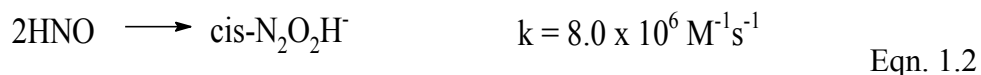


The ground state of  $^1\text{HNO}$  is a singlet state but the ground state of  $^3\text{NO}^-$  is a triplet (isoelectronic with  $\text{O}_2$ ).<sup>1</sup> Deprotonation is abnormally slow (Eqn. 1.1;  $k_f = 4.9 \times 10^4 \text{ M}^{-1} \text{ s}^{-1}$ ).<sup>2,9</sup> The  $^1\{\text{ON}\cdot\cdot\text{H}\cdot\cdot\text{OH}\}^\# \rightarrow ^3\{\text{ON}\cdot\cdot\text{H}\cdot\cdot\text{OH}\}^\#$  intersystem crossing involves the isoenergetic  $^1(n, n) \rightarrow ^3(n, \pi^*)$  molecular orbital change.<sup>4</sup> It is hypothesized that the combination of the spin prohibition and the reaction energetics creates the high barrier, resulting in the slow deprotonation.<sup>4</sup> The rate of protonation is likewise slow (millisecond lifetime, eqn. 1.1;  $k_r = 1.2 \times 10^2 \text{ s}^{-1}$ ).<sup>1</sup> Initially, the unusual change in spin states in the acid-base equilibrium of HNO was not realized and the  $\text{p}K_a$  of HNO was reported as 4.7 from pulse radiolysis experiments.<sup>1-4</sup> However, laser flash photolysis data of Angeli's salt together with thermodynamic calculations showed that HNO is actually a weak acid, with a  $\text{p}K_a$  of 11.4.<sup>1</sup> The  $\text{p}K_a$  value of  $^1\text{HNO}/^3\text{NO}^-$  was reported to be  $11.6 \pm 3.4$  from quantum mechanical calculations, cyclic voltammetry measurements, and chemical reduction

experiments.<sup>5</sup> Therefore, the protonated species (<sup>1</sup>HNO), not the nitroxyl anion, is the dominant species at physiological pH.<sup>1,2,5</sup>

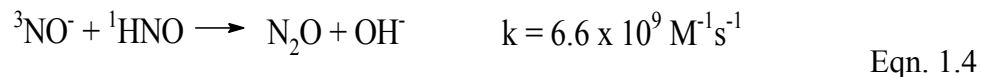
### 1.1.2 Dimerization of HNO

HNO's rapid dimerization and subsequent dehydration make it physically impossible to store HNO under normal laboratory conditions. Thus, HNO must be generated *in situ* for experimental purposes. More specifically, HNO dimerizes to give *cis*-N<sub>2</sub>O<sub>2</sub>H<sup>-</sup>; the rapid dehydration of *cis*-hyponitrate anion makes this process irreversible (eqn. 1.2 and 1.3).<sup>6</sup>



This reaction's rate constant at room temperature is  $(8 \pm 3) \times 10^6 \text{ M}^{-1}\text{s}^{-1}$ .

Notably, <sup>3</sup>NO<sup>-</sup> and <sup>1</sup>HNO also react rapidly, forming N<sub>2</sub>O with a rate constant of  $6.6 \times 10^9 \text{ M}^{-1}\text{s}^{-1}$  (eqn. 1.4).<sup>25</sup> This reaction is unexpectedly rapid for a spin-forbidden reaction. It is also surprising because <sup>1</sup>HNO reacts slowly with <sup>3</sup>O<sub>2</sub> ( $k \sim 10^3 \text{ M}^{-1}\text{s}^{-1}$ ).<sup>26</sup> However, this may be attributed to <sup>3</sup>NO<sup>-</sup> being more nucleophilic than <sup>3</sup>O<sub>2</sub> due to the negative charge.<sup>25</sup>



## 1.2 BIOLOGICAL AND THERAPEUTIC SIGNIFICANCE OF HNO

The biological activities of nitrogen oxides have gained considerable interest. Indeed, Robert F. Furchgott, Louis J. Ignarro and Ferid Murad won the Nobel Prize in Physiology or Medicine in 1998 for their discovery that nitric oxide (NO) is a gaseous signaling molecule in the cardiovascular system.<sup>5</sup> The discovery has fostered increased interest in related nitrogen-containing species, including peroxynitrite (ONOO<sup>-</sup>), nitrogen dioxide (NO<sub>2</sub>), nitrate (NO<sub>3</sub><sup>-</sup>), nitrite (NO<sub>2</sub><sup>-</sup>), dinitrogen trioxide (N<sub>2</sub>O<sub>3</sub>), and ammonium (NH<sub>4</sub><sup>+</sup>). HNO gained significant attention due to its ability to treat congestive heart failure,<sup>27</sup> the likelihood that it acts as biological signaling molecule,<sup>9,28-31</sup> and its similarities and differences in reactivity versus NO.<sup>32</sup>

### 1.2.1 Therapeutic Relevance of HNO

Most research tied to HNO's use as a therapeutic is motivated by exploiting its reactivity in the heart muscle. Loss of contractive function in the heart muscle results in several

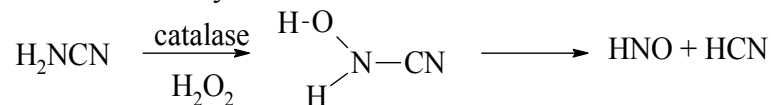
forms of heart failure.<sup>27</sup> Despite considerable efforts, congestive heart failure does not have an adequate therapeutic response. Inotropic agents that raise intracellular cAMP levels (beta-adrenergic agonists or phosphodiesterase type III inhibitors) result in harmful side effects in the long term.<sup>27</sup> In general, current therapeutics are used in palliative care or as management until transplant surgery or mechanical assist device implantation.<sup>27</sup> Additionally, no safe and effective therapies are currently available to enhance left ventricular function that also aid in decongestion in humans.<sup>27</sup>

HNO prodrugs are a new class of treatment for congestive heart failure with HNO inducing both venous and arterial dilation in failing hearts.<sup>33-35</sup> Once blood returns to the hypoxic tissue, reactive oxygen species (ROS) are produced.<sup>36</sup> Therefore, ideally inotropic/lusitropic agents should not lose their efficiency in the presence of ROS. Excitingly, in induced heart failure in dog models, HNO donors improve both contractility and relaxation of the heart muscle and are resistant to scavenging by superoxide ( $O_2^{\bullet-}$ ).<sup>37</sup> Additional cardiac-related effects of HNO donors include positive inotropy/lusitropy, balanced vasodilation, left ventricular unloading effects, no alterations of  $Ca^{2+}$  homeostasis, no arrhythmogenesis, antiaggregant effects, anti-inflammatory and antiproliferative actions, and preconditioning actions.<sup>27</sup> A patented HNO prodrug CXL-1020 fully supports the experimental promise obtained thus far (see ClinicalTrials.gov NCT010960430).<sup>27</sup> Unfortunately, long-lasting intravenous infusions of CXL-1020 resulted in irritation at the injection site.<sup>27</sup> Following this, a second-generation HNO prodrug (BMS-986231) was initiated into phase 2a trials and demonstrated desired hemodynamic effects with few negative side effects after 30 days.<sup>33</sup> Further studies showed that the HNO prodrug was well-tolerated for 24-48 hours by patients who received it via continuous infusion; positive inotropy was observed.<sup>38</sup> It continues to be further assessed.<sup>33</sup>

HNO has therapeutic potential in other areas beyond congestive heart failure treatment. Researchers are investigating HNO's potential as an antioxidant and anticancer agent.<sup>39</sup> Still others are interested in its interaction with the nervous system.<sup>2,40,41</sup> However, this area of research is less promising as HNO donors appear to induce neurotoxicity.<sup>41</sup> An HNO prodrug is used as an anti-alcoholism treatment.<sup>42</sup> Currently, the HNO prodrug cyanamide is used to treat alcoholism in Japan, Canada, and Europe.<sup>42</sup> Cyanamide

generates both HNO and HCN upon decomposition (Scheme 1.2).<sup>42,43</sup> HNO inhibits aldehyde dehydrogenase,<sup>3,44,45</sup> which causes ethanol to be converted to acetate.<sup>42,43</sup>

Scheme 1.2. HNO release from cyanamide.



### 1.2.2 Mammalian Endogenous Production of HNO

Several studies suggest that HNO is produced endogenously.<sup>9,28-31</sup> For example, *in vitro* experiments show that nitric oxide synthases produce HNO from *L*-arginine in the absence of the tetrahydrobiopterin cofactor or by oxidation of the N-hydroxy-*L*-arginine intermediate.<sup>32,46-48</sup> Cells which have been pretreated with *S*-nitrosoglutathione and exposed to H<sub>2</sub>S generated nitrosothiol (HSNO); HSNO can react with H<sub>2</sub>S to give HNO and H<sub>2</sub>S<sub>2</sub>.<sup>29</sup> In addition, H<sub>2</sub>S-assisted Fe<sup>3+</sup> heme-catalyzed reduction of nitrite generates HNO.<sup>49</sup> Excitingly, the reaction of NO with thiols was shown to produce HNO.<sup>50</sup> Generally, hypoxic and physiological reducing environments are proposed to lead to HNO formation.<sup>26</sup> This is opposed to oxidizing environments which form nitrite, nitrate, peroxyxynitrite, NO<sub>2</sub>, and N<sub>2</sub>O<sub>3</sub> from NO.<sup>26</sup>

### 1.2.3 Chemical Differences between NO and HNO

NO is a gaseous signaling molecule that plays an important role in immune response, central nervous system regulation, and the maintenance of vascular tone.<sup>51</sup> Some properties attributed to nitric oxide (NO, ·NO) earlier may instead be due to HNO.<sup>32</sup> Additionally, interconversion between the two species has been proposed under physiological conditions. For example, the bond between the H—NO is relatively weak, suggesting that HNO could conceivably be oxidized to NO by hydrogen atom abstraction.<sup>51</sup> Therefore, a fundamental area of HNO and NO research revolves around the similarities and differences between the two molecules' chemistries.

NO and HNO exhibit some similar bioreactivities. The main biological targets of both species are thiols, metalloproteins, and radical species.<sup>51</sup> The two species can be anti-oxidant or pro-oxidant depending on their environments.<sup>51</sup> However, HNO and NO exhibit differences with their respective biological and physiological reactivities. For example, NO reacts with O<sub>2</sub><sup>•-</sup> to form peroxyxynitrite/peroxyxynitrous acid (ONOO(H)), a highly reactive nitrogen species, but HNO does not react appreciably with O<sub>2</sub><sup>•-</sup>.<sup>32</sup> NO also

reacts with O<sub>2</sub> to generate oxidants, whereas HNO may show oxidative behavior in anaerobic environments.<sup>51</sup> Most notably, while NO does not react *directly* with thiols, HNO reacts directly with thiols.<sup>32</sup> HNO therefore can modify protein-containing thiol residues and consequently impact protein activity.<sup>32</sup> The high reactivity of HNO with thiols is often used as a means to distinguish between the two species' chemistries, as thiols can be added to trap HNO.<sup>51</sup>

### 1.3 KINETIC AND MECHANISTIC STUDIES ON THE REACTIONS OF BIOLOGICALLY RELEVANT MOLECULES WITH HNO

Kinetic and mechanistic studies on the reactions of biologically relevant molecules with HNO provide insights into how HNO will behave *in vivo*. As noted previously, it is important to understand HNO's bioreactivity not only because of its use in therapeutics but also due to its hypothesized role as a biological signaling molecule. Several researchers investigated HNO's reaction with various biologically relevant molecules. These studies primarily use the HNO donor Angeli's salt (see Figure 1.3).<sup>52-54</sup> Specifically, rate constants for the reactions of HNO with thiols, O<sub>2</sub>, tempol, tempo, NH<sub>2</sub>OH, NADH and NADPH, selenomethionine, ascorbate, superoxide dismutase (SOD), MetHb, catalase, and Fe(III) cytochrome c have been determined indirectly using a competitor (Fe(III) cytochrome c or NADH) or using the dimerization of HNO to give N<sub>2</sub>O and H<sub>2</sub>O as a competing reaction.<sup>53,55</sup>

HNO acts as a selective electrophile in biological systems and appears to prefer soft nucleophiles.<sup>2,56-58</sup> In particular, HNO reacts with thiolates. The nucleophilic thiol attacks the electrophilic nitrogen of HNO to form N-hydroxysulfenamide (eqn. 1.5). If excess thiol is present, N-hydroxysulfenamide reacts further with thiol to yield the corresponding disulfide and hydroxylamine (eqn. 1.6). Under biological conditions, the disulfide is reduced back to the original thiol. A competing reaction is N-hydroxysulfenamide rearranging to give a sulfinamide (eqn. 1.7).<sup>28</sup>

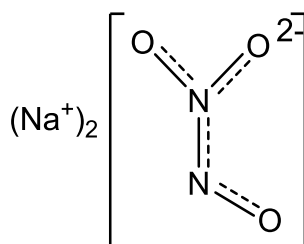
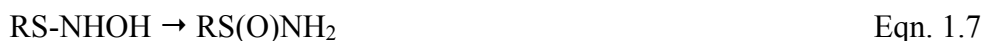
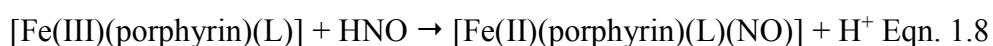


Figure 1.3. Structure of Angeli's Salt.



The rate constants for HNO scavenging by various thiols were determined to be on the order of  $10^6 \text{ M}^{-1}\text{s}^{-1}$ .<sup>2</sup> Specifically, the rate constant for the reaction between glutathione and HNO is  $2 \times 10^6 \text{ M}^{-1}\text{s}^{-1}$ .<sup>52</sup> This is notable because cells have high concentrations (mM) of glutathione so it has been suggested that glutathione scavenging is the predominant fate of HNO in biological systems.<sup>2</sup>

In addition to HNO's reaction with thiols, another main biological target for HNO are metalloproteins.<sup>2</sup> HNO can reduce metal centers and metalloproteins.<sup>59</sup> For example, HNO can react with ferric hemes ( $\sim 10^5 \text{ M}^{-1}\text{s}^{-1}$ ), yielding ferrous heme-nitrosyl complexes (eqn. 1.8).<sup>60</sup>



Some examples of the reaction in eqn. 1.8 include reactions with methemoglobin,<sup>57,61,62</sup> metmyoglobin,<sup>57,61,62</sup> Fe(III) microperoxidase-11,<sup>63</sup> and Fe(III)TPPS.<sup>60,64</sup> Reductive nitrosylation occurs for other porphyrins<sup>65</sup> and can occur via two pathways: (1) via direct coordination of HNO to the metal center or (2) via electron transfer to the metal center which is followed by NO coordination to the metal center.<sup>59</sup> HNO will also reduce horseradish peroxidase<sup>57,61,62</sup> and  $\text{Ni(CN)}_4^{2-}$ .<sup>66</sup> HNO can also oxidize metal centers. For example, in the reaction of cob(II)alamin and HNO, HNO reduces cob(II)alamin to cob(I)alamin and a second HNO molecule then oxidizes cob(I)alamin to cob(II)alamin.<sup>67</sup>

Finally, it is predicted that HNO will react with radical species via hydrogen atom donation (eqn. 1.9).<sup>2</sup>



While it is believed that thiols, metalloproteins, and radical species are HNO's main biological targets, other targets have been explored. Theoretical computations predict that HNO will not react with water or alcohols.<sup>2</sup> Kinetic studies suggest that the rates of HNO's reactions with common reductants such as ascorbate and NAD(P)H are one or two orders of magnitude slower than HNO's reaction with glutathione.<sup>2</sup> Notably, HNO can either react directly or combine with other reactive oxygen or nitrogen species in

order to oxidize biomolecules.<sup>2</sup> For example, HNO reacts with NO, forming  $\text{N}_2\text{O}_2^-$ .  $\text{N}_2\text{O}_2^-$  reacts rapidly with NO forming  $\text{N}_3\text{O}_3^-$ , which then decays to form  $\text{N}_2\text{O}$  and  $\text{NO}_2^-$ .<sup>26</sup> However, the reaction of  $^1\text{HNO}$  with  $^3\text{O}_2$  is slow due to their different spin states ( $k \sim 10^3 \text{ M}^{-1}\text{s}^{-1}$ ).<sup>68</sup> The mechanism for the reaction has been of much interest but no consensus has been reached.<sup>48,54,69</sup> HNO oxidizes certain nitrogenous moieties such as diazenes ( $\text{RN}=\text{NH}$ ).<sup>58</sup>

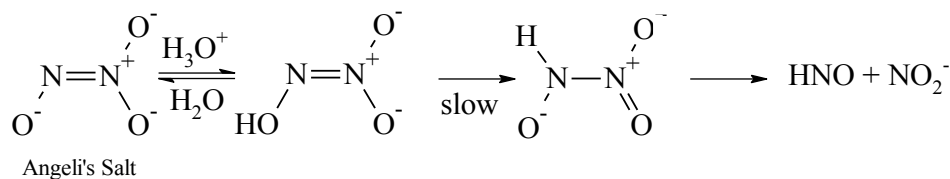
#### 1.4 HNO DONATING MOLECULES

Due to HNO's rapid dimerization, molecules that decompose to generate HNO must be used to study HNO's properties and reactivities. These HNO donating molecules must be used judiciously according to the type of study of interest as the chemistry of the HNO donor itself can have significant effects on the chemistry observed. Consequently, the mechanism of HNO donor decomposition is often investigated to allow for the donor's effective use in relevant studies.<sup>3,25,70-72</sup> Ideally, an HNO donor would produce HNO at biologically relevant pH conditions ( $\sim \text{pH } 7$ ) in aqueous solution. Additionally, HNO donors would decompose to give non-reactive byproducts in conjunction with HNO upon chemical or photochemical activation. If performing *in vivo* studies, slow decomposition of the donors to generate HNO may be desired. On the other hand, kinetic and mechanistic studies call for rapid release of HNO to allow rate constants of the reactions of HNO with other species to be directly determined; that is, competition experiments would not be required.<sup>1,52</sup> Finally, site-specific release of HNO may be preferable in cell studies.

##### 1.4.1 Thermally Decomposing HNO Donor Molecules

###### 1.4.1.1 Angeli's Salt and Other Diazeniumdiolates

The most commonly used HNO donor is the diazeniumdiolate (NONOate) called Angeli's salt ( $\text{Na}_2\text{N}_2\text{O}_3$ ;  $\text{p}K_{\text{a}1}(\text{H}_2\text{N}_2\text{O}_3) = 2.39$ ,  $\text{p}K_{\text{a}2} 9.35$ ; Figure 1.3).<sup>73</sup> The decomposition of Angeli's salt is first-order, is pH-independent ( $4 < \text{pH} < 8$ ;  $6.8 \times 10^{-4} \text{ s}^{-1}$ ),<sup>74</sup> and yields HNO and one equivalent of  $\text{NO}_2^-$  (Scheme 1.3).<sup>39</sup> The rate of decomposition is easily monitored spectroscopically by the loss of the wavelength maximum at 250 nm for  $\text{N}_2\text{O}_3^{2-}$  ( $\epsilon$  of  $5500 \text{ M}^{-1} \text{ cm}^{-1}$ ) or at 237 nm ( $6100 \text{ M}^{-1} \text{ cm}^{-1}$ ) for  $\text{HN}_2\text{O}_3^-$ .<sup>75,76</sup> In 0.1 M NaOH, Angeli's salt is essentially stable.

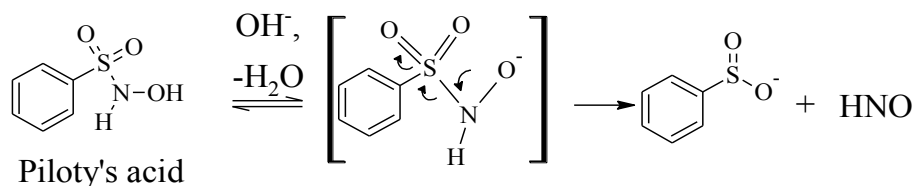
Scheme 1.3. HNO release from diazeniumdiolates.<sup>77</sup>

Unfortunately, nitrite formation can interfere when studying HNO's reactivity.<sup>73,78</sup> In addition, the half-life for HNO generation by Angeli's salt is ~17 min at pH 7.4 (25 °C).<sup>77,79</sup> Another potential issue is that the Angeli's salt's anion ( $\text{N}_2\text{O}_3^{2-}$ ) can react directly with metal centers.<sup>65,78</sup> Other NONOates that incorporate primary amines, such as isopropyl NONOate ( $\text{Na}[(\text{CH}_3)_2\text{CHNH}(\text{N}(\text{O})\text{NO})]$ ), release HNO and NO at physiological conditions.<sup>80</sup>

#### 1.4.1.2 *N*-Hydroxysulfonamides

A widely used HNO donor is Piloty's acid ( $\text{C}_6\text{H}_5\text{SO}_2\text{NHOH}$ ; *N*-hydroxybenzenesulfonamide). Upon deprotonation, Piloty's acid releases HNO and one equivalent of benzenesulfinate via S-N bond heterolysis, Scheme 1.4.

Scheme 1.4. Mechanism of Piloty's acid's decomposition and release of HNO.



The main drawback for Piloty's acid is that its  $\text{pK}_a$  is relatively high ( $\text{pK}_a$  9.29).<sup>81</sup> At physiological pH conditions, the rate of decomposition is very slow ( $t_{1/2} = 5500$  min)<sup>82</sup> and Piloty's acid decomposes to form a nitroxide radical [ $\text{PhSO}_2\text{N}^*(\text{OH})$ ] which then releases NO rather than HNO.<sup>81</sup> Thus, Piloty's acid is not an HNO donor under physiologically relevant pH conditions.

Because Piloty's acid releases HNO only in alkaline solution, researchers have focused on synthesizing Piloty's acid derivatives in an attempt to resolve this limitation (Figure 1.4).<sup>71,83-85</sup> This includes *N*-hydroxybenzenecarboximidic acid derivatives, which are not very soluble in water.<sup>71</sup> *N*-Hydroxysaccharin, toluene sulfohydroxamic acid (TSHA), methanesulfohydroxamic acid (MSHA), and MSHA derivatives require basic conditions to generate HNO or enzymatic activation to release HNO.<sup>86-88</sup> Several aryl-substituted

Piloty's acid derivatives were developed to lower the  $pK_a$  using electronic withdrawing substituents.<sup>39,70,85,89</sup> Trifluoromethanesulfonylhydroxamic acid ( $t_f$ -MSHA,  $CF_3SO_2NHO(H)$ ;  $pK_a$   $5.89 \pm 0.05$ ;  $t_{1/2} \sim 13$  min) was shown to release HNO under physiological pH conditions, cleanly decomposing to generate HNO and  $CF_3SO_2^-$ .<sup>90</sup> In general, the use of Piloty's acid and its derivatives to generate HNO is not ideal for physiologically related studies, as HNO generation is slow at neutral pH conditions.

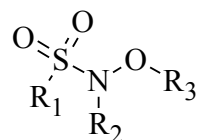
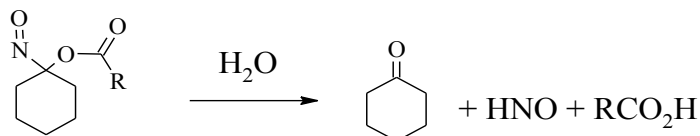


Figure 1.4. Structure of *N*-alkoxysulfonamide compounds.

#### 1.4.1.3 Acyloxy Nitroso Compounds

Another class of HNO donors are the acyloxy nitroso compounds which release HNO upon cleavage of the ester bond, Scheme 1.5.<sup>91</sup>

Scheme 1.5. Hydrolysis of acyloxy nitroso compounds to release HNO.



One advantage of these bright blue compounds is that the rate of HNO release ( $t_{1/2} \sim$  min) is controlled by the R substituent.<sup>91</sup> However, these donors do react directly with thiols and are consequently not useful for cell culture or *in vivo* experiments.<sup>73</sup> They also produce nitrite in relatively small amounts under neutral pH conditions.<sup>91</sup>

#### 1.4.1.4 Cyanamide and Other *N*-substituted Hydroxylamines

More recently, a series of *N*-substituted hydroxylamines were developed by Guthrie *et al.*<sup>92</sup> based on the HNO prodrug, cyanamide (Figure 1.5). After enzyme catalyzed oxidation by hydrogen peroxide, the *N*-substituted hydroxylamine intermediate decomposes to generate HNO and cyanide (Scheme 1.2).<sup>73,93</sup> *N*-substituted hydroxylamine-based HNO donors were synthesized following this carbon-based leaving group strategy to generate HNO under physiological conditions in the absence of an enzyme. The rate and amount of HNO released from these donors is dependent on the leaving group. For example, *N*-substituted hydroxylamine derivatives of Meldrum's acid (2,2-dimethyl-1,3-dioxane-4,6-dione) produce an HNO/NO mixture,<sup>92</sup> but the *N*-substituted hydroxylamine derivative of bartituric acid and pyrazolone incorporating the

O-methyloxime substituent release HNO (pH 7.4,  $t_{1/2}$  = 0.7 min and 9.5 min respectively, 37 °C).

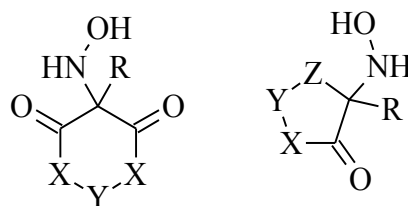
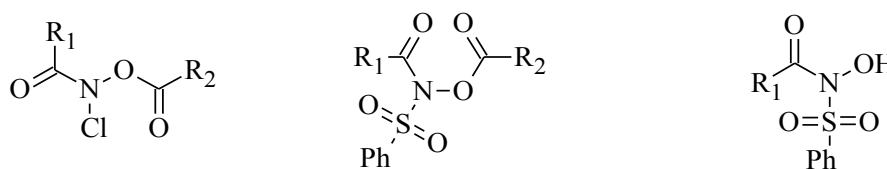


Figure 1.5. Structures of N-substituted hydroxylamines.

Recent work by the Toscano group explored *N,O*-bis-acylated hydroxylamine derivatives with chloro or arenesulfonyl leaving groups and related *N*-hydroxy-*N*-acylsulfonamides (Figure 1.6).<sup>94</sup> The half-life of these donors is controlled by the ester group and/or sulfonyl leaving group and varies from seconds to hours at biologically relevant pH conditions.<sup>94</sup>



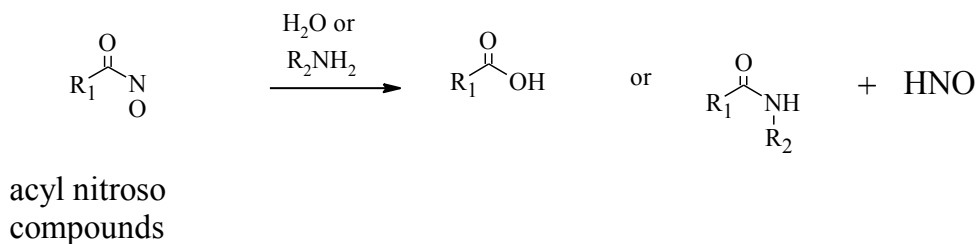
N-chloro-N-acyloxyamides    N-arene-N-acyloxyamides    N-hydroxy-N-acylsulfonamides

Figure 1.6. Toscano's N-substituted hydroxylamines.

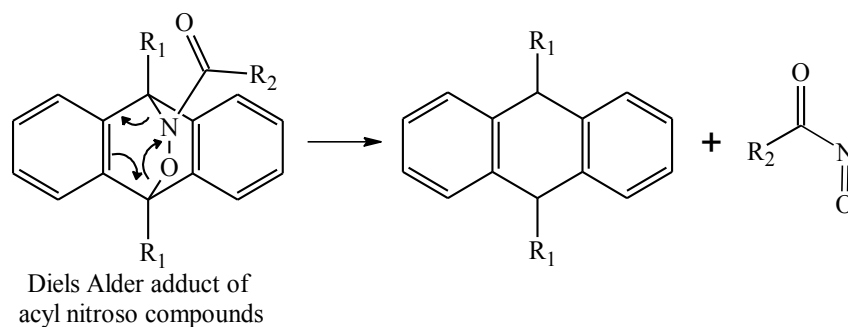
#### 1.4.1.5 Acyl Nitroso Compounds and Related Derivatives

Acyl nitroso HNO donors (Scheme 1.6) produce HNO upon nucleophilic attack. However, these highly reactive intermediates must be generated *in situ*.<sup>91,95</sup> King and colleagues protected the acyl nitroso moiety by means of hetero-Diels-Alder chemistry with anthracene derivatives.<sup>96</sup> These species release HNO once the Diels-Alder adduct thermally decomposes via a retro-Diels-Alder reaction to produce the acyl nitroso compound, Scheme 1.7 (R = CH<sub>3</sub>;  $t_{1/2}$  = 24 min at 40 °C).<sup>69,97</sup>

Scheme 1.6. Release of HNO from acyl nitroso compounds.



Scheme 1.7. Release of acyl nitroso compounds from acyl nitroso-9,10-dimethylantracene cycloadducts.



#### 1.4.1.6 Other HNO Donors

Other HNO donors exist that do not fall under the main classes previously discussed. *Trans*-[Ru(NO)(NH<sub>3</sub>)<sub>4</sub>P(O<sup>-</sup>)(OEt)<sub>2</sub>](PF<sub>6</sub>)<sub>2</sub> releases NO in addition to HNO.<sup>98</sup> The {CoNO}<sup>8</sup> complex releases HNO once exposed to water.<sup>99</sup> Hydroxylamine-N-sulfonate releases HNO under alkaline conditions.<sup>100</sup> N-hydroxysulfonimidamides release HNO but are unstable.<sup>84</sup>

#### 1.4.1.7 Release of HNO from pH Photoactuation

Doctorovich *et al.* employed a derivatized *tris*(bipyridine)ruthenium(II) chloride pH photoactuator to spatially and temporally increase the pH, resulting in HNO generation from decomposition of the 4-nitro derivative of Piloty's Acid.<sup>40</sup> This approach would presumably be applicable to other HNO donors that require alkaline solutions to decompose.

### 1.4.2 Photoactive HNO Donors

An appeal has been made by researchers interested in HNO's bioreactivity for photoactivatable HNO donors.<sup>39,101</sup> Ultrafast HNO donors are required for fundamental reactivity studies. Initially it was as a result of laser flash photolysis (LFP) of Angeli's

salt that the  $pK_a$  of  ${}^1\text{HNO}/{}^3\text{NO}^-$  was revised from 4.7 to 11.4, despite both NO and HNO being generated.<sup>1</sup> Additionally, photoactivatable HNO donors pave the way for photoactivated delivery of HNO to specific physiological targets.<sup>101</sup>

#### ***1.4.2.1 Introduction to Photophysical and Photochemical Processes***

Organic molecular photochemistry is the study of the interaction of light with organic molecules.<sup>102</sup> The processes resulting from the interaction of light with organic molecules can be classified as either photophysical processes or photochemical processes.<sup>102</sup> Photophysical processes result in a net physical change while photochemical processes result in a chemical change.

Photoexcitation of an organic molecule is the process where a photon at the appropriate frequency is absorbed by the molecule, generating an electronically excited molecule.<sup>102</sup> The absorption of light by a ground state molecule into an excited state can induce significant electronic and structural changes in the molecule. The movement of the electrons is fast ( $10^{-16}$  -  $10^{-15}$  s), especially compared to the motion of the nuclei (called the Franck-Condon Principle).<sup>102,103</sup> Consequently, despite the change in electronic configuration, the nuclei retain the original configuration and solvent cage (called the Franck-Condon excited state) as the electrons move. The Franck-Condon excited state undergoes rapid thermal relaxation to its lowest vibrational level ( $10^{-13}$  -  $10^{-14}$  s; Scheme 1.8).<sup>102,103</sup> Reorganization of the nuclear geometry and solvent cage follows ( $10^{-11}$  -  $10^{-13}$  s); the resulting state is commonly referred to as the equilibrium excited state ( $S_1$ ; Scheme 1.8).<sup>102,103</sup> From this state, multiple deactivation pathways can take place, including fluorescence ( $10^{-12}$  -  $10^{-6}$  s), intersystem crossing (ISC) to a triplet state ( $10^{-12}$  -  $10^{-4}$  s), and phosphorescence ( $10^{-6}$  -  $10^{-1}$  s) (Scheme 1.8).<sup>103</sup> These processes are photophysical processes in that no net chemical change occurs (Table 1.1). Photoexcitation can also initiate very rapid photochemical reactions. Photochemical reactions are gaining increasing interest because reactive pathways not accessible in the ground state can be accessible in an excited state. These reaction pathways include ionization, electron transfer, dissociation, addition, abstraction, and isomerization or rearrangement (Table 1.1).<sup>103</sup> Observed photoproducts can be formed directly from an excited state of a reactant (called primary processes) or via an intermediate formed from the excited state of the reactant (called secondary processes).<sup>103</sup>

Scheme 1.8. Jablonski diagram where valence electrons are excited by absorption of light to a singlet excited state ( $S_1$ ,  $S_2$ , etc.). Vibrational relaxation occurs rapidly via radiationless transitions to the lowest excited singlet state ( $S_1$ ). Fluorescence (re-emission of light) occurs from the lowest excited singlet state. Intersystem crossing may occur to a triplet state ( $T_1$ ), in which case phosphorescence may occur. Non-radiative decay may also occur to the electronic ground state. Photolytic pathways are discussed elsewhere.

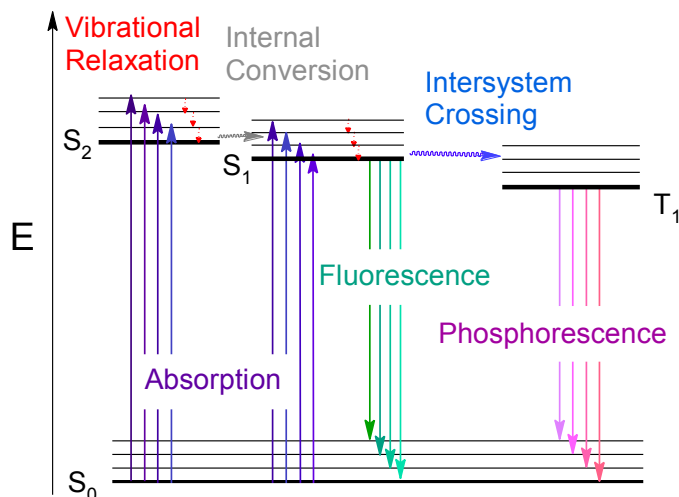


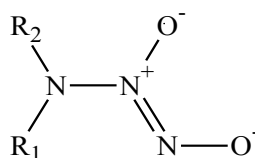
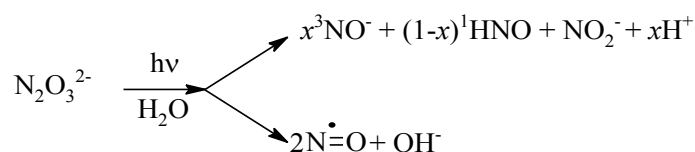
Table 1.1. Examples of photophysical and photochemical processes.<sup>103</sup>

Process	General Form
<i>Photophysical</i>	
Primary absorption	$S + h\nu \rightarrow S^*$
Excited-state absorption	$S^* + h\nu \rightarrow S^{**}$ $T^* + h\nu \rightarrow T^{**}$
Fluorescence emission	$S^* \rightarrow S + h\nu$
Stimulated emission	$S^* + h\nu \rightarrow S + 2h\nu$
Intersystem Crossing (ISC)	$S^* \rightarrow T^*$
Phosphorescence emission	$T^* \rightarrow S + h\nu$
Internal Conversion (IC)	$S^* \rightarrow S$
Collision-induced emission	$S^* + M \rightarrow S + M + h\nu$
Collisional deactivation	$S^* + M \rightarrow S + M$ $T^* + M \rightarrow S + M$
Electronic energy transfer	$S^* + S \rightarrow S + S^*$ $T^* + T \rightarrow T + T^*$
Excimer formation	$S^* + S \rightarrow (SS)^*$
Energy pooling	$S^* + S^* \rightarrow S^{**} + S$ $T^* + T^* \rightarrow S^* + S$
<i>Photochemical</i>	
Ionization	$A^* \rightarrow A^+ + e^-$
Electron transfer	$A^* + B \rightarrow A^+ + B^-$
Dissociation	$A^* \rightarrow B + C$ $A^* + B-C \rightarrow A + B + C$
Addition	$2A^* \rightarrow B$ $A^* + B \rightarrow AB$
Abstraction	$A^* + B-C \rightarrow A-B + C$
Isomerization or rearrangement	$A^* \rightarrow A'$

### 1.4.2.2 Photorelease of HNO from Angeli's Salt and Other Diazeniumdiolates

Photolysis of the anion of Angeli's salt produces a pH-dependent reaction mixture of  $^1\text{HNO}$ ,  $^3\text{NO}^-$ ,  $\text{NO}_2^-$ , and  $\text{NO}$ ; see Scheme 1.9.<sup>1,4</sup> Excitation of (Z)-1[N-(3-aminopropyl)-N-(3-aminopropyl)amino]diazene-1,2-diolate (DPTA NONOate, where  $\text{R} = \text{CH}_2\text{CH}_2\text{CH}_2\text{NH}_2$ ; Figure 1.7) was more selective towards HNO generation than Angeli's salt but still generated significant amounts of nitric oxide.<sup>25</sup> The photolytic mechanisms of diazeniumdiolates are not well-understood; however, HNO and  $\text{NO}_2^-$  are considered to be primary photoproducts.<sup>25</sup>

Scheme 1.9. Photolysis of Angeli's salt.



diazeniumdiolates

Figure 1.7. Structure of diazeniumdiolates.

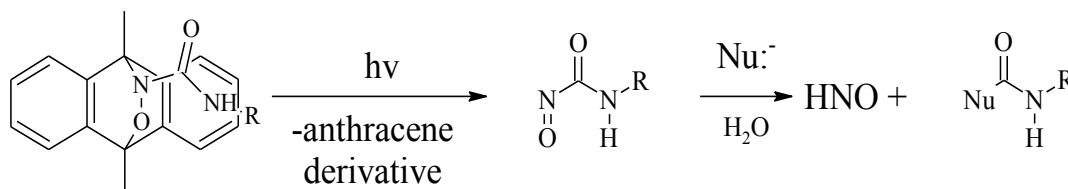
### 1.4.2.3 The Photocaging of HNO

Ideally, photocages have the following properties: (1) undergo a clean photoreaction with high quantum yields,  $\Phi_{\text{PP}}$ ; (2) contain chromophores with high molar absorption coefficients,  $\epsilon$ , above 300 nm; (3) produce non-reactive by-products; (4) release at rates that exceed the reaction of interest; (5) are soluble in aqueous (or mostly aqueous) media; (6) are pure and stable in the media of interest in the absence of light.<sup>10</sup> Regrettably, no single phototrigger meets all of these requirements. Therefore, when selecting a phototrigger, it is important to consider the desired application (e.g. cell studies, kinetic studies, etc.). Popular cages are typically organic, such as *p*-hydroxyphenacyl,<sup>104</sup> nitrobenzyl,<sup>12,20,105</sup> and coumarin derivatives.<sup>17</sup> Transition metal complexes have also been used as photoprotecting groups.<sup>106-108</sup>

### 1.4.2.3.1 Photorelease of HNO from Hetero-Diels-Alder Cycloadducts

The first reported examples of photocaged HNO-releasing compounds utilized 9,10-dimethylantracene tethered with acyl nitroso derivatives to form hetero-Diels-Alder cycloadducts (Scheme 1.10).<sup>109</sup> Photolysis of the cycloadducts released the acyl nitroso derivatives from 9,10-dimethylantracene by a retro-Diels Alder reaction. Modifications to the 9,10-anthracene substituents decreased the toxicity of byproducts while maintaining water-solubility.<sup>72,110</sup> The photoactive HNO donors were also evaluated for application in cellular studies<sup>110</sup> and demonstrated the ability to be activated in a site-specific and temporally controlled manner.<sup>96</sup> However, time-resolved IR studies indicate that the HNO generating pathway is relatively minor, with the major pathway proceeding via photo-induced homolytic C-N bond cleavage from this class of HNO donors.<sup>111</sup>

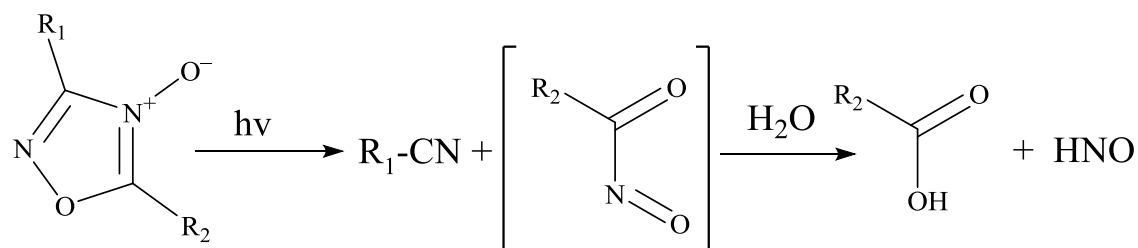
Scheme 1.10. Photorelease of HNO via hetero-Diels–Alder cycloadducts from acyl nitroso derivatives and 9,10-dimethylantracene.



### 1.4.2.3.2 Photorelease of HNO from 3,5-Heterocyclic Disubstituted 1, 2, 4-Oxadiazole-4-oxides

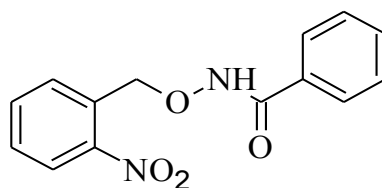
Photolysis of 1,2,4-oxadiazole-4-oxides releases nitrosocarbonyls, making the photocages a suitable option for release of HNO.<sup>112</sup> Photolysis of 3,5-diphenyl-1,2,4-oxadiazole-4-oxide generated benzonitrile and an acyl nitroso leaving group (Ph-CONO), which is known to decompose to generate HNO (Scheme 1.11). Preliminary time-resolved infrared spectroscopic evidence indicated HNO release.<sup>95</sup> The dimerization product of HNO, namely N<sub>2</sub>O, was detected from a series of 1,2,4-oxadiazole-4-oxides in aqueous solution after exposure to sunlight.<sup>112</sup> Further research has been carried out to modify the heterocyclic rings to improve nitrosocarbonyl generation and release of HNO.<sup>112</sup> The release of HNO is proposed to proceed via a triplet state, which would make the photorelease of HNO sensitive to oxygen (an established triplet quencher).<sup>112</sup> This is problematic for cell studies and complicates potential kinetic and mechanistic studies between HNO and relevant biomolecules.

Scheme 1.11. Photorelease of nitrosocarbonyls from 1,2,4-oxadiazole-4-oxides.



#### 1.4.2.3.3 Proposed Photorelease from a *o*-Nitrobenzyl Photocage

*o*-Nitrobenzyl caged benzohydroxamic acid was used as a model to investigate the ability of the photocage to release the acid without undergoing N-O bond homolysis (Figure 1.8).<sup>113</sup> Benzohydroxamic acid was selected as the caged compound because it is similarly structured to N-hydroxysulfonamide HNO donors.<sup>113</sup> N-O bond homolysis would undoubtedly prevent HNO formation from similarly structured leaving groups. Despite careful optimizations, the photocage was not selective for C-O bond cleavage.<sup>113</sup> It is likely that *o*-nitrobenzyl caged sulfonylhydroxamate HNO donors would also encounter N-O bond homolysis and consequently will not selectively release HNO. Furthermore, an additional problem was encountered because both the photocage and acid absorbed light at similar wavelength regions. Therefore the release of benzohydroxamic acid was wavelength dependent.<sup>10</sup> This study suggests that use of Piloty's acid-based HNO donating leaving groups are inherently problematic when the photocage absorbs in the same region.

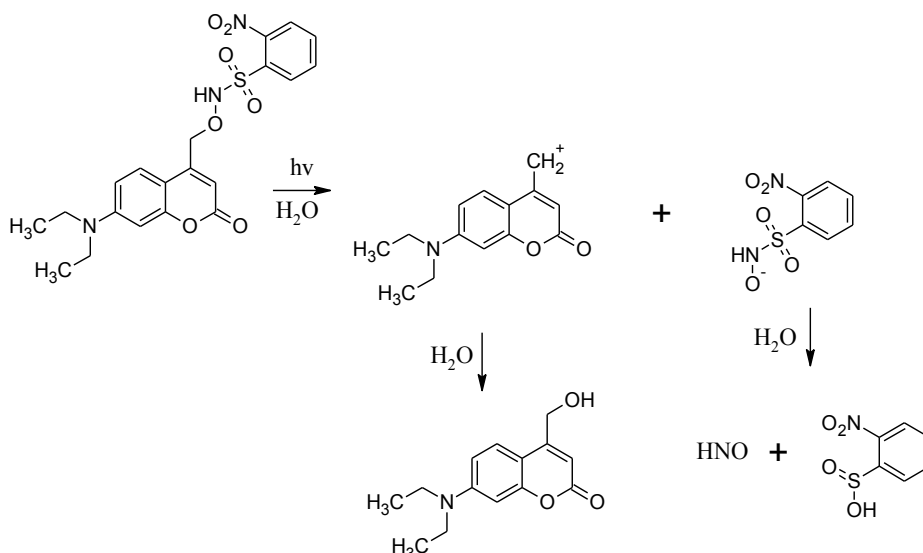
Figure 1.8. *o*-Nitrobenzyl chromophore tethered with benzohydroxamic acid.

#### 1.4.2.3.4 Photorelease of HNO from (7-diethylaminocoumarin-4-yl)methyl Photocages

Very recently, release of HNO was shown to occur from excitation of the (7-diethylaminocoumarin-4-yl)methyl photocage which was tethered to Piloty's acid derivatives bearing -NO<sub>2</sub> or -Br at the ortho position.<sup>114</sup> The researchers' goal was to develop photoactivatable HNO donors for use in cell assays.<sup>114</sup> Thus, a photocage that

absorbed visible light (400-430 nm) and was soluble in aqueous solution was selected.<sup>115</sup> HNO generation from visible light irradiation of the donors produced the corresponding benzene sulfonic acid and 7-diethylamino-4-hydroxymethylcoumarin (Scheme 1.12).<sup>114</sup> HNO was detected using GC-MS headspace analysis of the dimerization product, N<sub>2</sub>O,<sup>6</sup> and through HNO-specific fluorescence probe, P-Rhod.<sup>55</sup> However, this pathway was relatively minor (7% selectivity for -NO<sub>2</sub> derivative; -Br derivative is reported to be less selective).<sup>114</sup> The major pathway was proposed to occur via recombination of the conjugate base of the Piloty's acid derivative with the incipient carbocation intermediate formed during photoheterolysis generating a corresponding nitroso compound.<sup>114</sup> Despite the low selectivity, the -NO<sub>2</sub> derivative was shown to release HNO in living cells using probe, P-Rhod.<sup>114</sup>

Scheme 1.12. Photorelease the conjugate base of 2-nitro-*N*-hydroxybenzenesulfonamide from the (7-diethylaminocoumarin-4-yl)methyl photocage. 2-Nitro-*N*-hydroxybenzenesulfonamide subsequently thermally decomposes to then release HNO.

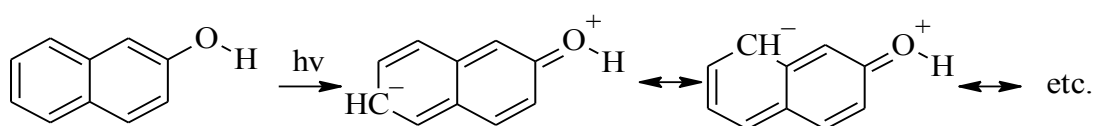


## 1.5 PHOTOCHEMISTRY OF HYDROXYARENES

Hydroxyarenes have been used to investigate the role of solvent in proton transfers,<sup>116</sup> possible applications in photoclick chemistry,<sup>117</sup> use as laser dyes,<sup>118,119</sup> the generation of biologically relevant quinone methides,<sup>120-123</sup> and ability to photoprotect molecules.<sup>117,124,125</sup> Notably, hydroxyarenes are useful photocages for poor leaving groups, such as alcohols, carboxylic acids, and phenols.<sup>124</sup> Upon electronic excitation, hydroxyarenes undergo significant electron redistribution in the singlet excited state (Scheme 1.1).<sup>126</sup> The electron redistribution may enable a hydroxyarene to undergo

excited state proton transfer (ESPT) to and from heteroatoms and even carbon atoms. While hydroxyarenes can undergo ISC to form triplet states, these proton transfers generally occur in the singlet state but have been occasionally observed in the triplet state as well.<sup>122</sup> In this section, a brief introduction to organic molecular photochemistry is presented. Following this, ESPTs are discussed in terms of excited state hydroxyarenes that can (1) transfer a proton to solvent, (2) accept a proton from solvent, (3) undergo intramolecular proton transfer, and (4) both accept and donate a proton from or to solvent. Other established photochemical processes involving hydroxyarenes are also discussed.

Scheme 1.13. Change in electronic density upon excitation of exemplar 2-naphthol in the  $S_1$  state in  $H_2O$ .<sup>126</sup>

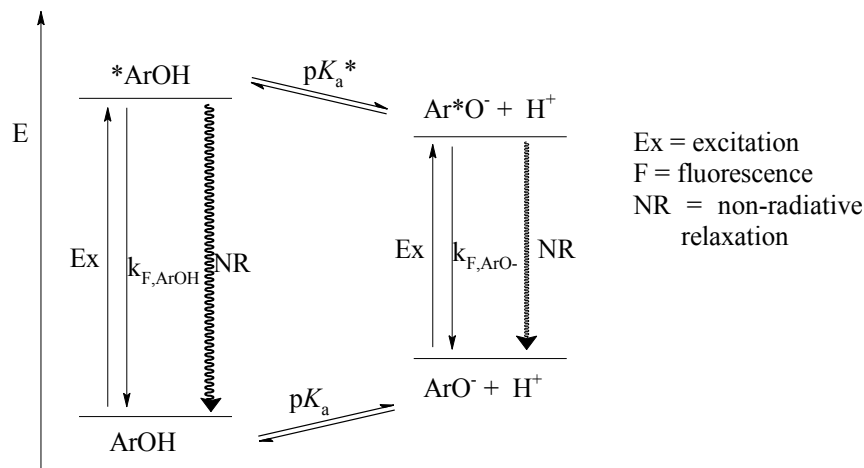


### 1.5.1 Hydroxyarenes and Photoacidity

Hydroxyarenes are typically photoacids. Photoacids are compounds that become more acidic in the singlet excited state ( $pK_a^* < pK_a$ ) due to a dramatic shift in their electronic structure. In other words, photoacids are compounds that are weak acids in their ground states; in their excited states, acidity increases by 7-10 orders of magnitude.<sup>127</sup> A traditional Forster cycle shows that in both the ground state and the excited state,  $ArOH/ArO^-$  and  $^*ArOH/^*ArO^-$  are in equilibrium as Bronsted-Lowry acid-base pairs (Scheme 1.14). A classic exemplar of this behavior is 2-naphthol, which contains a photoacidic OH. Upon excitation of 2-naphthol in water ( $pK_a$  9.30), two emissive species are observed ( $pK_a^*$  2.8) attributable to  $^*ArOH$  ( $\lambda_{max} = 360$  nm) and  $^*ArO^-$  ( $\lambda_{max} = 420$  nm).<sup>116</sup> The rate of excited state proton transfer to solvent (PTTS) is greater than  $5 \times 10^{10} s^{-1}$  for strong photoacids.<sup>127</sup> Scheme 1.16 depicts the current understanding of the mechanism of PTTS. Molecules that undergo ESPTs are proposed to be: (1) excited into a locally excited  $^*ArOH$ , (2) undergo electron transfer to an ion-pair  $^*ArO^- \cdots H^+$  associated with  $n-\pi^*$  CT from the oxygen to the ring system which is in equilibrium with  $^*ArOH$ , and (3) separation of the ion pair, forming  $^*ArO^-$ .<sup>128,129</sup> However, overall, the traditional Jablonski diagram (Scheme 1.14) gives a good description for most photoacids because  $k_R/k_{-R} \sim 1$  and  $k_{sep}/k_{-R} \gg 1$ . Notably, the stepwise movement of the electron transfer followed by a proton transfer distinguishes ESPT from proton coupled

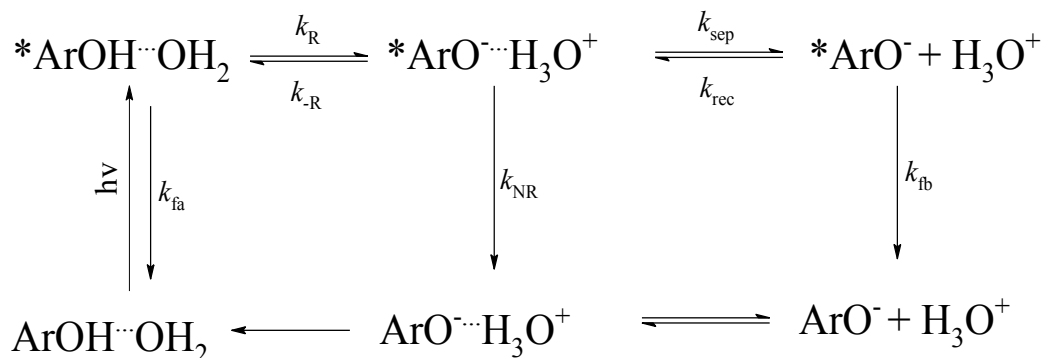
electron transfers (PCET).<sup>130-133</sup> Even under a relaxed PCET definition that includes stepwise movements, the electron transfer and proton transfer in ESPT originate from the same orbital; thus, ESPT is still distinguished from PCET.

Scheme 1.14. Traditional Jablonski diagram showing the Forster cycle.



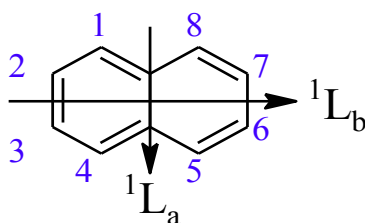
Solvent plays a large role in the photoprotolytic cycle (Scheme 1.16). The first two intermediates are in equilibrium with each other,<sup>128,129,134,135</sup> but the excited state energies (and thus the relative populations) of  $*\text{ArOH}$  and  $*\text{ArO}^{\cdot-} + \text{H}^+$  may be governed by solvent relaxation.<sup>136</sup> Essentially,  $k_R$  and  $k_{-R}$  may change over time with solvent relaxation.<sup>136</sup> The transition to form  $*\text{ArO}^{\cdot-}$  is governed by the electrical potential existing between the  $*\text{ArO}^{\cdot-}$  and the deprotonating entity (typically solvent water).<sup>116</sup> For example, in water, the proton from the photoacid can be transferred to a nearby water molecule and can “hop” via proton hopping within the water-hydrogen-bonded network.<sup>129</sup> Experimentally, the fluorescence spectra of hydroxyarenes have been investigated in order to understand factors that promote or inhibit ESPTs from the molecule. For example, the intensity of  $\text{ArO}^{\cdot-}$  emission increases with increasing concentrations of water as the emission from  $\text{ArOH}^*$  decreases.<sup>137</sup> Generally, photoacids (i.e. phenol, 1-naphthol, 2-naphthol) do not undergo PTTS in nonpolar solvents (hexane) or polar, aprotic solvents (ethyl acetate, DMSO).

Scheme 1.15. Protolytic dissociation mechanism under neutral pH conditions where  $k_R$  and  $k_{-R}$  are the rate constants of forward and backward proton transfer along the hydrogen bond;  $k_{\text{sep}}$  and  $k_{\text{rec}}$  are the separation and formation of the ion-pair (typically separated by 2-3 hydrogen-bonded water molecules),  $k_{\text{NR}}$  corresponds to non-radiative decay (fluorescence of this pair is not observed in typical experimental conditions).<sup>128,129,135</sup>



Photoacidity is dependent on the electronic structure of the chromophore.<sup>138</sup> As an exemplar, the effect of adding substituents to naphthalene is considered. Using Platt notation, the two lowest energy electronic structures of naphthalene are  $^1L_b$  and  $^1L_a$ , which have dipole moments perpendicular to each other (Scheme 1.16).<sup>139</sup> Substitution of a hydroxyl group onto either the 1- or 2- position to give 1-naphthol and 2-naphthol, respectively, breaks the  $D_{2h}$  symmetry; the two electronic states change in relative energy and also relative magnitudes of the transition dipole moments. For 1-naphthol, the lowest excited state is  $^1L_a$ , and for 2-naphthol, the lowest excited state is  $^1L_b$ .<sup>139,140</sup>  $^1L_a$  is more locally polarized than  $^1L_b$ , and as a consequence, 1-naphthol exhibits a larger difference between  $\text{p}K_a$  and  $\text{p}K_a^*$  compared to 2-naphthol (Scheme 1.16).<sup>140</sup> Ring substituents on the 1, 4, 5, and 8 positions affect the charge transfer from the hydroxyl oxygen for the  $^1L_a$  transition, and substituents on the 2, 3, 6, and 7 positions affect the polarization of both the  $^1L_a$  and  $^1L_b$  states, resulting in mixing (Scheme 1.16).<sup>141</sup>

Scheme 1.16. Naphthalene's structure with the first two transition dipole moments with numbering system of naphthalene; carbon 4a and 8a are unmarked.



### 1.5.2 Hydroxyarenes and Photobasicity

Photobases are more basic in their excited states than in their ground states ( $pK_b^* < pK_b$ ).<sup>142,143</sup> The mechanisms of proton transfers involving photobasic sites are not as well-studied compared to proton transfers to solvent molecules. Heteroatoms available on an aromatic structure typically serve as the basic site.<sup>144</sup> In aromatic molecules, electron donors donate more strongly in the excited state.<sup>145</sup> Some examples of molecules which undergo ESPTs to heteroatoms include 7-hydroxycoumarin dyes and 1-naphthol sulfonates.<sup>146</sup> Photobases typically accept protons from solvent.

Proton transfers to carbon atoms do not readily occur in the ground state due to the absence of hydrogen bonding between solvent and the aromatic carbon atoms.<sup>117,143,145,146</sup> However, proton transfers from the solvent to a photobasic carbon have been found to be  $10^{11}$ - $10^{14}$  times faster than in the ground state.<sup>147,148</sup> ESPTs to aromatic carbons have been reported in 1-naphthol,<sup>149</sup> 1,1'-bi-2-naphthol,<sup>144</sup> nitrostyrenes,<sup>147,148</sup> (nitrophenyl)acetylenes,<sup>145</sup> and 9-phenylxanthen-9-ol.<sup>150</sup> ESPTs to aromatic carbons have also been observed via deuterium incorporation.<sup>151</sup>

### 1.5.3 Bifunctional Hydroxyarenes: Solvent-Assisted Phototautomerization

In solvent-assisted phototautomerization, protons can be transferred from the photoacidic site to the photobasic site via solvent. An example of solvent-assisted phototautomerization is 6-carboxy-2-naphthol which has both a photoacidic (naphtholic OH) and photobasic sites (carboxylate).<sup>152</sup> For this molecule, four excited species are observed via fluorescence spectroscopy: HOOC-ROH, <sup>-</sup>OOC-ROH, <sup>-</sup>OOC-RO<sup>-</sup>, and HOOC-RO<sup>-</sup>.<sup>152</sup>

Kasha distinguished between three known types of solvent-assisted phototautomerization mechanisms: concerted biprotonic transfer, dynamic catalysis of proton transfer, and proton-relay transfer.<sup>153</sup> Concerted biprotonic transfer involves tautomerization in the absence of an internal hydrogen bond, via a single adjacent solvent molecule, and occurs in a concerted manner.<sup>153</sup> As the term indicates, only two hydrogen bonds are involved in concerted biprotonic transfer (Figure 1.9). Molecules that undergo intrinsic intramolecular proton transfers can also undergo concerted biprotonic transfers if the cyclic hydrogen bonds monosolvate.<sup>153</sup> Dynamic catalysis involves a similar transfer of protons, but in a stepwise fashion, a doubly hydrogen bonded component rearranges upon excitation of the aromatic molecule (Figure 1.10). Finally, proton-relay transfer involves

multi-proton bridged solvates.<sup>151,153,154</sup> In the simplest example, concerted biprotonic phototautomerization is in essence a two-proton relay transfer (Figure 1.11). However, proton-relay transfers typically involve multiple solvent molecules acting as a “wire” or “bridge” between the proton-donating and proton-accepting sites.

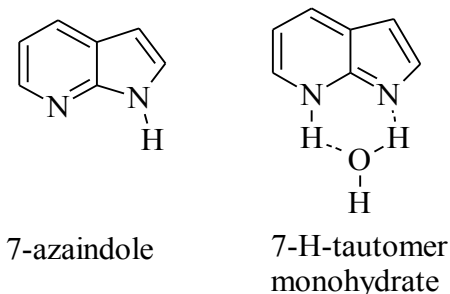


Figure 1.9. Example of concerted biprotonic transfer for 7-azaindole to form 7-H-tautomer monohydrate.

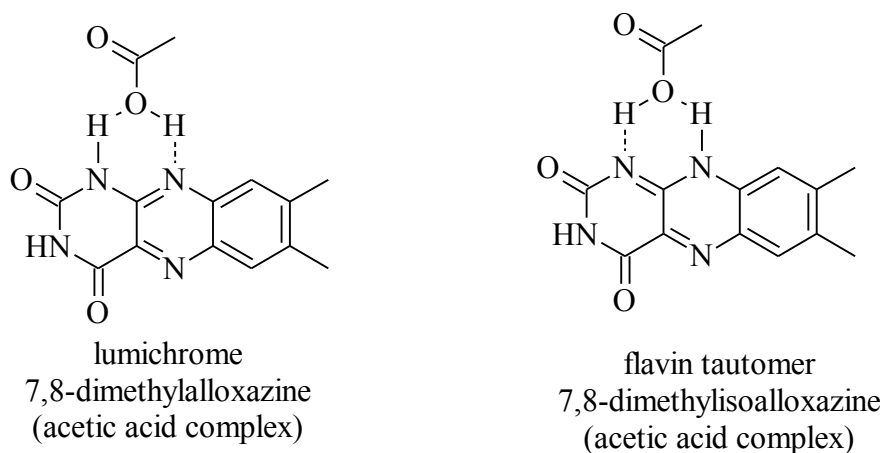


Figure 1.10. Example of stepwise ESPT for lumichrome in the presence of acetic acid to form a flavin tautomer.

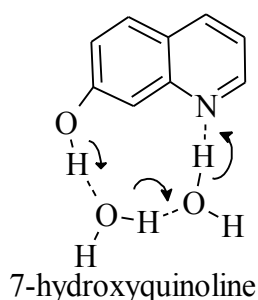
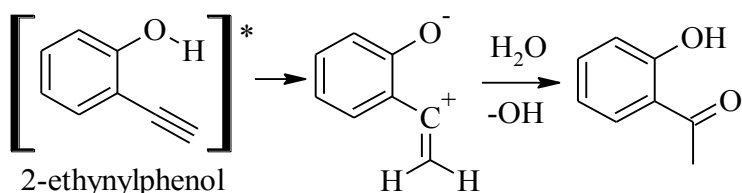


Figure 1.11. Example of ESPT occurring via proton-relays for 7-hydroxyquinoline.

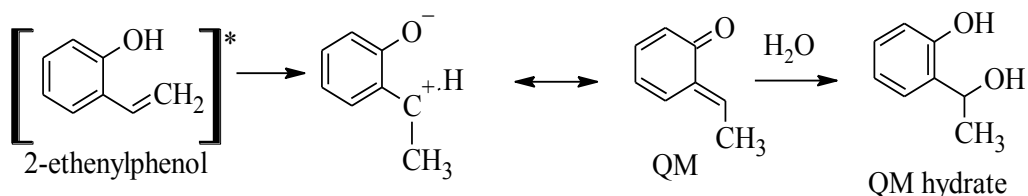
Some molecules can undergo irreversible phototautomerization to form a long-lived intermediate species. In 1984, Isaks, Yates, and Kalandropoulos demonstrated the first example of irreversible phototautomerization by showing that photoexcitation of 2-

ethynylphenol and *o*-hydroxystyrene produces a hydrated photoproduct in aqueous solutions.<sup>155</sup> They proposed that ESPT occurs from the phenol to the beta-carbon in the alkynyl/alkenyl substituent due to the photoacidic nature of the phenol moiety and simultaneous increase in basicity of the alkynyl/alkenyl moiety upon excitation (Scheme 1.17). Heterolytic cleavage of the phenolic OH produces a zwitterionic species. Hydration of the zwitterion generated a stable photoproduct. Foster, Baker, Brousmiche, and Wan later pointed out the importance of the resonance structure of the intermediate species for 2-ethynylphenol, namely a quinone methide (QM, Scheme 1.18), which are commonly encountered intermediates in many areas of chemistry and biology.<sup>100-102</sup> Significantly, QM-forming molecules can release substituents on the methylene carbon, enabling them to function as a photoprotecting group.<sup>120</sup>

Scheme 1.17. Reaction scheme for the photohydration of 2-ethynylphenol.



Scheme 1.18. Reaction scheme for the photohydration of 2-ethenylphenol.

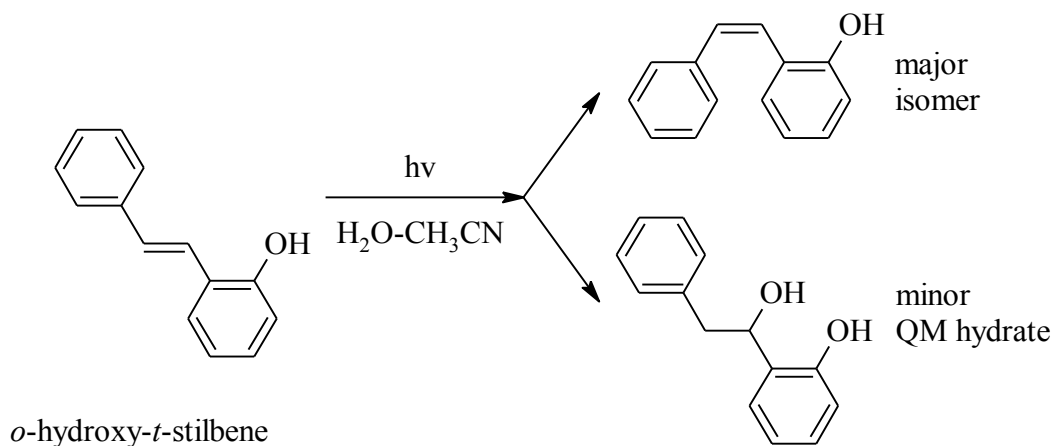


Many researchers utilized the photoexcitation of hydroxyarenes as a means to generate and study QMs.<sup>121-123,156-170</sup> More specifically, the groups of Wan,<sup>156,159,162,166,171-174</sup> Phillips,<sup>151,175</sup> and Wirz,<sup>176</sup> Zhu,<sup>121,169,177,178</sup> and others<sup>120</sup> investigated the structural requirements for QM photogeneration, the rates of QM formation, and the rates of QM decay. Typically, observation of the hydrated (solvent = H<sub>2</sub>O) or methanolated (solvent = MeOH) analogue of the QM intermediate provides support for a QM intermediate.<sup>179</sup> Further investigation was completed using time-resolved absorption, systematic structural modifications, and fluorescence spectroscopy.<sup>122,180</sup> Notably, QMs can also be formed from loss of the leaving group from the conjugate base form of hydroxyarenes.<sup>167</sup>

This mechanism of QM formation can be probed by directly exciting the conjugate base in alkaline solutions.

The rate of QM formation has been investigated using multiple experimental techniques. Firstly, fluorescence quenching correlates well with increased QM production, indicating that QM formation is competitive with fluorescence (ps to  $\mu$ s).<sup>151,181-183</sup> Secondly, laser flash photolysis (LFP) studies indicated that formation of QMs typically occur within a ns-laser pulse (typically  $\sim$ 5-10 ns).<sup>156,184,185</sup> Thirdly, excitation of *o*-hydroxy-*t*-stilbene, which can undergo phototautomerization or *trans-cis* photoisomerization, was investigated.<sup>159</sup> The major product was the *cis*-isomer and the minor product was the QM hydrate, which shows that phototautomerization is not competitive with *trans-cis* photoisomerization (fs to a few picoseconds; Scheme 1.19).<sup>159</sup> Ultra-fast time resolved spectroscopy suggests that QM formation occurs within picoseconds to a few microseconds.<sup>151,173,187</sup>

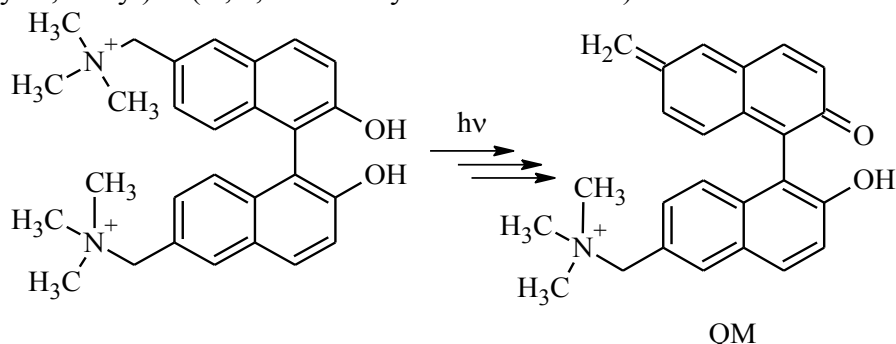
Scheme 1.19. Excitation of *o*-hydroxy-*t*-stilbene.



A recent fs-TA study indicated that phototautomerization is not necessarily synonymous with QM formation, but instead phototautomerization is an initial step in a series of steps prior to QM formation.<sup>151</sup> Formation of a QM intermediate was investigated from excitation of 1,1'-(2,2'-dihydroxy-1,1'-binaphthyl-6,6'-diyl)bis(*N,N,N*-trimethylmethanaminium) bromide (BQMP-b; Scheme 1.20).<sup>151</sup> The authors propose that the  $S_1$  state of BQMP-b undergoes phototautomerization ( $\tau = 7.4$  ps) in aqueous solution, then eliminates the protonated leaving group ( $-HNMe_3^+$ ), and finally undergoes ground state intramolecular proton transfer ( $\tau = 1.8$   $\mu$ s) to yield a zwitterionic intermediate, whose resonance structure is a QM. To my knowledge, this is the first example of loss of leaving group followed by QM formation in a stepwise-fashion. Further studies on structurally

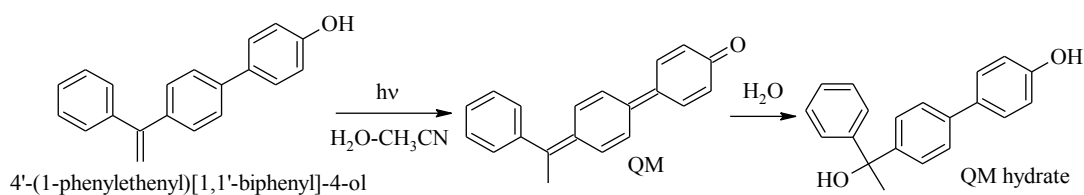
related molecules indicated that the leaving group is an important factor in the generation of QMs.<sup>187</sup>

Scheme 1.20. Formation of a QM from excitation of 1,1'-(2,2'-dihydroxy-1,1'-binaphthyl-6,6'-diyl)bis(N,N,N-trimethylmethanaminium) bromide.



Nanosecond laser flash photolysis is a useful method to observe the decay of a QM to its product species.<sup>167</sup> QMs formed through solvent-assisted phototautomerization can frequently be identified through careful selection of the solvent. In aprotic solvents, solvent-assisted phototautomerization cannot occur and QMs are not seen in the transient spectra, but in protic solvents QMs can be formed. For example, in laser flash photolysis experiments, 3-hydroxybiphenyl alcohols produced multiple transient species, one of which was produced only in aqueous solvent mixtures and was assigned to their corresponding QMs (Scheme 1.21).<sup>122</sup> One method of QM characterization in laser flash photolysis is to exploit their reactivity with nucleophiles. Indeed, many studies utilize the reactivity of QMs to confirm QM generation by characterizing the products of nucleophilic addition to the QM using steady state photolysis.<sup>184</sup> The nucleophilicity scale for o-QMs was determined to be  $RS^- \gg R_3N > PhO^- > RSH \sim RNH_2$  (bulky R substituents)  $> OH^- \gg H_2O \geq (Cl^-, AcO^-, \text{ or } ROH)$ .<sup>188</sup> However, the detection of QMs can be challenging because protic solvents also react rapidly with QMs, quenching their signals. In other studies, the highly absorbing but low-yield species, such as a phenoxyl or naphthoxyl radical (discussed further in Section 1.5.5), can overshadow the QM's absorption spectrum.<sup>166,185</sup> When decay of QMs is not readily identified in aqueous solution, non-nucleophilic but polar solvents (such as 2,2,2-trifluoroethanol (TFE) or 1,1,1,3,3,3-hexafluoro-2-propanol (HFIP)) can be used to slow the QM intermediate's decay.<sup>122,185,189,190</sup> It should be noted that highly absorbing but low-yield species, such as naphthoxyl radicals and radical cations (discussed in Sections 1.5.5), also decay more slowly in TFE versus aqueous solutions.<sup>185,191</sup>

Scheme 1.21. QM formation from excitation of 4'-(1-phenylethenyl)[1,1'-biphenyl]-4-ol in aqueous MeCN.



#### 1.5.4 Bifunctional Hydroxyarenes: Excited State Intramolecular Proton Transfer

Hydroxyarenes may contain photoacidic and photobasic sites adjacent to each other. In this case, the bifunctional molecule may be able to transfer a proton between the two sites upon excitation directly.<sup>127,146,154</sup> A zwitterion is typically formed with the proton donor being negatively charged and the proton acceptor being positively charged.<sup>146</sup> For example, 3-hydroxyflavone undergoes excited state intramolecular proton transfer (ESIPT) to form the pyrylium tautomer via an internal hydrogen bond (Figure 1.12).<sup>153</sup> The proton transfers are ultrafast intramolecular reactions which can occur as fast as 30-100 fs.<sup>132</sup> Note that the term ESIPT has been used in literature to describe processes that occur via solvent. In this thesis, ESIPT refers strictly to intramolecular processes that do not involve solvent. Classically, Kasha referred to this as intrinsic intramolecular proton transfer.<sup>153</sup>

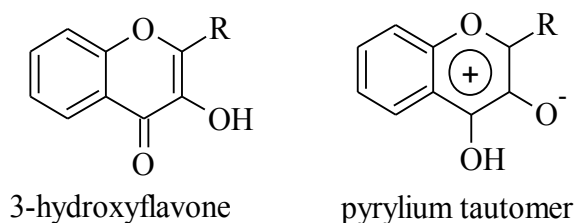


Figure 1.12. Example of intrinsic intramolecular proton transfer in 3-hydroxyflavone to form the pyrylium tautomer.

QMs formed from ESIPT are observed in both aprotic and protic solvents, making their identification more challenging than QMs generated from solvent-assisted phototautomerization. Methylated analogues of the hydroxyarenes in which the alcohol is substituted by  $-\text{OCH}_3$  are commonly used as negative controls to identify QM intermediates in time-resolved transient absorption spectra because methylated analogues of QM photogenerators do not form QMs.<sup>123,156,179</sup> For example, comparison of the time-resolved transient absorption spectra of 2-phenyl-1-naphthol versus its methylated analogue (Figure 1.13) enabled the identification of the QM generated by 2-phenyl-1-

naphthol.<sup>189</sup> The reactivity of QMs generated via ESIPT can also be studied in the presence of reactive nucleophiles (i.e. their lifetimes are longer in aprotic solvent (ns to 10 ms)).<sup>189,192</sup> Remarkably, a hydroxyarene may undergo ESIPT to form *o*-QM in aprotic solvents but switch in aqueous solvents to solvent-assisted phototautomerization to form a different QM.<sup>180,193</sup> For example, QM photogenerator 2-phenylphenol undergoes deuterium-exchange at the 2'-position on the phenyl group in non-aqueous solutions but at the 4'-position in aqueous solutions (Scheme 1.22).<sup>180,193</sup> Two spectroscopically unique QMs were identified from photolysis of 2-phenylphenol in MeCN (Scheme 1.22, QM-1) versus H<sub>2</sub>O (Scheme 1.22, QM-2).<sup>173</sup>

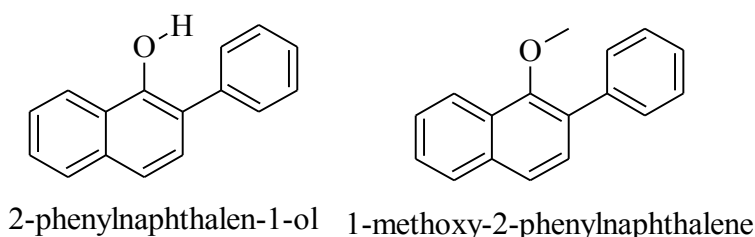
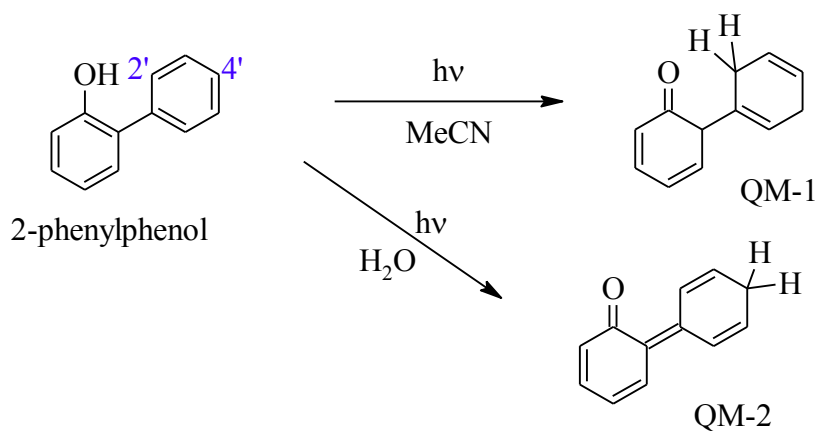


Figure 1.13. 2-Phenylnaphthalen-1-ol and its methylated analogue.

Scheme 1.22. Excitation of 2-phenylphenol in MeCN and in H<sub>2</sub>O.



### 1.5.5 Other Photochemical Processes for Hydroxyarenes

Hydroxyarenes may undergo photochemical processes other than ESPT, including ionization and electron transfer leading to bond homolysis or heterolysis. Typically, ionization and bond homolysis of the phenolic or naphtholic OH occur in low quantum yields but produce highly absorbing transient species. Therefore, they are an intrinsic aspect in the discussion of the photochemical processes for hydroxyarenes because if ignored, chemical processes observed in time-resolved photolysis studies are likely to be improperly assigned.

Firstly, hydroxyarenes can undergo ionization to form radical cations (ions that have both a positive formal charge and an unpaired electron), resulting from the photoejection of an electron (Eqn. 1.10):



Despite being long-lived species in the absence of bases,<sup>194</sup> the generation of radical cations is not easily detected using time resolved transient absorption spectroscopy due to low quantum yields (*i.e.*  $\phi = 0.02$  in naphthalene<sup>195</sup>) and the production of other transient species with overlapping absorption spectra.<sup>194,196</sup> However, radical cations from phenol or naphthol derivatives can be detected in non-aqueous solutions.<sup>194-199</sup> The solvents TFE and HFIP are known to stabilize radical cations.<sup>200</sup> Additionally, pulse radiolysis can be used to generate radical cations to confirm their assignment.<sup>196</sup> For example, 2-NpOH<sup>+</sup> was generated via pulse radiolysis of 2-naphthol (2-NpOH) in N<sub>2</sub>-saturated n-butyl chloride solution, showing absorbance bands at 360, 460 nm, and 570 nm.<sup>196</sup> The other product of the photoreaction (Eqn. 1.10), the solvated electron, is comparatively easier to identify in time resolved absorption spectra as it has a distinct absorption band at 630 nm.<sup>201</sup>

Secondly, phenoxyl or naphthoxyl radicals (ArO<sup>•</sup>) are formed via O—H bond homolysis after  $\pi$ - $\pi^*$  excitation<sup>202</sup> via a triplet state or via deprotonation of the radical cation (ArOH<sup>+</sup>).<sup>203</sup> These radicals are observed in the photolysis of 2-hydroxy-3-(diphenylhydroxymethyl)-anthracene,<sup>161</sup> 2-phenyl-1-naphthol,<sup>189</sup> phenyl-naphthols and naphthylphenols,<sup>189</sup> (4-hydroxyphenyl)-naphthalene derivatives,<sup>190</sup> and (2-adamantyl)naphthol derivatives.<sup>122</sup> Phenoxyl radicals are reported to be highly reactive towards phenols;<sup>204</sup> additionally, naphthoxyl radicals are likely reactive with oxygen according to theoretical computations.<sup>205</sup> However, due to their low quantum yields, the chemistry is relatively ambiguous for phenoxyl or naphthoxyl radicals. Like radical cations, pulse radiolysis can be used to study phenoxyl or naphthoxyl radical species. For example, the absorption spectra for 2-NpO<sup>•</sup> was determined from pulse radiolysis of an N<sub>2</sub>-saturated aqueous solution of NaN<sub>3</sub> and 2-NpOH; the species exhibits two absorption bands with  $\lambda_{\text{max}}$  at 350 (shoulder at 380) and 475 nm.<sup>196</sup>

As a final note, arylmethides can undergo bond homolysis or heterolysis of the ArCH<sub>2</sub>-X bond.<sup>206-208</sup> Bond homolysis yields radical products such as a methylated species (ArCH<sub>3</sub>), dimers, or in methanol, ArCH<sub>2</sub>CH<sub>2</sub>OH.<sup>206</sup> Bond heterolysis yields a

carbocation/anion pair ( $\text{ArCH}_2^+/\text{X}^-$ ), where the carbocation typically reacts with solvent to form a hydrated or methylated species.<sup>206,207</sup>

# CHAPTER 2: METHODS AND INSTRUMENTATION

---

This chapter describes the materials, analytical methods, and instrumentation used to probe HNM-protected HNO donors described in all subsequent chapters. One to three step syntheses are presented herein. The majority of the synthetic work was completed by collaborators at Kent State University.<sup>209</sup> Photophysical and photochemical characterizations were completed using several static and time-resolved spectroscopic methods. Gas chromatography-mass spectrometry (GC-MS), high performance liquid chromatography-high resolution mass spectrometry (LC-HRMS), UV-vis spectroscopy, and nuclear magnetic resonance (NMR) spectroscopy were used to characterize primary and secondary photoproducts. Photoproduct quantum yields were determined using actinometry. Time-resolved spectroscopic methods were chosen to probe the photophysical properties and photolytic processes observed upon excitation of the HNM-protected HNO donors and model compounds.

## 2.1 INSTRUMENTATION

### 2.1.1 Anaerobic Chamber

Anaerobic solutions were prepared by purging with argon or nitrogen and were stored inside an MBRAUN Labmaster 130 glovebox (1250/78, equipped with O<sub>2</sub> and H<sub>2</sub>O sensors) under a nitrogen atmosphere.

### 2.1.2 pH Measurements

Buffer solutions were made using inorganic or organic salts and were adjusted using concentrated HCl or NaOH. The pH of solutions was measured at room temperature using an Orion Star A211 pH meter equipped with a Mettler-Toledo pH combination micro electrode. The probe was filled with 3.0 M KCl solution and calibrated using standard pH 2.00, 4.00, 7.00 and 10.00 and 12.00 buffers. Unless otherwise noted, all measurements were carried out at room temperature.

In this thesis, mixed solvent conditions are used. To compare the  $pK_a$  values to similar molecules in aqueous solution, the measured pH values were converted to the hydrogen ion activity ( $pa_H$ ) using a standard correction:

$$pa_H = pH_{measured} - (E_j - \log \gamma_H) \quad \text{Eqn. 2.1}$$

where  $E_j$  is the liquid junction potential, and  $\gamma_H$  is the transfer activity coefficient of the proton.<sup>135,210</sup> For aqueous MeCN mixtures, a value of -0.87 was obtained by interpolating data from literature.<sup>135,210</sup> However, in the steady state photolysis experiments, the sample volumes prepared were too small (0.500 mL) for an accurate pH measurement to be recorded; furthermore, many solutions were anaerobic. Another method of correction was therefore employed. The effective pH of solutions can be calculated to a good degree of approximation from the concentration of  $H_3O^+$  contributed from the aqueous portion of the solvent mixture to give  $pH_D$  (i.e. Sørensen's definition of pH).<sup>211</sup> To confirm this, pH measurements were taken for five buffers and their corresponding solvent mixtures (80:20 v/v MeCN to aqueous buffer; Figure 2.1). The calculated values for  $pH_D$  were compared to the  $pa_H$  values,<sup>211</sup> correlating with an  $R^2$  value of 0.996 with an average difference of  $pH \pm 0.28$ . Therefore, this method can be used to estimate pH values to  $pH \pm 0.28$ .

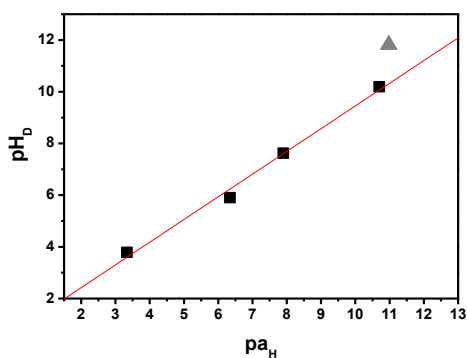


Figure 2.1. Correlation between  $pa_H$  and  $pH_D$  for solvent mixtures in 80:20 v/v MeCN to aqueous solution. The data point at 11.0 (gray triangle) was excluded from the analysis due to the alkaline error associated with the measurement.

### 2.1.3 NMR Spectroscopy

$^1H$ ,  $^{13}C$ ,  $^{31}P$ , and  $^{19}F$  NMR structure characterizations were performed with a Bruker Ascend 400 NMR spectrometer using MestRec version 5.3.1. Chemical shifts are reported in parts per million downfield from the internal reference of 3-(trimethylsilyl)propionic-2,2,3,3- $d_4$  acid sodium salt (TSP) or tetramethylsilane (TMS)

(0.00 ppm) for  $^1\text{H}$  NMR spectroscopy and trifluorotoluene (-63.72 ppm) for  $^{19}\text{F}$  NMR spectroscopy. For NMR experiments under anaerobic conditions, air-tight J-Young NMR tubes (Wilmad, 535-JY-7) were used.

## 2.2 MATERIALS

### 2.2.1 Reagents

Sodium benzenesulfinate ( $\text{NaC}_6\text{H}_5\text{SO}_2$ , 98%) was purchased from AK Scientific Inc, trifluoromethanesulfonic acid ( $\text{CF}_3\text{SO}_3\text{H}$ , 98%) from Sigma-Aldrich, sodium methanesulfinate ( $\text{NaCH}_3\text{SO}_2$ , 92% stated purity by the manufacturer) from AK Scientific Inc., and all buffers were purchased from Labserv, Sigma-Aldrich or AK Scientific Inc. Hydroxocobalamin hydrochloride ( $\text{HOCbl.HCl}$ , >95% purity as stated by manufacturer) was purchased from Fluka. Tris(4,6-dimethyl-3-sulfonatophenyl)phosphine trisodium salt hydrate (TXPTS,  $\geq 97\%$  stated purity by manufacturer) was purchased from Strem. NMR solvents ( $\text{CD}_3\text{CN}$ ,  $\text{DMSO-d}_6$ ,  $\text{CD}_3\text{OD}$ , and  $\text{D}_2\text{O}$ ) were supplied by Merck Millipore or Sigma-Aldrich. Unless otherwise noted, all commercial chemicals were used directly without purification. Pure water was obtained using a Purite's Purewater 300 system.

$\text{HNO}$  donors **1-4**, 3-hydroxynaphthalene-2-carbaldehyde (**6**), 6-(hydroxymethyl)naphthalen-2-ol (**7**), 6-hydroxynaphthalene-2-carbaldehyde (**8**), and 6-(hydroxyimino)methyl-naphthalen-2-ol (**10**) were synthesized Dr. Yang Zhou and Mohammad Saifur Rahman in accordance with previously published thesis work.<sup>211</sup> Dr. Sonya Adas and Jiuhong Zhang synthesized N-hydroxytrifluoromethanesulfonamide ( $\text{CF}_3\text{SO}_2\text{NHOH}$ ) as described in the literature.<sup>90</sup>

### 2.2.2 Syntheses

#### 2.2.2.1 *Angeli's Salt*

The synthesis of Angeli's salt has been published elsewhere.<sup>82</sup>  $\text{NH}_2\text{OH}\cdot\text{HCl}$  (0.50 g) was dissolved in 0.50 mL of water and heated gently. Solid  $\text{NaOH}$  (0.88 g) was dissolved in 100%  $\text{CH}_3\text{OH}$  (6.00 mL) with prolonged sonication. The  $\text{NH}_2\text{OH}\cdot\text{HCl}$  solution was transferred dropwise with stirring into the  $\text{NaOH}$  solution. The reaction mixture was filtered through a sintered funnel and the  $\text{NaCl}$  precipitate discarded. The filtrate containing pure  $\text{NH}_2\text{OH}$  was transferred to a Schlenk flask and purged with nitrogen for  $\sim 5$  min.  $\text{N}_2$ -purged *n*-butylnitrate (0.80 mL) was then added dropwise via a syringe with

stirring. The precipitate was left in solution in a refrigerator overnight. After 7 hr, the product was filtered, re-dissolved in the minimal amount of 0.10 M NaOH (0.50 mL), and precipitated with excess ethanol (~ 20 mL, 100%). The purified product was dried under vacuum ( $2 \times 10^{-2}$  mbar) overnight. The procedure was repeated twice, with yields of 43% and 49%. The purity of Angeli's salt was checked by UV-vis spectroscopy ( $\epsilon_{248 \text{ nm}} = 8.30 \times 10^3 \text{ M}^{-1} \text{ cm}^{-1}$ ) and found to be  $\geq 99\%$ .

#### 2.2.2.2 *Piloty's Acid*

The synthesis for Piloty's acid has been published elsewhere.<sup>212</sup>  $\text{NH}_2\text{OH}\cdot\text{HCl}$  (0.50 g) was dissolved in MeOH/ $\text{H}_2\text{O}$  (3:2; 5 mL) and cooled to 0 °C in an ice bath.  $\text{K}_2\text{CO}_3$  (1.00 g) was dissolved in 2 mL of water and added dropwise to the reactant solution while stirring. The reaction was left for 2 hr to react with stirring. A white precipitate was filtered off through a celite pad. Silica gel (pore size 60 Å; 4 g) was added to the filtrate. The solvent was then evaporated to yield a crude product absorbed onto the silica. The silica/crude product mixture (~68 g) was slurried with eluent (30% EtOAc/petroleum ether) and added to a medium column (1 inch x 12 inches). Fractions of pure product were collected and taken down to dryness. The purity of Piloty's acid was checked via  $^1\text{H}$  NMR spectroscopy and the yield was 29%.  $^1\text{H}$  NMR (400 MHz,  $d_6$ -acetone)  $\delta = 8.86, 8.72, 7.94, 7.93, 7.92, 7.71, 7.69, 7.64, 7.62, 7.60$  ppm (see Appendix A).

#### 2.2.2.3 *N-Methylsulfonylhydroxylamine (MSHA)*

The synthesis for N-methylsulfonylhydroxylamine (MSHA) has been published elsewhere.<sup>212</sup> Hydroxylamine hydrochloride (1.04 g) and *tert*-butyldimethylsilyl chloride (TBS-Cl, 2.46 g, 1 equiv.) were added to a two-necked round bottom flask (100 mL). Dimethylformamide (DMF, anhydrous, 50 mL) was added with stirring. The mixture was stirred until the solids completely dissolved. The solution was cooled to 0 °C under nitrogen using an ice bath. Triethylamine (6.26 g, 65.5 mmol, 5 equiv.) was added dropwise over 15 minutes so that the temperature remained below 10 °C. A large amount of white solid precipitated out, indicating the expected triethylammonium chloride formation. The ice bath was removed, and the solution was stirred at room temperature for 16 hr. An ice bath was used to bring the reactant solution to 0 °C. Methanesulfonyl chloride (1.04 mL, 1 equiv.) was added slowly so that the temperature remained less than 10 °C. The ice bath was removed, and the solution was left to stir for 19 hr. The suspension was poured into a mixture of saturated ammonium chloride solution (50 mL), water (50

mL), and hexane (100 mL). The aqueous layer was extracted and washed with additional hexane (2 x 50 mL) resulting in a yellow aqueous layer. The organic layers were combined and were washed with water (6 x 100 mL) to remove any remaining triethylammonium chloride. The organic layer was then dried with MgSO<sub>4</sub> and the solvent evaporated on a rotary evaporator to reveal a colorless oil-like substance (1.09 g, 32% yield). <sup>1</sup>H NMR (400MHz, CDCl<sub>3</sub>) δ = 6.40 (s, 1 H), 3.05 (s, 3 H), 0.91 (s, 9 H), 0.23 (s, 6 H) ppm (see Appendix A).

The resulting TBS-protected MSHA (1.09 g, 4.8 mmol, 1 equiv.) was dissolved in THF (30 mL) and the solution was cooled to 0 °C in an ice water bath with stirring. Glacial acetic acid (1.4 mL, 24 mmol, 5 equiv.) was added dropwise, followed by the addition of TBAF (1 M in THF, 7.5 mL, 7.5 mmol, 1.6 equiv.). The temperature remained below 10 °C. The ice/water bath was then removed, and the solution was stirred for 3 hr. The product mixture was then poured into water (10 mL) and EtOAc (40 mL) added to this mixture. The layers did not separate cleanly. Additional water was added (75 mL) followed by the addition of sodium chloride until saturation was observed. The aqueous layer was collected and extracted three times with EtOAc (50 mL). The organic layers were collected, combined, and dried with MgSO<sub>4</sub>. The product mixture was then put through a silica gel plug to remove impurities. The filtrate was taken to dryness on the rotary evaporator. Chloroform (50 mL) was added to the product and the solution was left overnight (~10 °C). The precipitate was then collected using filtration and dried under vacuum for 2 days. The resulting product was a white solid (0.15 g, 29% yield, ~97% purity). <sup>1</sup>H NMR (400MHz, DMSO) δ = 9.56 (d, 1 H), 9.04 (d, 1 H), 2.92 (s, 3 H) (see Appendix A).

#### 2.2.2.4 Nitroxylcobalamin (NO-Cbl(III))

The synthesis for nitroxylcobalamin (NO<sup>-</sup>-Cbl(III); also called nitrosylcobalamin<sup>213</sup>) described in the literature<sup>211</sup> was modified to use Angeli's salt instead of the HNO donor diethylammonium (Z)-1-(N,N-diethylamino)diazen-1-ium-1,2-diolate (DEA-NONOate) because Angeli's salt was readily available. A freshly prepared anaerobic solution of Angeli's salt (0.01397 g, 2.5 equiv.) in NaOH (0.1 M) was added quickly to an anaerobic solution of HOCbl•HCl (0.06324 g) dissolved in TES buffer (0.10 M, 500 μL, pH 7.4). The product solution was stirred continuously to ensure complete mixing and the reaction left to proceed at room temperature for 3 hr. Formation of the desired product was checked by UV-vis spectroscopy. The product was precipitated by dropwise addition to

cold acetone (20 mL, -20 °C), filtered and dried under vacuum for three days at 25 °C. Both the synthesis and handling of the final product were carried out inside a glove box under a nitrogen atmosphere. The yields (two independent syntheses) were 59 and 84%. The purity assessed by <sup>1</sup>H NMR spectroscopy was 98 ± 2 %. Exposure of 3 mL of a 50 mM solution of NO<sup>-</sup>-Cbl(III) to air resulted in a rapid conversion of NO<sup>-</sup>-Cbl(III) to H<sub>2</sub>OCbl<sup>+</sup> and NO<sub>2</sub>Cbl.<sup>214</sup> <sup>1</sup>H NMR (400 MHz, D<sub>2</sub>O) characteristic peaks δ = 7.31 (s, 1 H), 7.12(s, 1 H), 6.71(s, 1 H), 6.25(s, 1 H), 6.17 (d, *J* = 4.0 Hz 1 H) (see Appendix A).

#### 2.2.2.5 3-(Hydroxymethyl)-2-naphthol (Diol **5**)

The synthesis for diol **5** has been published elsewhere.<sup>215</sup> A solution of 3-hydroxy-2-naphtholic acid (0.849 g) dissolved in anhydrous THF (35 mL) was added at room temperature to a suspension of lithium aluminium hydride (LAH; 0.432 g, 9.02 mol) in dry THF over 15 minutes with stirring in an ice bath. The reaction was left to stir for three hr at room temperature. The reaction was then quenched by adding the product mixture dropwise into ~150 mL of wet diethyl ether, chilled with ice. Then HCl (3 M, 50 mL) was added to the product solution. The ether layer was separated, and the aqueous layer was extracted with diethyl ether. The organic layers were combined and taken down to dryness and recrystallized in 20:80 EtOH:H<sub>2</sub>O at 90 °C. After filtration, the filtrate was cooled and product was collected (0.5782 g). The purity assessed by <sup>1</sup>H NMR spectroscopy was 98 ± 2 %. The percent yield was 74%. <sup>1</sup>H NMR (400 MHz, d<sub>6</sub>-acetone) δ = 8.74 (OH), 7.82, 7.77, 7.75, 7.66, 7.64, 7.36, 7.34, 7.33, 7.26, 7.25, 7.24, 7.18, 4.88, 4.46 (OH) ppm (see Appendix A).

### 2.3 STEADY STATE SPECTROSCOPY

#### 2.3.1 Electronic Absorption

UV-vis kinetic data were obtained using an Agilent Cary 100 UV-vis spectrophotometer with a thermostatted cell compartment (25.0 °C). Typically, quartz cuvettes with 10 mm pathlengths were used. However, where noted as anaerobic, Schlenk cuvettes equipped with side arm balls and fitted with J-Young air-tight caps were used. The spectra were analyzed using Origin (version 6.1 or 9.3).

To determine the molar extinction coefficient, solutions of 53.0, 104, 154, and 203 μM were prepared and their absorbance measured. The plots of concentration versus

absorbance at  $\lambda_{\text{max}}$  were linear, and the molar extinction coefficient was calculated from the slope ( $y = mx$ ; see Appendix C).

### 2.3.2 Determination of Acid Dissociation Constants

Spectrophotometric titration studies were completed using the Agilent Cary-100 UV-vis spectrophotometer. Aqueous solutions of the compounds were circulated using a peristaltic pump through a 1 cm path length quartz flow-through cell at 25.0 °C. The initial absorbance spectrum was recorded. Small volumes of 1 M NaOH or 1 M HCl were added (dilutions did not exceed 5%). Spectra of static samples were recorded after the pH stabilized. The absorbance was plotted as a function of pH according to the following equation:

$$A_{\text{obs}} = \frac{A_i + A_f \times 10^{(\text{pH} - \text{p}K_a)}}{1 + 10^{(\text{pH} - \text{p}K_a)}} \quad \text{Eqn. 2.2}$$

where  $A$  is the observed value, and  $A_i$  and  $A_f$  are the absorbances of the acid and conjugate base, respectively (refer to derivation of Eqn. 2.2 in Appendix B).

### 2.3.3 Electronic Emission

Emission measurements were recorded using a Varian Cary Eclipse Fluorescence Spectrophotometer. Quartz fluorimeter cells were purchased from Global Sciences. To ensure the integrity of the samples, UV-vis absorption spectra were recorded before and after fluorescence measurements were taken. Changes in UV-vis spectra indicated decomposition of the sample and these samples and their spectra were discarded. To minimize intermolecular interactions and re-absorption of light, absorbances were kept less than 0.1 a.u. at the wavelength of excitation and longer wavelengths. For pH dependence studies, the molecules were excited at their respective isosbestic points to equally excite the protonated and deprotonated conjugates. The following buffers (5.0 mM) were used: sodium monophosphate ( $\text{p}K_a = 2.15$ , pH 3.0), potassium acetate ( $\text{p}K_a = 4.76$ , pH 5.0), sodium monophosphate ( $\text{p}K_a = 6.82$ , pH 7.0), sodium borate ( $\text{p}K_a = 9.24$ , pH 9.0), and sodium bicarbonate ( $\text{p}K_a = 10.29$ , pH 11.0). For pH 1 and pH 14, 0.1 M HCl and 0.1 M NaOH were used, respectively. Low concentrations of buffer salts were used to prevent precipitation of the buffer salt in mixed solvent conditions.

At low concentrations, the fluorescence intensity is dependent on the concentration of the fluorophore and the data must be treated accordingly. Consequently, the datasets are reported in two different ways: intensity and relative intensity. Plots showing “intensity”

on the y-axis are used to compare spectral shapes *only*. Plots with “relative intensity” can be used for comparison of both spectral shapes and their peak intensities. These spectra were recorded as quickly as possible (typically within one hour) to minimize fluctuations in the excitation light intensity with no changes in instrumental settings (e.g. excitation wavelength, slit widths, scanning rates). Additionally, the spectra have been corrected for any differences in absorbance at the wavelength of excitation.

## 2.4 PHOTOPRODUCT CHARACTERIZATIONS

### 2.4.1 Steady State Photolysis Studies

Unless otherwise noted, steady state photolysis studies were performed using a Rayonet mini-photoreactor with  $350 \pm 50$  nm bulbs (RMR-600, 4 W, 8 lamps). A cooling fan maintained the temperature during sample irradiation. Unless otherwise noted, samples (500-750  $\mu$ L) were prepared in anaerobic solutions in NMR tubes fitted with J-Young caps. The purity of the sample was checked prior to irradiation using  $^1\text{H}$ ,  $^{31}\text{P}$ , and/or  $^{19}\text{F}$  NMR spectroscopy. The decomposition reactions were monitored using  $^1\text{H}$ ,  $^{31}\text{P}$ , or  $^{19}\text{F}$  NMR spectroscopy. The following buffers (5.0 mM) were used: sodium monophosphate ( $pK_a = 2.15$ , pH 3.0), potassium acetate ( $pK_a = 4.76$ , pH 5.0), sodium monophosphate ( $pK_a = 6.82$ , pH 7.0), sodium borate ( $pK_a = 9.24$ , pH 9.0), and sodium bicarbonate ( $pK_a = 10.29$ , pH 11.0). For pH 1 and pH 14, 0.1 M HCl and 0.1 M NaOH were used respectively.

Select photolysis studies were done using a Xe lamp (150 watt) fitted with a monochromator. For these studies, samples (3-4 mL) were prepared in fluorimeter cuvettes and irradiated using either filtered (reported wavelength plus or minus two nm) or unfiltered (broad spectrum) light from the Xe lamp.

### 2.4.2 GC-MS Headspace Analysis

Gas-chromatography-mass spectrometry (GC-MS) analyses were performed on an Agilent GC 7890B system with a 5677B MSD equipped with an Agilent 122-5532G column. Headspace samples were taken from each reaction vessel by means of a GERSTEL MPS Headspace Autosampler with a 2.5 mL gas-tight syringe. Aliquots (250.0  $\mu$ L) were injected in the split mode. The species of interest passed through the column with the solvent plug. GC conditions were as follows: flow rate, 1.4 mL/min;

injection temperature, ambient room temperature; column oven temperature, 26°C. Spectra were obtained in normal scanning mode (36-100  $m/z$ ).

### 2.4.3 LC-HRMS Analysis of Photoproducts

Prior to sample analysis, the instrument was calibrated with formic acid. Authentic samples and irradiated samples were initially prepared in 1.0-3.0 mM concentrations and then were diluted to 10-100  $\mu\text{M}$  in MeCN. Samples were centrifuged prior to analysis. Samples were analyzed by LC-MS, using an InertSustain HP C18 (2.1  $\times$  250 mm, 3  $\mu\text{m}$  particle size, GL Sciences) column coupled to a Bruker microTOF-Q II electrospray ionization (ESI) mass spectrometer (parameters are described in Table 2.1). The LC conditions were based on methods reported by Tang *et al*<sup>216</sup> and included a column temperature of 30°C and a mobile phase comprised of A: H<sub>2</sub>O and B: MeCN at a flow rate of 250 or 300  $\mu\text{L}/\text{min}$ . A LC-MS run consisted of the following elution program: 0–2 min: 5→15% B, 2–3 min: 15→40% B, 3–12 min: 40→80% B, 12-13 min: 80→90% B, 13–15 min: 90% B, 15–18 min: 5% B. The sample injection volume was 10  $\mu\text{L}$ . The mass spectra were analyzed using DataAnalysis Version 4.0 (Bruker Daltonik GmbH).

Table 2.1. ESI-MS operating parameters.

ESI-MS operating parameters	
Polarity	Negative
Scan mass range [ $m/z$ ]	50–700
End plate offset [V]	–500
HV capillary [V]	3200
Dry gas flow [ $\text{L min}^{-1}$ ]	10.0
Dry gas temperature [°C]	220
Nebulizer gas [bar]	0.4

### 2.4.4 Photoproduct Quantum Yields

Quantum yields are defined as the number of events per photons absorbed.<sup>217</sup>

$$\Phi = \frac{\text{number of events}}{\text{number of photons absorbed}} \quad \text{Eqn. 2.3}$$

Thus, two pieces of information are required to determine the photoproduct quantum yield for a photochemical process. The number of reacted molecules per unit time can be calculated from the ratio of the moles of photoproducts generated compared to the starting material. The number of photons absorbed per unit time can be determined using chemical actinometry. A chemical actinometer is a reference compound undergoing a photochemical reaction that has a well-established quantum yield. It is used to determine

the photon flux from the monochromatic light source. The quantum yields are then calculated relative to the actinometer using the following equation:

$$\Phi = \frac{\text{number of reacted molecules}}{\varphi \times t \times \frac{A_{\text{sample}}}{A_{\text{act}}}} \quad \text{Eqn. 2.4}$$

where  $\varphi$  = photon flux in einsteins  $\text{s}^{-1}$ ,  $t$  = irradiation time of sample, and  $A_{\text{act}}$  and  $A_{\text{sample}}$  are the absorbance at the irradiation wavelength of the actinometer and sample, respectively.<sup>218</sup>

A correction for the reflectance  $R$  was applied when the actinometer and sample were prepared in different solvent conditions.<sup>219</sup>

$$\varphi_b = \frac{\varphi}{1-R} \quad \text{Eqn. 2.5}$$

where  $\varphi$  is the photon flux calculated from the actinometer,  $\varphi_b$  is the photon flux of the beam, and  $R$  is defined as:<sup>219</sup>

$$R = \left[ \frac{n_1 - n_2}{n_1 + n_2} \right]^2 \quad \text{Eqn. 2.6}$$

Herein, relative photoproduct quantum yields were determined by comparison to azobenzene, which has a known quantum yield for *trans*  $\rightarrow$  *cis* isomerization of ( $\Phi_{313\text{nm}} = 0.14$ ; in methanol) when irradiated at 313 nm (see Appendix C for an example).<sup>220</sup> The light source was the Xe lamp (150 watt) fitted with a monochromator (slit width 2.0 mm,  $313 \pm 3$  nm). Azobenzene ( $\sim 70 \mu\text{M}$  in MeOH; stored in the dark) was irradiated at various time intervals using a Xe lamp fitted with a monochromator (slit width 2.0 mm,  $313 \pm 3$  nm) in a 1 cm quartz fluorimeter cuvette. The conversion of the *trans*  $\rightarrow$  *cis* isomer was monitored using UV-vis spectroscopy. The photon flux,  $\varphi$  (einsteins  $\text{s}^{-1}$ ) was calculated as described by established procedures:

$$\varphi = \frac{F(\lambda) \times \Delta A_{358} \times V}{t \times l} \quad \text{Eqn. 2.7}$$

where  $F(\lambda)$  is equal to  $5.30 \times 10^{-6}$  einsteins  $\text{cm}^{-2}$  for 313 nm irradiation,  $\Delta A_{358}$  is the change in absorbance at 358 nm,  $V$  is the sample volume in  $\text{cm}^3$ ,  $t$  is the time of irradiation, and  $l$  is the pathlength in cm.<sup>219</sup> Conversion of *trans*-azobenzene to *cis*-azobenzene did not exceed 10%.

To verify the method, the photoproduct quantum yield for azobenzene was cross-correlated that for ferrioxalate,  $[\text{Fe}^{\text{III}}(\text{ox})_3]^{3-}$ . The actinometer, potassium ferrioxalate ( $\text{K}_3[\text{Fe}(\text{C}_2\text{O}_4)_3] \cdot 3\text{H}_2\text{O}$ ), was synthesized according to literature by another member of our research group.<sup>219</sup> A solution of potassium ferrioxalate (5.20 mM; 25.00 mL) was prepared in 0.05 M  $\text{H}_2\text{SO}_4$ . An aliquot (3.000 mL;  $V_1$ ) of the yellow-green potassium ferrioxalate solution was irradiated at various intervals using the Xe lamp fitted with a monochromator (slit width 2.0 mm,  $313 \pm 3$  nm) in a 1 cm quartz fluorimeter cuvette. Following irradiation, an aliquot of the irradiated solution (500  $\mu\text{L}$ ;  $V_2$ ) was transferred to a 5.00 mL volumetric flask containing 1,10-phenanthroline solution (0.1 % w/V, 2.00 mL stored in the dark) in sodium acetate buffer (1.0 M, 250  $\mu\text{L}$ , pH 4.1); the volumetric flask was made up to 5.00 mL ( $V_3$ ) with water. After 20 min, UV-vis spectra were recorded and analyzed at 510 nm ( $\epsilon(510\text{nm})=11,000 \text{ M}^{-1}\text{cm}^{-1}$ ). The reduction of  $[\text{Fe}^{\text{III}}(\text{ox})_3]^{3-}$  to  $[\text{Fe}^{\text{II}}(\text{ox})_3]^{2-}$  (which was reacted further with 1,10-phenanthroline to form  $[\text{Fe}(\text{phen})_3]^{2+}$ ) did not exceed 10% conversion.

The two actinometers were cross-correlated by calculating the photon flux using the methods described in the literature.<sup>218</sup> The extinction coefficient of  $[\text{Fe}(\text{phen})_3]^{2+}$  ( $1.11 \times 10^4 \text{ M}^{-1}\text{cm}^{-1}$ )<sup>221</sup> was used to calculate the moles of Fe(II)-phenanthroline. The photon flux was calculated according to:

$$\varphi = \frac{\text{moles of Fe(II)-phenanthroline}}{\Phi(\lambda) \times t} \quad \text{Eqn. 2.8}$$

where  $\Phi(\lambda) = 1.24$  at 313 nm<sup>221</sup> and  $t$  = irradiation time. The moles of conversion of  $[\text{Fe}^{\text{III}}(\text{ox})_3]^{3-}$  to  $[\text{Fe}^{\text{II}}(\text{ox})_3]^{2-}$  can be back-calculated from the formation of  $[\text{Fe}(\text{phen})_3]^{2+}$  as observed at 510 nm. Conversions did not exceed 10%. Using the cross-correlation (Eqn. 2.4), the photoproduct quantum yield for ferrioxalate using the photon flux calculated from azobenzene was  $1.19 \pm 0.06$  and the photoproduct quantum yield for azobenzene using the photon flux calculated from the ferrixolate actinometer was  $0.10 \pm 0.03$ . The literature values for the photoproduct quantum yields of ferrioxalate and azobenzene are 1.24 and 0.14, respectively.<sup>219</sup>

## 2.5 TRANSIENT ABSORPTION SPECTROSCOPY (TRA)

### 2.5.1 Laser Flash Photolysis

All transient spectra and lifetimes were obtained using the LKS80 Applied Photophysics LFP spectrophotometer with a Nd:YAG laser (Quintel Q-smart 450, < 60 mJ per pulse) fitted with 2<sup>nd</sup> and 4<sup>th</sup> harmonic generators with a pulse width of ~5 ns. A second monochromator was installed between the Xe lamp and sample compartment. This was done to prevent undesired photodegradation of the samples by the pulsed Xe lamp. The optimal slit widths for the monochromators were determined experimentally to be 1.0 and 2.5 mm for the primary monochromator and the installed monochromator, respectively (Figure 2.2 and Table 2.2).

Table 2.2. Effect of monochromators' slit widths on probe signal amplitude and scatter from 355 nm excitation of ruthenium trisbipyridine dichloride in aerobic water.

Primary Monochromator Slit Width (mm)	Installed Monochromator Slit Width (mm)	$\Delta A_{370\text{nm}}$ (a.u.)	Scatter (a.u.)
1.0	--	0.080	0.0002
1.0	2.5	0.080	0.0020
1.0	2.0	0.080	0.0040
1.0	2.0	0.086	0.0080
1.5	2.0	0.080	0.0080
1.5	3.0	0.077	0.0040
1.5	3.5	0.077	0.0040
1.0	1.5	0.080	0.0160
1.0	1.0	n/a	n/a

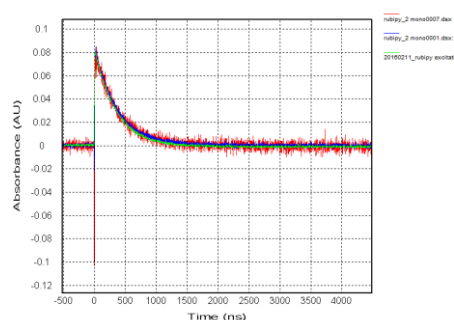


Figure 2.2. Examples of averaged laser excitation of ruthenium trisbipyridine dichloride  $[\text{Ru}(\text{bipy})_3]$  in aqueous solution. The data were collected at 370 nm after photoexcitation at 355 nm. Green trace: 1.0 mm slit width, primary monochromator; secondary monochromator not installed. Blue trace: 1.0 mm slit width after sample, primary monochromator; 2.5 mm slit width, secondary monochromator. Red trace: 1.0 mm slit width after sample; primary monochromator; 1.5 mm slit width, secondary monochromator.

The power of the laser was measured using a pyroelectric joulemeter (Gentec, QE25LP-S-MB-QED) with a Maestro energy monitor. When noted, the power of the laser was decreased by increasing the laser sync delay (LSD). To verify that the ratio of the signal is directly proportional to the laser power, the laser power was varied and the amplitude of the signal monitored. A sample solution of **4** ( $\sim 150 \mu\text{M}$ , 75 mL) was prepared in a mixture of 80:20 v/v  $\text{CD}_3\text{CN}$  and 5.0 mM phosphate buffer, pH 7.0 and stored in the glove box (Figure 2.3 and Table 2.3). The pulse energy (mJ/pulse) correlates linearly with the absorbance change seen at 320 nm. The time constants seen for this process are within experimental error regardless of excitation energy (mJ/pulse).

Table 2.3. Absorbance change seen at 320 nm for the laser flash photolysis of **4** ( $\sim\mu\text{M}$ ) in 80:20 v/v MeCN to 5.0 mM phosphate buffer, pH 7.0 using a Nd:YAG laser fitted with 2<sup>nd</sup> and 4<sup>th</sup> harmonic generators operating at 60 mJ/pulse, 44 mJ/pulse, and 28 mJ/pulse. Three trials at each power are averaged.

Energy (mJ/pulse)	Abs Change (a.u.)	$\tau$ ( $\mu\text{s}$ )
27.5	0.043	$33.6 \pm 2.4$
43.9	0.068	$30.7 \pm 1.7$
60.9	0.090	$33.3 \pm 1.3$

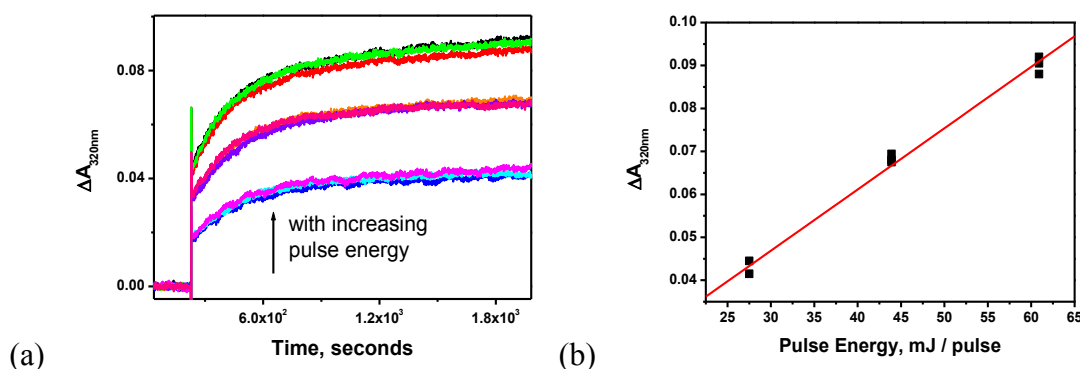


Figure 2.3. (a) Absorbance change seen at 320 nm for the laser flash photolysis of donor **4** ( $150 \mu\text{M}$ ) in 80:20 v/v MeCN to 5.0 mM phosphate buffer, pH 7.0 using a Nd:YAG laser fitted with 2<sup>nd</sup> and 4<sup>th</sup> harmonic generators operating at 60 mJ/pulse, 44 mJ/pulse, and 28 mJ/pulse. (b) Plot of pulse energy (mJ/pulse) to absorbance change seen at 320 nm (0 to 180  $\mu\text{s}$ ) for the laser flash photolysis of **4** ( $\sim\mu\text{M}$ );  $R^2 = 0.99597$ . Linearity indicates that the absorbance changes seen are due to excitation energy and not another process (concentration issues, photobleaching).

Two types of datasets were collected: kinetic data and spectral data. Kinetic data were strictly used for kinetic analysis (see example Figure 2.2). These samples were individually prepared (volume 3.00 mL). Where noted as  $\text{O}_2$ -purged, solvents were purged with  $\text{O}_2$  for 20-30 minutes in a septum-sealed round bottom flask (sample volume:

50 mL). Where noted as anaerobic, solutions were prepared anaerobically in a glove box and transferred to a septum-sealed cuvette. Samples were photolyzed one time per sample (3.00 mL) to ensure the integrity of the data and avoid excitation of photoproducts. The absorbance at the excitation wavelength was between 0.6 and 0.8 a.u. for all samples.

To obtain spectral data, sample solutions were flowed through the sample cuvette to ensure fresh sample solution in the cuvette for all experiments. Sample solutions (~50 mL) were prepared in a round bottom flask (100 mL). The solution was circulated using a peristaltic pump (1.0 mL/min) with stirring using Tygon MH pump tubing (152 mm). The inlet was placed in the bottom corner of the quartz cuvette and the outlet at the top to ensure fresh sample solutions were measured (Figure 2.4). The tubing was double coated with heat shrink to limit the hosing's gas permeability. When noted as anaerobic, the solution reservoir was continuously purged with argon before and during data collection. A control experiment was performed where oxygen-sensitive  $\text{NO}^-$ -Cbl(III) was circulated in the flow set-up for 30 minutes. Upon exposure to oxygen,  $\text{NO}^-$ -Cbl(III) forms  $\text{H}_2\text{OCbl}^+$  (red in color) and  $\text{NO}_2\text{Cbl}$ .<sup>214</sup> There was no observation of the solution's exposure to oxygen (i.e. the solution remained orange). When noted as oxygenated, oxygen was continuously purged through the sample solution reservoir. To ensure the integrity of the data, single shot experiments were recorded both without and with circulation from the peristaltic pump. Spectral kinetic data were collected only when both kinetic traces collected from static and flowed solutions were identical in rate and

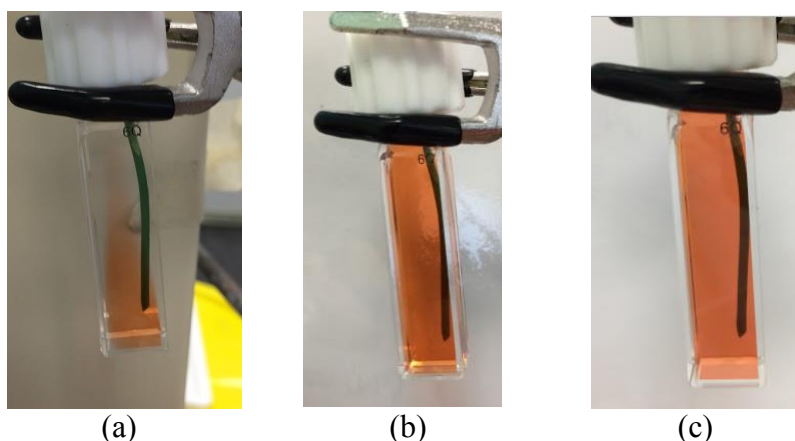


Figure 2.4. Flow set-up of cuvette. (a)  $\text{NO}^-$ -Cbl(III) solution flowed into anaerobic water ( $t = 0$  min); (b) successful transfusion of  $\text{NO}^-$ -Cbl(III) into cuvette ( $t = 1$  min); (c) preservation of oxygen-sensitive  $\text{NO}^-$ -Cbl(III) through continuous circulation into and out of an argon in solution reservoir ( $t = 30$  min).

absorbance change. Solutions were discarded after receiving more than one pulse per mL. Whenever possible,  $^1\text{H}$  NMR or  $^{19}\text{F}$  NMR spectroscopy was used to check that the photodegradation of the reactant was less than 15%.

Transient absorption spectra at select time points were obtained from single kinetic traces at a specific wavelength. Spectral kinetic data were stored as a function of absorbance change versus time for independent wavelengths (Figure 2.5(a)). These data were then exported as an Excel spreadsheet and processed in order to create plots of absorbance changes at select time points as a function of wavelength. This was achieved by first selecting individual time points of interest. Using Excel functions, the absorbance changes as function of wavelength for the time point of interest in addition to two time points on either side (five time points in total) were extracted from the data. The maximum number of points in time was collected for each kinetic trace (2000 absorbance changes over time per wavelength). The average change in absorbance for the extracted time points was calculated. This process was repeated for additional time points (typically 0.5, 1.0, 2.0, 3.0, and 6.0 estimated half-lives of a major process). These data were then replotted as absorbance change as a function of wavelength (e.g. Figure 2.5(b)).

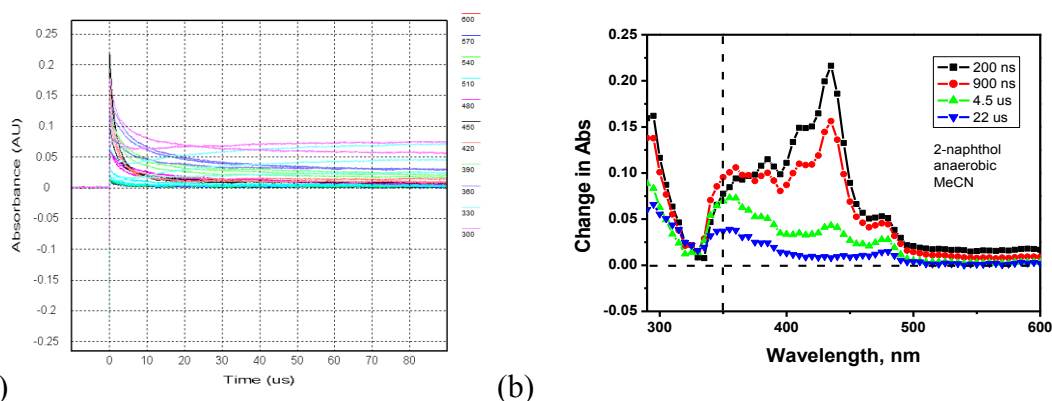


Figure 2.5. (a) Example of unprocessed spectral kinetic data. Laser flash photolysis of 2-naphthol in anaerobic MeCN. (b) Example of processed spectral kinetic data. Laser flash photolysis of 2-naphthol in anaerobic MeCN.

Due to complexity of the datasets, a rigorous analytical method was employed. Initially, the transient absorption spectra were collected. Kinetic data taken at absorption maxima were fitted to a single first-order or multi-exponential rate equations for six-half-lives of the process of interest using Origin (version 6.1). These rate constants were then tabulated. After all processes were identified based on solvent conditions and literature, global analyses of the datasets (Applied Photophysics – Pro-KIV) were completed using

the processes and initial rate constant estimates determined from single wavelength analyses (see Appendix D).

### 2.5.2 Nanosecond Transient Absorption

The ns-TA measurements were performed on a LP920 laser flash spectrometer (Edinburgh Instruments Ltd) located at the University of Hong Kong in the research laboratory of Prof. David Lee Phillips with assistance from his research group. Excitation of fresh samples was achieved using a Q-switched Nd:YAG laser (fourth harmonic line at  $\lambda = 266$  nm). A 450 W ozone-free Xe arc lamp with 10 Hz was used to probe the samples at different time points using a single shot operation versatile sample chamber with an integral controller, high-speed pump and probe port shutters, sample holder, and filter holders. The probe light was processed after being passed through various optimal elements, samples, a monochromator, and fast photomultiplier tube. A continuous spectrum between 280 and 800 nm was recorded simultaneously by an array detector fitted to the spectrograph excited port by a TDS 3012C digital signal analyzer. The sample solutions had an absorbance of  $\sim 0.5$  at 266 nm (1.0 cm cuvette). The sample solutions were flowed using a peristaltic pump at a high flow rate and were either purged continuously with argon or oxygen. Each sample's UV-vis spectrum was recorded before and after data collection. When appropriate, the percent decomposition of the sample was also checked using  $^{19}\text{F}$  NMR spectroscopy to ensure that less than 10% sample decomposed.

### 2.5.3 Femtosecond Transient Absorption

Ultrafast excitation of the samples was achieved using a femtosecond regenerative (1000 Hz) Ti:sapphire laser system (Spectra Physics, Spitfire-Pro) and an automated data acquisition system (Ultrafast systems, Helios model) at the University of Hong Kong in the research laboratory of Prof. David Lee Phillips with assistance from his research group. The amplifier was seeded with 120 fs output from the oscillator (Spectra Physics, Maitai). The third harmonic (267 nm) of the fundamental 800 nm from the regenerative amplifier was used to excite the sample solutions. The probe pulse was generated using  $\sim 5\%$  of the amplified 800 nm output passed through a  $\text{CaF}_2$  crystal to create a white-light continuum (spectral range of 330 to 600 nm). Fiber optics were coupled to a multichannel spectrometer with a CMOS sensor (1.5 nm intrinsic resolution). The probe beam was split so that one beam passed through the sample and another was directed to a reference

spectrometer which monitored fluctuations in the probe beam intensity. The instrument response was 150 fs and the optical delay stage had a maximum temporal delay of 3000 ps. At each temporal delay, spectra were averaged for  $\sim 0.5$  s. The data were stored as three-dimensional wavelength-time-absorbance matrices. Sample solutions (40 mL) were flowed through a 2 mm path length cuvette; the sample solutions had an absorbance of  $\sim 0.5$  at 266 nm in a 2 mm cuvette. Each sample's UV-vis spectrum was recorded before and after data collection. When appropriate, the percent decomposition of the sample was also checked using  $^{19}\text{F}$  NMR spectroscopy to ensure that less than 10% sample decomposed.

# CHAPTER 3: STOICHIOMETRIC HNO RELEASE FROM A PHOTOCAGED (6- HYDROXYNAPHTHALEN-2-YL)METHYL ANALOGUE OF PILOTY'S ACID

---

## 3.1 INTRODUCTION

HNO, a redox cousin of nitric oxide (NO), shows extremely promising pharmacological properties, including treating congestive heart failure.<sup>29,37,222</sup> Furthermore, there is increasing evidence that HNO is an endogenous signaling molecule, reacting in particular with thiol residues and transition metal centers of proteins.<sup>8,35</sup> As HNO rapidly dimerizes in aqueous solution,<sup>1</sup> HNO studies require compounds that release HNO upon demand. The release of HNO from an HNO donor molecule upon photoactivation is very attractive, especially when sub-second *in situ* generation of HNO is required for kinetic studies on the rapid reactions of HNO with biomolecules,<sup>1,25</sup> or *in situ* generation of HNO for biological studies.<sup>96,110,114</sup> Several classes of photoactive HNO donors have been developed.<sup>23,24,72,95,96,109-112,114</sup> To the best of our knowledge, 3-phenyl-5-(2-pyrrolyl)-1,2,4-oxadiazole-4-oxide has the highest selectivity (99%) for the release HNO upon light activation.<sup>112</sup> However, 1,2,4-oxadiazole-4-oxides are reported to release HNO via intermediate species released from the triplet excited states of the parent molecules; hence air-free conditions are required to prevent quenching of the triplet state by oxygen.

Piloty's acid (PhSO<sub>2</sub>NHOH) and related analogues spontaneously decompose cleanly to release HNO and the corresponding sulfinate in alkaline solution. *N*-hydroxysulfonamides (RSO<sub>2</sub>NHOH) have gained significant interest for HNO photorelease *via* photo-uncaging.<sup>23,24,114</sup> A new family of photactivatable HNO donors **1-3** using the (3-hydroxynaphthalen-2-yl)methyl (3,2-HNM) photocage was recently developed (Figure 3.1). The photolabile 3,2-HNM protecting group undergoes rapid photocleavage ( $k_{\text{release}} \approx 10^5 \text{ s}^{-1}$ ).<sup>120</sup> Release of HNO from donors **1-3** was demonstrated using the HNO trap aquacobalamin.<sup>23,24</sup> The HNO photorelease pathway also produced the corresponding sulfinate (RSO<sub>2</sub><sup>-</sup>) and a species that underwent nucleophilic attack from

solvent water to form diol **5** (Scheme 3.1, Pathway 1). However, other photolytic pathways were observed. The alkyl substituent on the leaving group influenced the ability of the HNO donors (**1-3**) to release HNO via concerted C-O and N-S bond cleavage versus elimination of *N*-hydroxysulfonamides ( $\text{RSO}_2\text{NHO}^-$ ; Scheme 3.1, Pathway 2).<sup>23,24</sup> Elimination of *N*-hydroxysulfonamides was not observed for the trifluoromethanesulfonamidoxy leaving group, donor **1**. Additionally, a competitive N-O bond cleavage pathway was observed for all three donors (**1-3**), which generated  $\text{CF}_3\text{SO}_2\text{NH}_2$  and aldehyde **6** (Scheme 3.1; Scheme 3.1, Pathway 3). The selectivity for HNO photorelease was at best 70% HNO (**1**, Figure 3.1).<sup>23,24</sup>

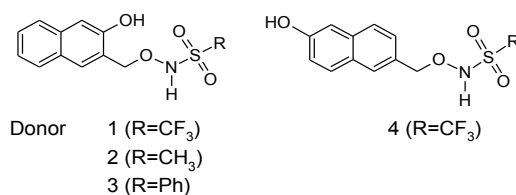
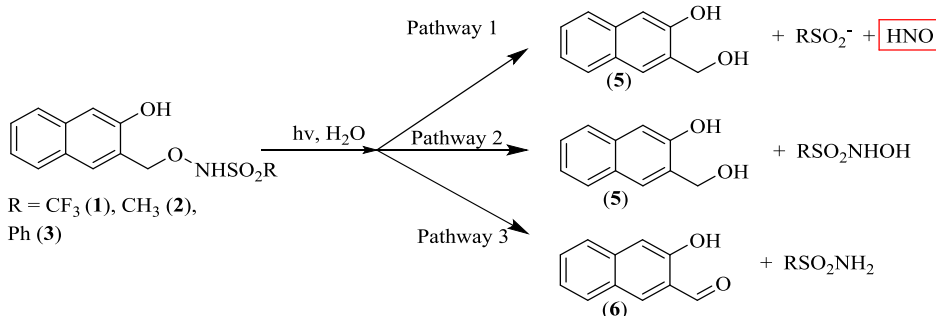


Figure 3.1. Structures of photoactive HNO donors **1-4**.

Scheme 3.1. Photolytic pathways accessible to donor **1-3**.



We hypothesized that the undesired N-O bond cleavage pathway proceeded via an excited state intramolecular proton transfer between the naphtholic OH and the nitrogen atom in the trifluoromethanesulfonamidoxy leaving group.<sup>23</sup> Hence, the research groups of Prof. Paul Sampson and Prof. Alexander Seed at Kent State University in the United States synthesized a structural analogue of donor **1** in which excited state intramolecular proton transfer was unlikely to occur. In this work, the photoproduct characterization of a photocaged trifluoromethanesulfonamidoxy analogue of Piloty's acid bearing a (6-hydroxynaphthalen-2-yl)methyl (6,2-HNM) phototrigger (**4**, Figure 3.1) is described. Evidence will be presented showing that donor **4** stoichiometrically generates HNO upon excitation following heterolytic C-O and N-S bond cleavages. Photolytic titrations of donor **4** as monitored by  $^{19}\text{F}$  NMR and  $^1\text{H}$  NMR spectroscopy will be presented in order to probe whether donor **4** decomposes cleanly upon excitation to generate the chemical

marker for HNO release and a stable aromatic photoproduct (see Chapter 1, Figure 1.2). HNO generation from photolysis of donor **4** will be established indirectly through the use of trapping molecules and through its dimerization product. Importantly, it will be shown that the chemical marker for HNO generation is produced in a 1:1 stoichiometric ratio with HNO following photolysis of donor **4**. This allows for the determination of the photoproduct quantum yields of HNO, which can be calculated using the chemical marker.

### 3.2 THERMAL STABILITY OF DONOR **4**

The thermal stability of photoactive HNO donors is a critical aspect for their effective use.<sup>109</sup> Hence, the thermal stability of donor **4** was investigated. Donor **4** was stable for at least one week in 50:50 MeCN to D<sub>2</sub>O in the presence of ambient light in the lab at room temperature, as observed by <sup>19</sup>F NMR spectroscopy (Figure 3.2).

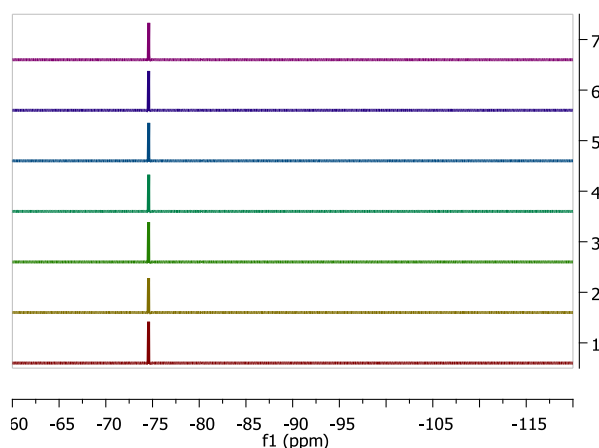


Figure 3.2. <sup>19</sup>F NMR spectra of donor **4** (4.0 mM) in 50:50 v/v MeCN to D<sub>2</sub>O immediately, 24, 48, 72, 96, 120, and 144 hr following sample preparation (Spectrum 1-7, respectively).

### 3.3 THE ACID-BASE CHEMISTRY OF DONOR **4**

Prior to investigating the photodecomposition of donor **4**, it is important to know which form of the molecule is present in solution. Hence, the p*K*<sub>a</sub> value(s) of donor **4** were determined. Initially, <sup>19</sup>F NMR and <sup>1</sup>H NMR spectra were recorded for donor **4** (0.50-1.00 mM) at a series of pH conditions to gain a preliminary understanding of any acidic or basic sites (Figure 3.3 and Figure 3.4). Mixed solvent conditions (80:20 v/v CD<sub>3</sub>CN to buffered aqueous, 0.1 M HCl, or 0.1 M NaOH) were used because the donors are not readily soluble in aqueous solutions. The chemical shifts observed in the <sup>19</sup>F NMR and <sup>1</sup>H NMR spectra indicate that there are two deprotonation sites in donor **4** (Figure 3.3 and

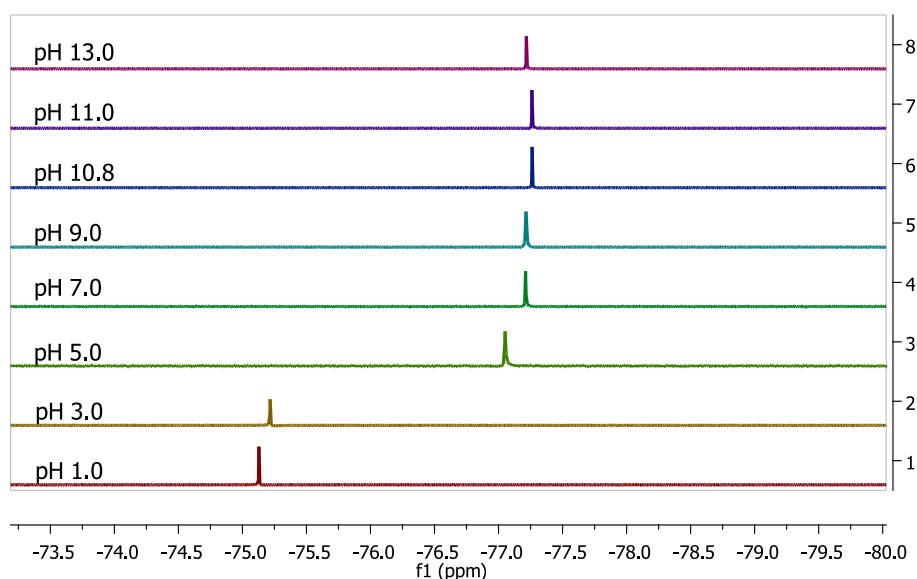


Figure 3.3.  $^{19}\text{F}$  NMR spectra of donor **4** (1.00 mM) in aerobic 20% v/v aqueous MeCN, where the aqueous component is 0.1 M HCl, 0.1 M NaOH, 5.0 mM phosphate buffer (pH 3.0, 7.0), 5.0 mM acetate buffer (pH 5.0), 5.0 mM borate buffer (pH 9.0), or 5.0 mM carbonate buffer (pH 11.0).

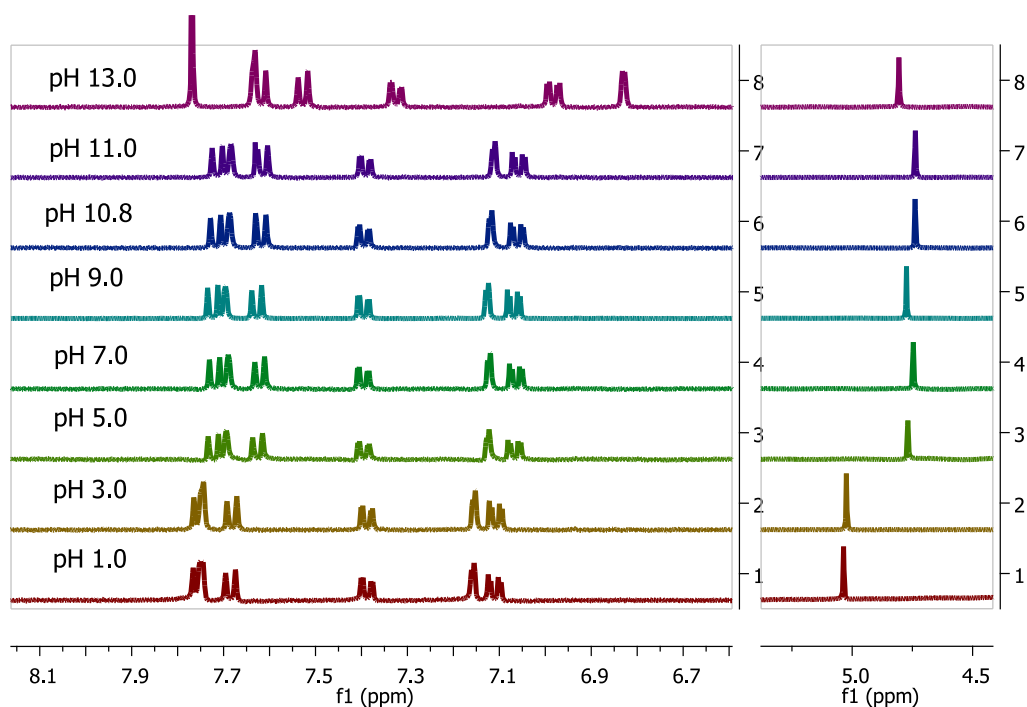


Figure 3.4.  $^1\text{H}$  NMR spectra of donor **4** (1.00 mM) in aerobic 20% v/v aqueous MeCN, where the aqueous component is 0.1 M HCl, 0.1 M NaOH, 5.0 mM phosphate buffer (pH 3.0, 7.0), 5.0 mM acetate buffer (pH 5.0), 5.0 mM borate buffer (pH 9.0), or 5.0 mM carbonate buffer (pH 11.0). Residual chloroform is observed at 7.77 ppm.

Figure 3.4). The  $^1\text{H}$  NMR chemical shifts for the donor **4** were assigned in order to identify the sites of deprotonation (Figure 3.5). As the pH increases from pH 1.0 to pH 5.0, H8 and  $\text{CH}_2$  shift upfield, indicating that the protons experience an increase in

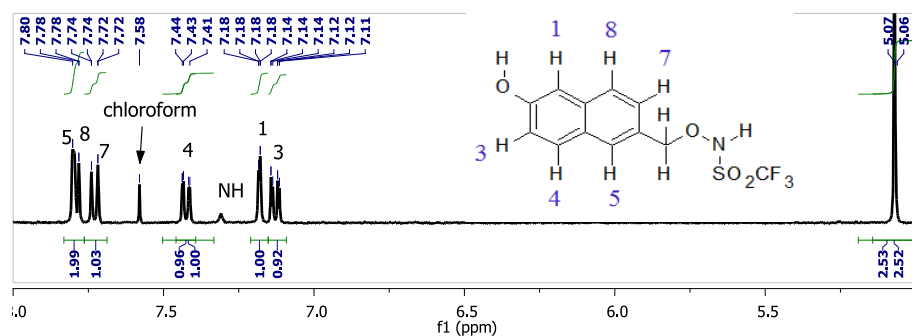
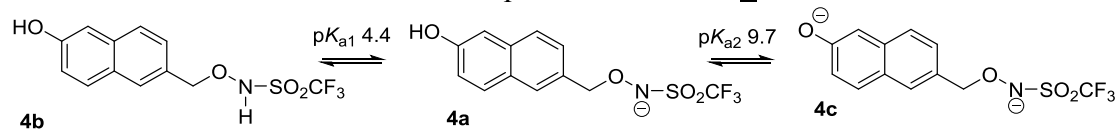


Figure 3.5.  $^1\text{H}$  NMR spectrum of donor **4** in  $\text{CD}_3\text{CN}$ .  $^1\text{H}$  NMR peaks are assigned as depicted in the inset. The peak at  $\delta$  5.07 ppm corresponds to the methylene protons.

electron density (Figure 3.4). In the  $^{19}\text{F}$  NMR spectra, a significant shift of the  $-\text{CF}_3$  is observed as the pH increases from pH 1.0 to pH 5.0 (Figure 3.3). This is consistent with an acidic site on the leaving group. Given that  $\text{p}K_{\text{a}}$  values of 6.33 and 10.8 have been reported for  $\text{CF}_3\text{SO}_2\text{NH}_2$ <sup>223</sup> and  $\text{CH}_3\text{SO}_2\text{NH}_2$ ,<sup>224</sup> respectively, the  $\text{p}K_{\text{a}1}$  was assigned to deprotonation of species **4b** to **4a** (Scheme 3.2). The ability of the sulfonamide NH to deprotonated even in acidic conditions was somewhat unexpected because for the structurally related Piloty's acid ( $\text{Ph-SO}_2\text{NHO}(\text{H})$ ), much less acidic deprotonation has been reported ( $\text{p}K_{\text{a}(\text{OH})} = 9.29$ ).<sup>225</sup> The dissociable proton in Piloty's acid was examined using  $^{15}\text{N}$  NMR spectroscopy by Bonner *et al.*<sup>225</sup> and the pH dependent shift ( $\text{p}K_{\text{a}(\text{OH})} = 9.29$ ) of the  $^{15}\text{N}$  NMR spectra was shown to correlate with OH deprotonation rather than NH deprotonation. Between pH 11.0 and 13.0, the aromatic protons H1, H3, H7, and H8 clearly shift upfield. The  $^{19}\text{F}$  NMR chemical shifts change only slightly in this pH region. This suggests that the second ionization site is far removed from the leaving group. Based on structurally similar molecules, the second site of deprotonation is assigned to the naphtholic O(H).<sup>135</sup> Due to the mixed solvent conditions, aqueous  $\text{p}K_{\text{a}1}$  and  $\text{p}K_{\text{a}2}$  (Scheme 3.2) were not estimated from the NMR data as aqueous acetonitrile is known to increase the  $\text{p}K_{\text{a}}$  values of similarly structured compounds compared to values reported in water (e.g. for 1-naphthol,  $\text{p}K_{\text{a}(\text{OH})} = 9.2$  in  $\text{H}_2\text{O}$  and  $\text{p}K_{\text{a}(\text{OH})} = 11.9$  in 2:1 MeCN to  $\text{H}_2\text{O}$ ).<sup>135</sup>

Scheme 3.2. Ground state ionization equilibria for donor **4**.



UV-vis spectrophotometric titrations were performed in order to establish the equilibrium constants of the two ionization sites. The ground state protonation/deprotonation

equilibria of **4** were investigated by adding aliquots of acid (~1 M HCl; negligible change in total volume of the solution) to aqueous solutions of **4** ( $3.0 \times 10^{-5}$  and  $1.0 \times 10^{-4}$  M, 30 mL; see Figure 3.6(a)). Aqueous solutions of **4** were circulated using a peristaltic pump through a 1 cm path length quartz flow-through cell at 25.0 °C. Spectra were recorded after the pH stabilized in the reservoir flask. The absorbance was plotted as a function of pH and the data fitted using the equation:

$$A_{obs} = \frac{A_i + A_f \times 10^{pH - pK_a}}{1 + 10^{pH - pK_a}} \quad \text{Eqn. 4.1}$$

where  $A_{obs}$  = observed absorbance, and  $A_i$  and  $A_f$  are the absorbance values of **4** and its conjugate acid, respectively. (Note that data were not collected at  $pH < 2.0$ , as **4** was found to be unstable under these conditions, as indicated by an increased absorbance at wavelengths less than 205 nm.) Upon completing the spectrophotometric titration, the solution pH was returned to ~pH 7 to verify that compound **4** had not decomposed during the experiments. The experimentally determined  $pK_{a1}$  value for donor **4** is  $4.4 \pm 0.1$  (see Scheme 3.2).

Aliquots of a base (1.0 M NaOH) were also added to an aqueous solution of donor **4** ( $2.0 \times 10^{-5}$  M, 30 mL; see Figure 3.6(b)). Once again, the total volume change was negligible. The experimentally determined  $pK_{a2}$  value for the OH substituent of **4** was  $pK_{a2} = 9.7 \pm 0.1$  (Scheme 3.2).

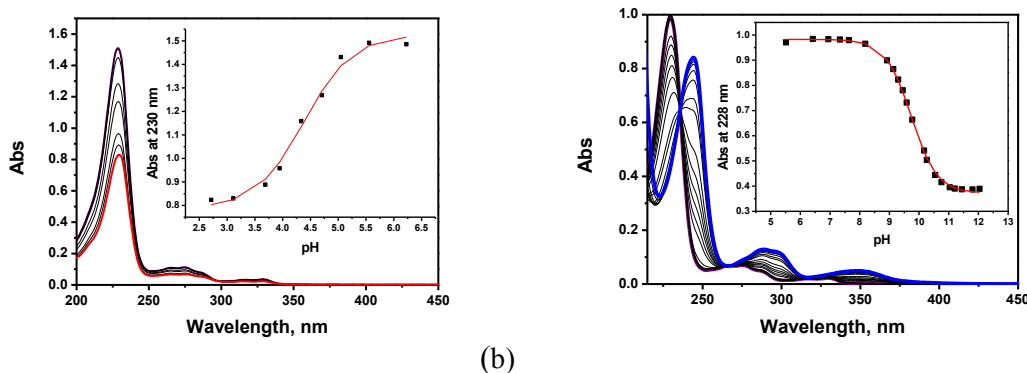


Figure 3.6. (a) UV-Vis spectra of **4** ( $3.0 \times 10^{-5}$  M) as a function of pH (aqueous solution, 25.0 °C). Inset: Absorbance at 230 nm plotted as a function of pH. Data were fitted to equation (4.1), giving  $pK_a = 4.4 \pm 0.1$ . (b) UV-Vis spectra of **4** ( $2.0 \times 10^{-5}$  M) as a function of pH (aqueous solution, 25.0 °C). Inset: Absorbance at 228 nm plotted as a function of pH. Data were fitted to equation (4.1), giving  $pK_a = 9.7 \pm 0.1$ .

3.4 PHOTODECOMPOSITION OF DONOR **4** IN AQUEOUS CONDITIONS3.4.1 Stoichiometric Release of a Chemical Marker  $\text{CF}_3\text{SO}_2^-$  for the Release of HNO following Excitation of **4**

*N*-Hydroxysulfonamides produce HNO in a 1:1 ratio with the corresponding sulfinate.<sup>23,24,70,85,90,101,209,212</sup> Thus, observation of sulfinate  $\text{CF}_3\text{SO}_2^-$  would suggest that selective HNO generation occurred from photolysis of donor **4**. Hence, as an initial study, the steady state photolysis of **4** (0.500 mM) in an anaerobic mixture of 80:20 v/v  $\text{CD}_3\text{CN}$  to 5.0 mM phosphate buffer solution, pH 7.0) was monitored using  $^{19}\text{F}$  NMR spectroscopy (Figure 3.7). This solvent condition was selected due to the poor solubility of **4** in aqueous solutions. Anaerobic conditions were selected to avoid the formation of singlet oxygen from interactions of oxygen with the triplet states of **4** or its photoproducts. The photodecomposition was monitored over time by  $^{19}\text{F}$  NMR spectroscopy, giving an observed rate constant of  $k_{\text{obs}} = 0.29 \pm 0.02 \text{ min}^{-1}$  ( $t_{1/2} = 2.5 \text{ min}$ ). The primary fluorinated photoproduct was  $\text{CF}_3\text{SO}_2^-$  ( $\delta$  -88.7 ppm; 98%), which was identified using authentic

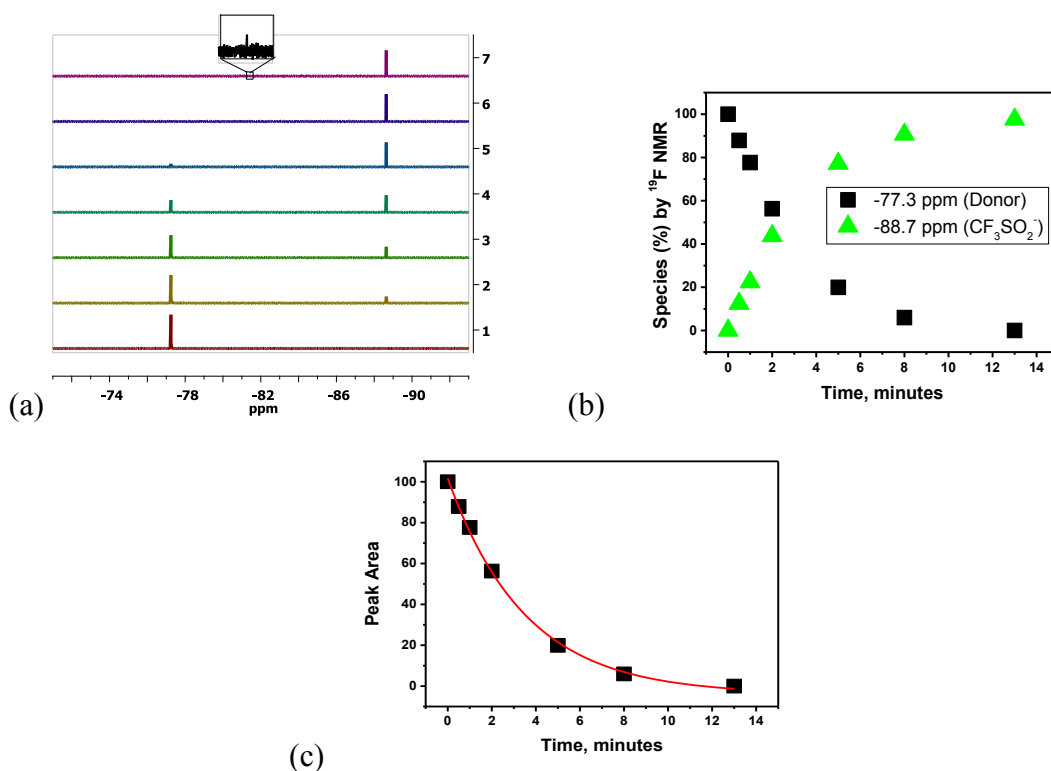


Figure 3.7. (a)  $^{19}\text{F}$  NMR spectra as a function of irradiation time (Rayonet photoreactor, 8 x 350 nm bulbs, 4 W; 0.5, 1, 2, 5, 8, and 13 min;  $\pm 5$  s) for the photodecomposition of HNO donor **4** (0.500 mM) in an anaerobic mixture of 80:20 v/v  $\text{CD}_3\text{CN}$  to 5.0 mM phosphate buffer solution, pH 7.0. (b) Plot of observed species as a function of irradiation time. Final composition:  $\text{CF}_3\text{SO}_2^-$  ( $\delta$  -88.7 ppm; 98%);  $\text{CF}_3\text{SO}_2\text{NH}_2$  ( $\delta$  -81.2 ppm; 2%). (c) Best fit of the peak area of donor **4** ( $-\text{CF}_3$ ) to a first-order rate equation, giving  $k_{\text{obs}} = 0.29 \pm 0.02 \text{ min}^{-1}$ .

samples. No secondary reactions are observed using  $^{19}\text{F}$  NMR spectroscopy. Observation of  $\text{CF}_3\text{SO}_2\text{NH}_2$  (2%;  $\delta$  -81.2 ppm) suggests that O-N bond cleavage can also occur for **4** as a minor pathway. However, observation of  $\text{CF}_3\text{SO}_2^-$  as the primary photoproduct (98%) suggests that stoichiometric HNO photorelease may occur from irradiation of **4**.

### 3.4.2 Influence of the Concentration of **4** on Pathway Selectivity

Photochemical experiments are typically performed with low concentrations of the analyte(s) to avoid intermolecular interactions<sup>226</sup> and inner filter effects.<sup>221</sup> The influence of the reactant concentration on the photoproduct ratio was investigated for donor **4**. A series of sample solutions of **4** (0.100 mM, 1.00 mM, 5.00 mM, and 15.0 mM) in solvent mixtures of 80:20 v/v MeCN to 5.0 mM phosphate buffer (pH 7.0) were analyzed using  $^{19}\text{F}$  NMR spectroscopy following total photolysis (Figure 3.8). Under high concentrations (5.0 and 15.0 mM), an additional species ( $\delta$  -74.95 ppm, ~5%) was formed. Figure 3.9

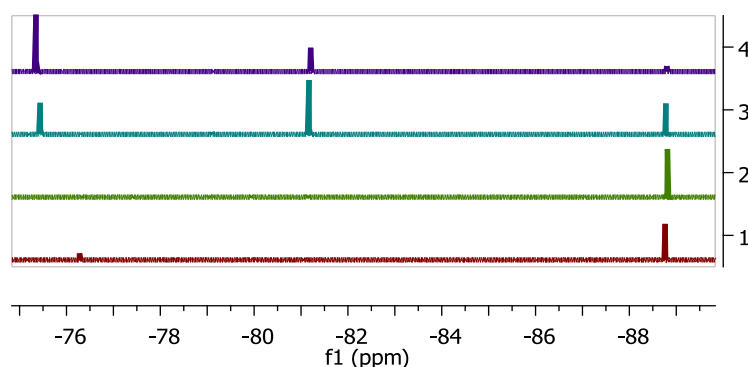


Figure 3.8.  $^{19}\text{F}$  NMR spectra of photolyzed solutions of **4** (Spectrum 1: 0.100 mM, Spectrum 2: 1.00 mM, Spectrum 3: 5.00 mM, and Spectrum 4: 15.0 mM) upon complete decomposition of **4** in 80:20 v/v  $\text{CD}_3\text{CN}$  to 0.1 M phosphate buffer, pH 7.0 using a Rayonet photoreactor, 8 x 350 nm bulbs, 4 W.  $\text{CF}_3\text{SO}_2^-$ :  $\delta$  -88.8 ppm.  $\text{CF}_3\text{SO}_2\text{NH}_2$ :  $\delta$  -81.2 ppm. Unknown an additional species:  $\delta$  -74.45 ppm. **4**:  $\delta$  -76.4 ppm.

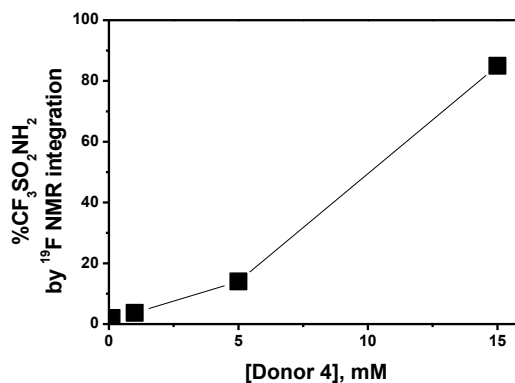


Figure 3.9. N-O bond cleavage pathway selectivity (indicated by % $\text{CF}_3\text{SO}_2\text{NH}_2$ , by total integration) as a function of concentration of **4**. Photolysis performed in solvent mixtures of 80:20 v/v  $\text{CD}_3\text{CN}$  to 5.0 mM phosphate buffer, pH 7.0.

shows that as the concentration of **4** increases, the N-O bond cleavage pathway is increased. This experiment indicates that intermolecular interactions or loss of buffering capacity occur at concentrations  $> 2.5$  mM for **4**. Henceforth, the concentrations of irradiated samples of **4** were kept below 2.5 mM for all subsequent experiments.

### 3.4.3 Stoichiometric HNO Photorelease as Evidenced by Aquacobalamin

#### Trapping Correlated with $\text{CF}_3\text{SO}_2^-$ Formation

Aquacobalamin ( $\text{H}_2\text{OCbl(III)}^+$ ) reacts stoichiometrically (1:1) with HNO donor Angeli's salt to form nitroxylcobalamin,  $\text{NO}^-$ -Cbl(III) (also called nitrosylcobalamin<sup>213</sup>).<sup>78</sup> Importantly,  $\text{H}_2\text{OCbl(III)}^+$  reacts selectively with HNO as opposed to  $\text{NO}$ .<sup>227</sup> Quantification of cobalamins may be achieved through analysis of the aromatic region of the  $^1\text{H}$  NMR spectra of cobalamins.<sup>228</sup>

#### 3.4.3.1 Control Experiments on the Photostability of $\text{HOCbl}$ and $\text{NO}^-$ -Cbl(III)

$\text{H}_2\text{OCbl(III)}^+$  was evaluated as a stoichiometric HNO trap for HNO generated from photolysis of donor **4**. Typically, studies using  $\text{H}_2\text{OCbl(III)}^+$  are performed in entirely aqueous conditions as the aqua ligand is labile.<sup>229</sup> However, donor **4** is not very soluble in water and therefore mixed solvent conditions must be used in photolysis experiments. One concern when using mixed solvent conditions with  $\text{H}_2\text{OCbl(III)}^+$  is that the solvent can substitute the aqua ligand. Therefore, aqueous MeCN was selected for HNO trapping studies using  $\text{H}_2\text{OCbl(III)}^+$ .

The stability of  $\text{H}_2\text{OCbl(III)}^+$  in aqueous MeCN was first investigated. A solution of  $\text{H}_2\text{OCbl(III)}^+$  (0.200 mM) was monitored using UV-vis spectroscopy in an anaerobic mixture of 40:60 v/v MeCN to 5.0 mM phosphate buffer (pH 7.0) after 5, 20, and 50 minutes following sample preparation (Figure 3.10). Small absorbance changes (0.007 a.u.) were observed. The sample was then irradiated for 50 minutes (Xe lamp, monochromator slit width = 5.0 mm, 331 nm) in order to investigate the photostability in this solvent condition. Again, small absorbance changes (0.006 a.u.) were observed. Addition of the HNO donor Angeli's salt (1.2 mol equiv) fully converted  $\text{H}_2\text{OCbl(III)}^+$  to  $\text{NO}^-$ -Cbl(III) as indicated by an isosbestic point at 493 nm. The shift in isosbestic point (498 nm to 493 nm) is attributed to the mixed solvent condition.<sup>24</sup> This experiment indicates that  $\text{H}_2\text{OCbl(III)}^+$  interacts with solvent MeCN. However, the interactions may be limited by preparation of fresh samples.

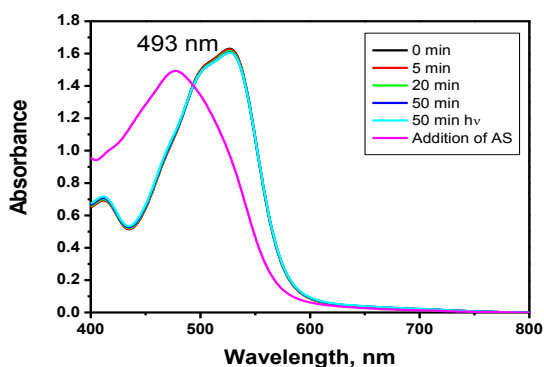


Figure 3.10. UV-vis spectra for  $\text{H}_2\text{OCbl(III)}^+$  (0.200 mM) in an anaerobic mixture of 40:60 v/v MeCN to 5.0 mM phosphate buffer (pH 7.0) after 5, 20, and 50 min sample preparation, following 50 min irradiation (Xe lamp, monochromator slit width = 5.0 mm, 331 nm), and following addition of Angeli's salt (1.2 mol equiv).

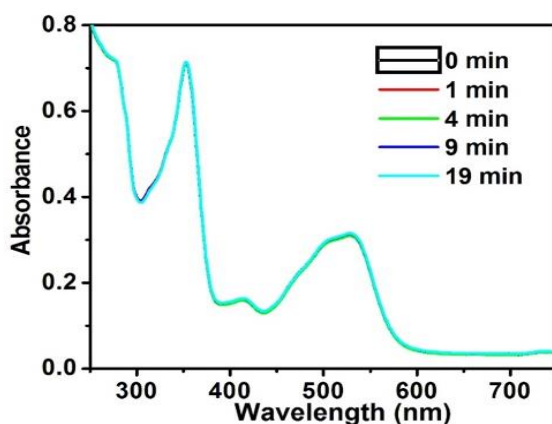


Figure 3.11. UV-vis spectra for  $\text{H}_2\text{OCbl(III)}^+$  (0.300 mM) before and after irradiation from a Xe lamp (150 W, monochromator slit width = 3.0 mm, full spectrum) in a mixture 40:60 v/v MeCN to 5 mM phosphate buffer (pH 7.0) at 25 °C for 1, 4, 9 and 19 min.

If the experiments cannot be performed in a timely manner, another option is to allow  $\text{H}_2\text{OCbl(III)}^+$  to equilibrate with the mixed solvent for a prolonged period of time. An anaerobic  $\text{H}_2\text{OCbl(III)}^+$  (0.300 mM) solution was prepared in a mixture of aqueous phosphate buffer (pH 7.00, 5.0 mM) and  $\text{CH}_3\text{CN}$  (40:60, v/v), and allowed to equilibrate overnight inside the glovebox until no absorbance changes were observed (data not shown). The photostability of  $\text{H}_2\text{OCbl(III)}^+$  was evaluated using a Xe lamp (150 W, monochromator slit width = 3.0 mm). UV-vis spectra of  $\text{H}_2\text{OCbl(III)}^+$  were recorded before and after irradiation by a Xe lamp (150 W, monochromator slit width = 3.0 mm) for 1, 4, 9 and 19 min (Figure 3.11). No observable changes were detected in the UV-vis spectra, indicating that  $\text{H}_2\text{OCbl(III)}^+$  is stable upon irradiation under these conditions.

As a further control, trap  $\text{H}_2\text{OCbl(III)}^+$  was photolyzed in the presence of 2-naphthol, which is structurally similar to the donor **4** but does not contain a leaving group. A sample

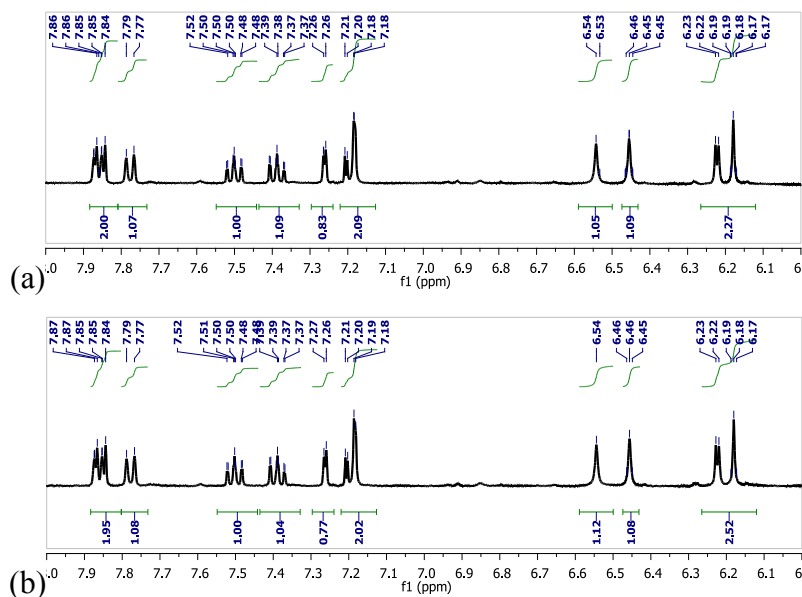


Figure 3.12.  $^1\text{H}$  NMR spectra of 2-naphthol (1.00 mM) and  $\text{H}_2\text{OCbl(III)}^+$  (1.20 mM) in anaerobic 40:60 MeCN to 0.1 M phosphate buffer (pD 7.0) upon sample preparation (a) and after 5 minutes irradiation (b). 2-Naphthol:  $\delta$  7.87, 7.85, 7.79, 7.77, 7.50, 7.37, 7.27, 7.26 ppm.  $\text{H}_2\text{OCbl(III)}^+$ :  $\delta$  7.18, 6.54, 6.46, 6.23, and 6.19 ppm.

of 2-naphthol (1.00 mM) and  $\text{H}_2\text{OCbl(III)}^+$  (1.20 mM) was prepared in an anaerobic mixture of 40:60 v/v MeCN to 0.1 M phosphate buffer (pD 7.0). Photolysis of the sample for 5 minutes in the photoreactor produced no novel species (Figure 3.12). Therefore, the trap  $\text{H}_2\text{OCbl(III)}^+$  is photostable under these experimental conditions and does not readily interact with hydroxyarenes.

Next, the photostability of the product of the reaction between  $\text{H}_2\text{OCbl(III)}^+$  and HNO, namely nitroxylcobalamin ( $\text{NO}^-$ -Cbl(III)), was investigated. A solution of  $\text{NO}^-$ -Cbl(III) in aqueous MeCN (60:40 v/v  $\text{CD}_3\text{CN}$  to 5.0 mM phosphate buffer (pH 7.0)) was irradiated using a photoreactor and examined by  $^{31}\text{P}$  NMR spectroscopy. The  $^{31}\text{P}$  NMR showed no decomposition (Figure 3.13). This indicates that  $\text{NO}^-$ -Cbl(III) is stable under these experimental conditions.

The effect of the intensity of the light source was next investigated by varying the irradiation light source. An anaerobic solution of  $\text{NO}^-$ -Cbl(III) ( $\sim 25 \mu\text{M}$ ) was prepared in a mixture of aqueous phosphate buffer (pH 7.00, 5.0 mM) and  $\text{CH}_3\text{CN}$  (40:60, v/v) inside the glovebox. UV-vis spectra for the solution were recorded before and after irradiation by a Xe lamp (150 W, monochromator slit width = 3.0 mm) for 0, 5, and 10 min (Figure 3.14). Small absorbance changes were observed. The sample was then photolyzed further using a Q-smart 450 pulsed Nd:YAG laser fitted with 2<sup>nd</sup> and 4<sup>th</sup> harmonic generators ( $\sim 5$

ns pulse width,  $\sim 60$  mJ/pulse). Photolysis of  $\text{NO}^-$ -Cbl(III) using the high energy light showed absorbance changes indicative of reduction of  $\text{NO}^-$ -Cbl(III) to a cobalt(II) species ( $\lambda_{\text{max}} = 480$  nm, shoulder 545 nm, 504 nm isosbestic point). Similar spectral changes occurred in aqueous solutions.<sup>230</sup> This suggests that the product  $\text{NO}^-$ -Cbl(III) is not photostable upon prolonged photolysis. A common approach in photochemical studies to limit any subsequent photochemistry of the initial photoproducts is to partially photolyze the reactant solution ( $\sim 10\%$  conversion).<sup>219</sup>

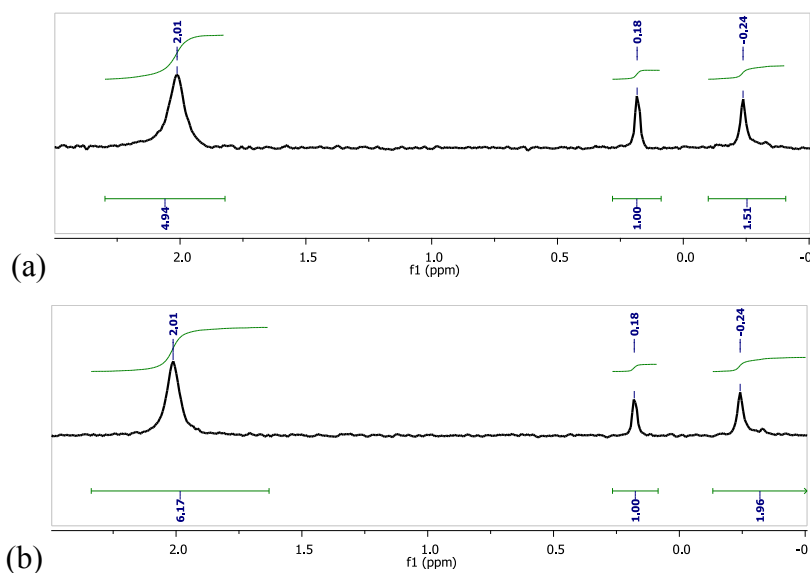


Figure 3.13. (a)  $^{31}\text{P}$  NMR spectra of  $\text{NO}^-$ -Cbl(III) (mM) in 60:40 v/v MeCN to 5.0 mM phosphate buffer (pH 7.0); (b) following irradiation for 20 min (Rayonet photoreactor, 8 x 350 nm bulbs, 4 W).  $\text{H}_3\text{PO}_4$  external standard in capillary insert:  $\delta$  -0.24 ppm. Phosphate buffer:  $\delta$  2.01 ppm.  $\text{NO}^-$ -Cbl(III):  $\delta$  0.18 ppm.

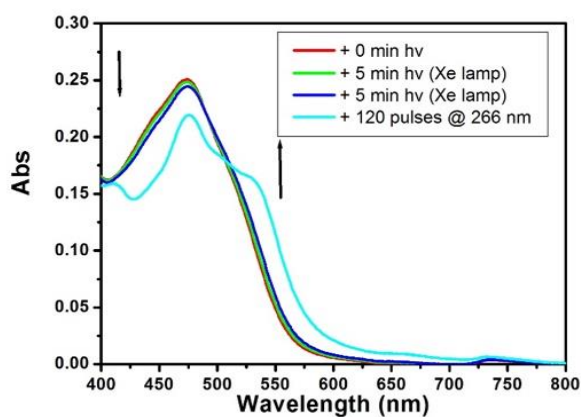


Figure 3.14. UV-vis spectra for  $\text{NO}^-$ -Cbl(III) ( $\sim 25$   $\mu\text{M}$ ) before and after irradiation using a Xe lamp (150 W, monochromator slit width = 3.0 mm, full spectrum) in a mixture of phosphate buffer (pH 7.0, 5.0 mM) and MeCN (40:60, v/v) at 25  $^\circ\text{C}$  for 0, 5, and 10 min. The sample was then irradiated using a Nd:YAG laser fitted with 2<sup>nd</sup> and 4<sup>th</sup> harmonic generators (1 Hz, 120 pulses,  $\sim 60$  mJ/pulse,  $\sim 5$  ns pulse width).

### 3.4.3.2 Partial Photolysis of Donor **4** in the Presence of the HNO Trap $H_2OCbl(III)^+$

It is well established that *N*-hydroxysulfonamides produce HNO in a 1:1 ratio with the corresponding sulfinate.<sup>23,24,70,85,90,101,209,212</sup> Hence, observation of  $CF_3SO_2^-$  likely indicates HNO release is occurring from photolysis of donor **4**. To confirm this, donor **4** was photolyzed in the presence of the HNO trap,  $H_2OCbl(III)^+$ , which reacts stoichiometrically with HNO to form  $NO^-Cbl(III)$ .<sup>24</sup> A partial conversion experiment was carried out to limit reactions of  $H_2OCbl(III)^+$  with possible secondary photoproducts and preserve the product species  $NO^-Cbl(III)$ . Irradiated samples of donor **4** (1.00 mM) and  $H_2OCbl(III)^+$  (Sample A: 1.20 mM, Samples B and C: 0.900 mM) were prepared in an anaerobic mixture of 40:60 v/v MeCN : 0.10 M deuterated phosphate buffer (pD 7.0). Samples A, B, and C were irradiated for 5 minutes using the photoreactor;  $^{19}F$  and  $^1H$  NMR spectra were subsequently recorded (Figure 3.15 and Figure 3.16). Photolysis of donor **4** in the presence of  $H_2OCbl(III)^+$  resulted in new  $^1H$  NMR peaks at  $\delta$  8.31, 7.94, 7.75, 7.11, 6.51, and 6.21 ppm (Figure 3.16). The presence of  $NO^-Cbl(III)$  in the product mixture was demonstrated by the observation of peaks at  $\delta$  6.21 ppm and 7.11 ppm (confirmed by recording the  $^1H$  NMR spectrum of an authentic sample of  $NO^-Cbl(III)$  in the same solvent mixture). The remaining aromatic peaks from  $NO^-Cbl(III)$  at  $\delta$  7.83, 7.29, and 6.48 ppm overlap with other species. The integrations of the peaks at  $\delta$  7.11 and 6.27 ppm for  $NO^-Cbl(III)$  versus the peak areas of  $H_2OCbl(III)^+$  ( $\delta$  6.44) were used to calculate the concentration of  $NO^-Cbl(III)$  generated from each sample at each time point (Table 3.1). Thus, as observed for the photolysis of the structural analogue donor **4**,

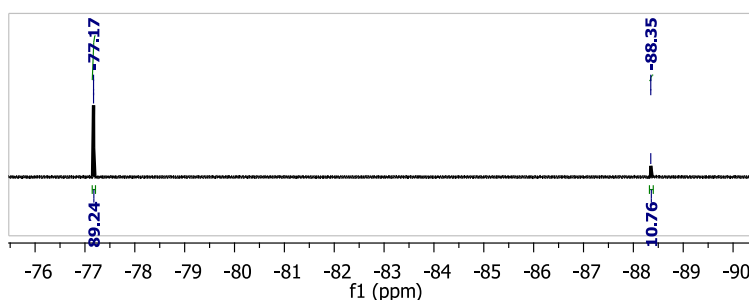


Figure 3.15.  $^{19}F$  NMR spectra of donor **4** (1.00 mM) and  $H_2OCbl(III)^+$  (0.900 mM) in an anaerobic mixture of 40:60 v/v MeCN to 0.1 M phosphate buffer (pD 7.0) upon after 5 min irradiation (Rayonet photoreactor, 8 x 350 nm bulbs, 4 W). Donor **4**:  $\delta$  -77.17 ppm.  $CF_3SO_2^-$ :  $\delta$  -88.35 ppm.

namely donor **1**,<sup>23,24</sup>  $\text{CF}_3\text{SO}_2^-$  formation serves as a chemical marker for HNO formation from photolysis of donor **4**.

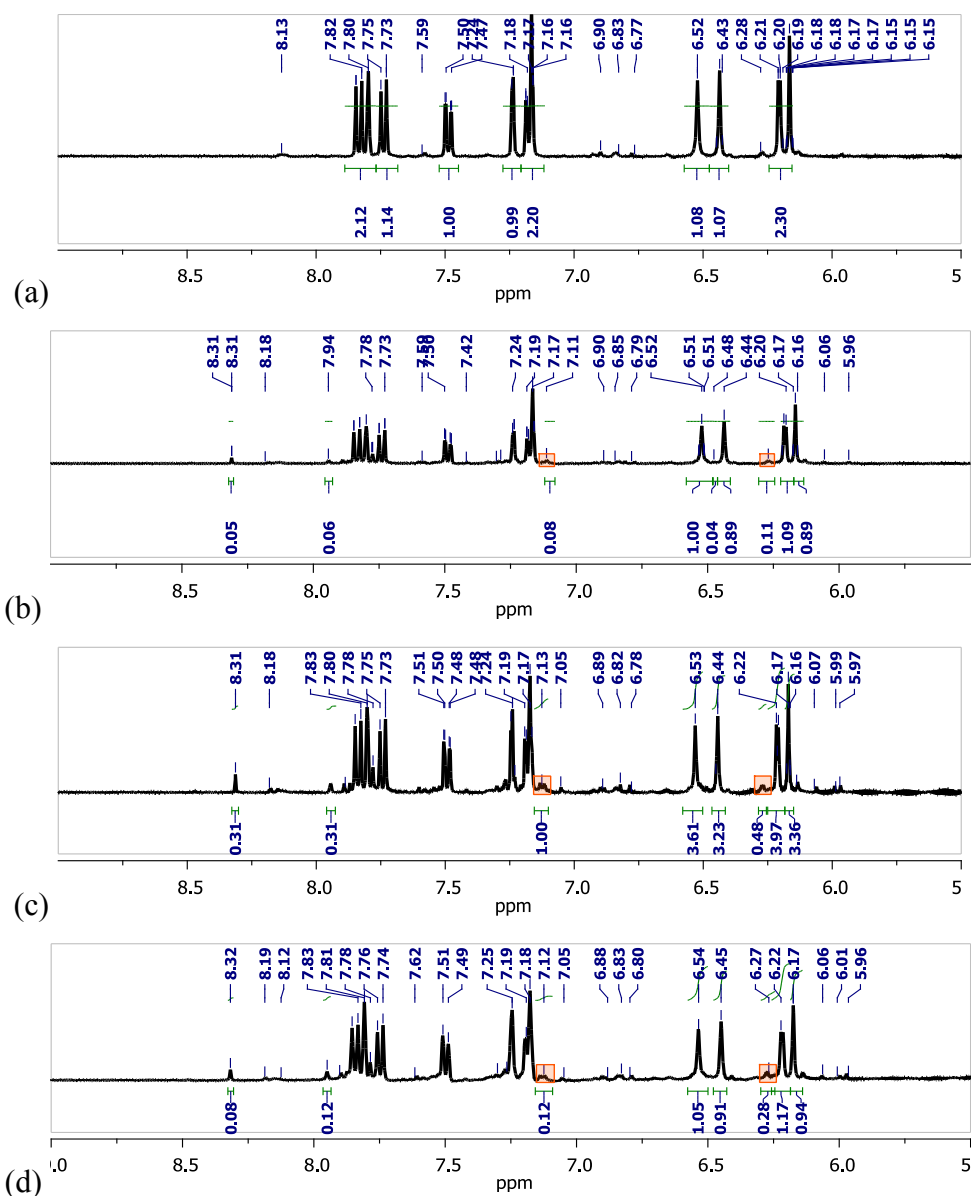


Figure 3.16.  $^1\text{H}$  NMR spectra of donor **4** (1.00 mM) and  $\text{H}_2\text{OCbl(III)}^+$  (0.900-1.00 mM) in an anaerobic mixture of 40:60 v/v MeCN : 0.10 M deuterated phosphate buffer (pD 7.0) immediately after sample preparation (A) and after 5 min irradiation (B, C, D; Rayonet photoreactor, 8 x 350 nm bulbs, 4 W). Donor **4**: 7.85, 7.82, 7.80, 7.75, 7.73, 7.50, 7.48, 7.24, 7.19 ppm.  $\text{H}_2\text{OCbl(III)}^+$ :  $\delta$  7.16, 6.52, 6.43, 6.21, and 6.17 ppm.  $\text{NO}^-$ -Cbl(III): 7.83 (overlapping), 7.29 (overlapping), 7.11, 6.48 (overlapping), 6.27 ppm; confirmed by recording authentic  $\text{NO}^-$ -Cbl(III) in the same solvent system. The peak positions vary by up to 0.02 ppm (within experimental error).

Table 3.1. Comparison of the concentrations of  $\text{CF}_3\text{SO}_2^-$  ( $\mu\text{M}$ ) and  $\text{NO}^-$ -Cbl(III) ( $\mu\text{M}$ ) in the product solution upon partial irradiation of donor **4** in an anaerobic mixture of 40:60 v/v MeCN to 0.1 M phosphate buffer (pD 7.0).

Trial	Irradiation time (min)	$[\text{CF}_3\text{SO}_2^-]$ ( $\mu\text{M}$ )	$[\text{NO}^-$ -Cbl(III)] ( $\mu\text{M}$ )
A	5	$111 \pm 3$	$103 \pm 10$
B	5	$146 \pm 4$	$153 \pm 15$
	8	$204 \pm 6$	$175 \pm 16$
C	5	$132 \pm 4$	$124 \pm 12$
	8	$197 \pm 6$	$161 \pm 13$

Samples B and C were irradiated for an additional three minutes so that 20% of donor **4** was decomposed. Using the methods described previously, the concentrations of  $\text{CF}_3\text{SO}_2^-$  and  $\text{NO}^-$ -Cbl(III) were again compared (Figure 3.17). The concentrations were no longer the same within experimental error (Figure 3.18). These findings suggest that secondary reactions occur upon continued photolysis of the reaction mixture.

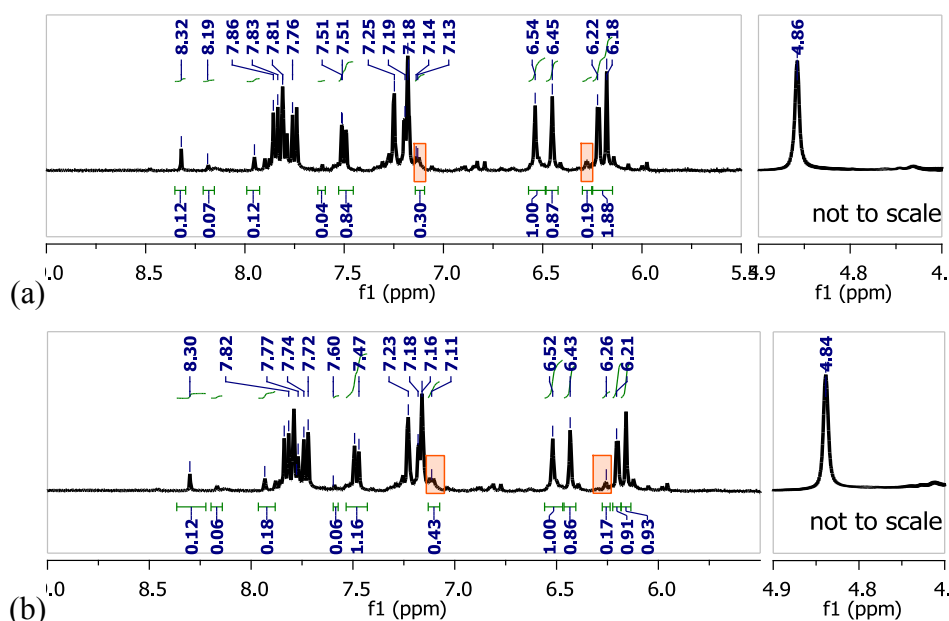


Figure 3.17.  $^1\text{H}$  NMR spectra of donor **4** (1.00 mM) and  $\text{H}_2\text{OCbl(III)}^+$  (1.00 mM) in an anaerobic mixture of 40:60 MeCN to 0.1 M phosphate buffer (pD 7.0) after 8 min irradiation (Rayonet photoreactor, 8 x 350 nm bulbs, 4 W); Spectrum (a): Sample B and spectrum (b): Sample C). Donor **4**:  $\delta$  7.85, 7.82, 7.80, 7.75, 7.73, 7.50, 7.48, 7.24, 7.19 ppm.  $\text{H}_2\text{OCbl(III)}^+$ :  $\delta$  7.16, 6.52, 6.43, 6.21, and 6.17 ppm.  $\text{NO}^-$ -Cbl(III): 7.83 (overlapping), 7.29 (overlapping), 7.11, 6.48 (overlapping), 6.27 ppm.

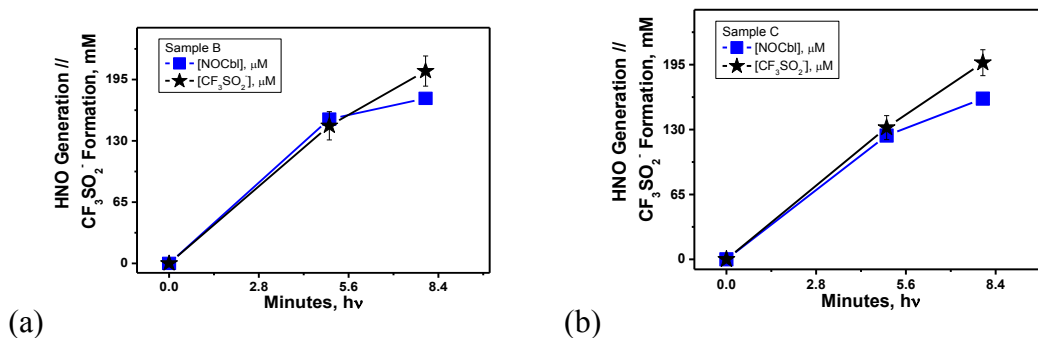


Figure 3.18. Concentration of NO<sup>-</sup>-Cbl(III) and CF<sub>3</sub>SO<sub>2</sub><sup>-</sup> as a function of irradiation time from a reaction mixture of donor **4** (1.00 mM) and H<sub>2</sub>OCbl(III)<sup>+</sup> (1.00 mM) in an anaerobic mixture of 40:60 MeCN to 0.1 M phosphate buffer (pD 7.0). Plot (a) shows the analysis of Sample B and plot (b) shows the analysis of Sample C.

### 3.4.4 Further Evidence of HNO Generation from Photolysis of Donor **4**

#### 3.4.4.1 Thiol Trapping of HNO

To gain further evidence of HNO generation, another trapping study was performed using the efficient HNO trap *L*-glutathione (GSH). HNO is very reactive with thiols, with at least two possible outcomes depending on the reaction conditions.<sup>231</sup> Nucleophilic thiol attacks the electrophilic nitrogen in HNO, forming a corresponding N-hydroxysulfenamide.<sup>231</sup> Excess thiol generates the corresponding disulfide and hydroxylamine. In the absence of excess thiols, rearrangement occurs of the N-hydroxysulfenamide to form a sulfinamide.<sup>231</sup> Thus, formation of a sulfinamide or disulfide serves as additional supporting evidence to indicate HNO generation from the decomposition of a donor.

A solution of donor **4** (1.00 mM) and GSH (1.50 mM) was prepared in an anaerobic mixture of 60:40 v/v MeCN to 5.0 mM phosphate buffer (pH 7.0) in a NMR tube fitted with a J-Young cap. Following photolysis of **4**, an aliquot was withdrawn, diluted in deuterated solvent, and the <sup>19</sup>F NMR spectrum recorded. Complete photolysis of donor **4** generated a 1:1 mixture of CF<sub>3</sub>SO<sub>2</sub>NH<sub>2</sub> and CF<sub>3</sub>SO<sub>2</sub><sup>-</sup>. GSH is therefore in excess compared with the released HNO from photolysis of donor **4** (~3:1). Analysis of the sample using LC-HRMS showed that unreacted GSH (*m/z* 306.0763) and the expected product glutathione disulfide (GSSG; *m/z* 611.1435) were present in the photolysis solution. LC-HRMS analyses were carried out at the University of Auckland with assistance from Prof. M. Cather Simpson's research group. While thiols are not a

selective trap for HNO,<sup>231</sup> this experiment provides further support that donor **4** releases HNO upon photolysis.

#### 3.4.4.2 GC-MS Headspace Analysis of HNO's Dimerization Product N<sub>2</sub>O

HNO can be indirectly detected through its dimerization product, N<sub>2</sub>O.<sup>55,93,114,232-235</sup> Gas chromatography-mass spectrometry (GC-MS) headspace analysis of N<sub>2</sub>O is the most commonly used method of HNO detection.<sup>236,237</sup>

The headspace of an irradiated sample of **4** was analyzed using GC-MS to detect the N<sub>2</sub>O ion count. To quantify the amount of N<sub>2</sub>O generated, a calibration curve of the N<sub>2</sub>O count as a function of Angeli's salt concentration (0-0.500 mM) was prepared (Figure 3.19 and Table 3.2). The decomposition of Angeli's salt is first-order, is pH-independent ( $4 < \text{pH} < 8$ ;  $6.8 \times 10^{-4} \text{ s}^{-1}$ ),<sup>74</sup> and yields HNO and one equivalent of NO<sub>2</sub><sup>-</sup>.<sup>39</sup> Two samples of donor **4** (0.500 mM) were prepared in an anaerobic mixture of 5:95 v/v MeCN to 0.1 M phosphate buffer, pH 7.0. The samples were then sealed and irradiated for ~1 hr using the photoreactor. Using calibration curves prepared on the same day, the concentration of

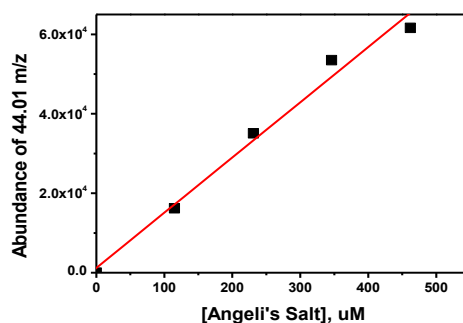


Figure 3.19. Calibration curve of Angeli's salt ( $\mu\text{M}$ ) versus abundance of N<sub>2</sub>O ( $44.01 \text{ m/z}$ , retention time 1.7 min).

Table 3.2. Abundance of N<sub>2</sub>O generated by Angeli's salt (AS) and from partial photolysis of **4** (0.500 mM) in an anaerobic mixture of 5:95 v/v MeCN to 0.1 M phosphate buffer, pH 7.0.

Donor <b>4</b> ( $\mu\text{M}$ )	AS ( $\mu\text{M}$ )	Abundance (Counts)	Corrected (Counts)
0	0	4204	0
0	0	4083	0
0	115	20,352	16,208
0	231	39,215	35,072
0	346	57,646	53,503
0	462	65,777	61,633
500	0	7116	2972
500	0	6699	2555

N<sub>2</sub>O generated from the complete photolysis of **4** (0.500 mM) in 5:95 v/v MeCN to 0.1 M phosphate buffer (pH 7.0) was 13 μM for Sample A and 10 μM for Sample B.

Following GC-MS analysis, the samples were taken down to dryness on a rotary evaporator and dissolved in CD<sub>3</sub>CN. Photoproducts were analyzed by <sup>19</sup>F NMR spectroscopy. The <sup>19</sup>F NMR spectra (CF<sub>3</sub>SO<sub>2</sub><sup>-</sup>) indicated that 28% and 23% of samples A and B underwent C-O bond cleavage to release HNO. Hence, the expected concentration of HNO generated from Sample A and B are 140 μM and 115 μM, respectively. The GC-MS headspace analysis of N<sub>2</sub>O indicated that only 13 μM (Sample A) and ~10 μM (Sample B) had been converted to HNO. This further confirms that HNO is generated from the photolysis of **4**. However, the amount of N<sub>2</sub>O generated from **4** was ~10% of the expected concentration based on CF<sub>3</sub>SO<sub>2</sub><sup>-</sup> observation.

Similarly structured hydroxyarenes photoeject electrons upon excitation.<sup>194-199</sup> Furthermore, N<sub>2</sub>O is known to react readily with solvated electrons.<sup>238</sup> Whether or not the solvated electrons ejected from the hydroxyarene are responsible for the reduction in the amount of the observed N<sub>2</sub>O was studied. In this study, 2-naphthol was used as a model compound in order to generate solvated electrons. Angeli's salt (Na<sub>2</sub>N<sub>2</sub>O<sub>3</sub>; pK<sub>a1</sub>(H<sub>2</sub>N<sub>2</sub>O<sub>3</sub>) = 2.39, pK<sub>a2</sub> 9.35) was used to generate N<sub>2</sub>O for this study.<sup>73</sup> In order to quantify the amount of N<sub>2</sub>O generated, a calibration curve of the N<sub>2</sub>O counts as a function of Angeli's salt concentration (0-1.04mM) was prepared in 5.0 mM phosphate buffer (pH 7.0) solutions (total volume of 5.000 mL) with 5% by vol. of MeCN. Two samples of 2-

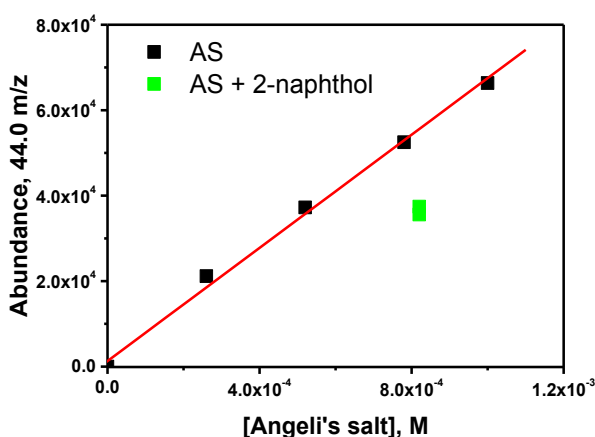


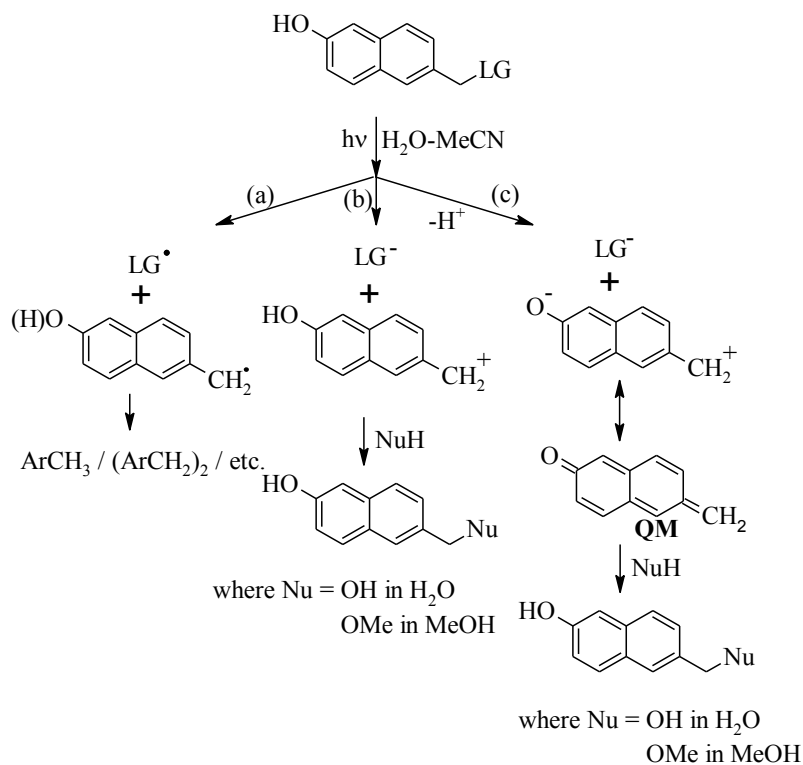
Figure 3.20. Concentration of Angeli's salt in 5.0 mM phosphate buffer (pH 7.0) solutions (total volume of 5.000 mL) with 5% by vol. of MeCN plotted against GC-MS headspace analysis of N<sub>2</sub>O (*m/z* 44.0). Photolysis of 2-naphthol (1.04 mM) and Angeli's salt (0.820 mM; Rayonet photoreactor, 8 x 350 nm bulbs, 4 W) decreased N<sub>2</sub>O counts by ~35% (green).

naphthol (1.04 mM) and Angeli's salt (0.820 mM) were also prepared in 5.0 mM phosphate buffer, pH 7.0 solutions (total volume of 5.000 mL) with 5% by vol. of MeCN. All samples were left to react overnight ensuring that the Angeli's salt fully decomposed. Next, the samples containing 2-naphthol were irradiated for 1 hr. Figure 3.20 gives a plot of the abundance of  $N_2O$  (44.0  $m/z$ ) versus the initial concentration of  $N_2O$ . Photolysis of 2-naphthol reduced the concentration of  $N_2O$  by ~35%. Therefore, this method of HNO detection is not quantitative for photoactive HNO donors that incorporate naphtholic photocages. However, the amount of  $N_2O$  generated from **4** was ~10% of the expected concentration based on  $CF_3SO_2^-$  observation. This suggests that an additional process is decreasing the amount of  $N_2O$  generated from photolysis of **4**.

### 3.4.5 Characterization of Aromatic Photoproducts

Initial insights into the mechanism of HNO generation from photolysis of **4** can be drawn from the characterization of the aromatic photoproducts. HNM-protected molecules can undergo bond homolysis or heterolysis of the  $ArCH_2-X$  bond (Scheme 3.3, Pathway (a))

Scheme 3.3. Possible photodecomposition mechanisms leading to the release of leaving group (LG) from photolysis of a 6,2-HNM photocaged molecule. Bond homolysis is shown in pathway (a), heterolytic cleavage in pathway (b), and heterolytic cleavage resulting in QM formation in pathway (c).



and Pathway (b), respectively).<sup>206-208</sup> Bond homolysis yields products of radical-radical reactions such as a methylated species ( $\text{ArCH}_3$ ), dimers, or  $\text{ArCH}_2\text{CH}_2\text{OH}$  in methanol.<sup>206-208</sup> Bond heterolysis yields a cation/anion pair ( $\text{ArCH}_2^+/\text{X}^-$ ), where the cation typically reacts further with  $\text{NuH}$ .<sup>206-208</sup> For donor **4**, this cation would be the (6-hydroxynaphthalen-2-yl)methyl cation **9**. Similarly structured hydroxyarene photocages undergo phototautomerization and heterolytic bond cleavage to form a quinone methide (QM) and release leaving group ( $\text{LG}^-$ ; Scheme 3.3, Pathway (c)); QMs readily react with nucleophiles (such as water or methanol) to form a stable hydrated or methylated photoproducts.<sup>121-123,156-170</sup>

Based on the observed aromatic photoproducts of donor **1** (Scheme 3.1, Pathway 1),<sup>24,209</sup> the expected aromatic photoproduct from photolysis of donor **4** is 6-(hydroxymethyl)naphthalen-2-ol (diol **7**). However, the GC-MS headspace analysis of  $\text{N}_2\text{O}$  generated by photolysis of donor **4** suggested that HNO may react with a primary photoproduct, transient species, or an intermediate species. Hence, careful characterization of the aromatic photoproduct **4** was carried out using  $^1\text{H}$  NMR spectroscopy to provide insights into both the mechanism of photodecomposition and possible reactions involving HNO in the photolytic solution.

$^1\text{H}$  NMR spectroscopy is a convenient method to characterize aromatic photoproducts. A solution of donor **4** (1.00 mM) in aerobic 80:20 v/v  $d_6$ -DMSO to 5.0 mM phosphate buffer solution (pH 7.0) was photolyzed as a function of time. An external standard (TSP) was included in the sample as a reference for integration purposes. The photolysis was monitored using  $^{19}\text{F}$  NMR spectroscopy (Figure 3.21) and  $^1\text{H}$  NMR spectroscopy (Figure 3.22). Donor **4** decomposed yielding  $\text{CF}_3\text{SO}_2^-$  (95% selectivity) and a mixture of aromatic photoproducts (Figure 3.22). Diol **7** can be characterized through its methylene protons ( $\delta$  4.62 ppm; Figure 3.23). The  $^1\text{H}$  NMR peaks of diol **7** and donor **4** significantly overlap (Figure 3.23). To further confirm diol **7**'s formation upon photolysis of donor **4**, the integration of the donor **4** ( $^{19}\text{F}$  NMR integration (by total integration)) was correlated with an overlapping peak between diol **7** and donor **4** in their  $^1\text{H}$  NMR spectra ( $\delta$  7.35 ppm) as a function of time (Figure 3.24). For longer photolysis times ( $t > 4$  min), the  $^1\text{H}$  NMR spectra indicate an increase in peak intensity at  $\delta$  7.35 ppm. This is assigned to growth of diol **7** ( $\delta$  7.35 ppm and  $\delta$  4.67 ppm; Figure 3.24). Additional photoproducts to diol **7** were identified through comparison to authentic samples (Figure 3.23), including 6-hydroxynaphthalene-2-carbaldehyde (aldehyde **8**) and 6-[(E)-

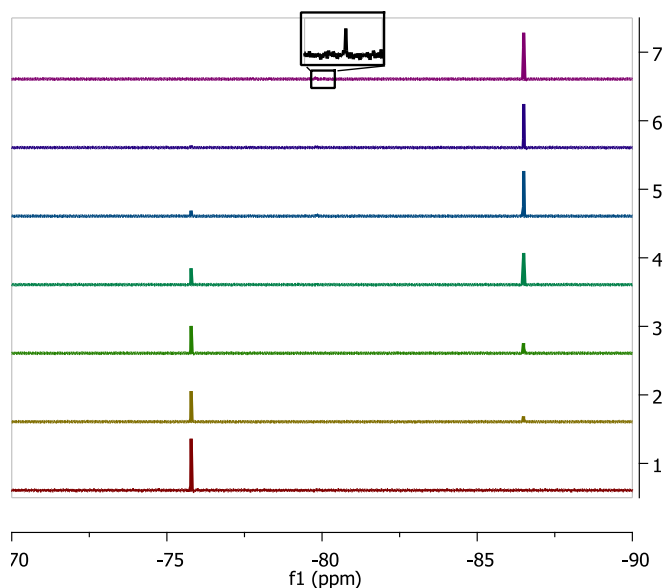


Figure 3.21.  $^{19}\text{F}$  NMR spectra for the photodecomposition of **4** (0.500 mM) in an aerobic mixture of 80:20 v/v  $\text{d}_6$ -DMSO to 5.0 mM phosphate buffer solution, pH 7.0, as a function of the total irradiation time (Rayonet photoreactor, 8 x 350 nm bulbs, 4 W; 0.50, 1.0, 1.5, 2.0, 4.0, 6.0, and 10.0 min). Complete decomposition of **4** produced a mixture of  $\text{CF}_3\text{SO}_2^-$  ( $\delta$  -86.55 ppm: 94%) and  $\text{CF}_3\text{SO}_2\text{NH}_2$  ( $\delta$  -79.82 ppm: 5%).

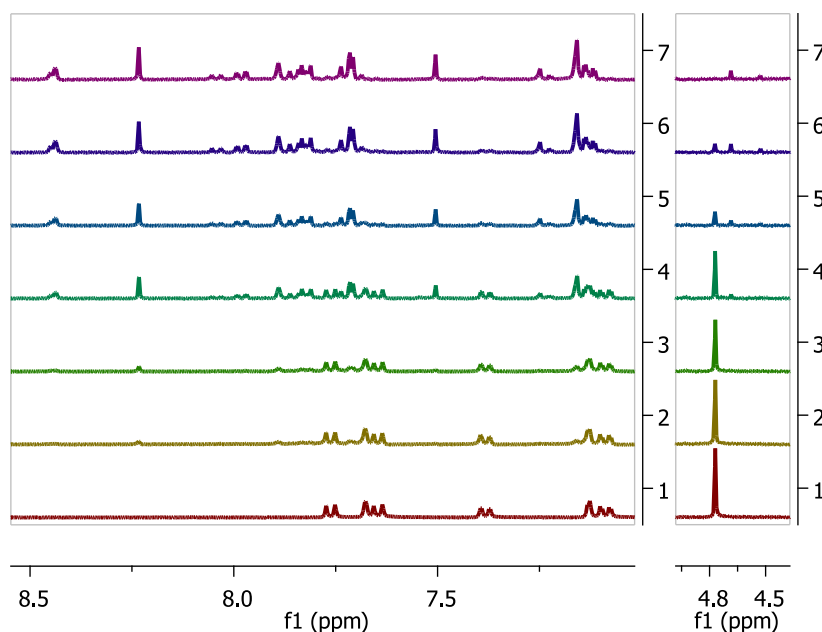


Figure 3.22.  $^1\text{H}$  NMR spectra for the photodecomposition of **4** (0.500 mM) in an aerobic 80:20 v/v  $\text{d}_6$ -DMSO to 5.0 mM phosphate buffer solution, pH 7.0, as a function of the total irradiation time (Rayonet photoreactor, 8 x 350 nm bulbs, 4 W; 0.50, 1.0, 1.5, 2.0, 4.0, 6.0, and 10.0 min).

(hydroxyimino)methyl]naphthalen-2-ol (oxime **10**). Another species was also observed (6-hydroxynaphthalene-2-carboxamide, amide **11**; discussed in following section). Clearly, photolysis of **4** does not cleanly generate one stable, primary photoproduct. The

two nitrogen-containing species, oxime **10** and amide **11**, provide evidence that HNO reacts with primary photoproducts, transient species, or intermediates.

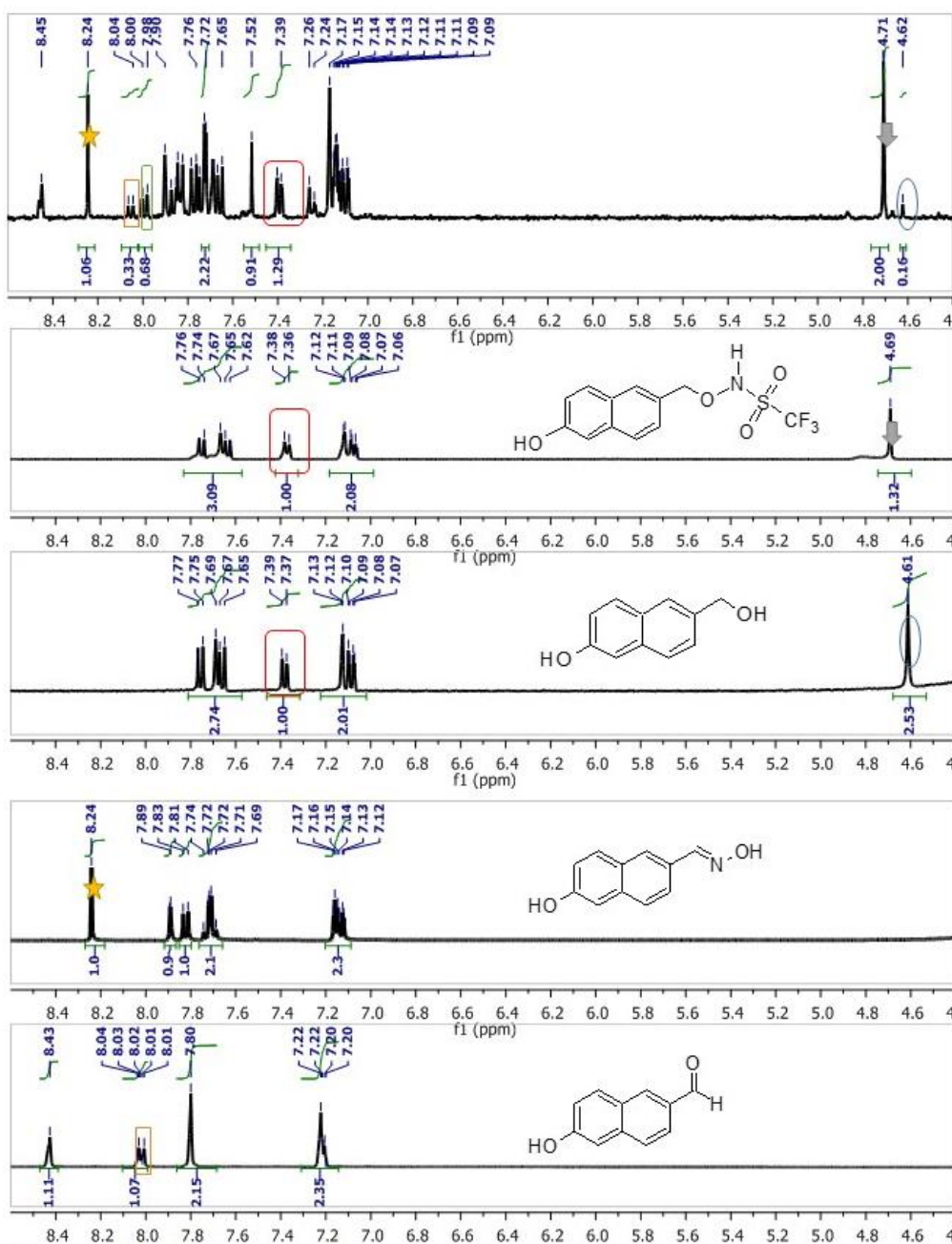


Figure 3.23. Comparison of the  $^1\text{H}$  NMR spectrum of the photolytic products derived from HNO donor **4** (0.500 mM) following 50% photodecomposition (95%  $\text{CF}_3\text{SO}_2^-$  in product mixture) with authentic samples of **4**, diol **7**, oxime **10**, and aldehyde **8** (in aerobic 80:20 v/v  $\text{d}_6$ -DMSO to 5.0 mM phosphate buffer solution, pH 7.0).

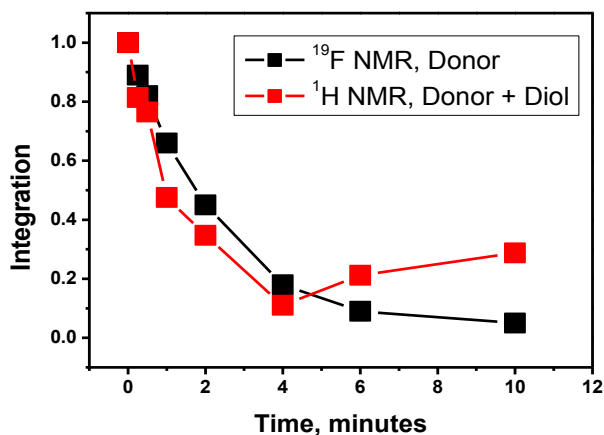


Figure 3.24. The photodecomposition of **4** (1.00 mM) in aerobic 80:20 v/v  $d_6$ -DMSO to 5.0 mM phosphate buffer solution, pH 7.0, as a function of the total irradiation time (Rayonet photoreactor, 8 x 350 nm bulbs, 4 W;  $\pm$  5 s) by  $^1\text{H}$  NMR ( $\delta$  7.35 ppm; overlapping with diol **7**) and  $^{19}\text{F}$  NMR ( $\delta$  -77.25 ppm) spectroscopy. Photolysis was 94% selective for the desired pathway.

Figure 3.25 shows the integrations of the observed aromatic compounds ( $\delta$  8.24 ppm, oxime **10**; 8.06 ppm, aldehyde **8**; 7.98 ppm, amide **11**; and 7.35 ppm, the overlapping peaks of donor **4** and diol **7**) plotted as a function of time. The summed integrations of the individually observed aromatic compounds were also plotted as a function of time. A loss in total integration is typically indicative of homolytic bond cleavage which can

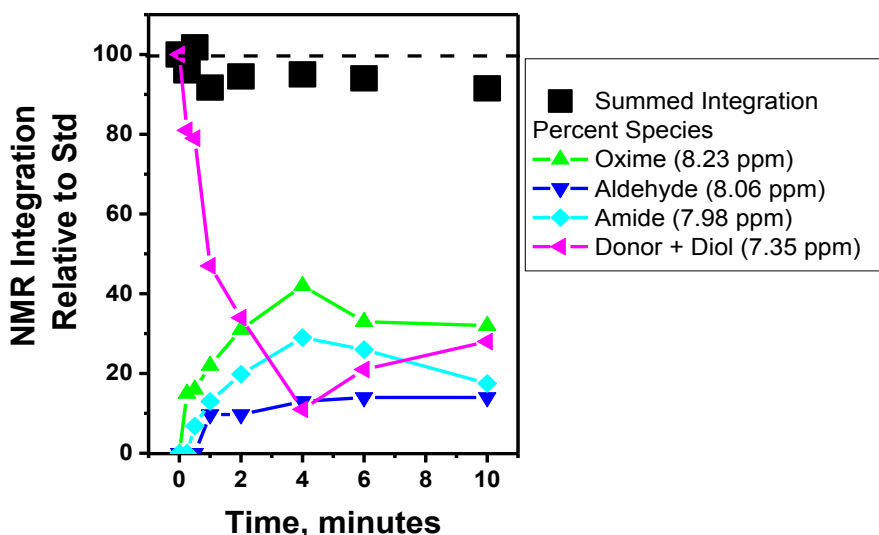


Figure 3.25. Total integration and observed photoproducts as a function of time (Rayonet photoreactor, 8 x 350 nm bulbs, 4 W) from the photodecomposition of **4** (1.00 mM) in aerobic 80:20 v/v  $d_6$ -DMSO to 5.0 mM phosphate buffer solution, pH 7.0. The integrations of the listed peaks were calculated relative to an external standard.

produce a plethora of dimers formed from radical couplings. Importantly, the total integration did not vary beyond  $\pm 10\%$ . Hence, the primary photoproducts were successfully characterized by  $^1\text{H}$  NMR spectroscopy. Furthermore, it is unlikely that HNO photorelease from **4** proceeds via homolytic bond cleavage because radical couplings (e.g. a multitude of dimers or a methylated species) were not observed.

### 3.5 ORIGIN OF 6-[(*E*)-(HYDROXYIMINO)METHYL]NAPHTHALEN-2-OL

Stoichiometric formation of HNO (as observed from  $\text{H}_2\text{OCbl(III)}^+$  trapping) was observed upon photolysis of **4** in aqueous MeCN in a partial photolysis experiment (Section 3.4.3). However, two nitrogen containing species (oxime **10** and amide **11**) were observed by  $^1\text{H}$  NMR spectroscopy in the photoproduct mixture in the absence of an HNO trap (Section 3.4.5). This suggests that HNO can react with **4**'s photoproducts, transient species, or intermediate species.

#### 3.5.1 Reactivity of HNO with Diol **7**

The photoproduct characterization suggested that the anticipated primary photoproduct diol **7** may react with HNO. To investigate this, a solution of diol **7** (5.0 mM) and Angeli's salt (1.5 eq.) was prepared in an anaerobic mixture of 5:95 v/v MeCN to 0.1 M phosphate buffer, pH 7.0. Angeli's salt decomposes in neutral pH conditions to form one equivalent of HNO and of  $\text{NO}_2^-$  ( $t_{1/2} \sim 17$  min).<sup>39</sup> The reaction was left to proceed for three hours. The product mixture was taken down to dryness and dissolved in  $\text{CD}_3\text{CN}$ . Figure 3.26 shows that no additional species were observed, indicating that HNO does not react with diol **7**.

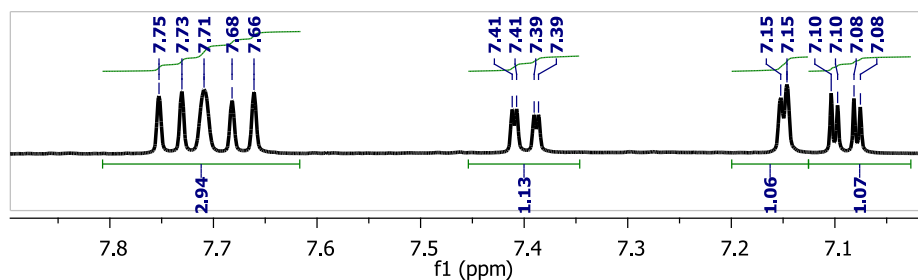


Figure 3.26.  $^1\text{H}$  NMR spectrum from the reaction of diol **7** (5.00 mM) and Angeli's salt (1.5 equiv) in an anaerobic mixture of 5:95 v/v MeCN to 0.1 M phosphate buffer, pH 7.0. Reaction was left to proceed for three hr, taken down to dryness, and dissolved in  $\text{CD}_3\text{CN}$ .  $^1\text{H}$  NMR shifts of diol **7** are observed at  $\delta = 7.75, 7.73, 7.71, 7.68, 7.66, 7.41, 7.39, 7.15, 7.10, 7.08, 5.45$  ppm (compared with authentic sample).

The reactivity of HNO with diol **7** was investigated while the sample was continuously irradiated. N-Hydroxytrifluoromethanesulfonamide ( $\text{CF}_3\text{SO}_2\text{NHOH}$ ) was selected as the HNO donor because it cleanly generates 1 mol. equiv. of HNO in neutral pH conditions ( $t_{1/2} \sim 13$  min)<sup>90</sup> and absorbs weakly at the excitation wavelengths ( $\sim 350$  nm; Figure 3.27). A solution of the diol **7** (0.500 mM) was prepared in an anaerobic mixture of 5:95 v/v MeCN to 0.1 M phosphate buffer, pH 7.0 (total volume of 1.420 mL) in NMR tubes with a J-Young fitting. An aliquot of a stock solution of HNO donor  $\text{CF}_3\text{SO}_2\text{NHOH}$  (580  $\mu\text{L}$  of  $\sim 3$  mM, 90% purity, in MeOH) was added directly to the reactant solution (final concentration of  $\sim 750$   $\mu\text{M}$ , total volume 2.000 mL).  $\text{CF}_3\text{SO}_2\text{NHOH}$  was synthesized by collaborators at Kent State University, USA, and had partially decomposed upon transport to form  $\text{CF}_3\text{SO}_2^-$  and HNO. The NMR tube was immediately taken out of the glove box and irradiated in the photoreactor (350 nm bulbs) for 1 hr. The product solution was then taken down to dryness on a rotary evaporator and dissolved in  $\text{CD}_3\text{CN}$ .  $^{19}\text{F}$  NMR and  $^1\text{H}$  NMR spectra were recorded.  $\text{CF}_3\text{SO}_2\text{NHOH}$  cleanly generated HNO, as indicated by  $\text{CF}_3\text{SO}_2^-$  in the  $^{19}\text{F}$  NMR spectrum.<sup>90</sup> The  $^1\text{H}$  NMR spectrum of the product mixture shows that only intact diol **7** was observed, implying that the excited state(s) and transient specie(s) of diol **7** do not react with HNO (Figure 3.28).

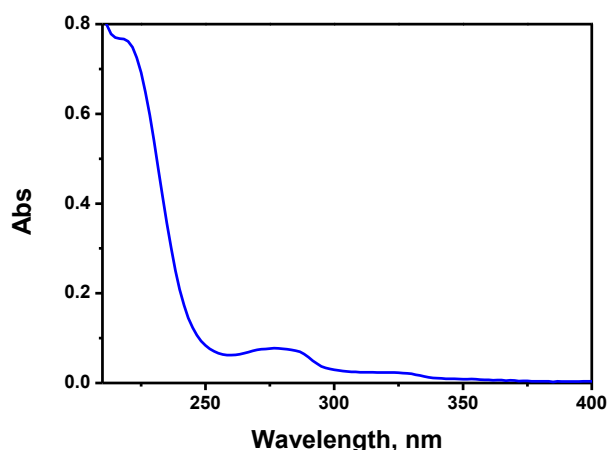


Figure 3.27. UV/Vis spectrum of  $\text{CF}_3\text{SO}_2\text{NHOH}$  (0.02 M) in anhydrous methanol.

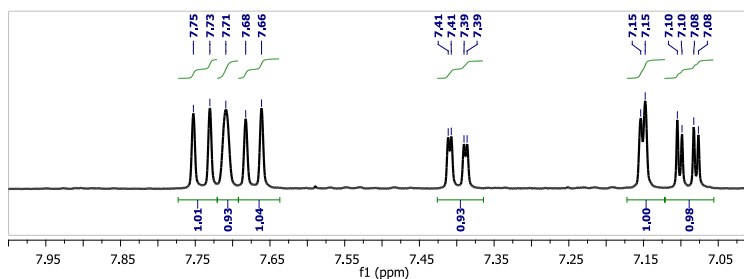


Figure 3.28.  $^1\text{H}$  NMR spectrum of the steady state photolysis product mixture from diol **7** and  $\text{CF}_3\text{SO}_2\text{NHOH}$  (1.5 equiv.) in an anaerobic mixture of 5:95 v/v MeCN to 0.1 M phosphate buffer, pH 7.0 (Rayonet photoreactor, 8 x 350 nm bulbs, 4 W). Product was taken to dryness and dissolved in  $\text{CD}_3\text{CN}$ .  $^1\text{H}$  NMR shifts of diol **7** were assigned to  $\delta$  7.75, 7.73, 7.71, 7.68, 7.66, 7.41, 7.39, 7.15, 7.10, 7.08, 5.45 ppm from comparison to authentic sample.

The stability of diol **7** in methanol was also investigated. Importantly, if heterolytic bond cleavage occurs to release the leaving group (OH), either a cation **9** or a QM intermediate species is formed (Scheme 3.3); both of these species are reactive with solvent MeOH. Photolysis of diol **7** in 1:1 MeOH to 5 mM deuterated phosphate buffer (pD 7.0) did not produce any additional peaks as observed in the  $^1\text{H}$  NMR spectrum (Figure 3.29). This implies that  $-\text{OH}$  acts as a very poor leaving group from the 6,2-HNM-photocage and that diol **7** is photostable under these experimental conditions.<sup>124</sup>

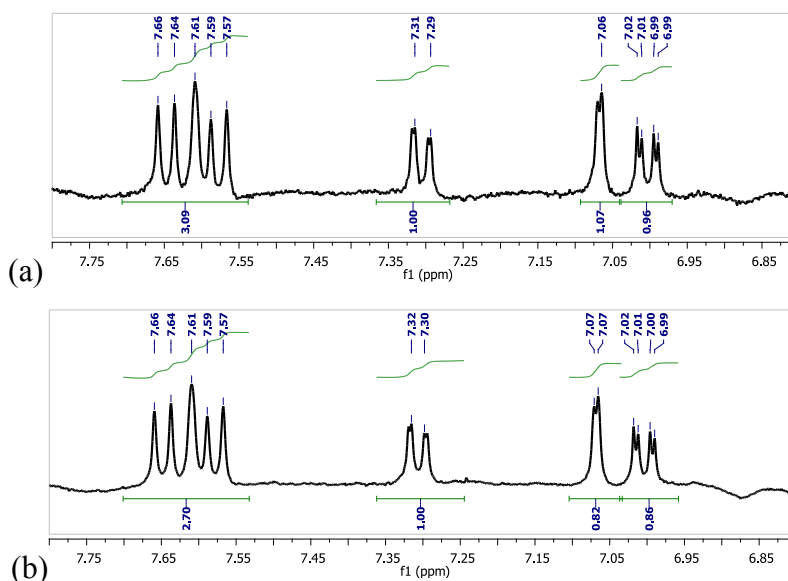


Figure 3.29.  $^1\text{H}$  NMR spectra of an authentic sample of diol **7** in 1:1 MeOH to 5.0 mM phosphate buffer (pD 7.0) (a) before and (b) after irradiation (35 minutes irradiation, Rayonet photoreactor, 8 x 350 nm bulbs, 4 W); referenced to solvent residual peak.

These experiments indicate that diol **7** and HNO do not readily react, nor do the excited states of diol **7** react with HNO. Furthermore, diol **7** does not appear to undergo heterolytic bond cleavage as no methylated species were formed upon photolysis of diol

7 in methanol (Scheme 3.3). Therefore, the nitrogen-containing products observed from photolysis of 4 (oxime 10 and amide 11) do not originate from any chemistry or photochemistry associated with diol 7.

### 3.5.2 Reactivity of HNO with Transient or Intermediate Species Generated by Photolysis of 4

From Scheme 3.3, it can be seen that the expected transient or intermediate species of heterolytic cleavage is a carbocation or a QM. Both of these species are reactive with nucleophiles. HNO is known to act as a nucleophile.<sup>231</sup> Hence, the possibility that HNO reacts with a transient or intermediate species formed from photolysis of 4 was investigated. Photolyses of 4 were performed in the presence and absence of the HNO trap  $\text{H}_2\text{OCbl(III)}^+$ . The experiments were performed in methanol to determine if methylated species would be formed from nucleophilic attack of solvent MeOH on the transient species generated by photolysis of 4 (Scheme 3.3).

Methanolysis of donor 4 (1.00 mM) was carried out in 60:40 v/v MeOH to 5.0 mM phosphate buffer solution, pH 7.0, and the product mixture analyzed using  $^{19}\text{F}$  NMR spectroscopy and LC-HRMS. LC-HRMS was selected as opposed to  $^1\text{H}$  NMR spectroscopy because an authentic sample of 6-(methoxymethyl)naphthalen-2-ol 13 was not available. An additional sample was prepared under the same conditions with HNO trap  $\text{H}_2\text{OCbl(III)}^+$  added to the solution (3 mol. equiv.). The samples were partially irradiated so that 25-33% of 4 decomposed (90% to 100% release of  $\text{CF}_3\text{SO}_2^-$  by  $^{19}\text{F}$  NMR spectroscopy). Following this, the two photolytic samples were diluted in MeCN to ~33-100  $\mu\text{M}$  of the initial concentration of the donor 4. Authentic samples of donor 4 (10  $\mu\text{M}$ ), diol 7 (10  $\mu\text{M}$ ), and  $\text{H}_2\text{OCbl(III)}^+$  (10  $\mu\text{M}$ ) were prepared in MeCN. Table 3.3 shows the LC-HRMS characterization of the photolytic product solutions. As previously observed from the photolysis of donor 4, diol 7, oxime 10, and aldehyde 8 were detected by HRMS in the photolytic mixture. Additional species were observed in the HRMS analysis, including 6-methylnaphthalen-2-ol (12) and species that are dimers based on their high molecular weights. These species likely result from homolytic bond cleavage(s)<sup>207</sup> of the donor 4 and/or its photoproducts; however, as they are not clearly observed in the  $^1\text{H}$  NMR spectra, they are minor products (< 10% of the photoproducts). Inclusion of the efficient HNO trap  $\text{H}_2\text{OCbl(III)}^+$  dramatically changed the species observed from photolysis of donor 4. The product of methanolysis, 6-(methoxymethyl)naphthalen-2-ol (13), was detected and oxime 10 was less abundant (Table 3.3). Hence, oxime 10

originates from the reaction of HNO with transient or intermediate species. Two important conclusions can be made from these results: (1) the aromatic transient species formed from photolysis of **4** is reactive with nucleophiles and (2) HNO can act as a nucleophile in the absence of an HNO trap.

Table 3.3. Mass assignments for the ion signals ( $m/z$ ) obtained from (A) a product mixture resulting from partial photolysis of donor **4** (1.00 mM; 25% conversion to  $\text{CF}_3\text{SO}_2^-$ ) and (B) a product mixture (100  $\mu\text{M}$  maximum concentration) resulting from partial photolysis of donor **4** (1.00 mM; 33% conversion to 9:1  $\text{CF}_3\text{SO}_2^-:\text{CF}_3\text{SO}_2\text{NH}_2$ ) and  $\text{H}_2\text{OCbl}^+$  (3 mol. equiv.) in an anaerobic mixture of 60:40 v/v MeOH to 5.0 mM phosphate buffer (pH 7.0).

Retention Time (min)	Molecular Formula / Assignment	Calculated [M-H] <sup>-</sup> ( $m/z$ )	Observed [M-H] <sup>-</sup> ( $m/z$ )	A Donor, 25% decomposition	B Donor, 33% decomposition, with $\text{H}_2\text{OCbl}^+$
7.7-7.8	$\text{C}_{11}\text{H}_9\text{NO}_2$ Amide <b>11</b> Oxime <b>10</b>	186.05605	186.0569	1200	200
8.7-8.9	$\text{C}_{11}\text{H}_8\text{O}_2$ Aldehyde <b>8</b> *	171.04515	171.0447	1000	400
9.1-9.2	Dimer A	Unknown	342.1117	50	-
9.5-9.6	$\text{C}_{11}\text{H}_{10}\text{O}$ Compound <b>12</b>	157.06589	157.0656	150	-
9.5-9.6	$\text{C}_{11}\text{H}_{10}\text{O}_2$ Diol <b>7</b>	173.06080	173.0607	300	-
9.9-10.0	Dimer B	Unknown	401.3002	30	50
10.0-10.1	$\text{C}_{11}\text{H}_7\text{NO}$ Naphthostyryl	168.04494	168.0454	2000	-
10.5-10.7	$\text{C}_{12}\text{H}_{12}\text{O}_2$ Compound <b>13</b>	187.076453	187.0736	-	50
11.3-11.4	Dimer C	Unknown	304.0271	200	1000
15.8-15.9	$\text{C}_{12}\text{H}_{10}\text{F}_3\text{NO}_4\text{S}$ Donor <b>4</b>	320.02099	320.0192	1300	2000

### 3.5.3 Photolysis of Oxime **10**

Thus far, it has been established that oxime **10** and diol **7** result from nucleophilic attack by either HNO or solvent water during the photolysis of donor **4**. We wished to also understand the origin of the other photoproducts, namely compound **11** and aldehyde **8**. To explore this, photochemical experiments were carried out on oxime **10**. The photochemistry of aromatic oximes ( $\text{ArCR}=\text{NR}'$ ) is well established.<sup>31</sup> Aromatic oximes generate their corresponding aldehydes ( $\text{ArCOR}$ ) and amines ( $\text{H}_2\text{NR}'$ ) or amides ( $\text{ArCONHR}$ ) upon photolysis.<sup>31</sup> A sample of oxime **10** (6.00 mM) in 60:40 v/v  $\text{CD}_3\text{CN}$  and 0.1 M phosphate buffer solution (pH 7.0) was irradiated by collaborators at Kent State University. Amide **11** (identified from comparison with a  $^1\text{H}$  NMR spectrum for this species in literature<sup>239</sup> ( $^1\text{H}$  NMR ( $d_6$ -DMSO):  $\delta$  7.13 (d, 2H), 7.26 (s, 1H), 7.69(d,

1H), 7.83 (d, 2H), 7.95 (s, 1H, -NH-), 8.33 (s, 1H), 9.44 (s, 1H, -OH)) and aldehyde **8** (identified using authentic sample) were observed in the photolytic mixture (Figure 3.30). Hence, amide **11** and aldehyde **8** are secondary photoproducts originating from the photolysis of oxime **10**.

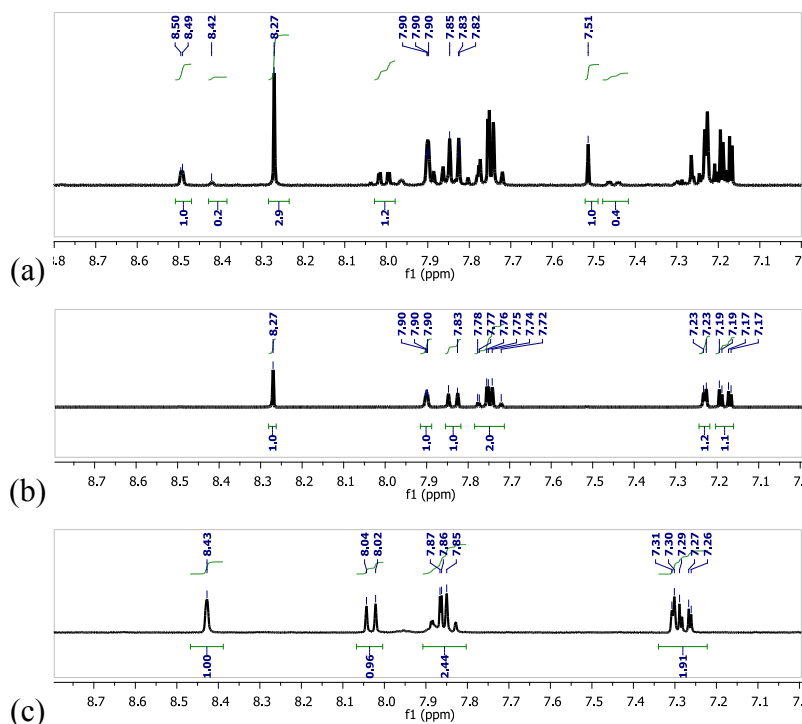


Figure 3.30. (a)  $^1\text{H}$  NMR spectrum of oxime **10** (6.00 mM) in 60:40 v/v  $\text{CD}_3\text{CN}$  and 0.1 M phosphate buffer solution (pH 7.0) following irradiation for 15 min ( $\sim 30\%$  decomposition, Rayonet photoreactor, 8 x 350 nm bulbs, 4 W). (b) Authentic sample of oxime **10** (6.00 mM) in the same solvent. (c) Aldehyde **8** in the same solvent.

### 3.6 EVIDENCE FOR CONCERTED RELEASE OF HNO AND $\text{CF}_3\text{SO}_2^-$

Previously, our research group observed that donor **2** and **3** ( $\text{R} = \text{CH}_3, \text{Ph}$ ; Figure 3.1) photodecompose to release HNO and  $\text{RSO}_2^-$  or to eliminate  $\text{RSO}_2\text{NHO}^-$  (Scheme 3.1, Pathway 1 and Pathway 2). The former pathway was identified through formation of  $\text{RSO}_2^-$  species under neutral pH conditions. The latter pathway was identified through observation of MSHA ( $\text{CH}_3\text{SO}_2\text{NHOH}$ ;  $\text{p}K_a$  9.79)<sup>212</sup> and Piloty's acid ( $\text{PhSO}_2\text{NHOH}$ ;  $\text{p}K_a$  9.29<sup>81</sup>).<sup>23</sup> Whereas MSHA and Piloty's acid are stable in the solvent conditions used in this study,  $\text{CF}_3\text{SO}_2\text{NHOH}$  is unstable at neutral pH conditions and spontaneously decomposes to HNO and  $\text{CF}_3\text{SO}_2^-$ .<sup>90</sup> Hence, donor **4** may potentially release HNO via  $\text{CF}_3\text{SO}_2\text{NHOH}$  ( $t_{1/2} \sim 13.0$  min, pH 7.0)<sup>23,24</sup> or via simultaneous HNO/ $\text{CF}_3\text{SO}_2^-$  release. However, no traces of the corresponding  $\text{CF}_3\text{SO}_2\text{NHOH}$  or its conjugate base were observed as intermediates during the photolysis of **4** (Figure 3.7).<sup>23,24</sup> This suggests that

concerted elimination leads directly to HNO release without the formation of a  $\text{CF}_3\text{SO}_2\text{NHO}^-$  intermediate.

To confirm these findings, the photolysis of **4** was carried out under pH conditions where  $\text{CF}_3\text{SO}_2\text{NHOH}$  would be expected to be stable ( $\text{p}K_a 5.89 \pm 0.05$ ).<sup>90</sup> The steady state photolysis of **4** (1.0 mM) was monitored over time in an anaerobic mixture of 80:20 v/v  $\text{CD}_3\text{CN}$  to 5.0 mM phosphate buffer solution (pH 3.0) (Figure 3.31(a)). Photolysis of **4** under these conditions produced two photoproducts (86:14  $\text{CF}_3\text{SO}_2\text{NH}_2$  to  $\text{CF}_3\text{SO}_2^-$ ) (Figure 3.31(b)). Neither  $\text{CF}_3\text{SO}_2\text{NHOH}$  nor additional species are observed. These data indicate that HNO release occurs via concerted C-O and N-S bond cleavages. The pH dependence of pathway selectivity is investigated in Chapters 4 and 5.

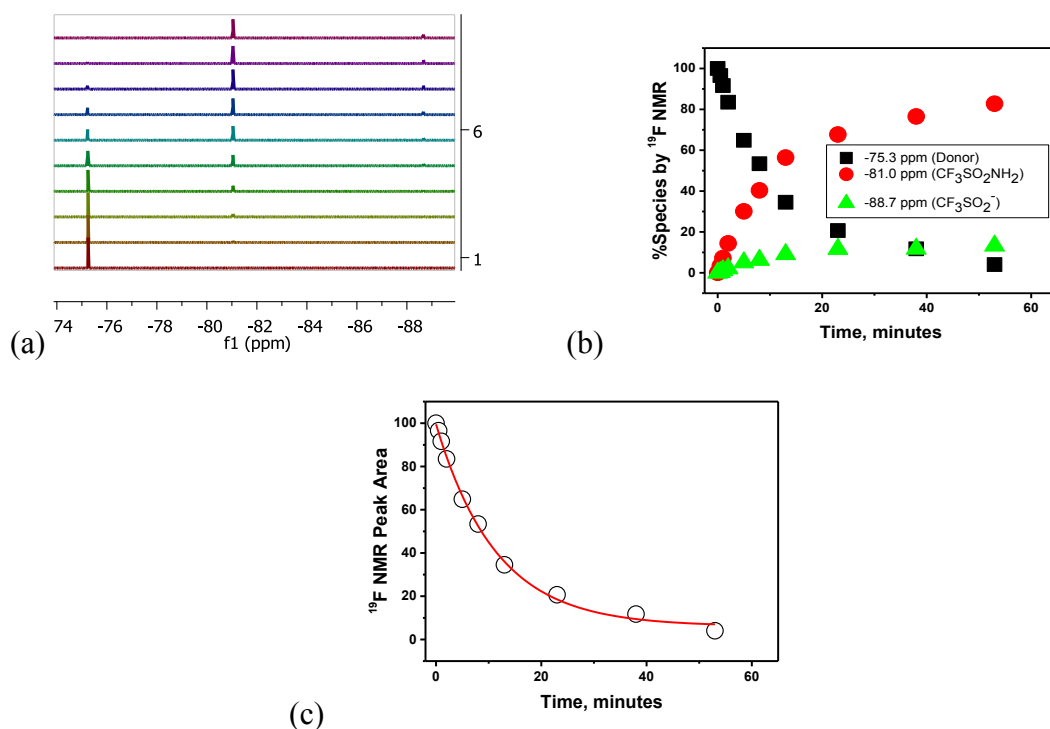


Figure 3.31. (a)  $^{19}\text{F}$  NMR spectra as a function of irradiation time (Rayonet photoreactor, 8 x 350 nm bulbs, 4 W; 0, 0.5, 1, 2, 5, 8, 13, 23, 38, and 53 min) for the photodecomposition of donor **4** (1.0 mM) in an anaerobic mixture of 80:20 v/v  $\text{CD}_3\text{CN}$  to 5.0 mM phosphate buffer (pH 3.0). (b) Plot of observed species as a function of irradiation time. (c) Best fit of the peak area of donor **4** ( $-\text{CF}_3$ ) to a first-order rate equation, giving  $k_{\text{obs}} = 0.09 \pm 0.01 \text{ min}^{-1}$ .

### 3.7 PHOTOPRODUCT QUANTUM YIELD OF HNO PHOTORELEASE

The photoproduct quantum yields of **4** (1-2 mM; 3.000 mL) were determined using azobenzene as an actinometer (see Chapter 2, Section 2.4.4) in anaerobic and aerobic

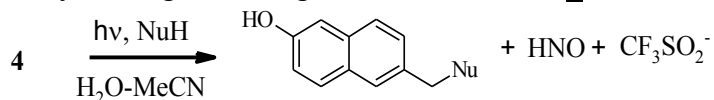
solvent mixtures of 60:40 v/v MeCN to 5.0 mM phosphate buffer solution (pH 7.0). The UV-vis spectra were measured for each sample prior to irradiation to accurately calculate the concentration of the samples (see example in Appendix C). Where noted as anaerobic, septa-sealed samples were bubbled with argon for ~90 s prior to irradiation. The samples were then irradiated in the cuvette at various time intervals. At each interval, an aliquot (0.275 mL) was withdrawn from the sample and added to an NMR tube with 0.275 mL MeOD or  $d_6$ -DMSO (internally referenced to trifluorotoluene; see an example in Appendix C). Using  $^{19}\text{F}$  NMR spectroscopy, the percentage of donor **4** converted was determined by integrating all  $^{19}\text{F}$  NMR peaks.  $^{19}\text{F}$  NMR spectroscopy was selected instead of  $^1\text{H}$  NMR spectroscopy because whereas the fluorinated photoproducts were stable upon irradiation, the protonated photoproducts underwent deuterium exchange, photobleaching, and/or secondary photochemistry, making their integration less reliable. The integrations obtained from the  $^{19}\text{F}$  NMR spectra were then converted to moles of photoproduct using the initial concentration of the donor and the volume of irradiated solution. The reported quantum yield is an average of three to seven conversions. Conversions did not exceed 10%. Under both conditions, **4** cleanly produced  $\text{CF}_3\text{SO}_2^-$  as observed by  $^{19}\text{F}$  NMR spectroscopy with a quantum yield of  $\Phi_{\text{PP}} = 0.50 \pm 0.07$  (unaffected by oxygen). As  $\text{CF}_3\text{SO}_2^-$  was shown to be a chemical marker of HNO photorelease, the photoproduct quantum yield of  $^1\text{HNO}$  photorelease from **4** is  $\Phi_{\text{PP}} = 0.50 \pm 0.07$ . Values ranging from 0.20-0.87 have been observed for similarly structured hydroxyarene systems (HO-Ar-CH<sub>2</sub>-LG).<sup>120,170</sup>

### 3.8 CONCLUSIONS

In summary, a photoactive Piloty's acid derivative comprising an HNO-generating trifluoromethanesulfonamidoxy moiety tethered to the 6,2-HNM photocage decomposes essentially stoichiometrically to release HNO upon light activation in solvent mixtures of MeCN and 5 mM phosphate buffer (pH 7.0) (Scheme 3.4). The photoactive donor **4** is thermally stable for several days in ambient conditions. Partial photodecomposition of donor **4** generated equal amounts of chemical marker  $\text{CF}_3\text{SO}_2^-$  and HNO (as indicated by  $\text{H}_2\text{OCbl(III)}^+$  reacting with HNO to form  $\text{NO}^-$ -Cbl(III)).<sup>24,209</sup> Similar results were observed for donor **1** using UV-vis spectroscopy and  $^{19}\text{F}$  NMR spectroscopy (discussed in Chapter 5, Section 5.5.2.1).<sup>24</sup> HNO generation from photolysis of donor **4** was confirmed using thiol trapping. Furthermore, our collaborators observed that continuous photolysis of donor **4** generates HNO by UV-vis spectroscopic observation of

$\text{H}_2\text{OCbl(III)}^+$  conversion to  $\text{NO}^- \cdot \text{Cbl(III)}$  and using 3-(diphenylphosphanyl)-4-(methoxycarbonyl)benzoic acid trapping of HNO to give the corresponding aza-ylide.<sup>209</sup> Typically, HNO generated from photoactive HNO donors is quantified using GC-MS headspace analysis of the dimerization product,  $\text{N}_2\text{O}$ ,<sup>6</sup> and further confirmed using an additional trapping method.<sup>2-4</sup> Although  $\text{N}_2\text{O}$  was observed upon photolysis of donor **4**, this method was not useful for quantification of HNO because electrons ejected from the photocage react with  $\text{N}_2\text{O}$ , decreasing the apparent yield of HNO.

Scheme 3.4. Pathway leading to HNO generation for donor **4**.



The photoproduct characterization results provide insights into the mechanism of HNO release from excitation of donor **4**. The photoproduct quantum yield ( $\Phi_{\text{PP}} = 0.50 \pm 0.07$ ) of HNO release (by chemical marker  $\text{CF}_3\text{SO}_2^-$ ) was unaffected by oxygen, indicating that HNO release proceeds via a singlet excited state species of donor **4**. Importantly, the generation of HNO proceeds via concerted heterolytic bond cleavages of the C-O and S-N bonds. The aromatic transient species formed upon the photolysis of donor **4** is clearly reactive with nucleophiles (e.g. MeOH,  $\text{H}_2\text{O}$ , HNO). In the absence of an effective HNO trap, HNO recombines with the transient species to form oxime **10**; this compound is not photostable and hence a mixture of aromatic photoproducts is observed in the absence an effective HNO trap.

$^1\text{H}$  NMR and UV-vis spectroscopic experiments showed that **4** exists in three protonation states ( $\text{p}K_{\text{a}(\text{NH})} = 4.39 \pm 0.06$  and  $\text{p}K_{\text{a}(\text{OH})} = 9.73 \pm 0.01$  as determined by UV-vis spectroscopic titrations). HNO is formed following photolysis of donor **4** when the donor molecule is excited under pH conditions where the leaving group nitrogen atom is deprotonated and naphtholic OH is protonated. However, hydroxyarenes are well known to undergo excited state proton transfers upon excitation.<sup>116</sup> Thus it is unclear if donor **4** undergoes excited state proton transfer(s) upon excitation and enters into another ionization state in the excited state. Whether excited state proton transfer(s) are an important part in HNO generation upon photoexcitation of donor **4** or not remains unclear. This will be investigated in Chapter 4.

# CHAPTER 4: ULTRAFAST GENERATION OF HNO FROM PHOTOLYSIS OF PHOTOCAGED (6- HYDROXYNAPHTHALEN-2-YL)METHYL ANALOGUE OF PILOTY'S ACID

---

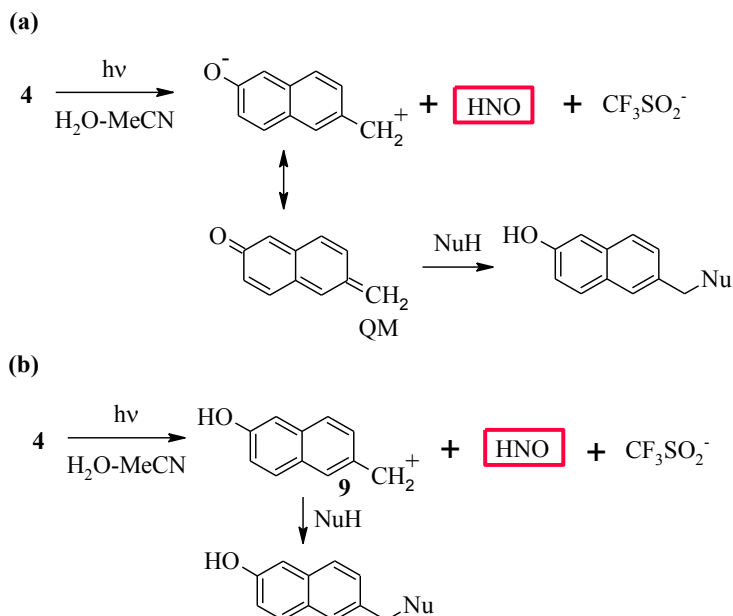
## 4.1 INTRODUCTION

Due to HNO's high reactivity with itself, molecules that decompose to generate HNO must be used to study HNO's properties and reactivity. These HNO donating molecules must be used judiciously according to the type of study of interest as the chemistry of the HNO donor itself can have significant effects on the chemistry observed. Hence a thorough understanding of the mechanism of HNO release from HNO donor molecules is a prerequisite to their effective use. Our research group is interested in pursuing kinetic and mechanistic studies that explore HNO's reactivity with biomolecules.<sup>78,240</sup> These studies call for rapid release of HNO to allow rate constants of the reactions of HNO with other species to be directly determined; that is, competition experiments would not be required and kinetic data for the reaction of interest would be obtained.<sup>1,52</sup>

The photoproduct characterization of donor **4** implied that photorelease of HNO proceeds via concerted heterolytic bond cleavages of the C-O and S-N bonds (Chapter 3, Section 3.6). Two possible photocleavage mechanisms are proposed (Scheme 4.1). A possible pathway involves excited state proton transfer(s) (ESPT) leading to bond cleavages of the C-O and S-N bonds and quinone methide (QM) formation (Scheme 4.1, Pathway (a)).<sup>155</sup> Ultra-fast time resolved spectroscopic experiments show that QM formation occurs on the picosecond to microsecond timescale; that is, it is highly dependent on the compound itself.<sup>151,173,187</sup> Additionally, (6-hydroxynaphthalen-2-yl)methyl (6,2-HNM) protected molecules and structurally related compounds can undergo bond heterolysis of the ArCH<sub>2</sub>-X bond, yielding the 6-hydroxynaphthalen-2-yl)methyl cation **9** for the 6,2-HNM-photocage and a corresponding anion (ArCH<sub>2</sub><sup>+</sup>/X<sup>-</sup>; Scheme 4.1, Pathway

(b)).<sup>206-208</sup> Heterolytic cleavages in excited state molecules typically occur on the picosecond timescale.<sup>241-243</sup> The cleavage mechanisms proceed at different rates and hence, identification of either mechanism provides insights into the rate of HNO generation from photolysis of donor **4**.

Scheme 4.1. Possible heterolytic bond cleavage pathways leading to HNO photorelease from donor **4**.



In this chapter, the kinetic and mechanistic studies of HNO generation from photolysis of donor **4** are discussed. Donor **4** was synthesized by the research groups of Prof. Paul Sampson and Prof. Alexander Seed at Kent State University in the United States. The role of ionization of **4** in the ground state on its pathway selectivity will be probed through product distribution studies as a function of pH and solvent. The role of ionization of **4** in the excited state on pathway selectivity will also be investigated. To achieve this, steady state emission studies will be detailed for **4** and a model compound 2-naphthol. Time-resolved transient absorption studies will also be presented in order to consider if the naphtholic OH can undergo excited state proton transfer upon excitation under conditions where HNO generation from photolysis of **4** is the dominant pathway. This information provides insights into the characterization of aromatic transient or intermediate species produced upon C-O bond cleavage (see Chapter 1, Figure 1.2). Importantly, time-resolved transient absorption studies will be described which suggest that HNO generation occurs on the picosecond timescale following excitation of donor **4** (see Chapter 1, Figure 1.2).

4.2 THE ROLE IONIZATION OF **4** IN PATHWAY SELECTIVITY

The effect of donor **4**'s ionization on pathway selectivity was examined. Scheme 4.2 shows that donor **4** contains two potentially acidic sites. Chapter 3 showed that donor **4** can photodecompose via two major mechanisms, producing HNO or undergoing undesired N-O bond cleavage (Scheme 4.3). To study the effect of donor **4**'s ionization state on pathway selectivity, a series NMR samples were prepared of donor **4** (0.500-1.00 mM) in solvent mixtures in which the aqueous portion (20 to 80% by vol.) in CD<sub>3</sub>CN and also pH the aqueous portion (pH 1-13) were varied. Figure 4.1 shows that the percentage

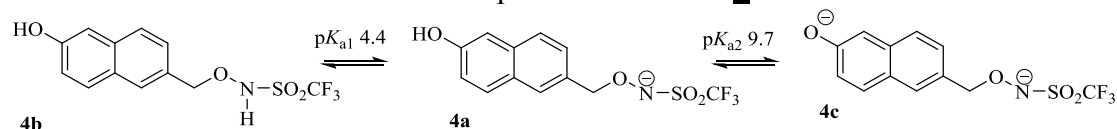
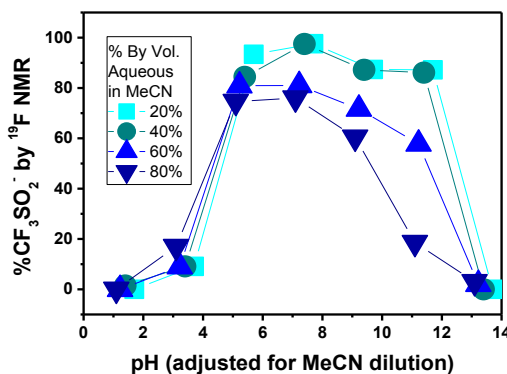
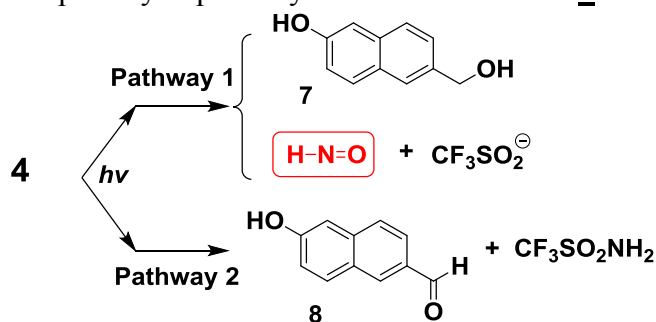
Scheme 4.2. Ground state acid-base equilibria for donor **4**.Scheme 4.3. Proposed photolytic pathways accessible to donor **4**.

Figure 4.1. Selectivity for HNO photorelease (from <sup>19</sup>F NMR total integration) according to pH of aqueous solution and concentration of aqueous component in CD<sub>3</sub>CN, where the aqueous component is 0.1 M HCl, 0.1 M NaOH, 5.0 mM phosphate buffer (pH 3.0, 7.0), 5.0 mM acetate buffer (pH 5.0), 5.0 mM borate buffer (pH 9.0), or 5.0 mM carbonate buffer (pH 11.0). Steady state photolysis samples of **4** (0.500-1.00 mM) were prepared in anaerobic solutions and irradiated using a Rayonet photoreactor (8 x 350 nm bulbs, 4 W) until completely degraded.

of  $\text{CF}_3\text{SO}_2^-$  from photolysis of donor **4** varied as a function of pH and the composition of the solvent mixture. Interestingly, donor **4** only produces HNO (by  $\text{CF}_3\text{SO}_2^-$  chemical marker) between  $\sim$  pH 5 and  $\sim$  pH 12 in 20-40% by vol. aqueous solution in  $\text{CD}_3\text{CN}$ . Additionally, the selectivity for HNO photorelease decreases as the aqueous portion of the solvent increases (for  $5 < \text{pH} < 12$ ). Aqueous acetonitrile is known to increase the  $\text{p}K_{\text{a}}$  values of similarly structured compounds compared to values reported in water (e.g. for 1-naphthol,  $\text{p}K_{\text{a}(\text{OH})} = 9.2$  in  $\text{H}_2\text{O}$  and  $\text{p}K_{\text{a}(\text{OH})} = 11.9$  in 2:1 MeCN to  $\text{H}_2\text{O}$ ).<sup>135</sup> When this is taken into consideration, donor **4**'s ground state  $\text{p}K_{\text{a}}$  values correlate well with the pH conditions in which the desired pathway is shut off ( $\text{p}K_{\text{a}(\text{NH})} = 4.4$  and  $\text{p}K_{\text{a}(\text{OH})} = 9.7$ ). It is clear that neither excitation of **4b** nor **4c** in aqueous solutions produces the desired pathway.

To further probe the mechanism of HNO photorelease, donor **4**'s emission was investigated in the solvent mixture (80:20 v/v MeCN to aqueous conditions). This ratio of solvent was selected as optimal selectivity for HNO release occurs in a ratio of 80:20 v/v MeCN to 5.0 mM phosphate buffer solution (pH 7.0). The emission from donor **4** is quenched from pH 5-9. At  $\text{pH} < 4$ , emission from the parent structure of **4** is observed as indicated by the band at 360 nm. The fluorescence quenching observed in this solvent mixture indicates that an excited state species of **4a** undergoes a competitive process which competes with fluorescence decay. Based on the pathway selectivity studies (Figure 4.2), the competitive deactivation process results in the release of HNO from **4a**.

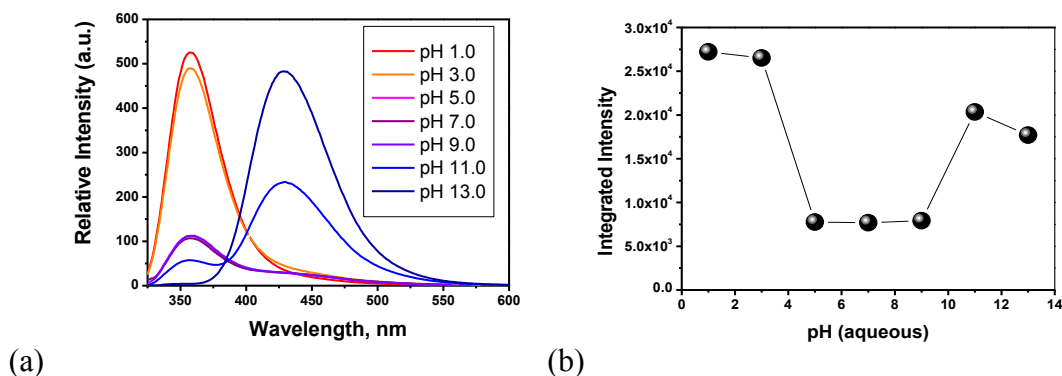
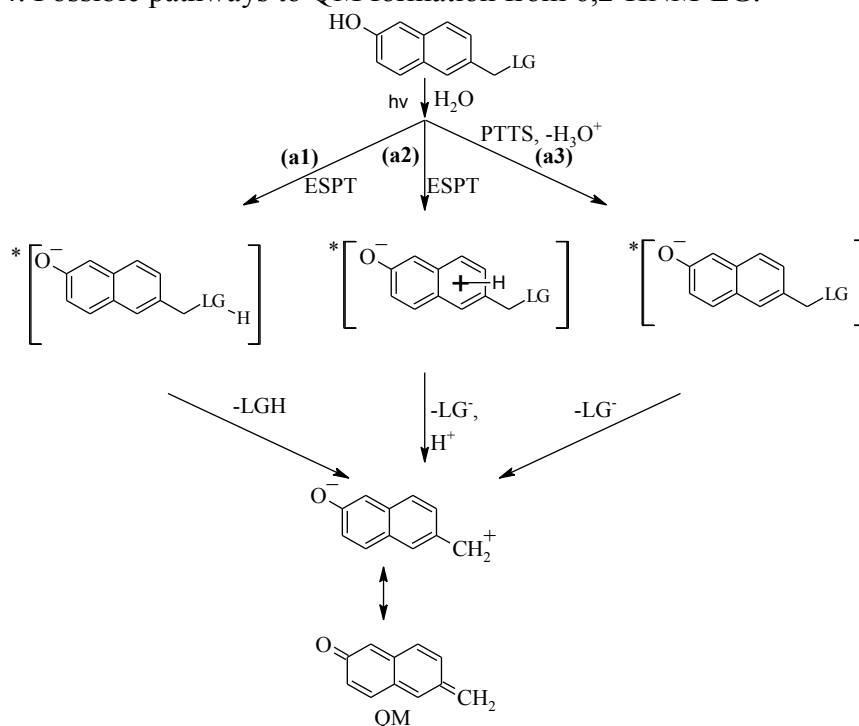


Figure 4.2. (a) Emission spectra of donor **4** ( $\sim \mu\text{M}$ ) in 80:20 v/v MeCN to aqueous conditions, 20 by vol aqueous in MeCN, where the aqueous component is 0.1 M HCl, 0.1 M NaOH, 5.0 mM phosphate buffer (pH 3.0, 7.0), 5.0 mM acetate buffer (pH 5.0), 5.0 mM borate buffer (pH 9.0), or 5.0 mM carbonate buffer (pH 11.0). Excitation wavelength is at an isosbestic point between **4a** and **4c** ( $\lambda_{\text{exc}} = 315$  nm). (b) Integrated intensity as a function of pH.

### 4.3 INVESTIGATION OF EXCITED STATE PROTON TRANSFERS TO AND FROM SOLVENT USING FLUORESCENCE SPECTROSCOPY

Heterolytic bond cleavage of the C-O and N-S bonds in the photolysis of donor **4a** may proceed via ESPT(s) to form a corresponding QM (Scheme 4.1, Pathway (a)). Hydroxyarenes can undergo ESPT(s) from the molecule to solvent (i.e. photoacidity),<sup>127</sup> to the molecule from solvent (e.g. photobasicity),<sup>147,148</sup> or both to and from the molecule (e.g. phototautomerization).<sup>152</sup> Three possible ESPT(s) event series that generate QMs from hydroxyarenes have been reported. First, phototautomerization can occur from a photoacidic OH to a site on the leaving group (LG) which generates a QM from loss of a protonated leaving group (Scheme 4.4, Pathway a1).<sup>155</sup> Second, phototautomerization can occur from a photoacidic OH to a site on the aromatic moiety, again generating a QM from loss of leaving group (Scheme 4.4, Pathway a2).<sup>151</sup> Third, excited state proton transfer to solvent (PTTS) leads to formation of the hydroxyarene's conjugate base in the excited state, which undergoes heterolytic bond cleavage to generate a QM (Scheme 4.4, Pathway a3).<sup>167</sup> Thus, understanding the ability of donor **4** to undergo ESPT(s) provides insights into its ability to release HNO via Scheme 4.1, Pathway (a). Herein, the ability of donor **4a** to undergo ESPT(s) to and from solvent on either the leaving group (-ONHSO<sub>2</sub>CF<sub>3</sub>, LG) or on the (6-hydroxynaphthalen-2-yl)methyl (6,2-HNM) photocage was systematically investigated using fluorescence spectroscopy.

Scheme 4.4. Possible pathways to QM formation from 6,2-HNM-LG.



### 4.3.1 Investigation of Excited State Proton Transfer to Solvent from Donor **4**

The ability of donor **4** to undergo excited state proton transfer to solvent (PTTS) was investigated. This event is required for all pathways leading to QM formation (Scheme 4.4). As a preliminary study, donor **4**'s emission spectrum was recorded in 5.0 mM phosphate buffer solution (pH 7.0; 5% by vol. of MeCN) and compared to its emission spectrum in MeCN and 0.1 M NaOH (5% by vol. of MeCN; Figure 4.3). At pH 7.0, multiple emissive bands were observed at 357 nm and 420 nm with a broad shoulder at 460 nm upon excitation of **4a**. It will be shown that the LG does not influence the fluorescence spectrum of the 6,2-HNM-photocage (Section 4.3.2); therefore, the band at 357 nm is assigned to emission from **4a** from comparison to **4b**'s emission in MeCN. The band at 420 nm is assigned to emission from **4c** formed from PTTS from comparison to **4c**'s emission in 0.1 M NaOH (5% by vol. of MeCN). The observation of the band at 420 nm in both neutral and alkaline conditions indicates that donor **4** contains a photoacidic site. Based on structurally related molecules, the photoacidic site is assigned to the naphtholic OH.<sup>137</sup> The emission observed above 525 nm from excitation in 5.0 mM phosphate buffer solution (pH 7.0; 5% by vol. of MeCN) indicates that **4a** may undergo ESPT to the molecule from solvent (investigated further in Section 4.3.2 and Section 4.3.3).

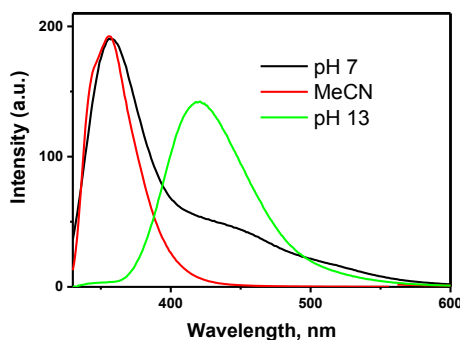


Figure 4.3. Emission spectra of donor **4** ( $\sim\mu\text{M}$ ) in 95% by vol. of 5.0 mM phosphate buffer pH 7.0 (5% MeCN), 95% by vol. of 0.1 M NaOH (5% MeCN), and in MeCN. ( $\lambda_{\text{exc}} = 315 \text{ nm}$ ).

Substituents on naphthols can drastically influence the degree of photoacidity.<sup>141</sup> The photoacidity of **4** was therefore compared to that of 2-naphthol in order to determine the effect of the  $-\text{CH}_2\text{ON}(\text{H})\text{SO}_2\text{CF}_3$  substituent on the 6 position. To achieve this, excited state equilibrium constants for the naphtholic OH ( $\text{p}K_{\text{a}(\text{OH})}^*$ ) of **4** were estimated using the 0-0 transition from the intersection point of mutually normalized absorption and

emission spectra.<sup>244</sup> The  $pK_a^*$  values were estimated in both aqueous and partially aqueous conditions. Assuming the entropy of dissociation is the same in both  $S_0$  and  $S_1$ ,  $pK_a^*$  can be estimated using the following equation:

$$pK_a^* = pK_a - \frac{E_{HA} - E_{A-}}{2.3RT} \quad \text{Eqn. 4.1}$$

where  $R$  is the gas constant ( $8.31 \text{ J mol}^{-1} \text{ K}^{-1}$ ),  $T$  is the temperature (K), and  $E_{HA}$  and  $E_{A-}$  are the energies of the electronic transitions for the acid and base determined from the 0-0 transition energies. The energies of the electronic transitions were estimated by averaging the frequencies of absorption and fluorescence maxima for the protonated and deprotonated species:

$$E_{HA} = Nhc \frac{1}{2(\lambda_{HA}^A + \lambda_{HA}^f)} \quad \text{Eqn. 4.2}$$

$$E_{A-} = Nhc \frac{1}{2(\lambda_{A-}^A + \lambda_{A-}^f)} \quad \text{Eqn. 4.3}$$

where  $\lambda^A$  and  $\lambda^f$  are the wavelengths (m) for the maxima of absorption ( $S_0 \rightarrow S_1$ ) and fluorescence spectra, respectively;  $N$  is Avogadro's constant ( $\text{mol}^{-1}$ );  $h$  is Planck's constant (J s); and  $c$  is the speed of light ( $\text{m s}^{-1}$ ). Notably, the Förster cycle calculation assumes that the proton transfer from the  $^*ArOH$  to  $^*ArO^-$  occurs rapidly and that the acid-base equilibrium is established during the lifetime of the excited states.<sup>245</sup> Therefore, this method is treated as an estimation and a means of comparison.<sup>245-247</sup>

In order to estimate errors using this method, the  $pK_{a(OH)}^*$  of a well-studied molecule was first calculated. The  $pK_{a(OH)}^*$  of 2-naphthol was estimated from the emission spectra taken in aqueous solutions ( $pK_{a(OH)}^* \approx 3.3 \pm 0.3$ ; Figure 4.4 and Table 4.1). This is in reasonable agreement with the literature value of 2.8 (error not reported, calculated from a fluorescence titration).<sup>116</sup> Adding MeCN to water causes a shift in ground state equilibrium, effectively increasing the  $pK_{a(OH)}$  from 9.3 to 10.3.<sup>135</sup> It was of interest to examine how the mixed solvent conditions affect the  $pK_{a(OH)}^*$  of 2-naphthol as mixed solvent conditions are primarily used in studies of the donor compounds due to their poor solubility. Therefore, the  $pK_{a(OH)}^*$  was also calculated for 2-naphthol under partially aqueous conditions (80:20 v/v MeCN to 0.1 M HCl or 0.1 M NaOH). In Chapter 3, donor **4** was shown to release HNO stoichiometrically in 80:20 v/v MeCN to 5 mM phosphate buffer solution (pH 7.0); hence the excited state behavior of **4** in mixed solvent conditions

was of interest. Dilution of water into MeCN had little effect on the excited state  $pK_{a(OH)}^* \approx 3.4 \pm 0.4$  as estimated by 0-0 transition energies (Table 4.1).

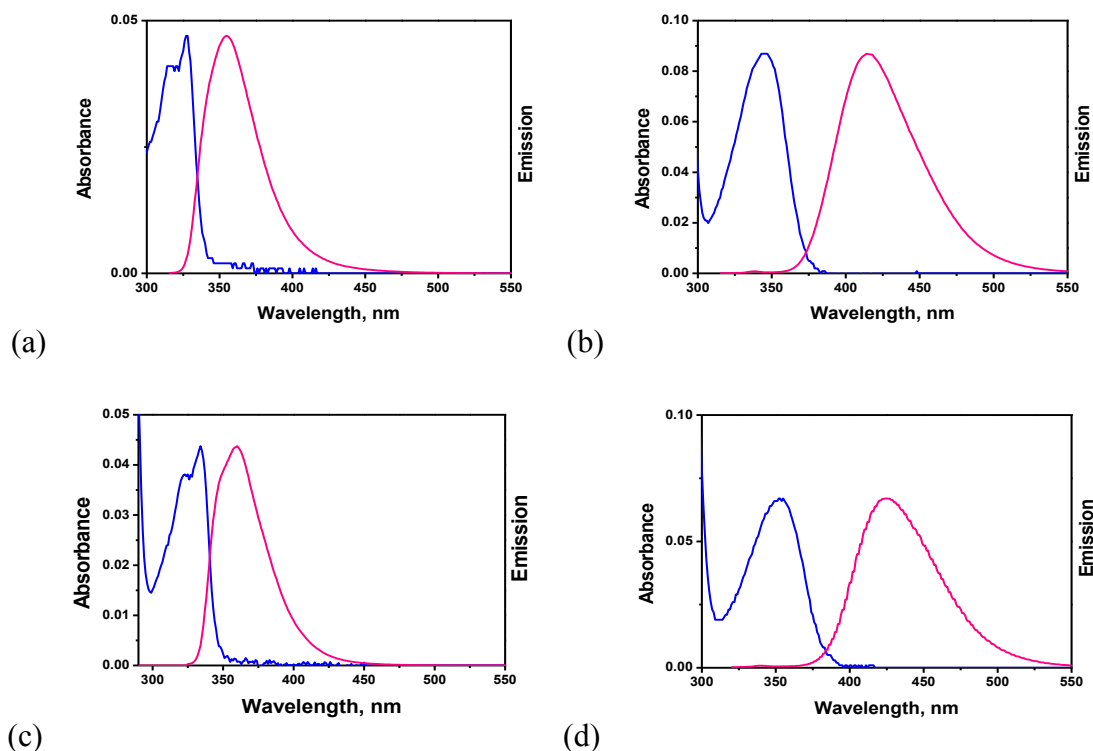


Figure 4.4. Absorption and fluorescence spectra of 2-naphthol in (a) 0.1 M HCl, (b) 0.1 M NaOH, (c) 80:20 v/v MeCN to 0.1 M HCl, and (d) 80:20 v/v MeCN to 0.1 M NaOH ( $\lambda_{exc} = 315$  nm).

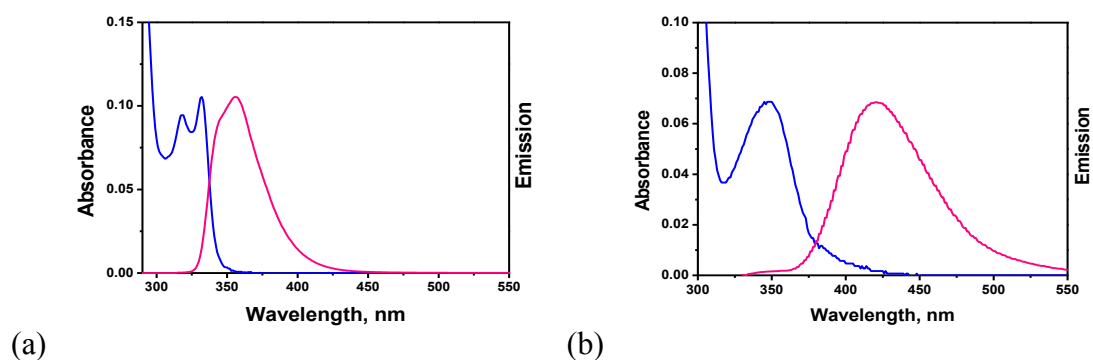


Figure 4.5. Absorption and fluorescence spectra of **4** in (a) MeCN and (b) 0.1 M NaOH ( $\lambda_{exc} = 315$  nm).

Table 4.1. Parameters used in Forster cycle  $pK_{a(OH)}^*$  calculation for 2-naphthol and donor **4**.

Solvent	$\lambda_{HA}^A$ (nm)	$\lambda_{HA}^f$ (nm)	$E_{HA}$ (J)	$\lambda_{A-}^A$ (nm)	$\lambda_{A-}^f$ (nm)	$E_{A-}$ (J)	$pK_{a(OH)}$	$pK_{a(OH)}^*$
<b>2-Naphthol</b>								
<b>0.1 M HCl or 0.1 M NaOH</b>	328	355	$3.51 \times 10^5$	347	414	$3.17 \times 10^5$	9.3	3.3
<b>80:20 v/v MeCN to 0.1 M HCl or 0.1 M NaOH</b>	330	357	$3.49 \times 10^5$	355	425	$3.09 \times 10^5$	10.3	3.4
<b>Donor 4</b>								
<b>MeCN/0.1 M NaOH</b>	330	354	$3.50 \times 10^5$	356	421	$3.13 \times 10^5$	9.73	3.4

Estimating the  $pK_{a(OH)}^*$  of **4** is more complex than that of 2-naphthol because **4** may contain photobasic sites as indicated by its emission spectrum in 0.1 M HCl (5% by vol. of MeCN; see Section 4.3.3). Therefore, isolating the equilibrium between **4** and its conjugated base is a primary concern. An estimation of the  $pK_{a(OH)}^*$  was calculated between **4** and its naphtholate analogue by comparing the emission spectra taken in MeCN (Figure 4.5(a)) and in 0.1 M NaOH in MeCN (Figure 4.5(b)). Using this method, the excited state  $pK_{a(OH)}^*$  of **4** is estimated to be  $pK_{a(OH)}^* \approx 3.4 \pm 0.4$  (Table 4.1). This is in good agreement with that of the model compound, 2-naphthol ( $pK_{a(OH)}^* \approx 3.4 \pm 0.4$ ). Hence, substitution of  $-\text{CH}_2\text{ON}(\text{H})\text{SO}_2\text{CF}_3$  of the 6 position does not significantly influence the degree of photoacidity of the naphtholic OH. This is attributed to the methylene carbon, which separates the electron-rich oxygen from the aromatic ring; hence, **4a** and **4b** would have similar  $pK_{a(OH)}^*$  values.

### 4.3.2 Investigation of Excited State Proton Transfer Occurring to Leaving Group of Donor **4** from Solvent

The influence of the leaving group (LG) on the photophysical properties of the 6,2-HNM-photocage was investigated. Table 4.2 shows that the  $-\text{CH}_2\text{ONHSO}_2\text{CF}_3$  substituent of **4** did not influence the absorbance spectral shape of the naphtholic structure ( $\lambda_{S2max}^A = 275\text{--}285$  nm;  $\lambda_{S1max}^A = 330\text{--}335$  nm). The influence of the LG on the emission spectra of the 6,2-HNM-photocage was also investigated. 2-Naphthol and donor **4**'s photophysical characteristics were compared in a series of aprotic solvents, where ESPT cannot occur. In aprotic solvent, donor **4** is in the neutral form (**4b**; Scheme 4.2). Figure 4.6 (a) and (b) show that 2-naphthol and **4b** have near identical emission spectra in MeCN or in DMSO. It is well known that substitution on aromatic rings can have large effects on a molecule's

absorption and emission spectra.<sup>141</sup> However, for donor **4**, the methylene carbon separates the electron withdrawing LG from the aromatic ring. Importantly, this experiment indicates that addition of the  $-\text{CH}_2\text{ONHSO}_2\text{CF}_3$  substituent to 2-naphthol does not change the spectral shape of the parent molecule.

Table 4.2. Optical properties of 2-naphthol in water<sup>248</sup> and donor **4** measured in MeCN and DMSO. Absorbance maximum for  ${}^1\text{L}_b \leftarrow \text{S}_0$  transitions =  $\lambda_{S1max}^A$ ; absorbance maximum for  ${}^1\text{L}_a \leftarrow \text{S}_0 = \lambda_{S2max}^A$ , nm; molar extinction coefficient =  $\epsilon$ .

Compound	$\lambda_{S2max}^A$ (nm)	$\epsilon$ ( $\text{M}^{-1}\text{cm}^{-1}$ )	$\lambda_{S1max}^A$ (nm)	$\epsilon$ ( $\text{M}^{-1}\text{cm}^{-1}$ )	$\lambda_{max}^f$ (nm)	Stokes Shift, ( $\Delta\text{nm}$ )
<b>Water</b>						
2-Naphthol <sup>248</sup>	285	3100	330	--	353	23
<b>MeCN</b>						
2-Naphthol	275	--	330	--	359	29
Donor <b>4</b>	278	5500	330	1760	356	26
<b>DMSO</b>						
2-Naphthol	--	--	335	--	360	25
Donor <b>4</b>	--	5200	335	1935	361	26

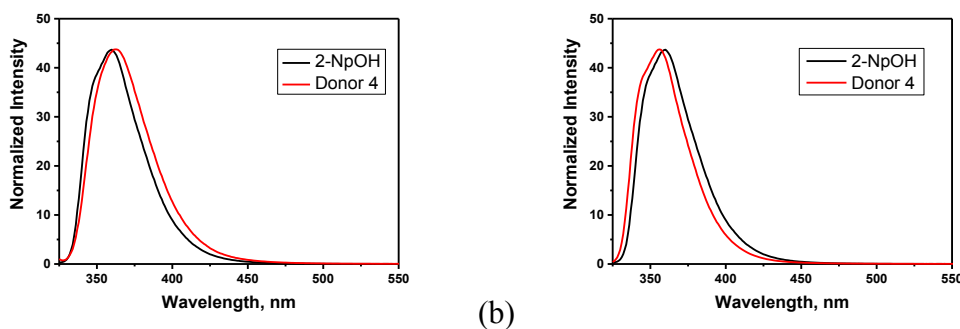


Figure 4.6. (a) Emission spectra of 2-naphthol and **4** in DMSO ( $\lambda_{\text{exc}} = 315$  nm). (b) Emission spectra of 2-naphthol and **4** in MeCN ( $\lambda_{\text{exc}} = 315$  nm).

Fluorescence spectroscopy is a useful tool to investigate ESPT's from hydroxyarenes.<sup>137</sup> Hence fluorescence spectroscopy was considered as a means to probe whether or not ESPT occur on the leaving group. However, it is clear that the sites of protonation are well separated from the aromatic rings by the methylene carbon. Therefore, alternative methods to fluorescence spectroscopy must be used to decipher if donor **4** undergoes an ESPT event involving the leaving group (e.g. HNO versus  ${}^1\text{NO}^-$  release; investigated later in Section 4.5).

### 4.3.3 Investigation of Excited State Proton Transfer to an Aromatic Carbon in Donor **4** from Solvent

Hydroxyarenes can undergo ESPT to a site on a carbon atom in the aromatic ring(s).<sup>151</sup> The ability of **4b** to accept protons in the excited state from solvent water was examined (Scheme 4.4, Pathway a2). The emission spectrum of **4b** was recorded in MeCN (where ESPT cannot occur) and upon addition of aliquots of 0.1 M HCl. Excitation of 2-naphthol in 0.1 M HCl did not display an emissive sideband, indicating that the LG on **4** influences the photobasicity of the aromatic moiety (Figure 4.7(a)). The emissive side band ( $\lambda_{nm} = 425\text{-}500$  nm) was dependent on the concentration of acid (0.1 M HCl) in the solvent mixture (co-solvent MeCN; Figure 4.7(b)). This study indicates that the sideband (425-550 nm) is associated with emission from an excited state generated from ESPT from solvent to an aromatic carbon atom. To further confirm this, excitation of donor **4** was investigated in solvent 2,2,2-trifluoroethanol (TFE). TFE is a fluorinated alcohol that exhibits a high hydrogen bonding (HB) donor strength but poor HB accepting strength (Table 4.3). Figure 4.8 shows the emission spectra of donor **4b** in TFE. The emission maximum ( $\lambda_{Fmax} = 354$  nm) is similar to that observed previously in MeCN (Figure 4.6(b)) and thus is assigned to emission from **4b** (Scheme 4.2). An emissive sideband is observed with  $\lambda_{Fmax} = 458$  nm. Hence, this study indicates that ESPT can occur from solvent to an aromatic carbon atom upon excitation of **4b** (Scheme 4.4, Pathway a2).

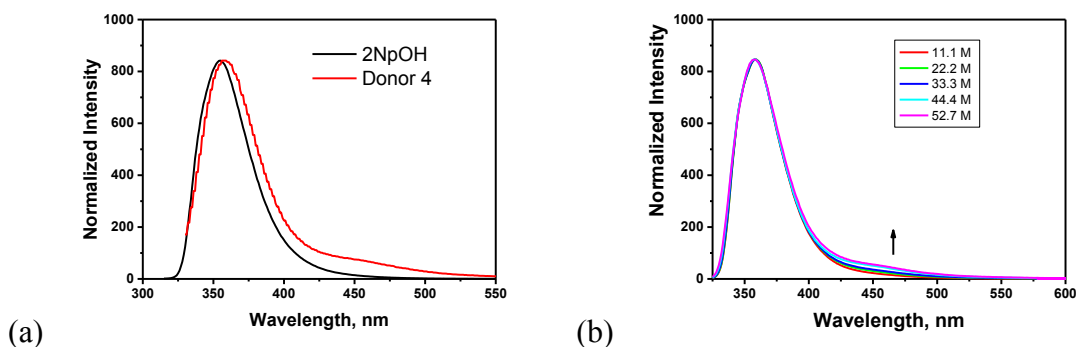


Figure 4.7. (a) Emission spectra of 2-naphthol and donor **4b** in 0.1 M HCl (5% MeCN by vol.;  $\lambda_{exc} = 315$  nm). (b) Emission spectra of donor **4b** ( $\sim 25$   $\mu\text{M}$ ) in MeCN with increasing concentrations of aqueous acid (0.1 M HCl) in MeCN ( $\lambda_{exc} = 315$  nm).

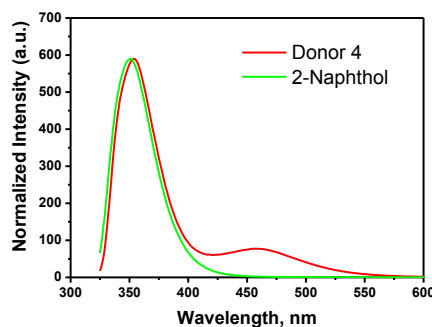


Figure 4.8. Emission spectra of donor **4b** ( $\mu\text{M}$ ) and 2-naphthol ( $\mu\text{M}$ ) in TFE ( $\lambda_{\text{exc}} = 315$  nm).

Table 4.3. Kamlet-Taft solvatochromatic parameters for solvents used in this thesis.<sup>249</sup>

Solvent	Dipolarity/ Polarizability $\pi^*$	HB Donor Strength $\alpha$	HB Acceptor Strength $\beta$
Water	1.09	1.17	0.18
Trifluoroethanol	0.73	1.51	0.00
Methanol	0.60	0.93	0.62
MeCN	0.75	0.19	0.35
DMSO	1.00	0.00	0.76

#### 4.4 THE ABILITY OF DONOR **4** TO UNDERGO EXCITED STATE PROTON TRANSFER TO SOLVENT IN PARTIALLY AQUEOUS CONDITIONS

The emission studies implied that donor **4** contains both photobasic and photoacidic sites. Hence, it is possible that QM formation from photolysis of **4** may occur via phototautomerization involving the aromatic moiety (Scheme 4.4, Pathway a2) or from PTTS followed by loss of leaving group from the naphtholate analogue (Scheme 4.4, Pathway a3). Solvent plays a large role in ESPTs.<sup>136</sup> The influence of solvent on the photodecomposition of **4** was therefore investigated.

##### 4.4.1 The Effect of Solvent on Pathway Selectivity

The effect of the percentage of 5.0 mM phosphate buffer (pH 7.0) in a phosphate buffer/ $\text{CD}_3\text{CN}$  solvent mixture on the percentage of  $\text{CF}_3\text{SO}_2^-$  product and hence the amount of HNO generated was investigated. Samples were prepared and irradiated until fully converted to photoproducts. Figure 4.9 shows that increasing additions of 5.0 mM phosphate buffer (pH 7.0) increases the selectivity towards the HNO photorelease (as indicated by  $\text{CF}_3\text{SO}_2^-$  generation). Maximum selectivity was reached between 20-40% by vol. of 5.0 mM phosphate buffer (pH 7.0) in  $\text{CD}_3\text{CN}$ . Donor **4** (mM) is not readily soluble in higher aqueous solvent conditions, and thus, photolysis experiments could not be carried out at concentrations >80% by vol.  $\text{H}_2\text{O}$  in  $\text{CD}_3\text{CN}$ . Clearly excitation of **4b** in

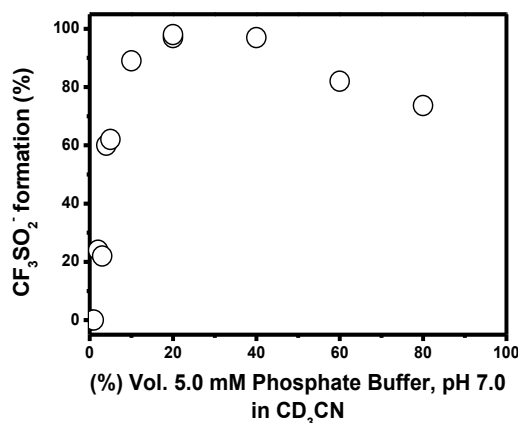


Figure 4.9. Effect of solvent composition on the percentage of HNO generated upon irradiation of HNO donor **4** (0.50-2.00 mM; Rayonet photoreactor, 8 x 350 nm bulbs, 4 W) in a mixture of phosphate buffer (5 mM, pH 7.00) and CD<sub>3</sub>CN (v/v).

the absence of a protic solvent does not generate the desired pathway (Scheme 4.3, Pathway 1). Interestingly, selectivity for HNO photorelease from **4a** decreased at higher percentages (> 40% by vol.) of 5.0 mM phosphate buffer (pH 7.0) in CD<sub>3</sub>CN (the reason for this is investigated further in Chapter 5).

#### 4.4.2 Emission Spectroscopic Investigation of the Solvent Dependence of Excited State Proton Transfer to Solvent

Pathway selectivity from photolysis of donor **4** is near ~100% for HNO photorelease in low concentrations of water (e.g. 80:20 v/v MeCN to 5.0 mM phosphate buffer solution, pH 7.0). Whether or not PTTS could occur for the photoacidic naphtholic OH at such low concentrations of water was of interest because PTTS is a requirement for QM formation (Scheme 4.3, Pathway 1). Therefore, the emission spectra of model compound 2-naphthol was recorded in a series of pH conditions in ~100% aqueous solution and in 80:20 v/v MeCN to aqueous solution. 2-Naphthol serves as a good model compound to examine PTTS because it stable upon irradiation<sup>149</sup> and has similar  $pK_a$  and  $pK_a^*$  values to donor **4** (Table 4.1). In aqueous solution, 2-naphthol showed an increase in emission from the conjugate base ( $\lambda_{max} = 415$  nm) at  $pH \geq 3.0$  ( $pK_{a(OH)^*} = 2.8$ ) (Figure 4.10(a)). Conjugate base emission is the result of 2-naphthol's excited state proton transfer to solvent. Unlike the data in highly aqueous conditions (Figure 4.10(a)), emission from 2-naphtholate ( $\lambda_{max} = 425$  nm) is not observed for pH conditions < 9.0 in a solvent mixture of 80:20 v/v MeCN to buffer (Figure 4.10(b)). The emission from the conjugate base correlates with the ground state  $pK_a$  value (= 9.3 in H<sub>2</sub>O)<sup>135</sup> instead of the  $pK_a^*$  value (= 2.8)<sup>116</sup> in 80:20

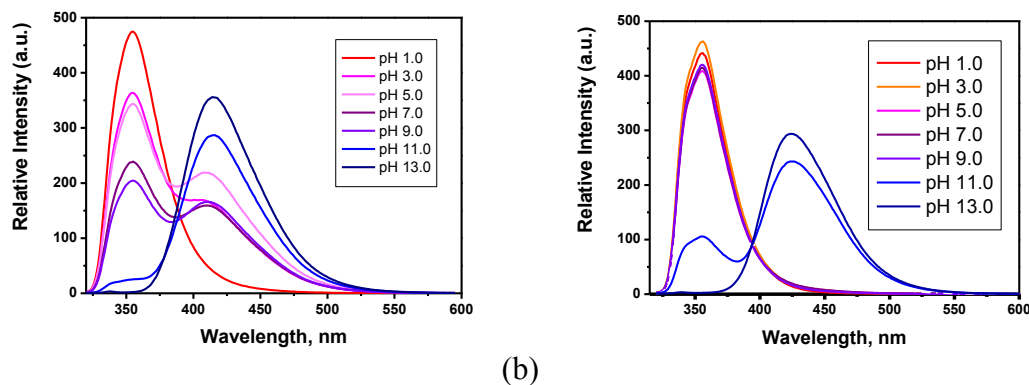


Figure 4.10. Emission spectra of 2-naphthol ( $\sim\mu\text{M}$ ) in (a)  $\sim 100\%$  aqueous conditions and (b) 80:20 v/v MeCN to aqueous solution, where the aqueous component is 0.1 M HCl, 0.1 M NaOH, 5.0 mM phosphate buffer (pH 3.0, 7.0), 5.0 mM acetate buffer (pH 5.0), 5.0 mM borate buffer (pH 9.0), or 5.0 mM carbonate buffer (pH 11.0). To avoid selective excitation of 2-naphthol or 2-naphtholate, the samples were excited at the isosbestic point between the two species ((a)  $\lambda_{\text{exc}} = 303 \text{ nm}$ ; (b)  $\lambda_{\text{exc}} = 308 \text{ nm}$ ).

v/v MeCN to buffer. This study suggests that 2-naphthol does not readily undergo PTTS in the latter solvent mixture. This indicates that PTTS is unlikely to occur for donor **4** in 80:20 v/v MeCN to 5.0 mM phosphate buffer (pH 7.0).

#### 4.4.3 Femtosecond Transient Absorption Spectroscopic Investigation of the Solvent Dependence of Excited State Proton Transfer to Solvent

The fluorescence studies indicated that deprotonation of the naphtholic OH in the excited state does not occur for naphtholic compounds in 80:20 v/v MeCN to 5.0 mM phosphate buffer (pH 7.0). To further investigate this, femtosecond transient absorption studies (fs-TA) were performed on 2-naphthol in 80:20 v/v MeCN to 5.0 mM phosphate buffer (pH 7.0). The experiments and analyses were performed on a research visit at the University of Hong Kong with assistance from the research group of Prof. David Lee Phillips. In order to identify the observed transient species, control studies were first performed in MeCN (where PTTS cannot occur) and in 5:95 v/v MeCN to 5.0 mM phosphate buffer (pH 7.0) (where PTTS is promoted).

Figure 4.11 shows the fs-TA spectra of 2-naphthol in MeCN. Bands at 340 nm and 440 nm appear within the first picosecond. The absorption change is indicative of populating the parent molecule's  $S_1$  (e.g. excited singlet state of 2-naphthol; absorption is from  $S_1$  to  $S_n$ ; Figure 4.11(a)). From  $\sim 1 \text{ ps}$  to 42 ps, absorbance at 340 nm decreases and absorbance at 440 nm increases (Figure 4.11(b)). This behavior is assigned to vibrational cooling of

the  $S_1$  states losing heat to the solvent.<sup>151</sup> Within the next three nanoseconds, bands at 340, 420, and 550 (shoulder) nm decrease, which is assigned to decay of 2-naphthol's  $S_1$  state (Figure 4.11(c)). The triplet state of the parent molecule is observed by a band decaying more slowly at 440 nm than the bands at 340 or 560 nm, which are indicative of  $S_1$  decay (Figure 4.11(d)).<sup>194</sup>

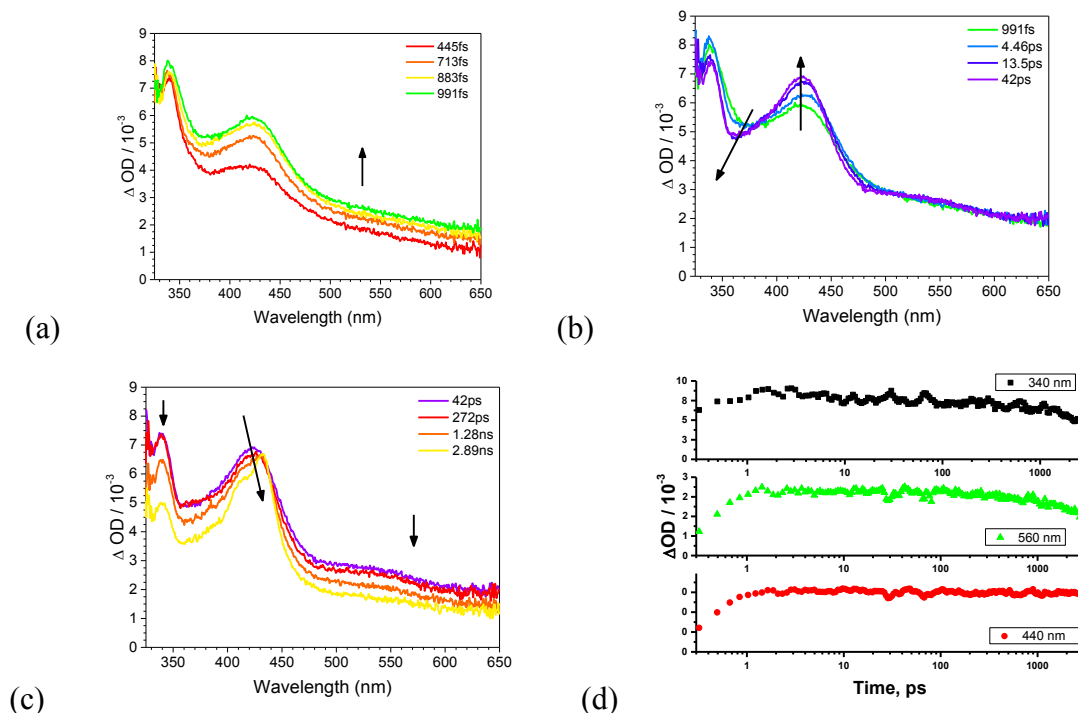


Figure 4.11. fs-TA of 2-naphthol in aerobic MeCN following excitation (a, b, and c;  $\lambda_{\text{exc}} = 267$  nm). Kinetics at 340, 560, and 440 nm are shown in (d).

Following excitation in 5:95 v/v MeCN to 5.0 mM phosphate buffer (pH 7.0; Figure 4.12), 2-naphthol produced a broadly absorbing species with maximum at 435 nm within the first 500 fs (Figure 4.12(a)). This process is assigned to population of an  $S_1$  state. Noticeably, the band previously observed at 340 nm (440 nm shoulder) upon excitation of 2-naphthol in MeCN is absent. Instead, the  $S_1$  state has a red-shift to  $\lambda_{\text{max}} = 440$  nm (broadly absorbing; Figure 4.13(a)). This implies that excitation in this solvent allows greater electron delocalization to the aromatic structure, enabling increased conjugation compared with the excited state species formed in MeCN. Within the next 320 ps, the band shows an overall absorbance decrease (Figure 4.12(b)). Over the next 3 ns, the overall decrease continues (Figure 4.12(c)). The band assigned to 2-naphthol's triplet state (as observed in MeCN,  $\lambda_{\text{max}} = 440$  nm,  $\Delta\text{OD} \sim 7 \times 10^{-3}$ ) is absent following excitation in 5:95 v/v MeCN to 5.0 mM phosphate buffer (pH 7.0; Figure 4.13(b)). The triplet state

of 2-naphtholate, which has an absorption band with  $\lambda_{\text{max}} = 460$  nm (observed in liquid paraffin), is not observed (Figure 4.12(c)).<sup>250</sup> ESPT occurs from a typical photoacid on the order of  $10^{10} \text{ M}^{-1}\text{s}^{-1}$ .<sup>251,252</sup> Based on this and the observed red-shifted absorption, we assign the broadly absorbing species at 440 nm that decays on the ps timescale to that of 2-naphtholate's  $S_1$  state (Figure 4.12(d)).

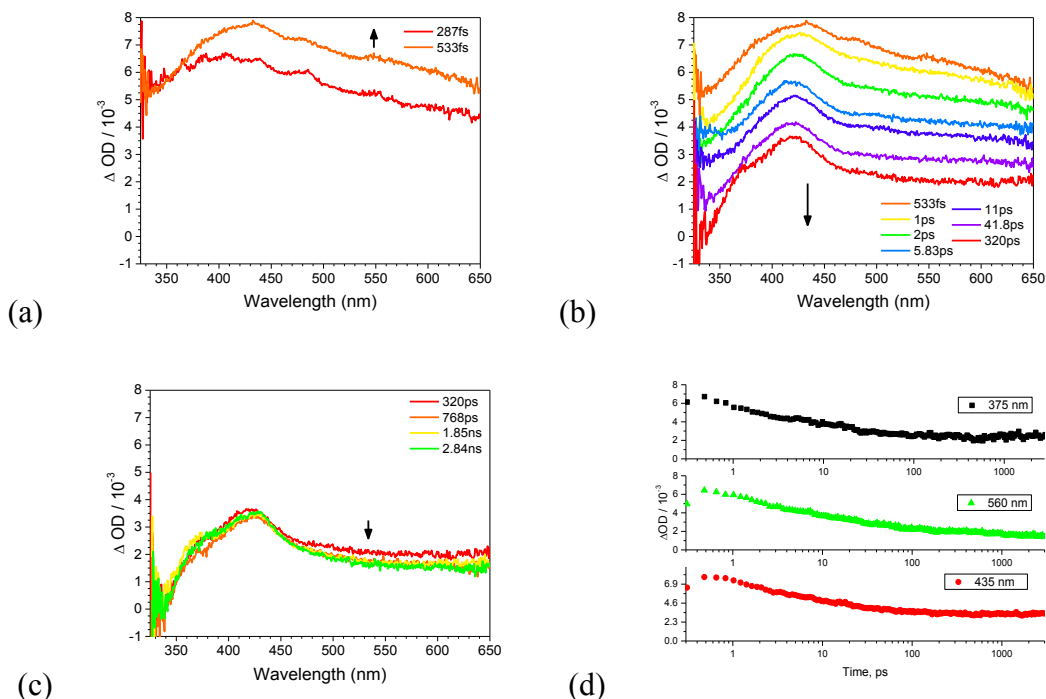


Figure 4.12. fs-TA of 2-naphthol in aerobic 5:95 v/v MeCN to 5.0 mM phosphate buffer solution (pH 7.0) following excitation (a, b, and c;  $\lambda_{\text{exc}} = 267$  nm). Kinetics at 375, 560, and 435 nm are shown in (d).

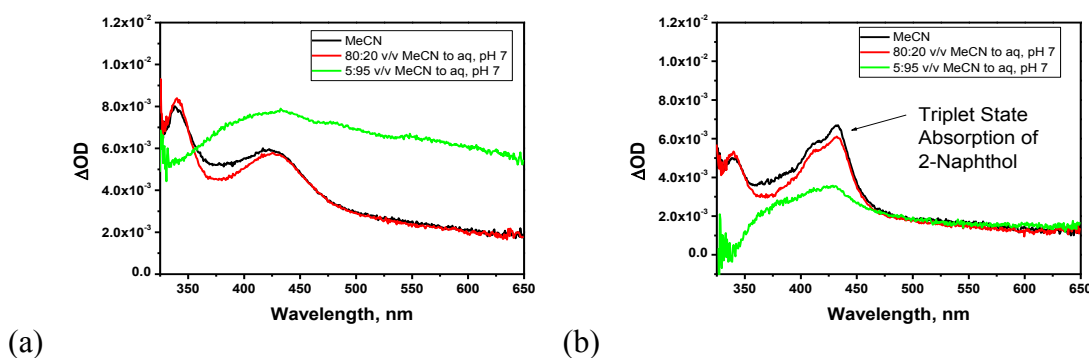


Figure 4.13. fs-TA of 2-naphthol in MeCN, 80:20 v/v, and 5:95 v/v MeCN to 5.0 mM phosphate buffer solution, pH 7.0 following excitation (a)  $\sim 1$  ps and (b)  $\sim 3$  ns after excitation.

Figure 4.14 shows the fs-TA spectra for 2-naphthol in 80:20 v/v MeCN to 5.0 mM phosphate buffer (pH 7.0). The spectroscopic features of 2-naphthol upon excitation are nearly identical to those observed in MeCN (Figure 4.11) rather than in 5:95 v/v MeCN

to 5.0 mM phosphate buffer solution (pH 7.0; Figure 4.12). A comparison between the three sets of data is made in Figure 4.13. These experiments support the observations made in the fluorescence experiments in that 2-naphthol does not readily undergo PTTS in 80:20 v/v MeCN to 5.0 mM phosphate buffer (pH 7.0). Based on these findings, it is unlikely that the HNM-protected HNO donors can undergo PTTS in 80:20 v/v MeCN to 5.0 mM phosphate buffer (pH 7.0) as the two structures have similar  $pK_a^*$  values (Section 4.3.1). Therefore, photorelease of HNO is unlikely to proceed via a mechanism involving a QM intermediate, as the naphtholic OH does not readily transfer to solvent in low aqueous concentrations in MeCN (Scheme 4.1, Pathway (a)).

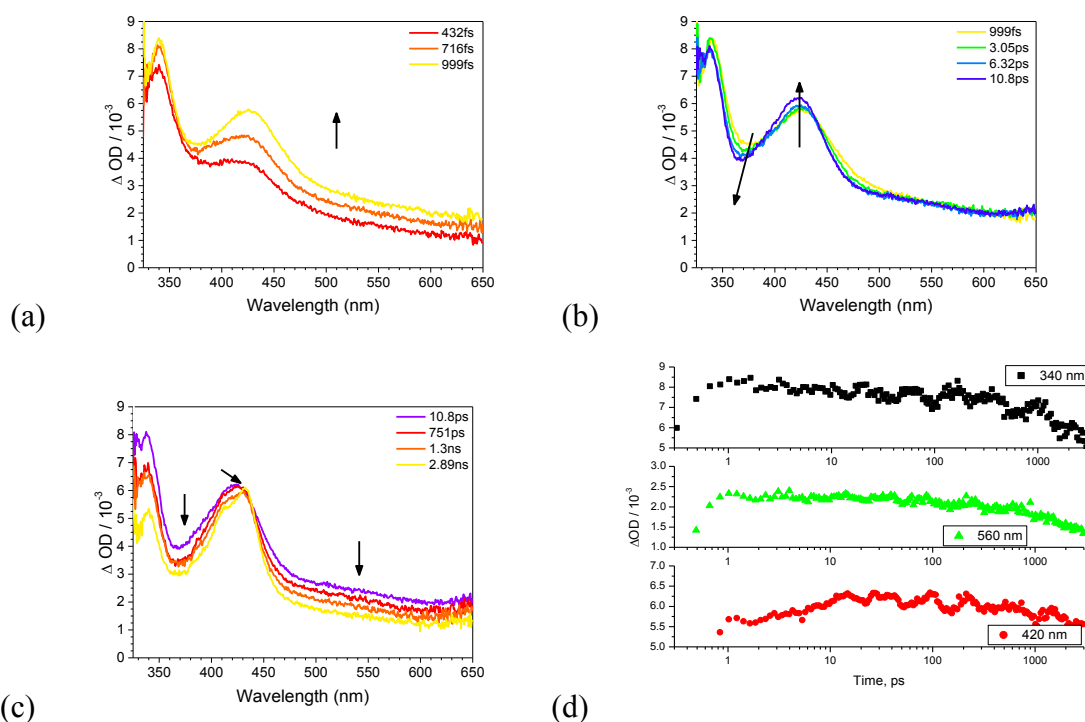


Figure 4.14. fs-TA of 2-naphthol in aerobic 80:20 v/v MeCN to 5.0 mM phosphate buffer solution (pH 7.0) following excitation (a, b, and c;  $\lambda_{\text{exc}} = 267$  nm). Kinetics at 340, 560, and 420 nm are shown in (d).

#### 4.5 INVESTIGATION OF THE RELEASE OF $^1\text{HNO}$ VERSUS $^1\text{NO}^-$ FROM EXCITATION OF DONOR **4**

It remains unknown whether or not the leaving group on donor **4a** undergoes any ESPTs. Previous work from our research group on the structural analogue of donor **4**, namely donor **1**, indicated that the N on the leaving group could serve as a basic site upon excitation of the molecule (investigated further in Chapter 5).<sup>23</sup> Hence, it is possible that

donor **4a** undergoes ESPT to the N atom upon excitation (Scheme 4.2). In this case, HNO would be directly released from excitation of donor **4**. Alternatively, donor **4** could release  $^1\text{NO}^-$  from **4a** as an intermediate species.

To explore the role of water in HNO generation from excitation of **4**, photolysis of donor **4** was performed in aprotic solvent (where ESPT cannot occur) with varying ratios of **4a** to **4b**. To achieve this, carboxylate salts were added in small molar equivalents (0-5 mol. equiv.) in aprotic solvent. Select carboxylate salts were used with conjugate acid  $pK_a$  values higher than the NH on the leaving group ( $pK_a = 4.39 \pm 0.06$ ) in order to deprotonate the N atom. To provide evidence of **4a** formation, the  $^1\text{H}$  NMR spectra of **4a**, **4b**, and **4c** in 80:20 v/v  $\text{CD}_3\text{CN}$  to aqueous (5.0 mM phosphate buffer, pH 7.0, 0.1 M HCl, and 0.1 M NaOH) were compared to **4b** in  $\text{CD}_3\text{CN}$  upon addition of acetate ( $\text{CH}_3\text{COOH}$ ;  $pK_a$  4.76). Figure 4.15 shows that the methylene carbon shifts from  $\delta$  5.04 ppm to 4.75 ppm and H5 experiences a downfield shift from 7.75 ppm to 7.69 ppm upon deprotonation of the NH of **4b** to give **4a** in 20% by vol. aqueous in MeCN. Similar shifts were observed for **4b** in  $\text{CD}_3\text{CN}$  upon addition of acetate: the methylene shifted from  $\delta$  5.07 to 4.65 ppm and H5 from 7.79 to 7.64 ppm upon addition of  $\sim 10$  mol. equiv. of acetate (Figure 4.16).

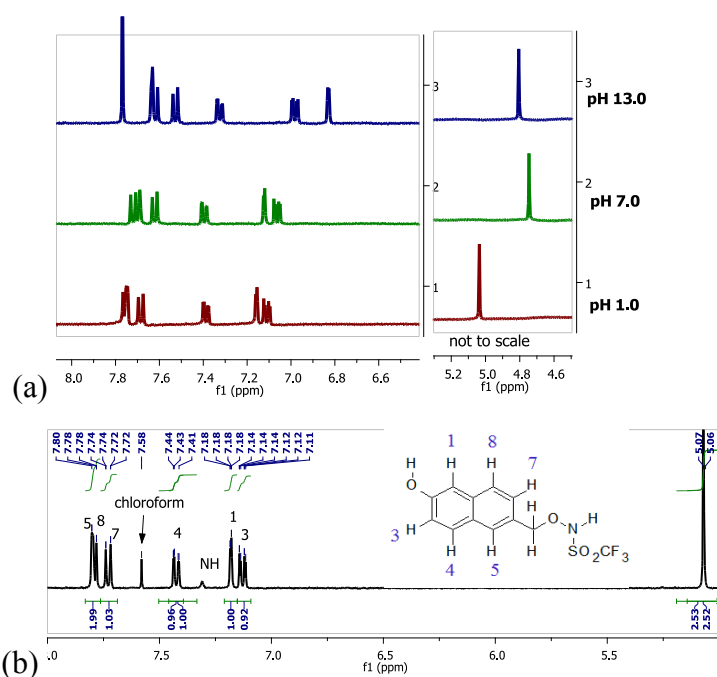


Figure 4.15. (a)  $^1\text{H}$  NMR spectra of donor **4** (1.00 mM) in aerobic 20% by vol. buffer in MeCN, where the aqueous component is 0.1 M HCl, 5.0 mM phosphate buffer (pH 7.0), or 0.1 M NaOH. Residual chloroform is observed at 7.63 ppm. (b)  $^1\text{H}$  NMR spectrum of donor **4a** in  $\text{CD}_3\text{CN}$  with peak assignments.  $^1\text{H}$  NMR peaks are assigned as depicted in the inset. The peak at  $\delta$  5.07 ppm corresponds to the methylene protons.

The spectrum of **4c** in 80:20 v/v CD<sub>3</sub>CN to 0.1 M NaOH (Figure 4.15) clearly results in different chemical shifts than observed for **4b** in CD<sub>3</sub>CN upon addition of acetate. Hence, this indicates that **4c** is not formed from **4b** in CD<sub>3</sub>CN upon addition of acetate. Formation of acetic acid (1.96 ppm in CD<sub>3</sub>CN) could not be observed due to overlap from the residual solvent (1.94 ppm).<sup>253</sup> The solvent peak ( $\delta$  1.94 ppm) overlapped with the acetate peak and the solubility of potassium acetate is poor; therefore, the mol. equiv. is an estimate only (approximately 0-10 mol. equiv.).

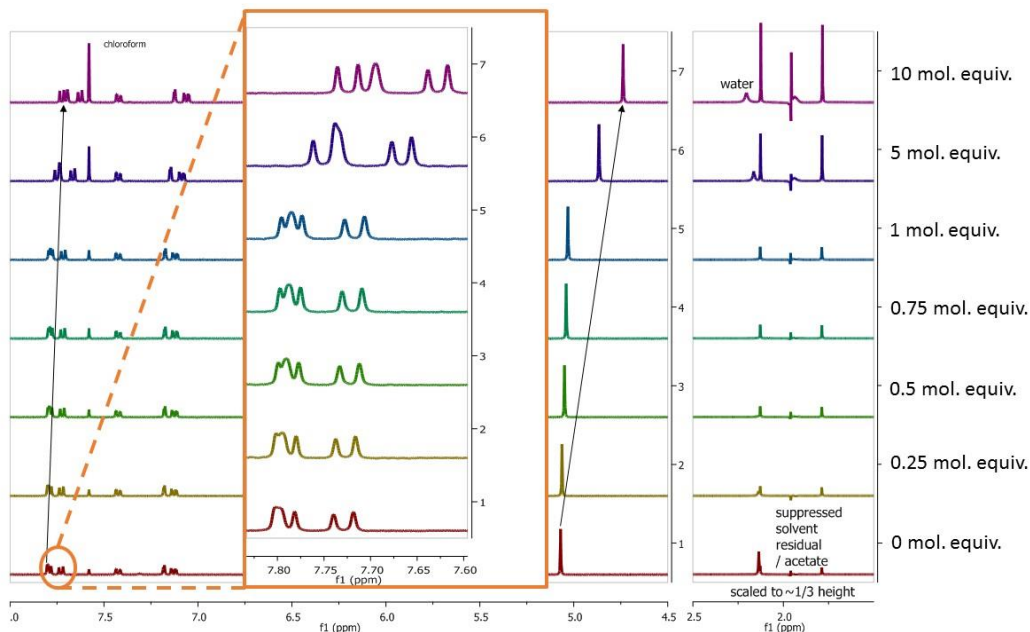


Figure 4.16. <sup>1</sup>H NMR spectra of donor **4** (1.00 mM) upon approximate mol. Equiv. additions of potassium acetate in CD<sub>3</sub>CN. Spectra referenced to chloroform ( $\delta$  7.58 ppm). Note: The solvent peak ( $\delta$  1.94 ppm) overlapped with the acetate peak and the solubility of potassium acetate is poor; therefore, the mol. equiv. is approximated (approximately 0-10 mol. equiv.). The <sup>1</sup>H NMR spectra clearly show a shift in aromatic (H5 proton:  $\delta$  7.79 to 7.64 ppm) and methylene ( $\delta$  5.07 to 4.65 ppm) protons.

Due to the issues associated with potassium acetate solubility in CD<sub>3</sub>CN, the addition of carboxylate salt to **4b** was further investigated in d<sub>6</sub>-DMSO. Upon the addition of acetate to **4b** in d<sub>6</sub>-DMSO, formation of acetic acid (1.91 ppm) is observed (Figure 4.17).

The stoichiometry required to achieve deprotonation of the NH was investigated by lithium acetate additions to donor **4b** (1.00 mM) in d<sub>6</sub>-DMSO using <sup>1</sup>H NMR spectroscopy. Small amounts (0-3.75 mol equiv.) of sodium acetate and 3-(trimethylsilyl)propionic-2,2,3,3-d<sub>4</sub> acid sodium salt (TSP) were added to <sup>1</sup>H NMR samples of **4b** in d<sub>6</sub>-DMSO (Figure 4.17; Figure 4.18). Acetic acid (CH<sub>3</sub>COOH; pK<sub>a</sub> = 4.76) and 3-(trimethylsilyl)propanoic acid (CH<sub>3</sub>)<sub>3</sub>SiCH<sub>2</sub>CH<sub>2</sub>COO(H) pK<sub>a</sub> = 4.98) have pK<sub>a</sub>

values higher than the NH on the leaving group ( $pK_a = 4.39 \pm 0.06$ ). Addition of acetate to **4b** in  $d_6$ -DMSO changed the  $^1\text{H}$  NMR shift of the methylene proton and suggested that 1 mol. equiv. acetate is required to form **4a** and the corresponding carboxylic acid (Figure 4.19). The addition of TSP in place of acetate achieved the same degree of spectral shift changes in the  $^1\text{H}$  NMR spectra (by analysis of methylene protons; Figure 4.19).

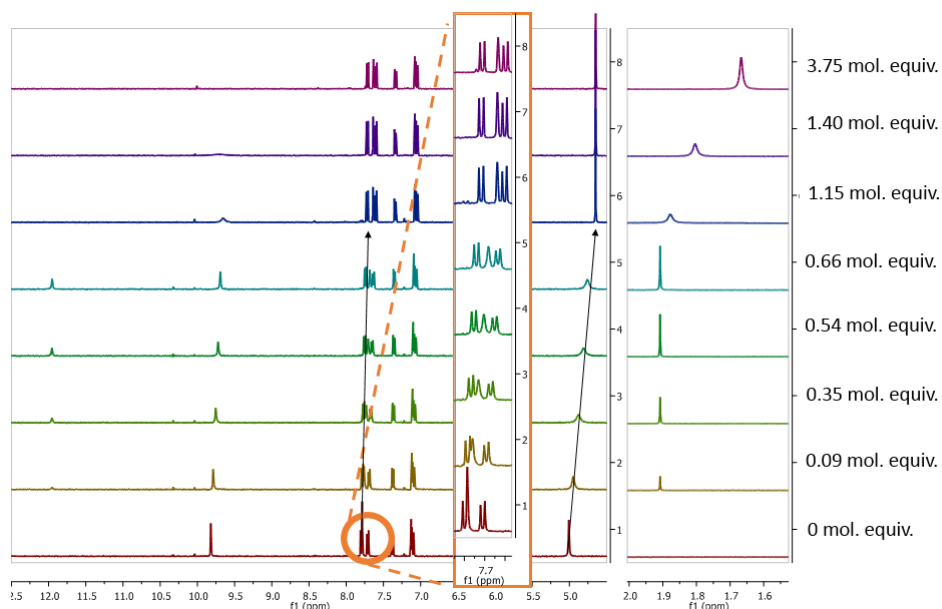


Figure 4.17.  $^1\text{H}$  NMR spectra of donor **4** (1.00 mM) upon additions of carboxylate salt (lithium acetate) in  $d_6$ -DMSO (0.03% TMS by manufacturer).

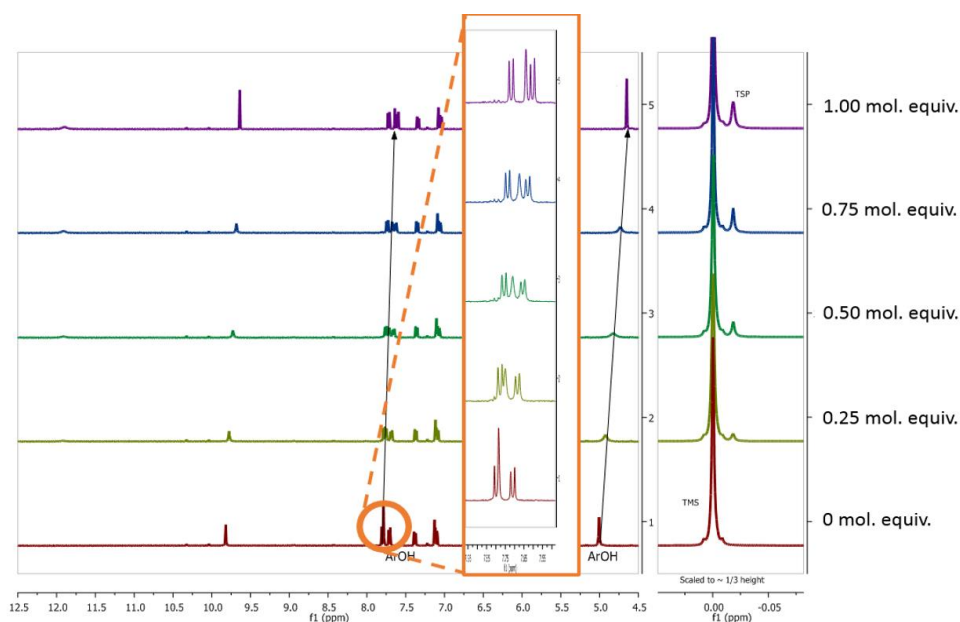


Figure 4.18.  $^1\text{H}$  NMR spectra of donor **4** (1.00 mM) upon additions of carboxylate salt (TSP) in  $d_6$ -DMSO (0.03% TMS by manufacturer).

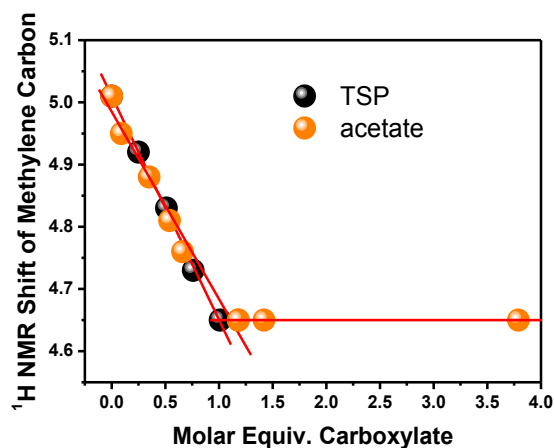


Figure 4.19. Molar equivalents of TSP and acetate to donor **4** (1.00 mM) in  $d_6$ -DMSO (0.03% TMS by manufacturer) versus methylene carbon shift.

To confirm that the carboxylate salt was interacting with the leaving group, the interactions between a series of naphtholic compounds and carboxylates salts were investigated.  $^1\text{H}$  NMR spectra were recorded of the naphtholic compounds with and without addition of carboxylate salts. Two naphthols without substitution were selected: 2-naphthol and 1-naphthol (Figure 4.20). Two diols, diol **7** and diol **5**, were selected for comparison purposes as they have a leaving group that is significantly less acidic (Figure 4.20). Finally, donor **4** and its structural analogue **1** were selected to probe the effect of carboxylate salt addition on the HNM-protected HNO donors. 2-Naphthol showed upfield shifts of the H5, H4, H8, H7, and H6 protons upon addition of carboxylate indicating an increase of electron density, whereas a downfield shift is observed on H3 indicating a decrease of electron density (Figure 4.21). Addition of acetate shifts 1-naphthol's H8, H3, and H6 upfield (Figure 4.22). Diol **5** showed upfield shifts on all protons except the methylene protons (Figure 4.23). Like 2-naphthol, diol **7** showed upfield shifts of H8 and a downfield shift was observed on H3 (Figure 4.24). However, donor **1** and donor **4** exhibited a distinctly different pattern as all of the aromatic protons experienced downfield shifts and the methylene carbons also experienced a downfield shift (Figure 4.25; Figure 4.26). Figure 4.20 summarizes the movement of electron density upon addition of acetate to naphtholic compounds as indicated by upfield or downfield shifts observed via  $^1\text{H}$  NMR spectroscopy. These results clearly indicate that addition of carboxylate salt to donor **1** and donor **4** produces changes in the electronic structure that are attributable to the leaving group. Hence, addition of carboxylate salt to **4b** in aprotic solvent deprotonates the NH on the leaving group.

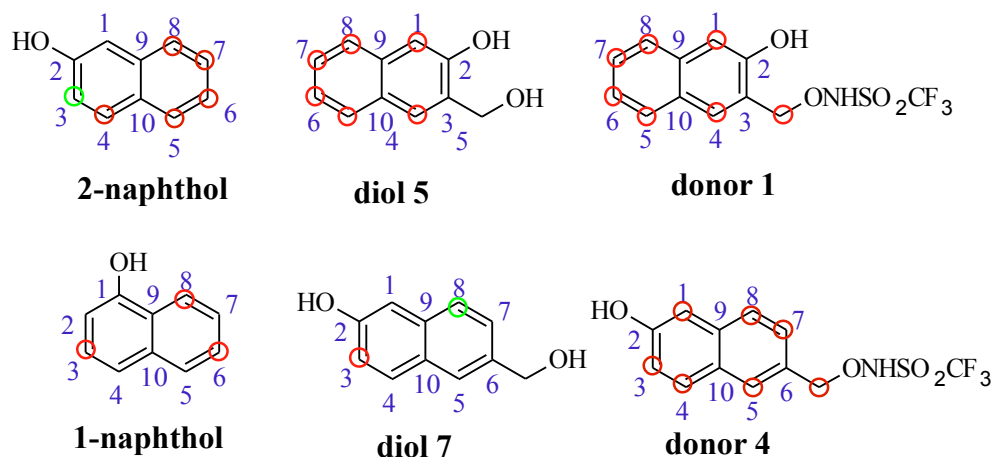


Figure 4.20. Transfer of electron density upon addition of acetate to naphtholic compounds as indicated by <sup>1</sup>H NMR upfield or downfield shifts. Green indicates a loss of electron density and red indicates a gain of electron density.

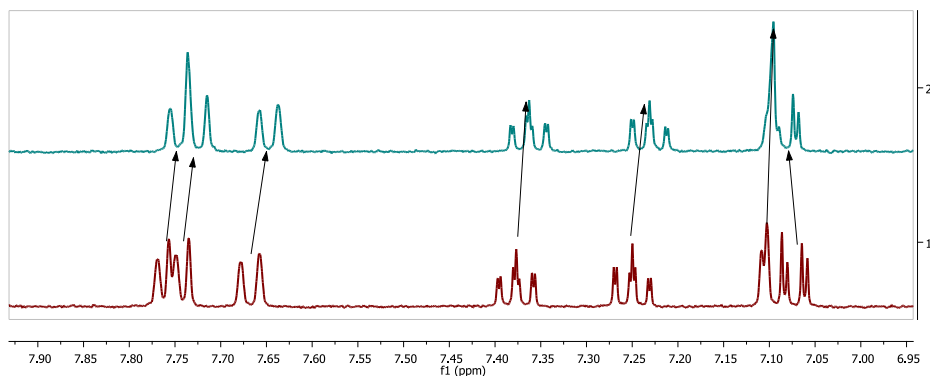


Figure 4.21. <sup>1</sup>H NMR spectra of 2-naphthol (1.00 mM) in d<sub>6</sub>-DMSO (Spectrum 1) and upon addition of lithium acetate (2 mol. equiv.) (Spectrum 2). <sup>1</sup>H NMR shifts: OH:  $\delta$  9.70 ppm (disappears upon acetate addition), H5:  $\delta$  7.77, 7.76 ppm, H4:  $\delta$  7.75, 7.74 ppm, H8:  $\delta$  7.68, 7.66 ppm, H7: 7.40-7.36 ppm, H6:  $\delta$  7.39-7.23 ppm, H1:  $\delta$  7.10 ppm, H3:  $\delta$  7.09 - 7.06 ppm.

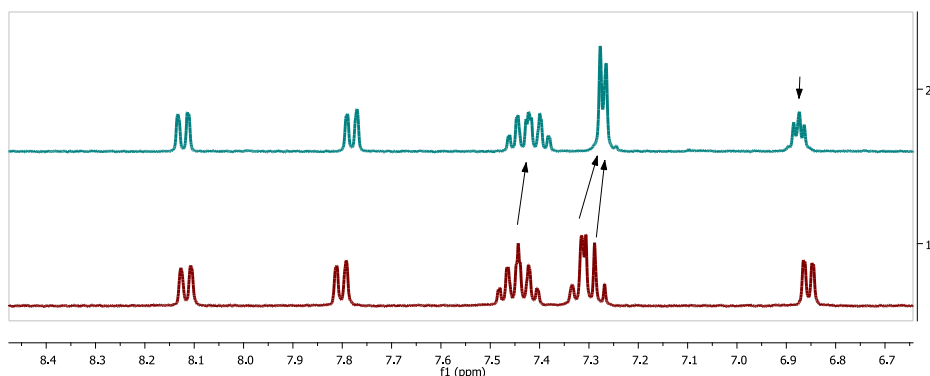


Figure 4.22. <sup>1</sup>H NMR spectra of 1-naphthol (1.00 mM) in d<sub>6</sub>-DMSO (Spectrum 1) and upon addition of potassium acetate (2 mol. equiv.) (Spectrum 2). <sup>1</sup>H NMR shifts: H:  $\delta$  8.13, 8.11 ppm, H4:  $\delta$  7.81, 7.79 ppm, H8:  $\delta$  7.48-7.41 ppm, H3/H6:  $\delta$  7.33-7.27 ppm; H2: 6.87, 6.85 ppm.

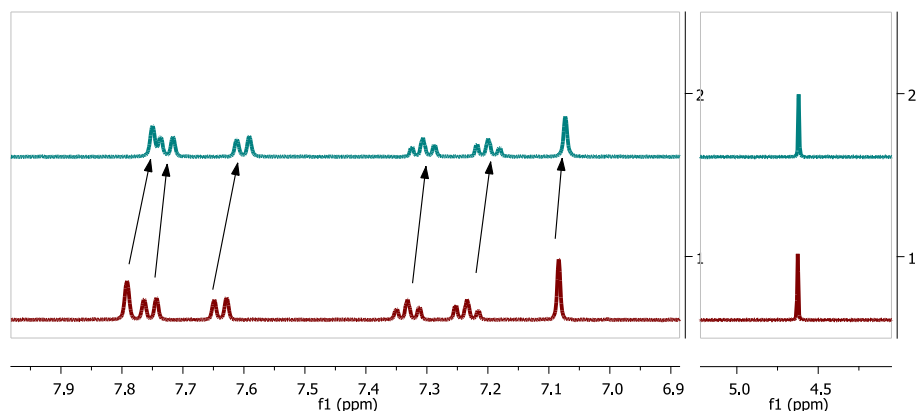


Figure 4.23.  $^1\text{H}$  NMR spectra of diol **5** (1.00 mM) in  $d_6$ -DMSO (Spectrum 1) and upon addition of potassium acetate (2 mol. equiv.) (Spectrum 2).  $^1\text{H}$  NMR shifts: H4:  $\delta$  7.79 ppm, H5:  $\delta$  7.76, 7.74 ppm; H8:  $\delta$  7.65, 7.63 ppm, H6/H7:  $\delta$  7.35-7.22 ppm, H1:  $\delta$  7.08 ppm,  $\text{CH}_2$ :  $\delta$  4.63 ppm.

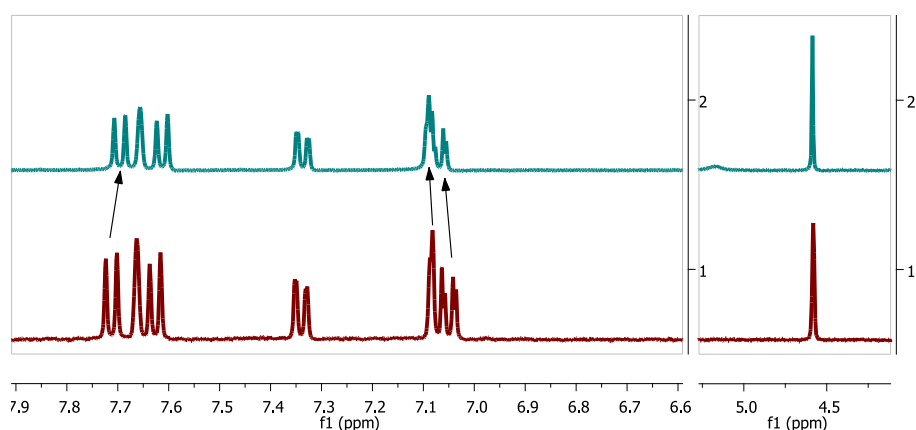


Figure 4.24.  $^1\text{H}$  NMR spectra of diol **7** (1.00 mM) in  $d_6$ -DMSO (Spectrum 1) and upon addition of potassium acetate (2 mol. equiv.) (Spectrum 2).  $^1\text{H}$  NMR shifts: H8:  $\delta$  7.72, 7.70 ppm; H5:  $\delta$  7.66; H7:  $\delta$  7.64, 7.62 ppm, H4:  $\delta$  7.35, 7.33 ppm, H1:  $\delta$  7.08 ppm, H3:  $\delta$  7.06, 7.04 ppm,  $\text{CH}_2$ : 4.58 ppm.

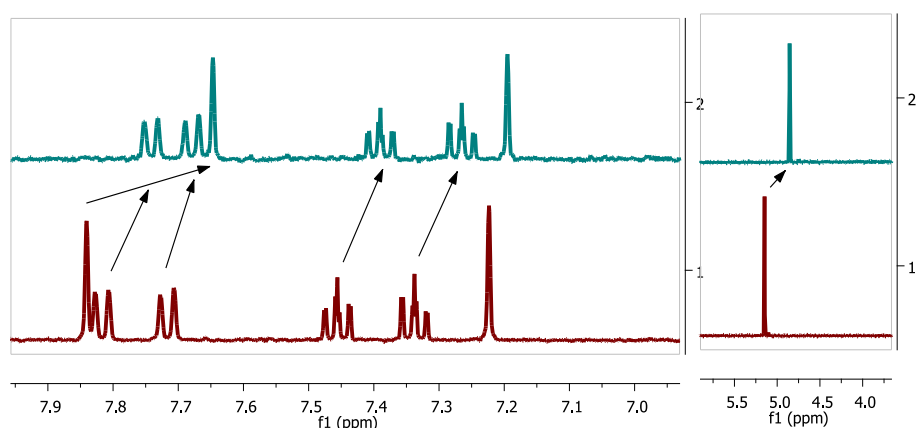


Figure 4.25.  $^1\text{H}$  NMR spectra of donor **1** (1.00 mM) in  $\text{CD}_3\text{CN}$  (Spectrum 1) and upon addition of TSP (1.6 mol. equiv.) (Spectrum 2).  $^1\text{H}$  NMR shifts: H4:  $\delta$  7.84 ppm, H5:  $\delta$  7.83, 7.81 ppm; H8:  $\delta$  7.73, 7.71 ppm, H6/H7:  $\delta$  7.46-7.34 ppm, H1:  $\delta$  7.22 ppm,  $\text{CH}_2$ :  $\delta$  5.15 ppm.

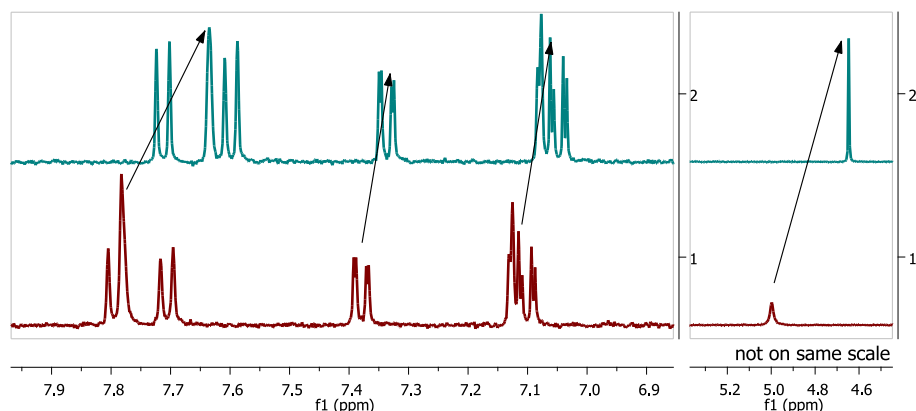


Figure 4.26.  $^1\text{H}$  NMR spectra of donor **4** (1.00 mM) in  $d_6$ -DMSO (Spectrum 1) and upon addition of lithium acetate (2 mol. equiv.) (Spectrum 2).  $^1\text{H}$  NMR shifts: OH: 9.81 ppm (disappears upon acetate addition); H8:  $\delta$  7.80, 7.78 ppm; H5:  $\delta$  7.78 ppm; H7:  $\delta$  7.72, 7.70 ppm; H4:  $\delta$  7.39-7.37 ppm; H1:  $\delta$  7.13 ppm; H3:  $\delta$  7.11-7.09 ppm;  $\text{CH}_2$ :  $\delta$  5.00 ppm.

The emission from **4a** versus **4b** in an aprotic solvent was next investigated. Figure 4.27(a) shows that addition of carboxylate salt (lithium acetate) quenched the fluorescence of donor **4** in DMSO. Upon addition of an excess of acetate (25 mol equiv), emission from the conjugated base ( $\lambda_{\text{max}} = 452$  nm) is observed; others have observed that addition of excess carboxylate salt enables ESPT from the photoacidic OH to the carboxylate to occur.<sup>254,255</sup> Maximum fluorescence quenching was observed upon addition of  $\sim 1:1$  donor **4** to lithium acetate (Figure 4.27(b)). Likewise, addition of a small excess of TSP (0-2.0 mol. equiv.) quenched fluorescence from the parent structure ( $\lambda_{\text{max}} = 360$  nm) without a concomitant increase from its conjugate base ( $\lambda_{\text{max}} = 453$  nm; Figure 4.28(a)). The Stern-Volmer plot indicates that a maximum fluorescence quenching is reached at near stoichiometric equivalents ( $\sim 0.8$  mol equiv and quenched by over 10-fold; Figure 4.28(b)). Notably, formation of **4a** as observed by  $^1\text{H}$  NMR spectroscopy was also observed upon addition of 1 mol. equiv. acetate (Figure 4.19). Therefore, the observed

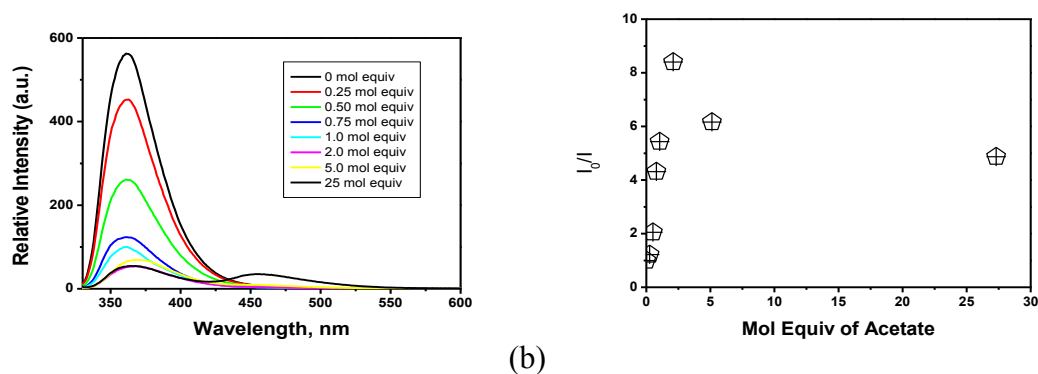


Figure 4.27. (a) Emission of donor **4** ( $\mu\text{M}$ ) and lithium acetate in DMSO. (b) Stern-Volmer quenching plot of **4** by lithium acetate in dry DMSO ( $\lambda_{\text{exc}} = 315$  nm).

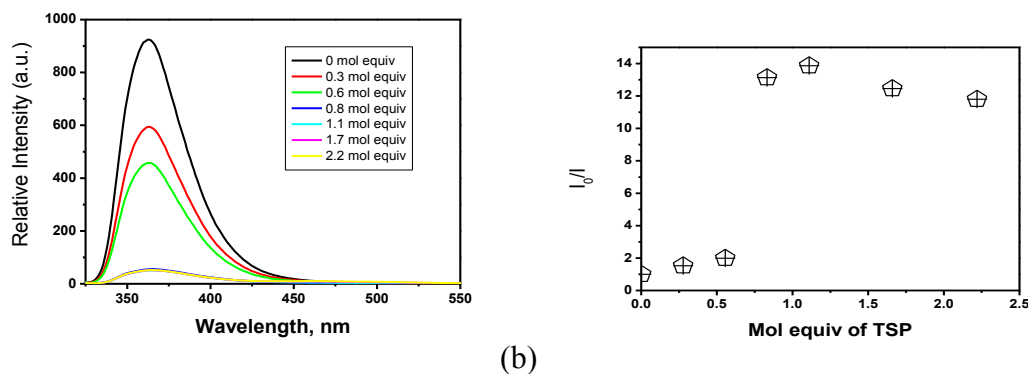


Figure 4.28. (a) Fluorescence of **4** ( $\mu\text{M}$ ) and TSP in dry DMSO. (b) Stern-Volmer quenching plot of **4** by TSP in dry DMSO ( $\lambda_{\text{exc}} = 315 \text{ nm}$ ).

fluorescence quenching upon formation of **4a** in this experiment indicates that a process competitive to fluorescence proceeds from excitation of **4a**.

Next, photolysis of **4a** versus **4b** was investigated in aprotic conditions. Two sets of irradiated samples of **4** (1.00 mM) were prepared in  $d_6$ -DMSO, one with 0-1.00 mol. equiv. of acetate and the second with 0-1.00 mol. equiv. of TSP. After 5 minutes of irradiation, the  $^{19}\text{F}$  NMR spectra were recorded (Figure 4.29 and Figure 4.30). The desired pathway (indicated by  $\text{CF}_3\text{SO}_2^-$ ) increased with increasing concentrations of either acetate or TSP. To compare their efficiencies, the percent yields of pathway 1 (Scheme 4.3; indicated by  $\text{CF}_3\text{SO}_2^-$ ) were plotted as a function of the concentration of carboxylate (calculated by  $^1\text{H}$  NMR integration; Figure 4.31). For both datasets, a linear relationship was observed, with  $\sim 100\%$   $\text{CF}_3\text{SO}_2^-$  observed at 1 mol. equiv. (Figure 4.31). It was observed that addition of one mol. equiv. of carboxylate salt was required to fully convert **4b** to **4a** (Figure 4.19). Hence, the varying ratios of pathway 1 to pathway 2 (Scheme 4.3) directly reflect the ratio of **4b** to **4a** (Figure 4.31). Importantly, this experiment shows that HNO photorelease proceeds from excitation of **4a**. Furthermore, **4a** does not undergo ESPT as only one molar equivalent of acid is present in an otherwise aprotic solution. This indicates that **4a** releases  $^1\text{NO}^-$  upon excitation.

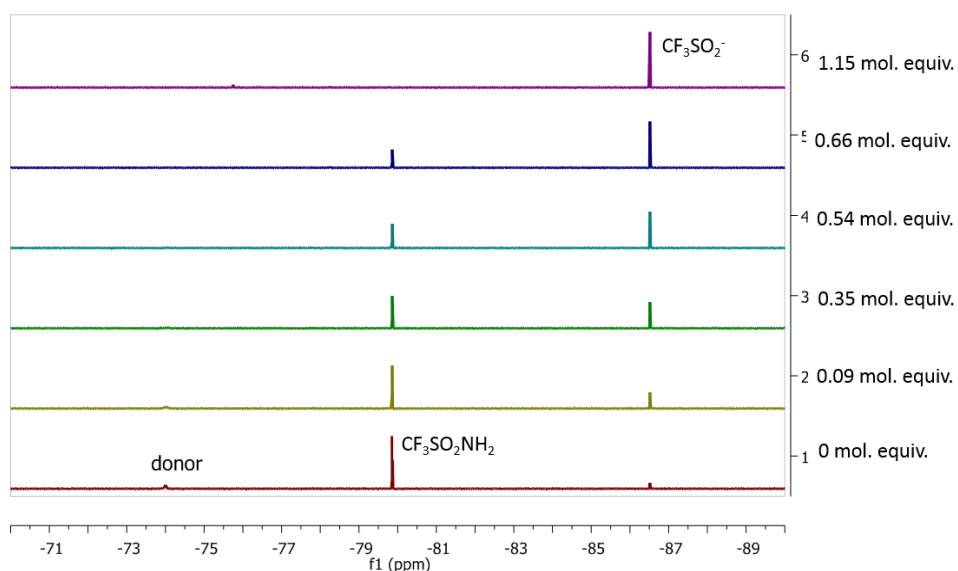


Figure 4.29.  $^{19}\text{F}$  NMR spectra of **4** (1.00 mM) after photolysis for 5 min (Rayonet photoreactor, 8 x 350 nm bulbs, 4 W) in  $d_6$ -DMSO (0.03% TMS by manufacturer) with 0-1.15 mol. equiv. of lithium acetate as determined by  $^1\text{H}$  NMR integration.

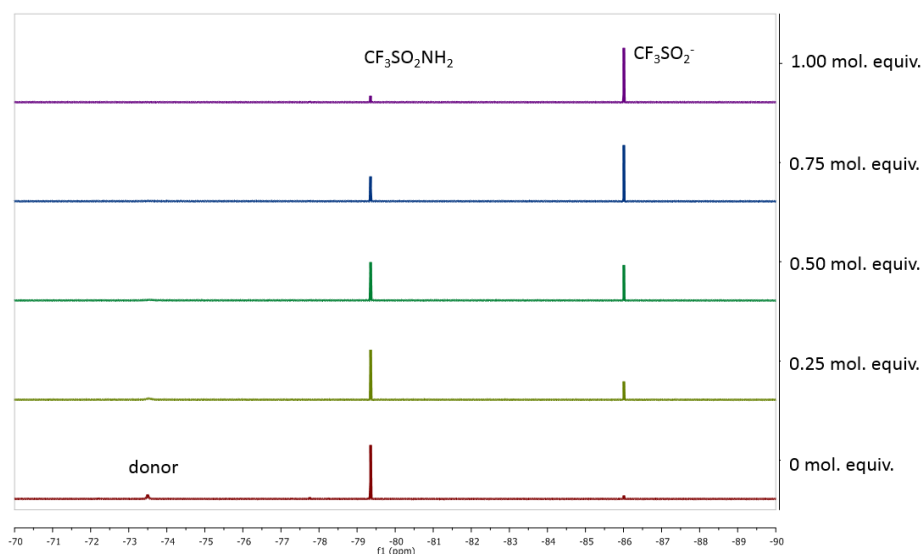


Figure 4.30.  $^{19}\text{F}$  NMR spectra of **4** (1.00 mM) after photolysis for 5 min (Rayonet photoreactor, 8 x 350 nm bulbs, 4 W) in  $d_6$ -DMSO (0.03% TMS by manufacturer) with 0-1.00 mol. equiv. of TSP as determined by  $^1\text{H}$  NMR integration.

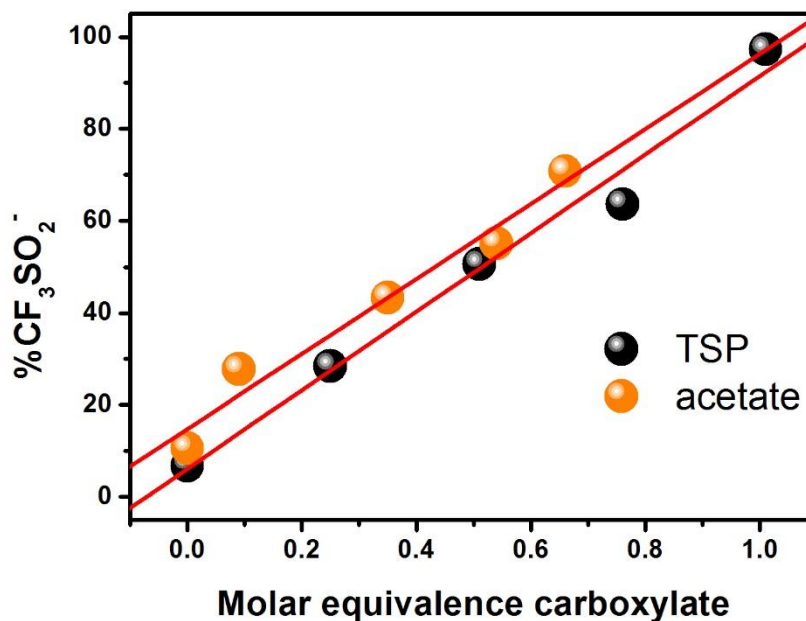


Figure 4.31. Mol. equiv. of acetate or TSP to **4** (1.00 mM) in  $d_6$ -DMSO (0.03% TMS by manufacturer) versus HNO photorelease (indicated by %CF<sub>3</sub>SO<sub>2</sub><sup>-</sup>) to N-O bond cleavage (indicated by CF<sub>3</sub>SO<sub>2</sub>NH<sub>2</sub>) after photolysis for 5 min (Rayonet photoreactor, 8 x 350 nm bulbs, 4 W).

#### 4.6 INVESTIGATION OF THE RATE OF <sup>1</sup>NO<sup>-</sup> RELEASE FROM EXCITATION OF **4A** USING FEMTOSECOND TRANSIENT ABSORPTION (FS-TA)

Control experiments with model compound 2-naphthol suggested that PTTS does not occur in partially aqueous conditions for the 6,2-HNM photocage (Section 4.3). Hence, HNO photorelease likely does not occur via formation of a QM (Scheme 4.1, Pathway (a)). (6-Hydroxynaphthalen-2-yl)methyl (6,2-HNM) protected molecules and structurally related compounds can undergo bond heterolysis of the ArCH<sub>2</sub>-X bond, yielding a (6-hydroxynaphthalen-2-yl)methyl cation **9** and anion pair (Scheme 4.1, Pathway (b)).<sup>206-208</sup> Furthermore, the results in Section 4.2 and Section 4.5 indicate that HNO photorelease is competitive with fluorescence decay. Typically, heterolytic cleavage occurs on the picosecond timescale from the singlet states of molecules.<sup>241</sup> Therefore, femtosecond transient absorption spectroscopy (fs-TA) was used to directly observe the excited states that lead to HNO generation from the HNM-protected HNO donors in aqueous solutions. 2-Naphthol was used to assist with identification of excited states attributable to photophysical or photochemical processes relating to the naphtholic structure (i.e., are not related to loss of leaving group; Section 4.4.3).

The photolysis of donor **4a** was investigated under conditions where HNO photorelease selectivity is maximized in 80:20 v/v MeCN to 5.0 mM phosphate buffer solution (pH 7.0; Figure 4.32). Within the first picosecond, bands at 335 and 430 nm appear, indicating population of an  $S_1$  state (Figure 4.32(a)). The absorption from this  $S_1$  state is spectroscopically different than **4a**'s  $S_1$  state in MeCN (Figure 4.33(a)). The band at 340 nm decreases and the band at 430 nm increases from  $\sim 1$  to 56 ps (Figure 4.32(b)). This process is similar to 2-naphthol's behavior (Figure 4.14). However, the spectral shape is significantly different in the 390-490 nm region to the absorption of the excited state species observed upon excitation of 2-naphthol in the same solvent condition (Figure 4.13) and upon excitation of **4b** in MeCN (where HNO release does not occur; Figure 4.33(a)). Therefore, this process is assigned to vibrational cooling resulting in a spectroscopically different transient species (Figure 4.32(b)). At this short time frame, it is likely that the non-radiative relaxation or fluorescence decay from **4a**'s  $S_1$  state has not yet occurred. This implies that the novel species is formed directly from **4a**'s  $S_1$  state. We tentatively assign this to an excited state species formed after C-O bond cleavage resulting in carbocation **9**. Over the next 3 ns, an overall absorbance decrease is seen, indicating

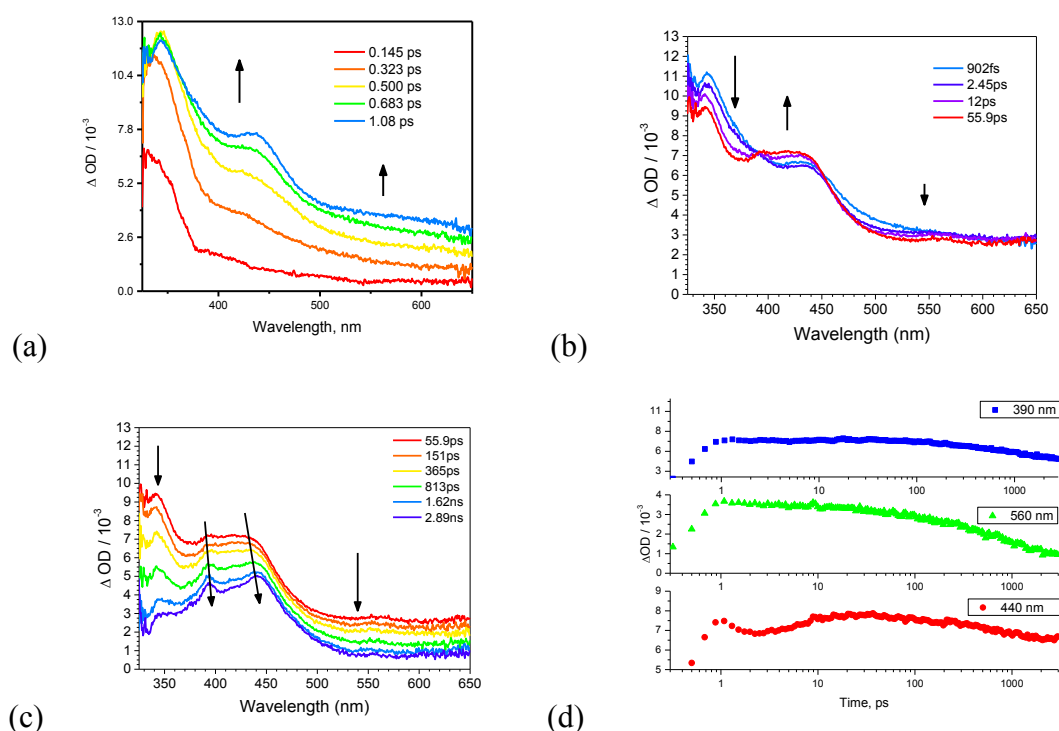


Figure 4.32. fs-TA of donor **4a** in aerobic 80:20 v/v MeCN to 5.0 mM phosphate buffer solution (pH 7.0) following excitation (a, b, and c;  $\lambda_{exc} = 267$  nm). Kinetics at 390, 560, and 440 nm are shown in (d).

decay of an  $S_1$  state (Figure 4.32(c)). Comparison to 2-naphthol's fs-TA spectrum in Figure 4.14 indicates that remaining intact **4a** undergoes intersystem crossing (ISC) to a triplet state of the parent molecule (440 nm; Figure 4.32(c)). Interestingly, a slowly decaying species at 390 nm is observed (Figure 4.33). The rate of decay suggests that the unassigned species is undergoing ISC into a triplet state (e.g. it decays more slowly than the band at 550 nm, which is indicative of  $S_1$  decay; Figure 4.32(d)). The species absorbing at 390 nm is unique to **4a** under conditions where HNO is generated. Further investigation is required to identify the species.

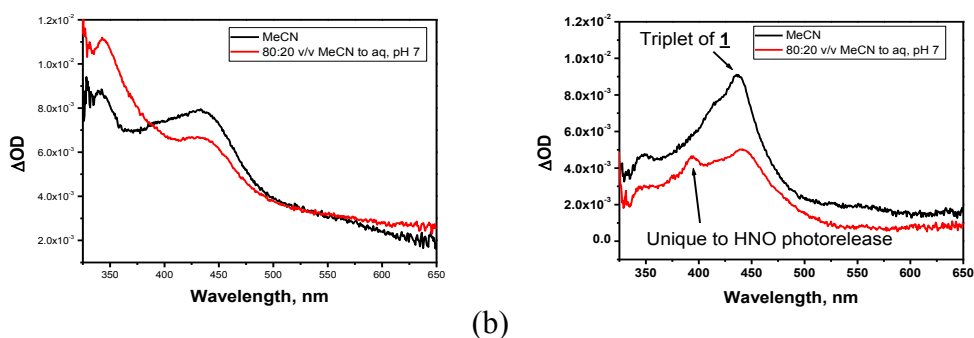


Figure 4.33. fs-TA of donor **4b** in MeCN and donor **4a** in 80:20 v/v MeCN to 5.0 mM phosphate buffer solution, pH 7.0 following (a)  $\sim 1$  ps and (b)  $\sim 3$  ns after excitation.

#### 4.7 CHARACTERIZATION OF UNIQUE TRIPLET SPECIES OBSERVED IN PHOTOLYSIS OF **4** USING NANOSECOND LASER FLASH PHOTOLYSIS

A unique transient species absorbing at 390 nm was observed following photolysis of **4** in 80:20 v/v MeCN to 5.0 mM phosphate buffer solution, pH 7.0. Interestingly, the fs-TA experiment indicated that a species absorbing at 390 nm undergoes ISC into a triplet state as it decays much more slowly than the singlet excited state species (Figure 4.32(d)). Under this solvent condition, HNO is produced stoichiometrically (see Chapter 3, Section 3.4.3). The fs-TA experiments suggested C-O bond cleavage occurs rapidly upon excitation (with nanoseconds). In order to assign this long-lived species, nanosecond laser flash photolysis (ns-LFP) experiments were performed on donor **4**.

Notably, hydroxyarenes may undergo alternative photochemical processes, including ionization and electron transfer leading to O-H bond homolysis or heterolysis.<sup>122,161,189,190,196,202-205</sup> Typically, ionization and bond homolysis of the phenolic or naphtholic OH occur in low quantum yields but produce highly absorbing transient species. Their identification is a key aspect to the analysis of ns-LFP. Therefore, a series

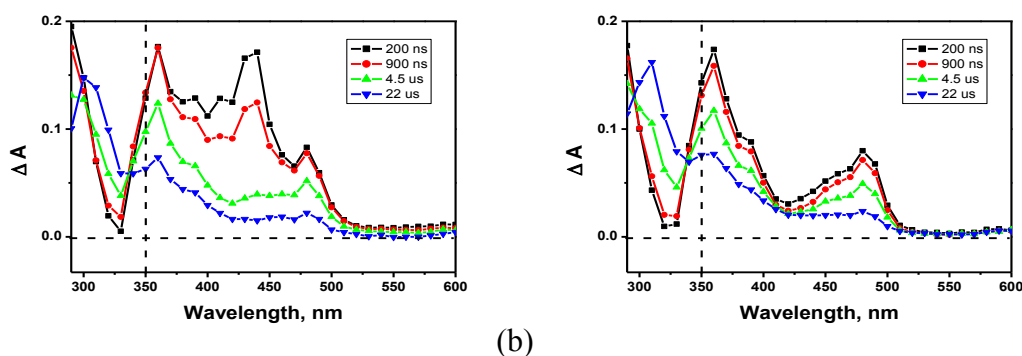


Figure 4.34. Transient absorption spectral changes for 2-naphthol (150  $\mu\text{M}$ ) in (a) anaerobic and (b) oxygenated 80:20 v/v MeCN to 5.0 mM phosphate buffer (pH 7.0;  $\lambda_{\text{exc}} = 266$  nm). The vertical dashed line indicates the approximate wavelength above which the ground state species does not absorb; hence at longer wavelengths, ground state bleach is not a concern.

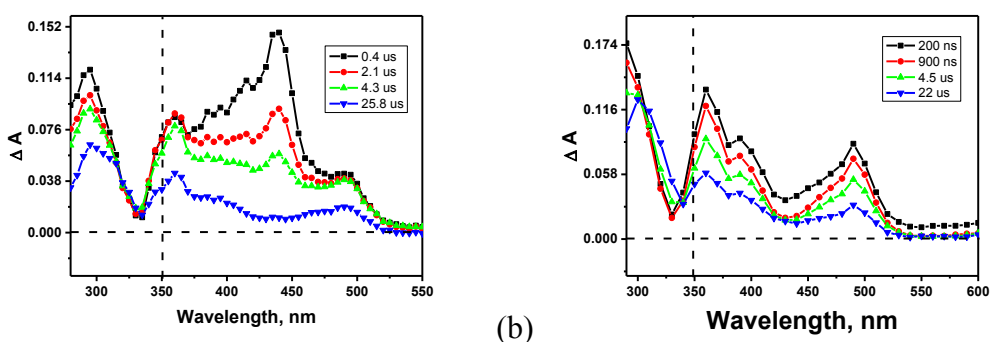


Figure 4.35. Transient absorption spectral changes for diol **7** (150  $\mu\text{M}$ ) in anaerobic and oxygenated 80:20 v/v MeCN to 5.0 mM phosphate buffer (pH 7.0;  $\lambda_{\text{exc}} = 266$  nm). The vertical dashed line indicates the approximate wavelength above which the ground state species does not absorb; hence at longer wavelengths, ground state bleach is not a concern.

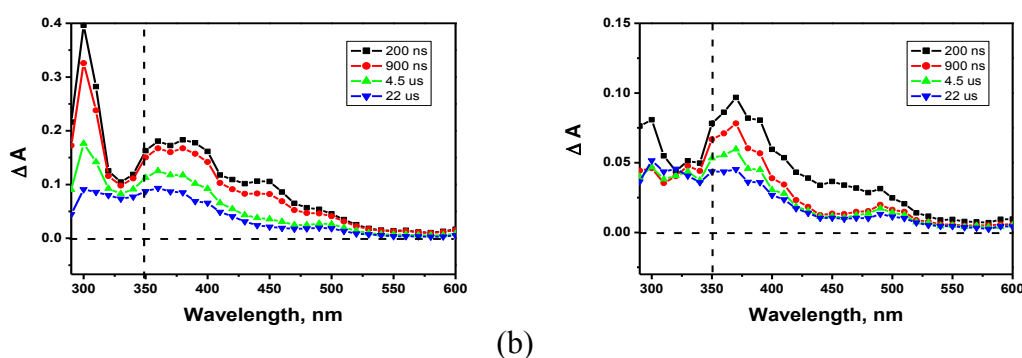


Figure 4.36. Transient absorption spectral changes for donor **4** (150  $\mu\text{M}$ ) in anaerobic and oxygenated 80:20 v/v MeCN to 5.0 mM phosphate buffer (pH 7.0;  $\lambda_{\text{exc}} = 266$  nm). The vertical dashed line indicates the approximate wavelength above which the ground state species does not absorb; hence at longer wavelengths, ground state bleach is not a concern.

of control experiments were performed to account for any interfering processes. 2-

Naphthol was selected as a control compound because it does not contain a leaving group and diol **7** was selected because it contains a poor leaving group.<sup>124</sup> Figure 4.34, Figure 4.35, and Figure 4.36 show transient absorption spectra built from ns-LFP data at selected wavelengths (method described in Chapter 2, Section 2.5.1) taken in anaerobic and oxygenated 80:20 v/v MeCN to 5.0 mM phosphate buffer (pH 7.0). A detailed analysis is presented in the following sections.

#### 4.7.1 Identification of Transient Naphthoxyl Radical Species

Under oxygenated conditions, the absorption of the naphthoxyl radical of 2-naphthol is clearly observed with  $\lambda_{\text{max}}$  at 360 nm and 480 nm (Figure 4.34(b)). The absorption spectra for 2-NpO<sup>•</sup> was determined from pulse radiolysis of an N<sub>2</sub>-saturated aqueous solution of NaN<sub>3</sub> and 2-NpOH; the species exhibits two absorption bands with  $\lambda_{\text{max}}$  at 350 (shoulder at 380) and 475 nm.<sup>196</sup> 2-NpO<sup>•</sup> decayed via two consecutive first-order processes ( $k_{\text{obs}} = (2.0 \pm 0.2) \times 10^5 \text{ s}^{-1}$  and  $k_{\text{obs}} = (2.7 \pm 0.1) \times 10^4 \text{ s}^{-1}$ ;  $\tau = 27\text{-}50 \text{ }\mu\text{s}$ ; Table 4.4). Phenoxy or naphthoxyl radicals (ArO<sup>•</sup>) are formed via O—H bond homolysis after  $\pi\text{-}\pi^*$  excitation<sup>202</sup> via a triplet state or from deprotonation of the radical cation (ArOH<sup>•+</sup>) of the parent molecule.<sup>203</sup> However, due to their low quantum yields, the chemistry is relatively ambiguous for phenoxy or naphthoxyl radicals. Similar experiments were carried out for diol **7** and donor **4**. Based on the spectral and kinetic similarities to 2-naphthol, absorption bands observed at 360 and 480 nm observed during the photolysis of diol **7** and donor **4** were assigned to their respective naphthoxyl radical species (Figure 4.35(b), Figure 4.36 (b), Table 4.4). Only the NpO<sup>•</sup> radicals are observed in the photolysis of 2-naphthol or

Table 4.4. Decay of triplet states and ArO<sup>•</sup> generated upon laser flash photolysis of 2-naphthol, diol **7** and donor **4** in 80:20 v/v MeCN to 5.0 mM phosphate buffer (pH 7.0) or 0.1 M NaOH (discussed in Section 4.7.4). Triplet decay rates were analyzed at 420 or 440 nm; amplitude at 440 nm is reported. Naphthoxyl radical decay rates were analyzed at 360 and 440 nm and global analysis (see Appendix D); amplitude at 360 nm is reported in 5.0 mM phosphate buffer (pH 7.0) and at 480 nm in 0.1 M NaOH.

Molecule	Triplet Decay		Naphthoxyl Radical			
	Rate constants Single $\lambda$ (s <sup>-1</sup> )	$\Delta A_{440}$ (a.u.)	Rate Constants Single $\lambda$ (s <sup>-1</sup> )	Rate Constants Global Analysis (s <sup>-1</sup> )	$\Delta A_{360}$ (a.u.)	$\Delta A_{480}$ (a.u.)
<b>2-NpOH</b>	$(5.7 \pm 0.4) \times 10^5$	0.18	$(2.0 \pm 0.2) \times 10^5$ $(2.7 \pm 0.1) \times 10^4$	$(2.38 \pm 0.01) \times 10^5$ $(4.02 \pm 0.01) \times 10^4$	0.18	--
<b>Diol 7</b>	$(3.3 \pm 0.2) \times 10^5$	0.15	$(1.8 \pm 0.6) \times 10^5$ $(3.1 \pm 0.4) \times 10^4$	$(2.44 \pm 0.01) \times 10^5$ $(3.58 \pm 0.01) \times 10^4$	0.15	--
<b>4a</b>	$(4.7 \pm 0.2) \times 10^5$	0.12	$(2.8 \pm 2.0) \times 10^5$ $(1.5 \pm 0.5) \times 10^4$	$(2.81 \pm 0.01) \times 10^5$ $(1.50 \pm 0.01) \times 10^4$	0.10	--
<b>2-NpO<sup>•</sup></b>	not observed	--	$(1.7 \pm 0.2) \times 10^5$ $(2.3 \pm 0.8) \times 10^4$	$(1.39 \pm 0.01) \times 10^5$ $(1.23 \pm 0.01) \times 10^4$	--	0.09
<b>4c</b>	not observed	--	$(1.6 \pm 0.8) \times 10^5$ $(1.5 \pm 0.2) \times 10^4$	$(1.35 \pm 0.01) \times 10^5$ $(1.98 \pm 0.01) \times 10^4$	--	0.09

diol **7** in oxygenated aqueous MeCN. In addition to analyzing kinetic data at a singular wavelength, each spectrum was analyzed using global analysis to verify that no additional processes were overlooked in the data gathered in oxygenated aqueous MeCN (Table 4.4). The global analysis of the transient absorption spectra for 2-naphthol and diol **7** (see Appendix D) were modeled using a two-component analysis ( $A \rightarrow B$ ,  $B \rightarrow C$ ). The global analysis was consistent with the analysis completed using data at a single wavelength (Table 4.4).

#### 4.7.2 Identification of Solvated Electrons

Hydroxyarenes can undergo ionization to form radical cations (ions that have both a positive formal charge and an unpaired electron), resulting from the photoejection of an electron (Eqn. 4.4):



Transient absorption spectra of donor **4** were collected using a nanosecond transient absorption (ns-TA) system which can acquire full spectra (290-800 nm) at a single time point. These experiments and analyses were done at the University of Hong Kong in the research laboratory of Prof. David Lee Phillips during a research visit. The transient absorption spectral changes of donor **4** following photoexcitation were monitored in anaerobic and oxygenated 80:20 v/v MeCN to 5.0 mM phosphate buffer solution (pH 7.0) conditions. From 200 ns to 22  $\mu\text{s}$ , the ns-TA spectra match well with the spectra obtained by combining ns-LFP kinetic data at individual wavelengths (Figure 4.37). An additional absorption band is observed at 750 nm, which is assigned to solvated electrons.<sup>201</sup> The generation of radical cations is not easily detected using time resolved transient

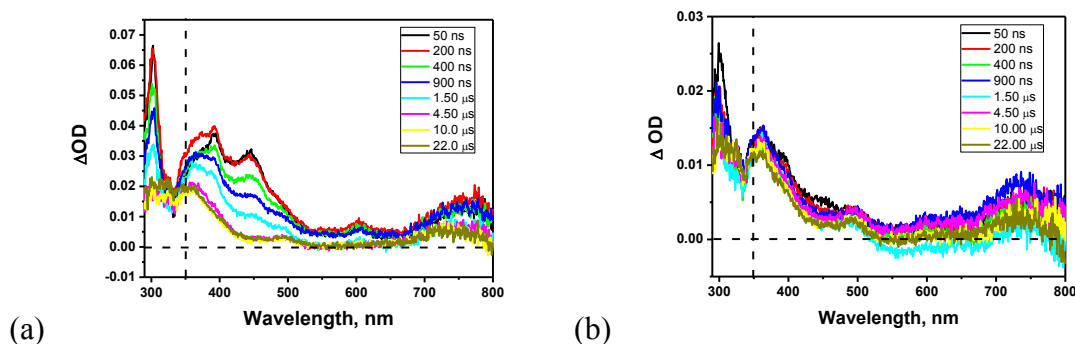


Figure 4.37. ns-TA for donor **4** (100-150  $\mu\text{M}$ ) in (a) anaerobic and (b) oxygenated 80:20 v/v MeCN to 5.0 mM phosphate buffer solution, pH 7.0;  $\lambda_{\text{exc}} = 266 \text{ nm}$ . The vertical dashed line indicates the approximate wavelength above which the ground state species does not absorb; hence at longer wavelengths, ground state bleach is not a concern.

absorption spectroscopy due to low quantum yields (*i.e.*  $\phi = 0.02$  in naphthalene<sup>195</sup>) and the production of other transient species with overlapping absorption spectra.<sup>194,196</sup> However, the observation of the solvated electrons confirms that donor **4** can form a radical cation upon excitation.

### 4.7.3 Identification of <sup>3</sup>ArOH Species

During the photolysis of the naphtholic compounds, an oxygen-dependent species is clearly observed in 80:20 v/v MeCN to 5.0 mM phosphate buffer (pH 7.0) absorbing between 400-470 nm (Figure 4.38, Figure 4.39, and Figure 4.40). For the model

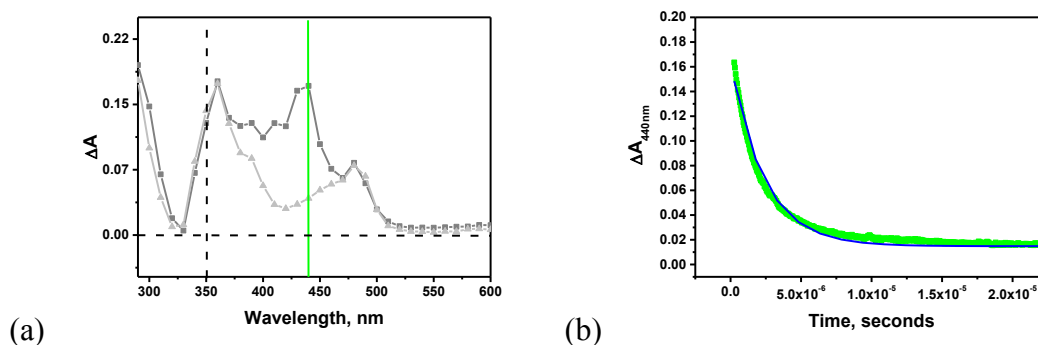


Figure 4.38. (a) Transient absorption spectral changes of 2-naphthol (150  $\mu\text{M}$ ) after 1000 ns following excitation in anaerobic (dark gray) and oxygenated (light gray) 80:20 v/v MeCN to 5.0 mM phosphate buffer solution, pH 7.0. Probe wavelength is highlighted in green. The vertical dashed line indicates the approximate wavelength above which the ground state species does not absorb; hence at longer wavelengths, ground state bleach is not a concern. (b) Best fit of the kinetic trace at 440 nm observed in anaerobic conditions to a first-order rate equation giving  $k_{\text{obs}} = (4.2 \pm 0.1) \times 10^5 \text{ s}^{-1}$ .

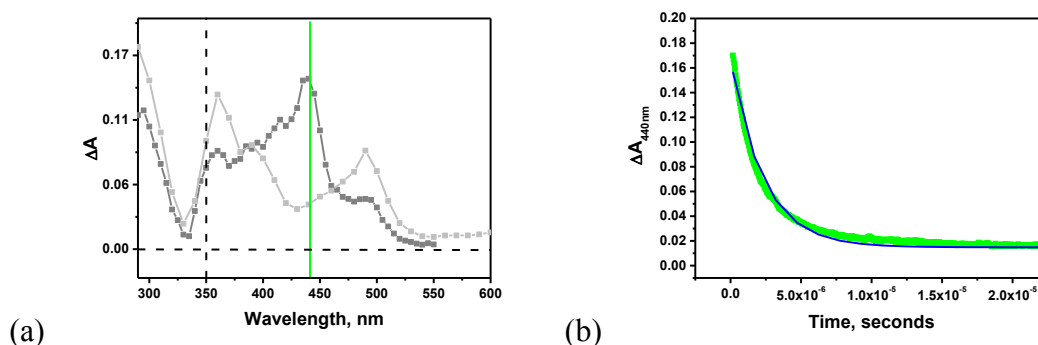


Figure 4.39. (a) Transient absorption spectral changes of diol **7** (150  $\mu\text{M}$ ) after 1000 ns following excitation in anaerobic (dark gray) and oxygenated (light gray) 80:20 v/v MeCN to 5.0 mM phosphate buffer solution, pH 7.0. Probe wavelength is highlighted in green. The vertical dashed line indicates the approximate wavelength above which the ground state species does not absorb; hence at longer wavelengths, ground state bleach is not a concern. (b) Best fit of the kinetic trace at 440 nm observed in anaerobic conditions to a first-order rate equation giving  $k_{\text{obs}} = (4.3 \pm 0.1) \times 10^5 \text{ s}^{-1}$ .

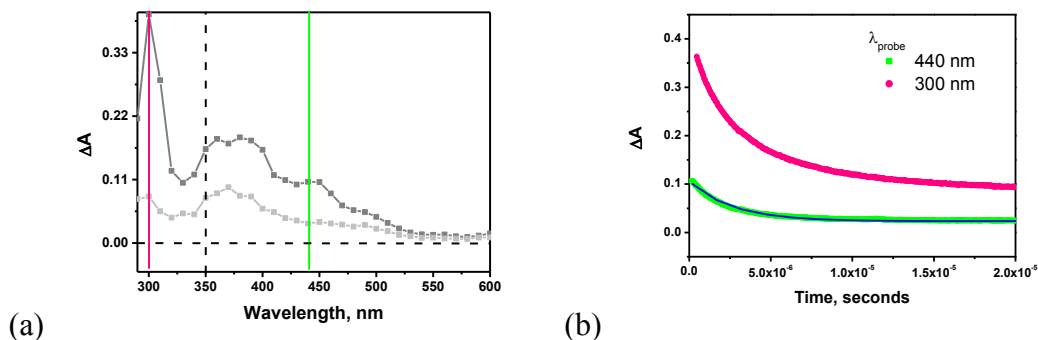


Figure 4.40. (a) Transient absorption spectral changes of donor **4** (150  $\mu\text{M}$ ) after 1000 ns following excitation in anaerobic (dark gray) and oxygenated (light gray) 80:20 v/v MeCN to 5.0 mM phosphate buffer solution, pH 7.0. The vertical dashed line indicates the approximate wavelength above which the ground state species does not absorb; hence at longer wavelengths, ground state bleach is not a concern. (b) Best fit of the kinetic trace at 440 nm observed in anaerobic conditions to a first-order rate equation giving  $k_{\text{obs}} = (4.3 \pm 0.1) \times 10^5 \text{ s}^{-1}$  (green) and at 300 nm giving  $k_{\text{obs}} = (2.6 \pm 0.1) \times 10^6 \text{ s}^{-1}$ .

compound 2-naphthol, the spectrum of its oxygen-dependent transient species observed here matched well with the absorption spectrum of 2-naphthol's triplet-triplet absorption previously reported.<sup>194</sup> The triplet decayed with an observed rate of  $k_{\text{obs}} = (5.7 \pm 0.4) \times 10^5 \text{ s}^{-1}$  (Figure 4.38 (a) and Table 4.4) in anaerobic 80:20 v/v MeCN to 5.0 mM phosphate buffer (pH 7.0). This is similar to rate data obtained by pulse radiolysis for the decay of the triplet of 2-naphthol in  $\text{N}_2$ -saturated benzene ( $k_{\text{obs}} = 1.0 \times 10^5 \text{ s}^{-1}$ ).<sup>195</sup> The triplet excited state typically has long lifetimes (ns to ms) due to the partially or completely forbidden electronic transitions when triplet excited state quenchers are absent (e.g. oxygen).<sup>256</sup> Based on the similarities in absorption maxima, amplitudes, and rate constants for decay (Figure 4.39, Figure 4.40, Table 4.4), the bands at  $\sim 400\text{--}470 \text{ nm}$  observed during the photolysis of diol **7** and donor **4** were also assigned to triplet states of the respective parent molecules. The additional band observed at 300 nm from photolysis of donor **4** is discussed further in the following sections (Figure 4.40).

Figure 4.41(a) shows the transient absorption 200 ns after LFP of 2-naphthol, diol **7**, and donor **4** in anaerobic mixtures of 80:20 v/v MeCN to 5.0 mM phosphate buffer solution (pH 7.0). Bands unique to donor **4** were observed at 300 nm and 390 nm. Importantly, by 22  $\mu\text{s}$ , transient species converge into similarly absorbing species for 2-naphthol, diol **7**, and donor **4**, indicating no additional processes are observed for donor **4** past 22  $\mu\text{s}$  (Figure 4.41(b)). Figure 4.40(b) shows that the bands are oxygen-dependent in amplitude ( $\Delta A_{300\text{nm}} = 0.08$  in oxygenated conditions and  $\Delta A_{300\text{nm}} = 0.4$  in anaerobic solution). The

fs-TA spectra also indicated that a triplet species was observable at 390 nm from photolysis of donor **4** in anaerobic 80:20 v/v MeCN to 5.0 mM phosphate buffer solution (pH 7.0; Section 4.6). The photophysical studies showed that the absorption and fluorescence of the naphtholic structure was unaffected by addition of a LG separated by the methylene carbon (Table 4.). The nearly identical transient absorption spectra of 2-naphthol and diol **7** fully support this conclusion. Hence, it is unlikely the additional absorption bands at 300 and 390 nm are attributable to addition of trifluoromethanesulfonamidoxy moiety to the 6,2-HNM-photocage.

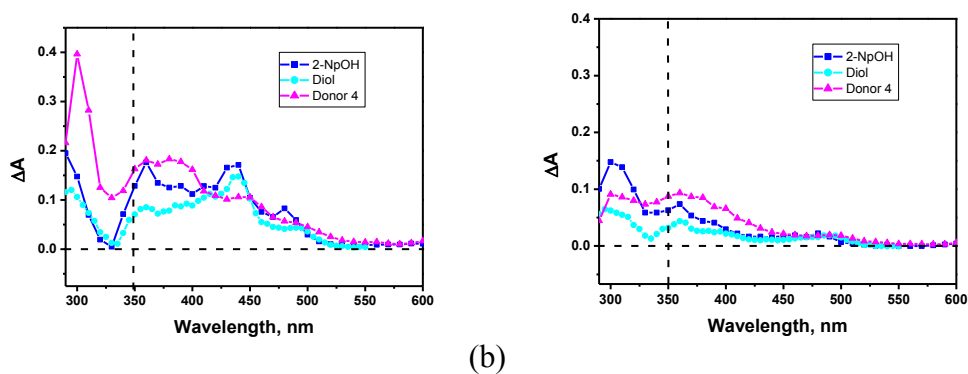


Figure 4.41. Plot of transient absorption spectra for 2-naphthol, diol **7**, and donor **4** in anaerobic 80:20 v/v MeCN to 5.0 mM phosphate buffer solution (pH 7.0) (a) 200 ns and (b) 22  $\mu$ s after excitation;  $\lambda_{\text{exc}} = 266$  nm. The vertical dashed line indicates the approximate wavelength above which the ground state species does not absorb; hence at longer wavelengths, ground state bleach is not a concern.

#### 4.7.4 Exclusion of $^3\text{ArO}^\cdot$

A species unique to photolysis of donor **4** in anaerobic 80:20 v/v MeCN to 5.0 mM phosphate buffer solution (pH 7.0) was observed in the fs-TA and ns-LFP data ( $\lambda_{\text{max}} = 300$  and 390 nm; Section 4.6 and Section 4.7.3). One possible albeit unlikely explanation of the unassigned species is that **4** partially undergoes ESPT from the naphtholic OH to solvent forming  $^3\text{ArO}^\cdot$ . Therefore, the transient absorption spectra were analyzed from the photolysis of **4c** (Scheme 4.3). Comparison studies were done using the model compound 2-naphtholate to assist with identification of the transient species.

Figure 4.42 shows the ns-LFP spectra for 2-naphthol and donor **4** in anaerobic and oxygenated solvent mixtures of 80:20 v/v MeCN to 0.1 M NaOH. Photolysis of 2-naphtholate and the conjugate base of **4** produced similar transient species with bands at 370 nm and 490 nm. The rates constants for two consecutive first-order reactions ( $k_{\text{obs}} = (1.7 \pm 0.2) \times 10^5 \text{ s}^{-1}$  and  $k_{\text{obs}} = (2.3 \pm 0.8) \times 10^4 \text{ s}^{-1}$ ; Table 4.4) of 2-naphtholate in

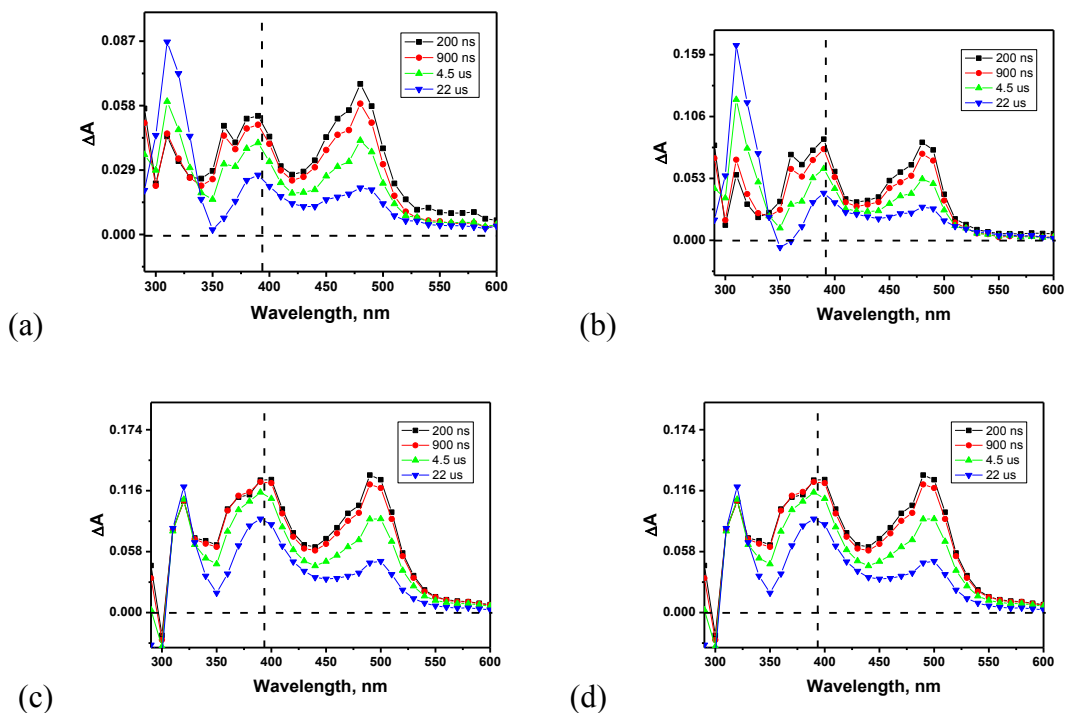


Figure 4.42. Laser flash photolysis of (a) 2-naphthol in anaerobic 80:20 v/v MeCN to 0.1 M NaOH, (b) 2-naphthol in oxygenated 80:20 v/v MeCN to 0.1 M NaOH, (c) **4** in anaerobic 80:20 v/v MeCN to 0.1 M NaOH, and (d) **4** in oxygenated 80:20 v/v MeCN to 0.1 M NaOH;  $\lambda_{\text{exc}} = 266$  nm. The vertical dashed line indicates the approximate wavelength above which the ground state species does not absorb; hence at longer wavelengths, ground state bleach is not a concern.

oxygenated solutions were of a similar magnitude to those observed previously in oxygenated MeCN (Table 4.4). Global analysis of the spectra confirmed the number of processes and rate constants for decay (Figure A6 and Table 4.4).

The spectrum of 2-naphtholate after 200 ns following excitation was compared to the spectrum of 2-naphthol taken in MeCN at the same time frame (Figure 4.43(a)). The absorbance changes are nearly identical at wavelengths  $> 390$  nm. Notably, 2-naphtholate absorbs at wavelengths shorter than 390 nm, whereas 2-naphthol absorbs at wavelengths shorter than 350 nm (Figure 4.44(a)). Hence, a ground state bleach for 2-naphtholate may account for differences observed in the absorbance of the naphthoxyl radical species. Thus, the species observed upon photolysis of 2-naphtholate was assigned to 2-NpO $\cdot$ . In the photolysis of **4** in alkaline conditions, a similarly absorbing species to 2-NpO $\cdot$  was observed with maxima at 390 and 490 nm (Figure 4.42). As analyzed by single wavelength kinetics and global analysis, the species showed similar rates of decay (Table

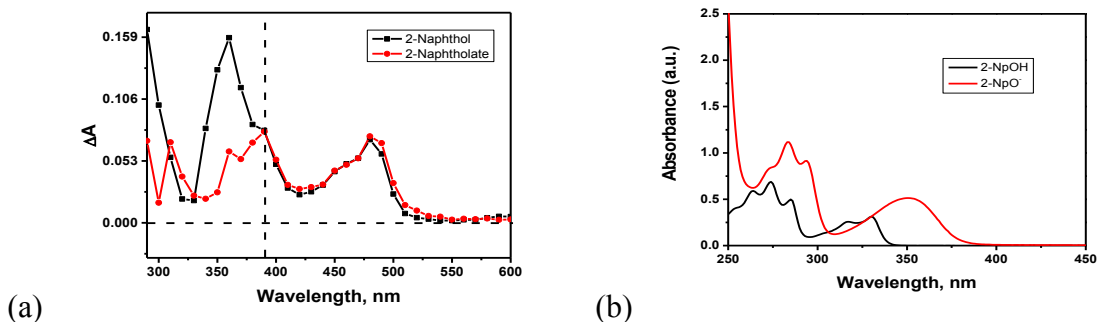


Figure 4.43. (a) Transient absorption spectral changes for 2-naphthol and 2-naphtholate (150  $\mu\text{M}$ ) in oxygenated 80:20 v/v MeCN to 5 mM phosphate buffer, pH 7.0 or to 0.1 M NaOH, respectively, following 200 ns after excitation. The vertical dashed line indicates the approximate wavelength above which the ground state species does not absorb; hence at longer wavelengths, ground state bleach is not a concern. The decreased absorbance change at 360 nm for 2-naphtholate is attributed to ground state bleach. (b) UV-vis absorbance spectrum of 2-naphthol (in MeCN) and 2-naphtholate (in 80:20 v/v MeCN to 0.1 M NaOH);  $\lambda_{\text{exc}} = 266$  nm.

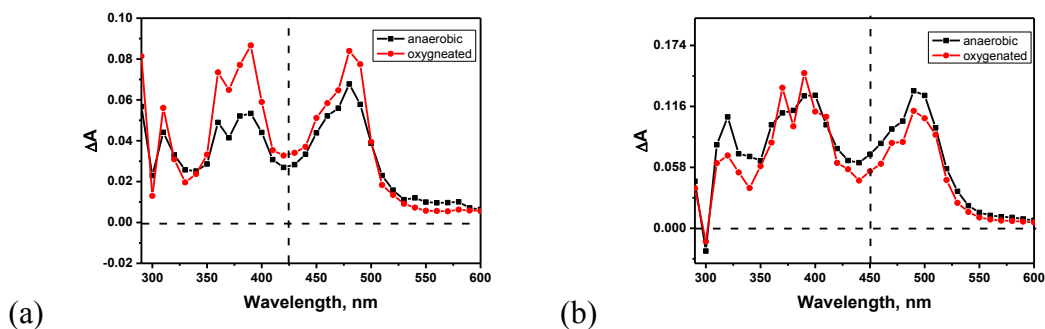


Figure 4.44. (a) Transient absorption spectral changes for 2-naphthol (150  $\mu\text{M}$ ) in anaerobic and oxygenated 80:20 v/v MeCN to 0.1 M NaOH at 200 ns. The vertical dashed line indicates the approximate wavelength above which the ground state species does not absorb; hence at longer wavelengths, ground state bleach is not a concern. (b) Transient absorption spectral changes for donor **4** (150  $\mu\text{M}$ ) in anaerobic and oxygenated 80:20 v/v MeCN to 0.1 M NaOH at 200 ns;  $\lambda_{\text{exc}} = 266$  nm.

4.4; see Appendix D). Thus, this species was assigned to  $\text{ArO}^{\bullet}$  formed from photolysis of **4c** (Scheme 4.2).

No oxygen-dependent bands or processes were observed in the photolysis of 2-naphtholate or **4** in 80:20 v/v MeCN to 0.1 M NaOH (Figure 4.44). The triplet state of 2-naphtholate has an absorption band with  $\lambda_{\text{max}} = 460$  nm (observed in liquid paraffin).<sup>250</sup> Either the triplet states of 2-naphtholate and analogues are short-lived or ISC is not favorable from the conjugate base species. Importantly, the bands unique to donor **4** following photolysis in 80:20 v/v MeCN to 5.0 mM phosphate buffer solution therefore cannot be assigned to absorption of the triplet state of **4c**.

### 4.7.5 Observation in Oxygenated Conditions

The oxygen-dependent species unique to photolysis of donor **4** in anaerobic 80:20 v/v MeCN to 5.0 mM phosphate buffer solution (pH 7.0;  $\lambda_{\text{max}} = 300$  and 390 nm) was further probed in order to gain insights about its identity and its role in HNO photorelease. Interestingly, the transient species was also observed in oxygenated conditions (80:20 v/v MeCN to 5.0 mM phosphate buffer (pH 7.0); Figure 4.45), albeit on a much shorter time frame. The global analysis of the transient absorption spectrum for donor **4** was modeled using a three component analysis (unassigned process: D→E; interfering ArO• processes: A→B, B→C; see Appendix D). The global analysis was consistent with the analysis completed using single wavelength kinetics (Table 4.4) and the decay of the species of interest was determined to be  $(2.10 \pm 0.01) \times 10^6 \text{ s}^{-1}$ . It is unusual that this species is observed under oxygenated conditions for two reasons. First, the oxygen dependence indicates that the species is in a triplet state. Second, triplet states from naphtholic compounds have not yet been observed in oxygenated conditions for any of the naphtholic compounds presented herein.

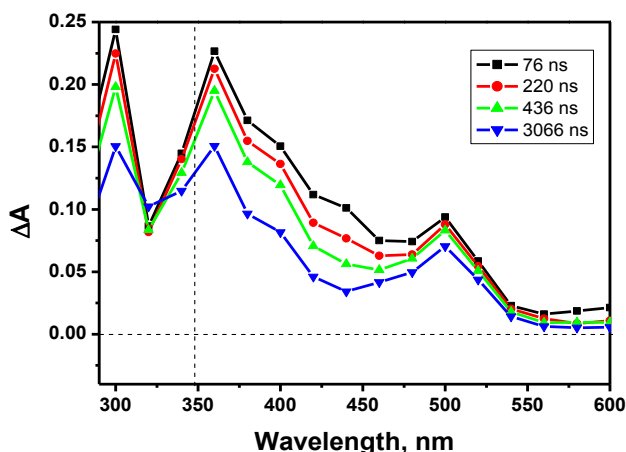


Figure 4.45. Transient absorption spectral changes for **4** (150  $\mu\text{M}$ ) in oxygenated 80:20 v/v MeCN to 5.0 mM phosphate buffer (pH 7.0;  $\lambda_{\text{exc}} = 266 \text{ nm}$ ). The vertical dashed line indicates the approximate wavelength above which the ground state species does not absorb; hence at longer wavelengths, ground state bleach is not a concern.

In Chapter 3, C-O bond cleavage followed by N-S bond cleavage was eliminated from consideration because only  $\text{CF}_3\text{SO}_2^-$  was observed in the photolytic solution (e.g. no observation of  $t_{\text{r}}\text{-MSHA}$ ). HNO could also be generated from N-S bond cleavage followed by C-O bond cleavage, generating an oxynitrene intermediate species.

However, oxynitrenes are known to be highly reactive with molecular oxygen.<sup>257</sup> Indeed, time-resolved IR-monitoring of benzyloxynitrene showed three additional signals, which were attributed to three product species simultaneously forming (PhCH=CH, PhCH<sub>2</sub>ONO<sub>2</sub>, and PhCH=O).<sup>257</sup> In the time-resolved studies presented in this thesis, no additional signals were observed from inclusion of oxygen in the solvent mixture upon photolysis of **1**. Hence, it is unlikely that HNO proceeds via an oxynitrene species as no transient or intermediate species were observed to be reactive with oxygen to generate a novel chromophore.

#### 4.7.6 Nucleophilic Quenching Studies

The solvent dependence of the species of interest was investigated. The concentration of water in MeCN was varied in order to determine if the rates of decay were dependent on water. MeCN (50 mL) and 5.0 mM phosphate buffer (pH 7.0, 50 mL) were individually saturated with oxygen in 100 mL round bottom flasks, each for 20 minutes. A series of samples were prepared using the oxygenated solutions and a stock solution of **4** in capped quartz fluorimeter cuvettes. The kinetic traces taken at 300 nm (0-2000 ns) were analyzed as pseudo first-order processes (Figure 4.46(a)). The observed rate constants were then

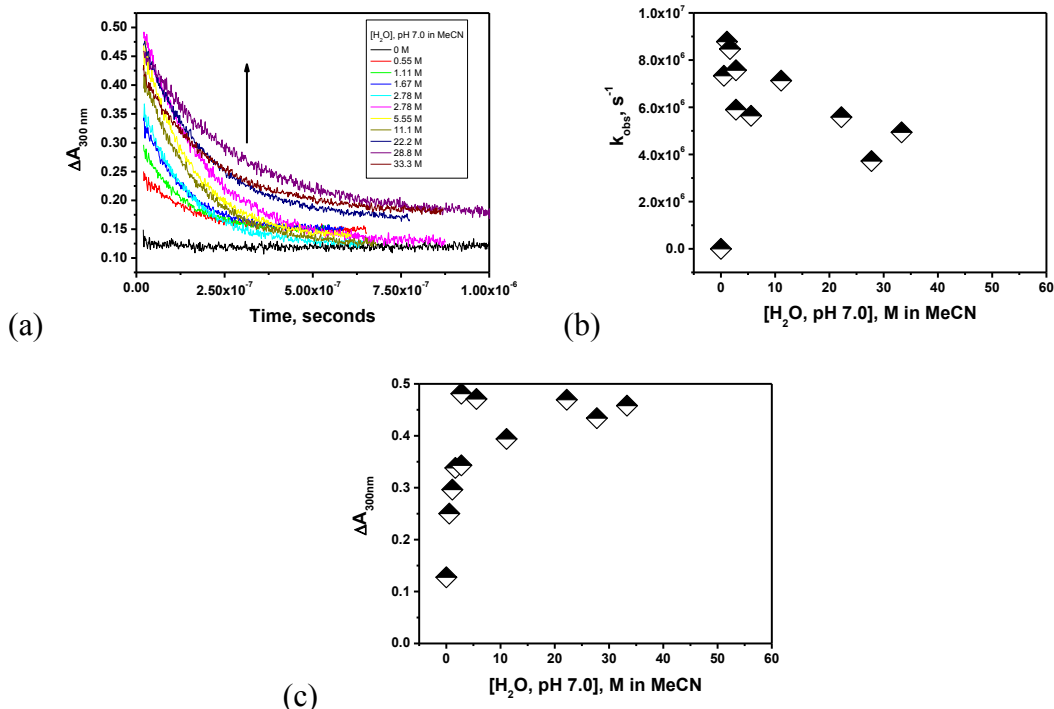


Figure 4.46. (a) Kinetic traces observed upon LFP of **4** (150  $\mu\text{M}$ ) in listed solvent condition (oxygen purged;  $\lambda_{\text{exc}} = 266\text{ nm}$ ). (b) Plot of observed pseudo-first order rate constant as a function of concentration of 5.0 mM phosphate buffer (pH 7.0) in MeCN; (c) Plot of amplitude of absorbance change as a function of concentration of 5.0 mM phosphate buffer (pH 7.0) in MeCN.

plotted against the concentration of buffered water in MeCN (Figure 4.46(b)). The rate of decay initially increased upon addition of a small amount of water (0.55 M) and then decreased from  $\sim 8.0 \times 10^6 \text{ s}^{-1}$  to  $\sim 5.0 \times 10^6 \text{ s}^{-1}$ . Notably, the amplitude of the absorbance change at 300 nm increased from  $\sim 0.1$  to  $\sim 0.5$  a.u. following addition of 5 M water to co-solvent MeCN; the amplitude of absorbance change at 300 nm plateaued following addition of higher concentrations (Figure 4.46(c)). The desired pathway (Pathway 1; Scheme 4.1) does not proceed in MeCN (Section 4.4.1). This further confirms that the transient species of interest here is related to HNO photorelease from **4**.

Nucleophilic quenching studies were also performed using nucleophile sodium azide. Oxygenated conditions were selected to limit the absorbance of the triplet state of **4** ( $^3\text{ArOH}$ ). Three individual samples of **4** (150  $\mu\text{M}$ ) were prepared in oxygenated 50:50 v/v mixtures of MeCN and 5.0 mM phosphate buffer, pH 7.0. Sodium azide was added at concentrations of 0 mM, 5 mM, and 15 mM from a concentrated stock solution prepared in 5.0 mM phosphate buffer, pH 7.0. Figure 4.47 shows that the unassigned triplet species was unresponsive to azide concentration with respect to both the rate of decay and amplitude of absorbance change. Therefore, the unassigned triplet species is not electrophilic. It was established earlier that the mechanism of HNO formation following photolysis of donor **4** does not proceed via a QM intermediate (Section 4.4). Given that QMs rapidly react with nucleophiles,<sup>188</sup> this species cannot be assigned to a QM (Scheme 4.1; Pathway b). Additionally, this species cannot be carbocation **2** as it would also undergo nucleophilic attack (Scheme 4.1, Pathway a).<sup>206-208</sup>

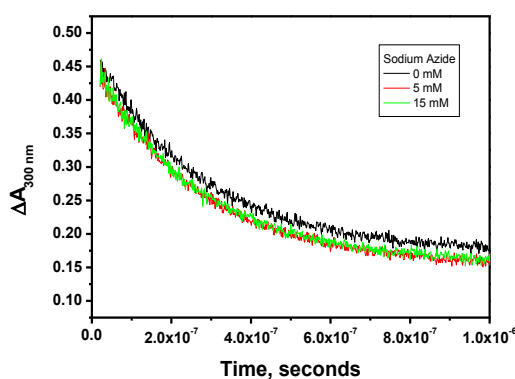


Figure 4.47. Absorbance change of **4** (150  $\mu\text{M}$ ) at 300 nm following excitation in 50:50 v/v MeCN to 5.0 mM phosphate buffer, pH 7.0 with sodium azide concentrations of 0 mM (red), 5 mM (blue), and 15 mM (green);  $\lambda_{\text{exc}} = 266 \text{ nm}$ .

### 4.7.7 pH Dependence

The pH dependence of the unassigned triplet species was examined by photolyzing **4** in 80:20 v/v MeCN to 5.0 mM phosphate buffer (pH 7.0) and in 80:20 v/v MeCN to 5.0 mM phosphate buffer (pH 3.0). Figure 4.48 shows that the change in pH had no influence on the rate of decomposition ( $6.7 \pm 0.3$ )  $\times 10^6$  s<sup>-1</sup>. However, the pH decrease reduced the magnitude of the absorbance change at 300 nm ( $\Delta A$  0.35 vs 0.10 a.u.; Figure 4.48). Note that other processes contribute to the change in absorbance. Earlier it was shown that **4** is less selective ( $\sim 15\%$  CF<sub>3</sub>SO<sub>2</sub><sup>-</sup>; Chapter 3, Section 3.6) towards HNO photorelease when the buffer pH is 3.0 (80:20 v/v MeCN to 5.0 mM phosphate buffer), whereas essentially only the HNO photorelease pathway is operational when **4** is photolyzed in pH 7.0. Again, this further indicates that the transient species of interest correlates with HNO generation from photolysis of donor **4**.

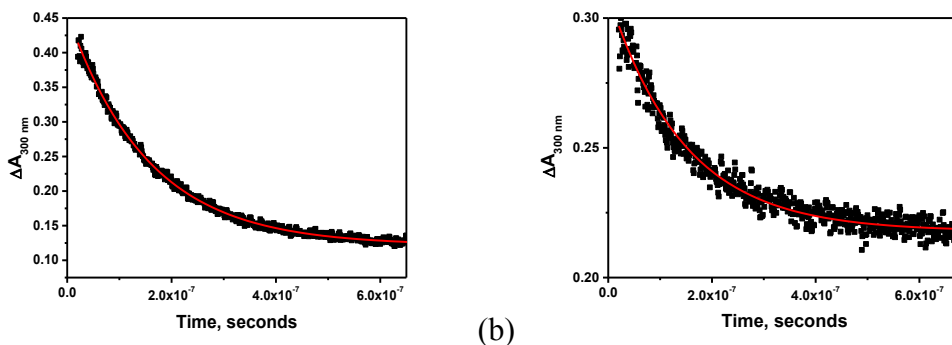


Figure 4.48. Kinetic traces observed upon LFP of **4** (150  $\mu$ M) in oxygenated (a) 80:20 v/v MeCN to 5.0 mM phosphate buffer, pH 7.0 and (b) 80:20 v/v MeCN to 5.0 mM phosphate buffer, pH 3.0;  $\lambda_{\text{exc}} = 266$  nm. The decay traces were analyzed as pseudo-first order processes, giving  $k_{\text{obs}} = (6.50 \pm 0.04) \times 10^6$  s<sup>-1</sup> and  $k_{\text{obs}} = (6.86 \pm 0.01) \times 10^6$  s<sup>-1</sup>, respectively.

### 4.7.8 Assignment of Species

It was previously established in Chapter 3 that HNO generation likely occurs via simultaneous heterolytic cleavage of C-O and S-N bonds (Scheme 4.1). The fs-TA spectral changes suggest that loss of leaving group occurs directly from an excited state of **4** within 50 ps, which is consistent with heterolytic cleavage events (Section 4.6).<sup>241</sup> Previously, the photoproduct characterizations indicated that a transient species formed from excitation of **4** undergoes nucleophilic attack from HNO to form 6-[(*E*)-(hydroxyimino)methyl]naphthalen-2-ol in the absence of an effective HNO trap (Chapter 3, Section 3.4). The formation of the band at 390 nm potentially arises from nucleophilic attack of HNO on carbocation **9**. The resulting compound appears to readily undergo

intersystem crossing into a triplet state. Whether  $^1\text{HNO}$  or  $^1\text{NO}^-$  was involved in the observed reaction was considered. The rate of protonation of  $^1\text{NO}^-$  is predicted to be  $2.5 \times 10^{11} \text{ s}^{-1}$  ( $t_{1/2} = 3.2 \text{ ps}$ ).<sup>4</sup> Inclusion of an effective HNO trap was shown to promote nucleophilic attack of the solvent on carbocation **9** (see Chapter 3, Section 3.4.5). Hence, it is likely that  $^1\text{HNO}$ , not  $^1\text{NO}^-$ , reacts with carbocation **9** (Figure 4.49).

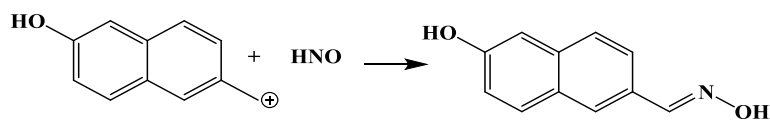


Figure 4.49. The reaction of (6-hydroxynaphthalen-2-yl)methyl cation and HNO to form 6-[(*E*)-(hydroxyimino)methyl]naphthalen-2-ol.

#### 4.8 INVESTIGATION OF THE REACTION BETWEEN $^1\text{HNO}$ AND CARBOCATION **9** USING TIME RESOLVED ABSORPTION SPECTROSCOPY

##### 4.8.1 Photolysis in MeCN

Importantly, donor **4a** cannot directly release  $^1\text{HNO}$  as the N atom on the leaving group is not protonated on the photoactive donor. Hence,  $^1\text{HNO}$  photorelease must proceed via  $^1\text{NO}^-$ . It is proposed that  $^1\text{HNO}$  subsequently can react with carbocation **9**, producing a triplet state species with bands at 300 and 390 nm. To further investigate this reaction, ns-LFP studies were performed on donor **4** with carboxylate salt in an aprotic solvent, MeCN, in order to potentially prevent the protonation of  $^1\text{NO}^-$  to  $^1\text{HNO}$  and therefore the subsequent reaction between  $^1\text{HNO}$  and carbocation **9**.

Figure 4.50 shows the absorbance changes observed upon excitation of donor **4** in the presence of 5.0 mol. equiv. acetate in oxygenated MeCN and anaerobic MeCN. Under these conditions, HNO photorelease selectively occurs because the carboxylate salt deprotonates **4b** to form **4a** (Section 4.6). In oxygenated MeCN, a species was observed with wavelength maximum at 360 nm and a shoulder at 480 nm, which decayed via two consecutive first-order reactions ( $k_{\text{obs}} = (4.3 \pm 0.8) \times 10^5 \text{ s}^{-1}$ ;  $\tau = 1.3\text{-}2.0 \text{ }\mu\text{s}$  and  $k_{\text{obs}} = (5.7 \pm 2.0) \times 10^4 \text{ s}^{-1}$ ;  $\tau = 9.0\text{-}17 \text{ }\mu\text{s}$ ). This species was assigned to the naphthoxyl radical based on previous assignments of 2-naphthol (Table 4.4). Two oxygen-dependent species were observed, absorbing at 300 nm, 390 nm, and 440 nm. The species absorbing at 440 nm decayed at a rate of  $k_{\text{obs}} = (4.5 \pm 0.3) \times 10^5 \text{ s}^{-1}$ ;  $\tau = 2.1\text{-}2.4 \text{ }\mu\text{s}$ . This species is assigned to that of the triplet state of **4a** (Table 4.4).

The species absorbing at 300 and 390 nm was oxygen-dependent but not fully quenched when solutions were saturated with oxygen (Figure 4.51). Similar spectral characteristics were seen previously in the LFP of **4a** in aqueous solvent conditions, where the decomposition of **4a** is selective for the desired pathway (Pathway 1, Scheme 4.3). Hence, the observed species is assigned to the triplet state of the product of the reaction between HNO and carbocation **9**. In hindsight, it is likely that  $^1\text{NO}^-$  can protonate even in MeCN due to the high  $\text{p}K_a \sim 23$  value of  $^1\text{HNO}/^1\text{NO}^-$  (in water; predicted based on thermodynamic data).<sup>1</sup>

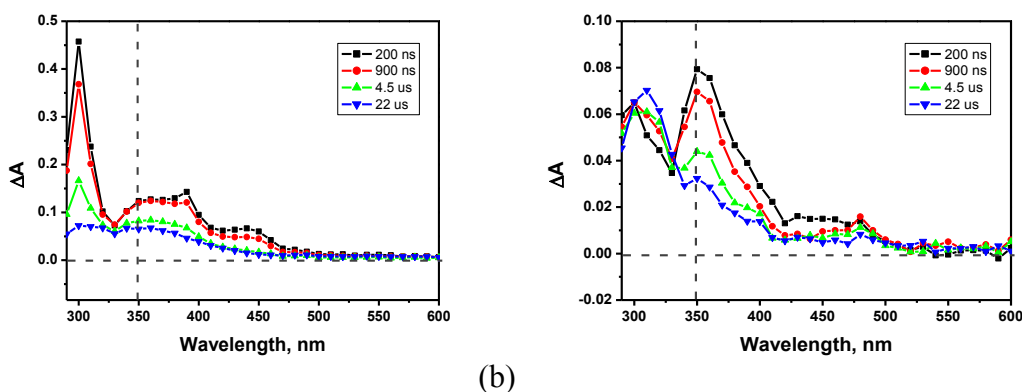


Figure 4.50. LFP of donor **4** (150  $\mu\text{M}$ ) and lithium acetate ( $\sim 5$  mol equiv) in (a) oxygenated and (b) Ar-purged MeCN;  $\lambda_{\text{exc}} = 266$  nm. The vertical dashed line indicates the approximate wavelength above which the ground state species does not absorb; hence at longer wavelengths, ground state bleach is not a concern.

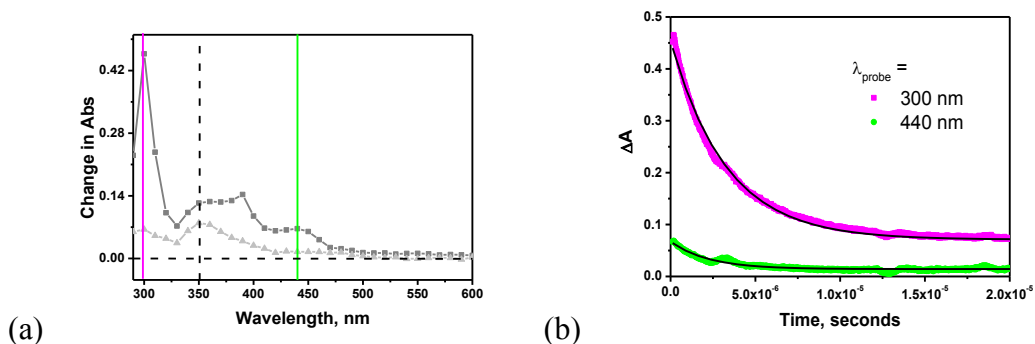


Figure 4.51. (a) Transient absorption spectral changes of donor **4** (150  $\mu\text{M}$ ) and lithium acetate ( $\sim 5$  mol equiv) 1000 ns following excitation in anaerobic (dark gray) and oxygenated (light gray) in MeCN. Probe wavelengths are highlighted in green and pink. The vertical dashed line indicates the approximate wavelength above which the ground state species does not absorb; hence at longer wavelengths, ground state bleach is not a concern. (b) Best fit of the kinetic trace at 440 nm observed in anaerobic conditions to a first-order rate equation giving  $k_{\text{obs}} = (4.5 \pm 0.3) \times 10^5 \text{ s}^{-1}$  (green) and best fit of the kinetic trace at 300 nm observed in anaerobic conditions to a first-order rate equation giving  $k_{\text{obs}} = (3.1 \pm 0.1) \times 10^5 \text{ s}^{-1}$  (pink).

### 4.8.2 Kinetic Isotope Effect

A kinetic isotope effect study was used to probe the rate of protonation of  $^1\text{NO}^-$  to  $^1\text{HNO}$ . The fs-TA was recorded for **4a** in 80:20 v/v MeCN to deuterated 5.0 mM phosphate buffer (pD 7.0; Figure 4.52) and compared with the fs-TA taken in the same solvent condition using non-deuterated buffer. In the deuterated solvent, the rate of intersystem crossing decreased as expected (Figure 4.52(d); 440 nm).<sup>258</sup> No other significant differences between photolysis of donor **4** in normal versus deuterated water were evident (Figure 4.52(d)). Therefore, the rate of protonation of  $^1\text{NO}^-$  to  $^1\text{HNO}$  is likely very rapid. This is in agreement with the predicted value of the rate of protonation of  $^1\text{NO}^-$  ( $k = 2.5 \times 10^{11} \text{ s}^{-1}$ ;  $t_{1/2} = 3.2 \text{ ps}$ ).<sup>4</sup>

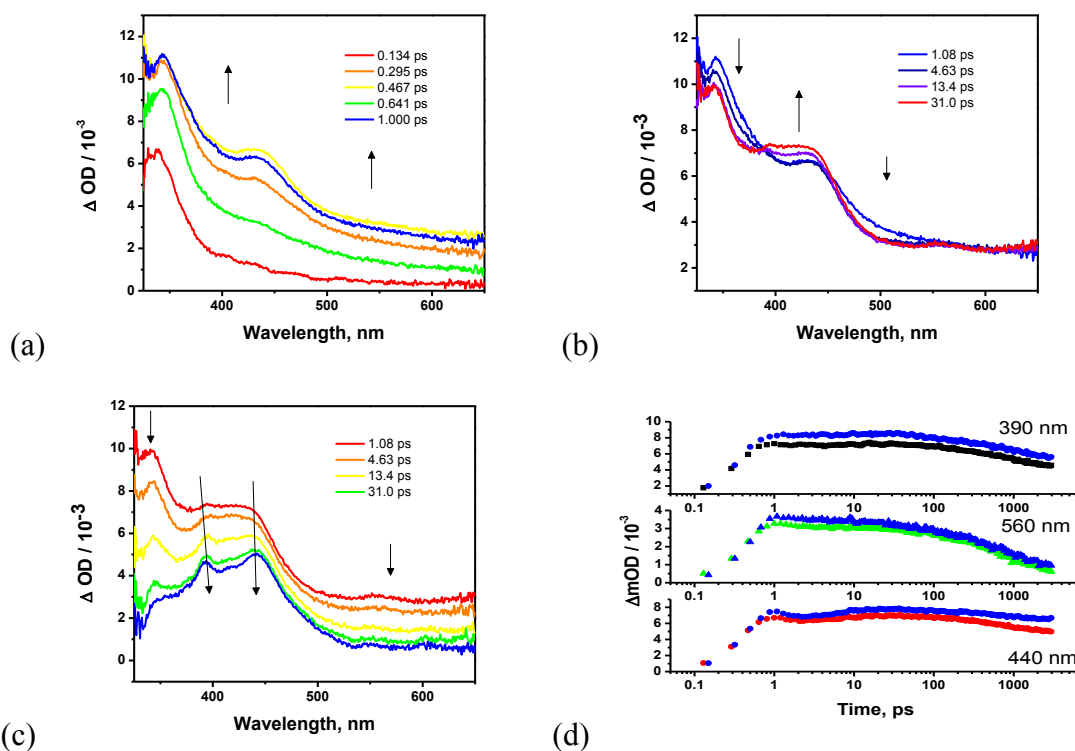


Figure 4.52. (a)-(c) fs-TA of donor **4** in aerobic 80:20 v/v MeCN to 5.0 mM phosphate buffer solution (pD 7.0) achieved from 267 nm excitation. (d) Kinetics from 390 nm, 560 nm, and 440 nm in deuterated water (blue) and water (colored).

### 4.9 CONCLUSIONS

Neither excitation of **4b** nor **4c** in aqueous solutions produced HNO, as N-O bond cleavages were instead observed. This is in agreement with the data presented in Chapter 3, indicating that HNO is released following photolysis of donor **4** when the donor molecule is excited under conditions where the leaving group nitrogen atom is

deprotonated and naphtholic OH is protonated. Hence, subsequent studies were carried out under neutral pH conditions, where **4a** is the dominant species.

Based on literature and previous work, two possible photocleavage mechanisms are likely (Scheme 4.1). The first mechanism involves ESPTs leading to loss of leaving group and quinone methide (QM) formation (Scheme 4.1, Pathway (a)).<sup>155</sup> Ultra-fast time resolved spectroscopic experiments suggests that QM formation occurs within picoseconds to a few microseconds.<sup>151,173,187</sup> Hence, the ability of donor **4** to undergo ESPT was investigated. The emission studies show that donor **4** contains both photoacidic and photobasic sites. This is typical behavior of substituted hydroxyarenes.<sup>143</sup> However, HNO photorelease from donor **4** occurred with high selectivity in partially aqueous conditions. Under these conditions, PTTS from the naphtholic OH does not occur as demonstrated by emission studies and fs-TA of model compound 2-naphthol. Similar results were observed for 2-naphthol-6-sulfonate ( $pK_a^* = 1.9$ ), with ESPT observed in MeCN-H<sub>2</sub>O mixtures when the water content was > 20 % by vol.<sup>259</sup> Others have proposed that geminate recombination of the dissociated naphtholic proton is likely to be favorable in mixed solvent conditions where the aprotic solvent is the major component as the proton cannot readily diffuse into solvent.<sup>260</sup> Based on this, a photolytic pathway involving a QM intermediate is unlikely (Scheme 4.1, Pathway (a)). The time-resolved spectroscopic studies also provides evidence that a QM intermediate is not involved in HNO generation from photolysis of donor **4** because a highly conjugated, long-lived species was not observed.<sup>163,175</sup>

Alternatively, HNM-protected molecules and similarly structured compounds can undergo ArCH<sub>2</sub>-X bond heterolysis, yielding a (6-hydroxynaphthalen-2-yl)methyl cation **9**/anion pair (ArCH<sub>2</sub><sup>+</sup>/X<sup>-</sup>; Scheme 4.1, Pathway (b)).<sup>206-208</sup> Importantly, excitation of donor **4a** in aprotic solvent in the presence of a carboxylate salt selectively generates the desired pathway (Scheme 4.3, Pathway 1). Hence, an HNO-generating mechanism proceeding via concerted C-O and N-S heterolytic bond cleavages from photoexcitation of **4a** is proposed. This mechanism is further supported by the fs-TA experiments, which indicated that donor **4** enters a spectroscopically unique excited state following vibrational relaxation. The trifluoromethanesulfonamidoxy moiety eliminates <sup>1</sup>NO<sup>-</sup>, not <sup>1</sup>HNO; <sup>1</sup>NO<sup>-</sup> rapidly protonates ( $pK_a$  (<sup>1</sup>HNO/<sup>1</sup>NO<sup>-</sup>) ~23<sup>1</sup>). Therefore, HNO generation following photolysis of **4a** is proposed to occur on the picosecond timescale. Evidence

for rapid release of HNO from an HNO donor within this time frame is, to our knowledge, unprecedented.

Careful analysis was completed of transient absorption data on the nanosecond timescale. Naphthoxyl radicals, solvated electrons, and the triplet state of the parent molecule were spectroscopically observed following photolysis of donor **4a**. An additional triplet state species was observed under conditions where HNO is generated from photolysis of **4a**. The species is not reactive with nucleophiles. Hence, the species is tentatively attributed to 6-[(*E*)-(hydroxyimino)methyl]naphthalen-2-ol, which is formed from the reaction of cation **2** and HNO (Figure 4.49). Further work using time resolved IR studies of the photolysis of donor **4a** are required to understand the exact rate of <sup>1</sup>HNO formation from <sup>1</sup>NO<sup>•</sup> and the rate of the reaction of HNO with carbocation **2**.

# CHAPTER 5: MECHANISTIC STUDIES OF N-O BOND CLEAVAGE FROM PHOTOCAGED (HYDROXYNAPHTHALENYL)METHYL ANALOGUES OF PILOTY'S ACID

---

## 5.1 INTRODUCTION

*N*-Hydroxysulfonamides (RSO<sub>2</sub>NHOH) are gaining significant interest for HNO photorelease *via* photo-uncaging.<sup>23,24,114</sup> However, less than stoichiometric HNO release is a common problem for photoprotected Piloty's acid analogues.<sup>23,24,114</sup> A series of (hydroxynaphthalenyl)methyl photocaged Piloty's acid analogues were recently developed by our collaborators (R = Ph, CH<sub>3</sub>, and CF<sub>3</sub>, Figure 5.1).<sup>23,24</sup> Depending on the solvent and HNO-generating leaving group, one or two undesired photolysis pathways were observed using the 3,2-HNM photocage (Scheme 5.1). Release of RSO<sub>2</sub>NHO(H) occurred for donors **2** and **3** (Scheme 5.1; Pathway (b)) and N-O bond cleavage was observed for donors **1**, **2**, and **3** (Scheme 5.1; Pathway (c)). The leaving group ability of sulfonates correlate with the pK<sub>a</sub> values for the related conjugated acids (pK<sub>a</sub>(MeSO<sub>2</sub>H) = 2.28,<sup>261</sup> pK<sub>a</sub>(PhSO<sub>2</sub>H) = 2.7,<sup>262</sup> and pK<sub>a</sub>(CF<sub>3</sub>SO<sub>2</sub>H) = -0.6<sup>262</sup>; Table 5.1). Use of the better trifluoromethanesulfonamidoxy leaving group eliminates the release of RSO<sub>2</sub>NHO(H) (Scheme 5.1; Pathway (b)).

The mechanism(s) of N-O bond cleavage from these compounds are not well understood. In this chapter, the mechanism(s) of N-O bond cleavage are investigated for two trifluoromethanesulfonamidoxy analogues of Piloty's acid bearing a (6-hydroxynaphthalen-2-yl)methyl (6,2-HNM) photocage or a (3-hydroxynaphthalen-2-yl)methyl (3,2-HNM) photocage. Under the optimal solvent conditions, donor **4** can achieve stoichiometric (~98%) selectivity for HNO photorelease (Scheme 5.2) and donor **1** can achieve at maximum 70% selectivity for HNO photorelease as opposed to N-O bond cleavage (Scheme 5.1, Pathway (a) and (c)). However, it was observed for both

molecules that the ratio of fluorinated photoproducts ( $\text{CF}_3\text{SO}_2^-/\text{CF}_3\text{SO}_2\text{NH}_2$ ) was highly dependent on solvent, reaching a minimum selectivity (0% for Scheme 5.1, Pathway (a)) in the absence of water in MeCN.<sup>23</sup>

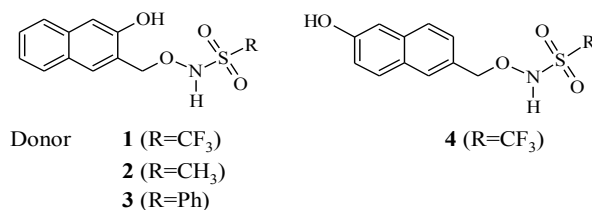


Figure 5.1. Structures of photoactive HNO donors.

Scheme 5.1. The major decomposition pathways observed upon photolysis of HNO donors **1-3**.<sup>23</sup>

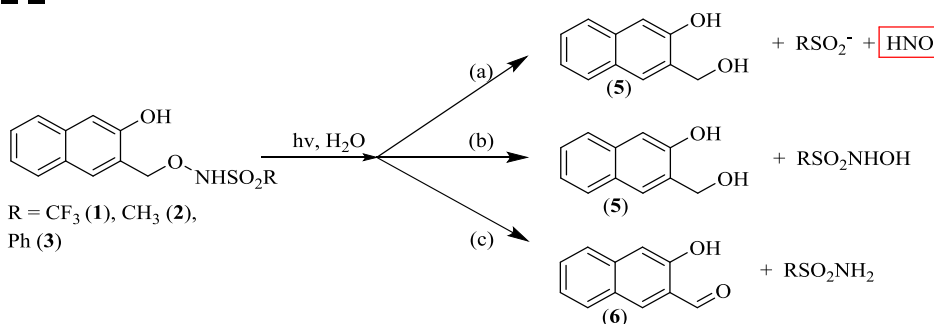
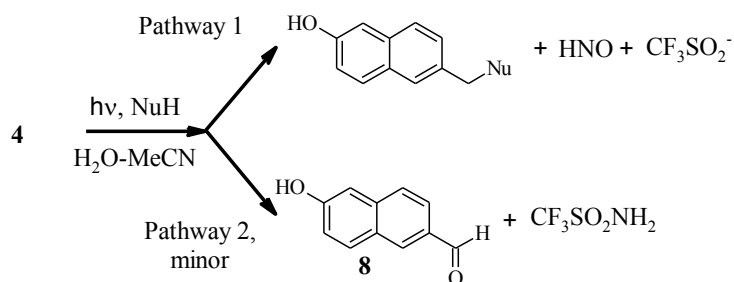


Table 5.1. Observed pathway ratios for HNM-photocaged HNO donors in aqueous MeCN (pH 7.0).

HNO Donor	Photocage	R	In Optimal Aqueous CD <sub>3</sub> CN Conditions			Ref.
			RSO <sub>2</sub> <sup>-</sup> [%]	RSO <sub>2</sub> NH <sub>2</sub> [%]	RSO <sub>2</sub> NHOH [%]	
<b>1</b>	3,2-HNM	CF <sub>3</sub>	60	40	0 <sup>[a]</sup>	23
<b>2</b>	3,2-HNM	CH <sub>3</sub>	9	77	14	23
<b>3</b>	3,2-HNM	Ph	23	77	-- <sup>[b]</sup>	23
<b>4</b>	6,2-HNM	CF <sub>3</sub>	98	0	0 <sup>[a]</sup>	This work

[a] CF<sub>3</sub>SO<sub>2</sub>NHOH readily decomposes at pH 7.0; however, it was shown that CF<sub>3</sub>SO<sub>2</sub>NHOH is not formed using steady state photolysis experiments over time and photolysis under conditions where CF<sub>3</sub>SO<sub>2</sub>NHOH is stable. [b] Small amounts were formed but were not precisely quantified due to the overlapping <sup>1</sup>H NMR resonances of the photoproducts.

Scheme 5.2. Photolytic pathways accessible to donor **4**.



The primary aim of this chapter is to identify strategies to prevent N-O bond cleavage for future photoactive HNO donors incorporating Piloty's acid analogues. First, the influence of the state of (de)protonation on pathway selectivity will be examined in order to identify forms of the donors that primarily undergo N-O bond cleavage. Kinetic and mechanistic studies will then be presented, including product characterizations, photoproduct quantum yields, and time-resolved transient absorption studies. Notably, donors **4** and **1** both contain a photoacidic site, the naphtholic OH. Hence, the role of excited state proton transfer in N-O bond cleavage will be a primary focus of this chapter. Emission studies, photoproduct characterization studies, and photoproduct quantum yield studies will be examined as a function of solvent in order to probe the influence of excited state proton transfer and excited state intramolecular proton transfer on pathways leading to N-O bond cleavage. Donors **4** and **1** were synthesized by the research groups of Prof. Paul Sampson and Prof. Alexander Seed at Kent State University in the United States.

## 5.2 INFLUENCE OF ACID SITES FOR POSSIBLE DEPROTONATION ON PATHWAY SELECTIVITY FOR N-O BOND CLEAVAGE

Previously, two sites of deprotonation on donor **4** were identified using  $^1\text{H}$  NMR and UV-vis spectroscopy (Scheme 5.3; see Chapter 3). To study the effect of donor **4**'s state of deprotonation on pathway selectivity, a series of NMR samples were prepared of donor **4** (0.500-1.00 mM) in solvent mixtures with either 80:20 or 60:40 v/v  $\text{H}_2\text{O}$  in  $\text{CD}_3\text{CN}$ , where the pH of the aqueous component was varied from pH 1 to 13. Figure 5.2 shows that the percentage of  $\text{CF}_3\text{SO}_2\text{NH}_2$  arising from N-O bond cleavage after photolysis of donor **4** varied as a function of the pH of the aqueous component of the solvent mixture. Donor **4** shows increasingly more selectivity towards N-O bond cleavage below pH 4 and above pH 10. Aqueous acetonitrile is known to increase the  $\text{p}K_{\text{a}}$  values of similarly structured compounds compared to values reported in water (e.g. for 1-naphthol,  $\text{p}K_{\text{a}(\text{OH})} = 9.2$  in  $\text{H}_2\text{O}$  and  $\text{p}K_{\text{a}(\text{OH})} = 11.9$  in 2:1 MeCN to  $\text{H}_2\text{O}$ ).<sup>135</sup> When this is taken into consideration, donor **4**'s ground state  $\text{p}K_{\text{a}}$  values correlate well with the pH conditions in which the N-O bond cleavage pathway is shut off ( $\text{p}K_{\text{a}(\text{NH})} = 4.4$  and  $\text{p}K_{\text{a}(\text{OH})} = 9.7$ ). It is clear that excitations of **4b** and **4c** results in N-O bond cleavage.

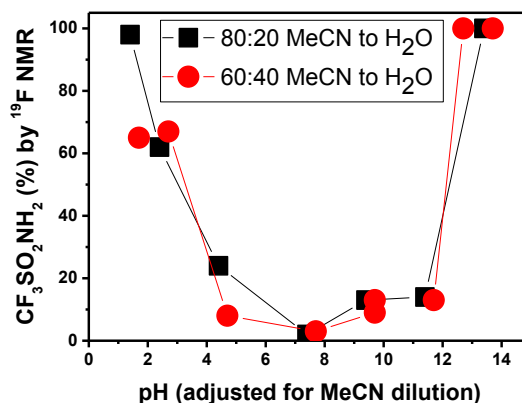
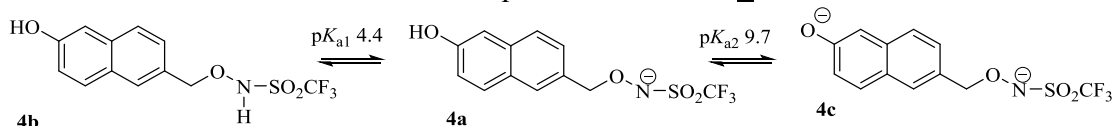
Scheme 5.3. Ground state ionization equilibria for donor **4**.

Figure 5.2. Selectivity for N-O bond cleavage (from <sup>19</sup>F NMR integration of CF<sub>3</sub>SO<sub>2</sub>NH<sub>2</sub> compared to other photoproducts). The concentration of aqueous component in CD<sub>3</sub>CN is 20% or 60% v/v aqueous MeCN, where the aqueous component is 0.1 M HCl, 0.1 M NaOH, 5.0 mM phosphate buffer (pH 3.0, 7.0), 5.0 mM acetate buffer (pH 5.0), 5.0 mM borate buffer (pH 9.0), or 5.0 mM carbonate buffer (pH 11.0). Steady state photolysis samples of **4** (0.500-1.00 mM) were prepared in anaerobic solutions and irradiated using a Rayonet photoreactor (8 x 350 nm bulbs, 4 W) until total degradation.

### 5.3 STUDIES ON N-O BOND CLEAVAGE FROM EXCITATION OF THE NEUTRAL FORM OF DONOR **4**

#### 5.3.1 Investigation of Homolytic versus Heterolytic Bond Cleavage

It was of interest to determine if N-O bond cleavage from **4b** is a heterolytic or a homolytic process. Bond homolysis yields radical products such as a methylated species (ArCH<sub>3</sub>), dimers, or in methanol, ArCH<sub>2</sub>CH<sub>2</sub>OH.<sup>206</sup> Bond heterolysis yields a carbocation/anion pair (ArCH<sub>2</sub><sup>+</sup>/X<sup>-</sup>).<sup>206,207</sup> The steady state photolysis of **4** (0.500 mM) in anaerobic CD<sub>3</sub>CN was monitored by <sup>19</sup>F NMR and <sup>1</sup>H NMR spectroscopy as a function of time (Figure 5.3(a)). Donor **4** decomposed via the N-O bond cleavage pathway as indicated by formation of a species at -79.9 ppm (CF<sub>3</sub>SO<sub>2</sub>NH<sup>•</sup>; identified through addition of water to the photolytic mixture to produce CF<sub>3</sub>SO<sub>2</sub>NH<sub>2</sub>) and -81.2 ppm (CF<sub>3</sub>SO<sub>2</sub>NH<sub>2</sub>; Figure 5.3 (b)). Clean first-order decay was observed ( $k_{obs} = 0.075 \pm 0.003 \text{ min}^{-1}$ ; Figure 5.3(c)). The <sup>1</sup>H NMR spectrum of **4**'s photoproducts showed a mixture of many aromatic photoproduct species after total decomposition (Figure 5.4). To identify the major aromatic photoproduct, the <sup>1</sup>H NMR spectrum after 3 minutes of irradiation was

examined (~20% conversion by  $^{19}\text{F}$  NMR; Figure 5.5). Aldehyde **8** was observed in a similar ratio compared to the starting material (~20%;  $\delta$  8.33, 10.03 ppm; Figure 5.5(b)). This indicates that N-O bond cleavage proceeds via largely heterolytic cleavage as no

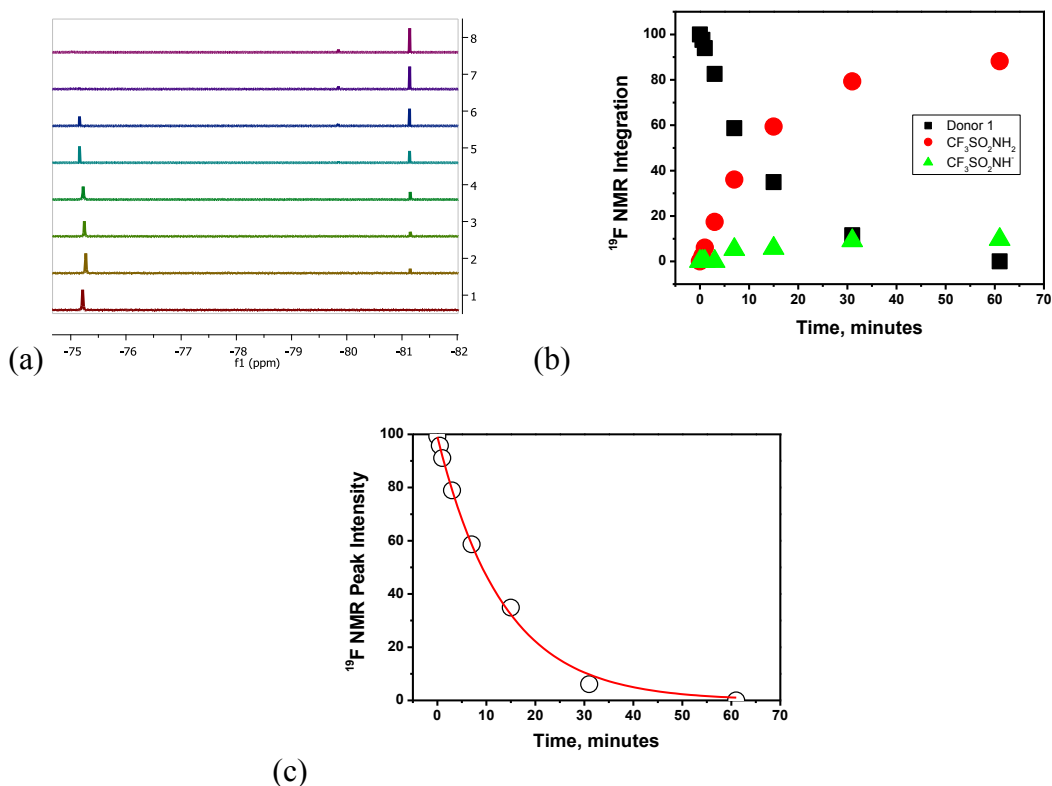


Figure 5.3. (a)  $^{19}\text{F}$  NMR spectra as a function of irradiation time (8 x 350 nm bulbs, 4 W; 0, 0.5, 1, 3, 7, 15, 31, and 61 min) for the photodecomposition of donor **4** (0.500 mM) in anaerobic  $\text{CD}_3\text{CN}$ . (b) Plot of observed species as a function of irradiation time. Final composition:  $\text{CF}_3\text{SO}_2\text{NH}_2$  ( $\delta$  -81.1 ppm; 88%);  $\text{CF}_3\text{SO}_2\text{NH}^-$  ( $\delta$  -79.9 ppm; 10%). (c) Best fit of the peak area of donor **4** ( $-\text{CF}_3$ ) to a first-order rate equation, giving  $k_{\text{obs}} = 0.075 \pm 0.003 \text{ min}^{-1}$ .

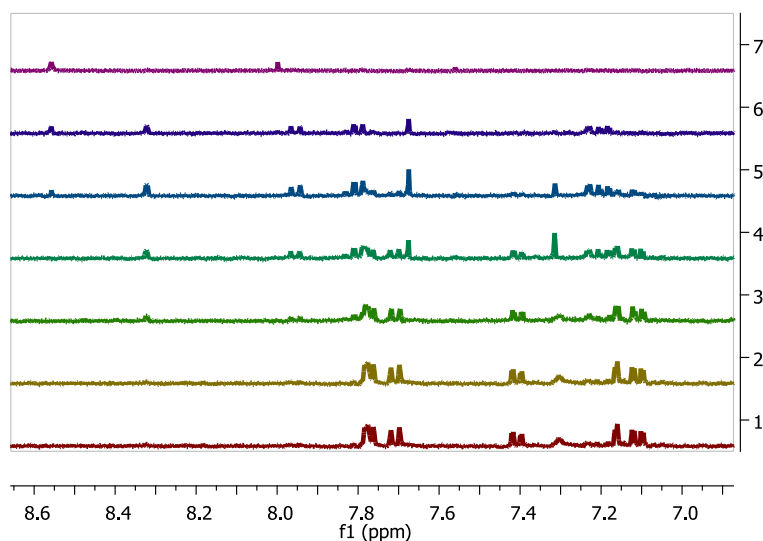


Figure 5.4.  $^1\text{H}$  NMR spectra as a function of irradiation time (8 x 350 nm bulbs, 4 W; 0, 0.5, 1, 3, 15, 31, and 61 min) for the photodecomposition of donor **4** (0.500 mM) in anaerobic  $\text{CD}_3\text{CN}$ .

evidence of homolytic products were observed. The decrease in overall intensity in the  $^1\text{H}$  NMR spectra is attributed to deuterium exchange, photobleaching, and/or secondary photochemistry of aldehyde **8** due to the prolonged irradiation ( $\sim 1$  hr; Figure 5.4).

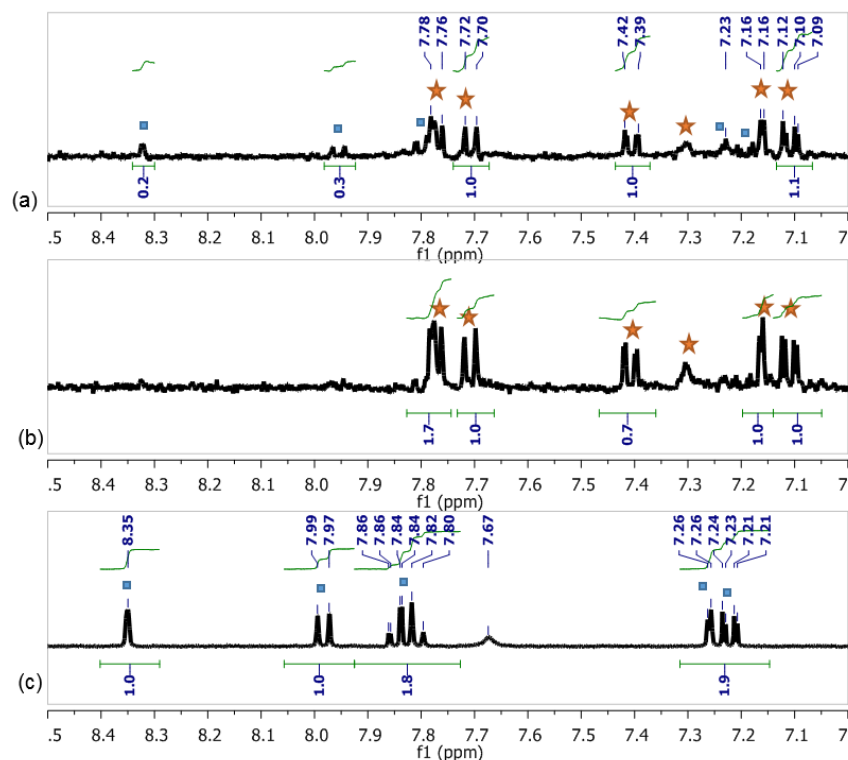


Figure 5.5. (a)  $^1\text{H}$  NMR spectrum of **4** in  $\text{CD}_3\text{CN}$  after 3 min. irradiation (18% conversion to  $\text{CF}_3\text{SO}_2\text{NH}_2$  by  $^{19}\text{F}$  NMR spectroscopy); (b)  $^1\text{H}$  NMR spectrum of an authentic sample of **4** in  $\text{CD}_3\text{CN}$ ; (c)  $^1\text{H}$  NMR spectrum of an authentic sample of aldehyde **8** in  $\text{CD}_3\text{CN}$ .

### 5.3.2 Photoproduct Quantum Yields

The efficiency of N-O bond cleavage proceeding from **4b** was examined by determining the photoproduct quantum yields using azobenzene actinometry.  $\text{CF}_3\text{SO}_2\text{NH}_2$  was used as a chemical marker for the N-O bond cleavage. Solutions of **4b** (1-2 mM; 3.000 mL) were prepared in select solvents. The UV-vis spectra were measured for each sample prior to irradiation to accurately calculate the concentration of the samples (see Appendix C). Where noted as anaerobic, septa-sealed samples were bubbled with argon for  $\sim 90$  s prior to irradiation. The samples were then irradiated in the cuvette at various time intervals. At each interval, an aliquot (0.275 mL) was withdrawn from the sample and added to an NMR tube with 0.275 mL MeOD or  $d_6$ -DMSO (internally reference to trifluorotoluene). Using  $^{19}\text{F}$  NMR spectroscopy, the percentage of decomposed **4b** was quantified using total integration.  $^{19}\text{F}$  NMR spectroscopy was selected instead of  $^1\text{H}$  NMR spectroscopy

because the fluorinated photoproducts were stable upon irradiation and the protonated photoproducts underwent deuterium exchange, photobleaching, and/or secondary photochemistry, making their integration unreliable. The integrations obtained from the  $^{19}\text{F}$  NMR spectra were then converted to moles of photoproduct using the initial concentration of the donor and the volume of irradiated solution. The reported quantum yield is an average of three to seven conversions. Conversions did not exceed 10%. In neat MeCN, **4b** had a photoproduct quantum yield of  $\Phi_{\text{PP}} = 0.18 \pm 0.04$  (unaffected by oxygen; Table 5.2). In DMSO, the photoproduct quantum yield for **4b** was  $\Phi_{\text{PP}} = 0.23 \pm 0.01$  (Table 5.2). Interestingly,  $\text{CF}_3\text{SO}_2^-$  was also observed in samples photolyzed in DMSO, which is likely due to the solvent containing small amounts of water which may enable deprotonation of **4b** to **4a**. The influence of donor **4**'s acid-base chemistry is further examined in a later section.

Table 5.2. Photoproduct quantum yields for HNO photorelease (as indicated by chemical markers  $\text{CF}_3\text{SO}_2^-$  or  $\text{CF}_3\text{SO}_2\text{NH}_2$ ) in aqueous solutions.

Solvent	Pathway 1, $\Phi_{\text{PP}}$	Pathway 2, $\Phi_{\text{PP}}$
MeCN	0	$0.18 \pm 0.04$ (aerobic) $0.18 \pm 0.02$ (anaerobic)
DMSO	$0.12 \pm 0.01$ (aerobic)	$0.23 \pm 0.01$ (aerobic)
60:40 v/v MeCN to 0.1 M NaOH	0	$0.25 \pm 0.04$ (aerobic) $0.28 \pm 0.03$ (anaerobic)

### 5.3.3 Nanosecond Transient Absorption Studies of **4b** in MeCN

The time-resolved spectroscopic characteristics of **4b** were next investigated. 2-Naphthol was used to assist with identification of excited states attributable to photophysical or photochemical processes relating to the naphtholic structure (that is, changes not related to N-O bond cleavage). Detailed analyses of Figure 5.6 and Figure 5.7 are presented in the following sections.

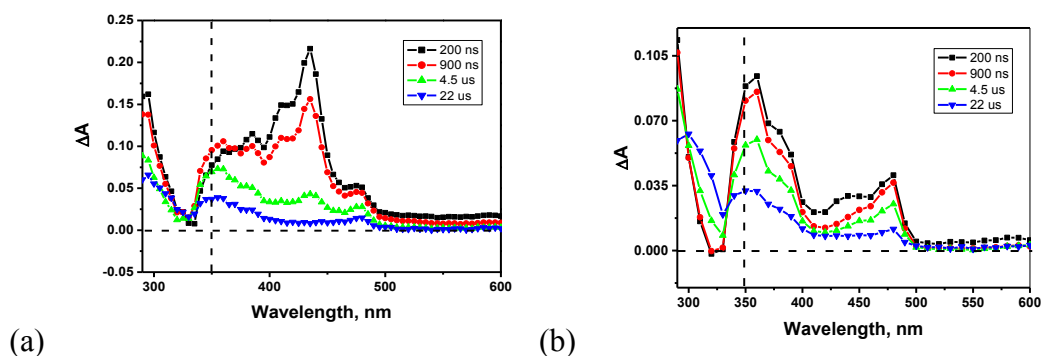


Figure 5.6. Transient absorption spectral changes of 2-naphthol (150  $\mu\text{M}$ ) in (a) anaerobic and (b) oxygenated MeCN. The vertical dashed line indicates the approximate wavelength above which the ground state species does not absorb; hence at longer wavelengths, ground state bleach is not a concern.

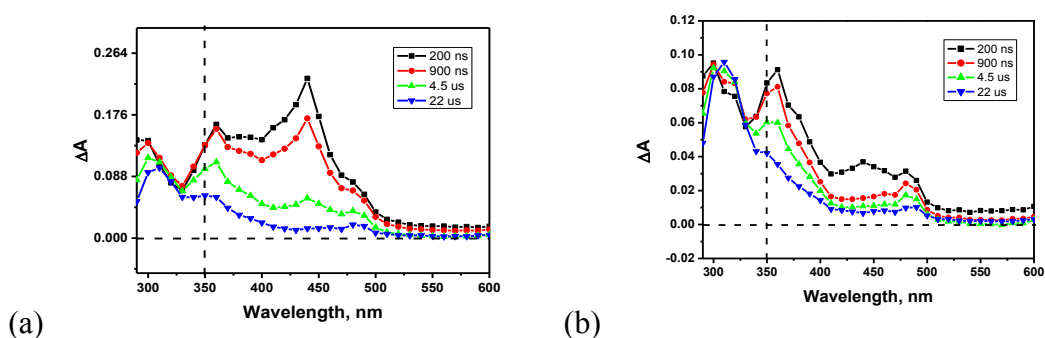


Figure 5.7. Transient absorption spectral changes of donor **4** (150  $\mu\text{M}$ ) in (a) anaerobic and (b) oxygenated MeCN. The vertical dashed line indicates the approximate wavelength above which the ground state species does not absorb; hence at longer wavelengths, ground state bleach is not a concern.

### 5.3.3.1 Identification of $^3\text{ArOH}$ Absorption Bands

In the photolysis of the naphtholic compounds, an oxygen-dependent species is clearly observed in MeCN absorbing between 400-470 nm. For model compound, 2-naphthol, the spectra of its oxygen-dependent transient species observed here matched well with the reported spectrum absorption spectra of 2-naphthol's triplet-triplet absorption<sup>194</sup> and that obtained in Chapter 4, Section 4.7.3. The triplet decayed at a rate of  $k_{\text{obs}} = (4.8 \pm 0.6) \times 10^5 \text{ s}^{-1}$ ;  $\tau = 2.0\text{-}2.1 \mu\text{s}$  (Figure 5.8(a) and Table 5.3). This is similar to the decay of the triplet state of 2-naphthol in  $\text{N}_2$ -saturated benzene obtained by pulse radiolysis ( $k_{\text{obs}} = 1.0 \times 10^5 \text{ s}^{-1}$ ).<sup>195</sup> Based on the similarities in absorption bands, amplitude, and decay rate constants (Figure 5.9 and Table 5.3), the oxygen-dependent band observed for donor **4** was also assigned to triplet state absorption.

Table 5.3. Decay of triplet states and naphthoxyl radicals generated upon laser flash photolysis of naphtholic compounds in MeCN. Triplet decay rates were analyzed as single decay kinetics at 420 or 440 nm; amplitude at 440 nm is reported. Naphthoxyl radical decay rates were analyzed at 360 and 440 nm and global analysis (see Appendix D); amplitude at 360 nm is reported.

Molecule	Triplet Decay		Decay Processes for Naphthoxyl Radicals		
	Rate Constants <i>Single <math>\lambda</math></i> ( $s^{-1}$ )	Amplitude (a.u.)	Rate Constants <i>Single <math>\lambda</math></i> ( $s^{-1}$ )	Rate Constants <i>Global Analysis</i> ( $s^{-1}$ )	Amplitude (a.u.)
<b>2-NpOH</b>	$(4.8 \pm 0.6) \times 10^5$	0.18	$(2.0 \pm 0.3) \times 10^5$ $(2.8 \pm 0.8) \times 10^4$	$(1.42 \pm 0.01) \times 10^5$ $(2.36 \pm 0.01) \times 10^4$	0.09
<b>Donor <u>4</u></b>	$(4.4 \pm 0.3) \times 10^5$	0.23	$(1.4 \pm 0.8) \times 10^5$ $(1.4 \pm 0.2) \times 10^4$	$(1.44 \pm 0.01) \times 10^5$ $(2.59 \pm 0.01) \times 10^4$	0.08

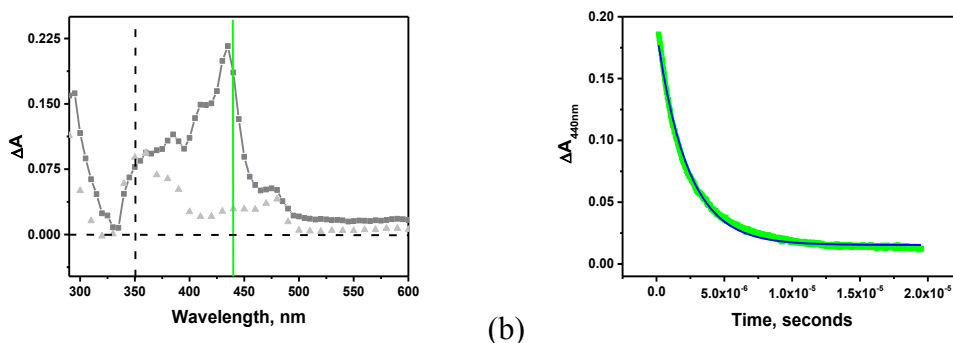


Figure 5.8. (a) Transient absorption spectral changes of 2-naphthol (150  $\mu\text{M}$ ) after 1000 ns following excitation in anaerobic (dark gray) and oxygenated (light gray) MeCN. Probe wavelength is highlighted in green. The vertical dashed line indicates the approximate wavelength above which the ground state species does not absorb; hence at longer wavelengths, ground state bleach is not a concern. (b) Best fit of the kinetic trace at 440 nm observed in anaerobic conditions to a first-order rate equation giving  $k_{\text{obs}} = (4.4 \pm 0.1) \times 10^5 \text{ s}^{-1}$ .

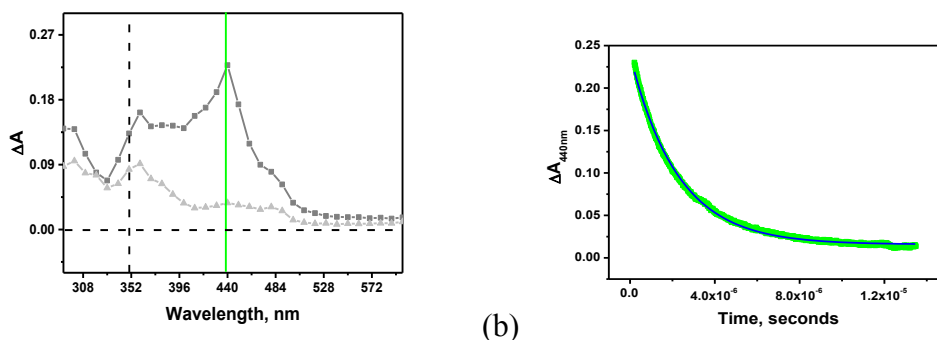


Figure 5.9. (a) Transient absorption spectral changes of donor 4 (150  $\mu\text{M}$ ) after 1000 ns following excitation in anaerobic (dark gray) and oxygenated (light gray) MeCN. Probe wavelength is highlighted in green. The vertical dashed line indicates the approximate wavelength above which the ground state species does not absorb; hence at longer wavelengths, ground state bleach is not a concern. (b) Best fit of the kinetic trace at 440 nm observed in anaerobic conditions to a first-order rate equation giving  $k_{\text{obs}} = (4.5 \pm 0.1) \times 10^5 \text{ s}^{-1}$ .

### 5.3.3.2 Identification of Solvated Electrons

Hydroxyarenes can undergo ionization to form radical cations (ions that have both a positive formal charge and an unpaired electron), resulting from the photoejection of an electron.<sup>195</sup> The ns-TA spectra reveal a band at 750 nm upon excitation of **4b** (see Figure 5.10). This band is assigned to solvated electrons.<sup>201</sup> The observation of solvated electrons indicates that radical cations are also likely formed but either rapidly decay or are not generated in sufficient quantum yields to be observed upon photolysis of **4b**.

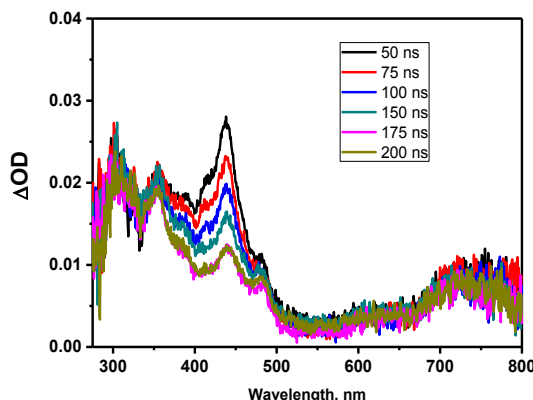


Figure 5.10. ns-TA spectrum from excitation of donor **4b** in aerobic MeCN.

### 5.3.3.3 Identification of Naphthoxyl Radical Species

Phenoxyl or naphthoxyl radicals ( $\text{ArO}^{\bullet}$ ) are formed via O—H bond homolysis after  $\pi$ - $\pi^*$  excitation<sup>202</sup> via a triplet state or via deprotonation of the radical cation ( $\text{ArOH}^{+\bullet}$ ).<sup>203</sup> However, due to their low quantum yields, the chemistry is not well established for phenoxyl or naphthoxyl radicals. The absorption spectrum of 2-NpO $^{\bullet}$  was reported from pulse radiolysis data and observed to have two absorption bands with  $\lambda_{\text{max}}$  at 350 (shoulder at 380) and 475 nm.<sup>196</sup> Under oxygenated conditions, photolysis of model compound 2-naphthol and donor **4** produced species with absorption bands at 360 nm and 480 nm (Figure 5.11). 2-Naphthol's radical species decayed via two consecutive first-order reactions ( $k_{\text{obs}} = (2.0 \pm 0.3) \times 10^5 \text{ s}^{-1}$ ;  $\tau = 4.3\text{-}5.9 \mu\text{s}$  and  $k_{\text{obs}} = (2.8 \pm 0.8) \times 10^4 \text{ s}^{-1}$ ;  $\tau = 27\text{-}50 \mu\text{s}$ ; Table 5.3). Based on the spectral and kinetic similarities to 2-naphthol,<sup>196</sup> the species observed upon photolysis of donor **4** in MeCN was assigned to the naphthoxyl radical species of donor **4** (Figure 5.11(a) and Table 5.3).

### 5.3.3.4 Observation of an Additional Species for Compound **4**

An unidentified band was observed at 310 nm for the photolysis of donor **4** ~900 ns after excitation (Figure 5.11(a)). The band does not change in intensity over time from ~900

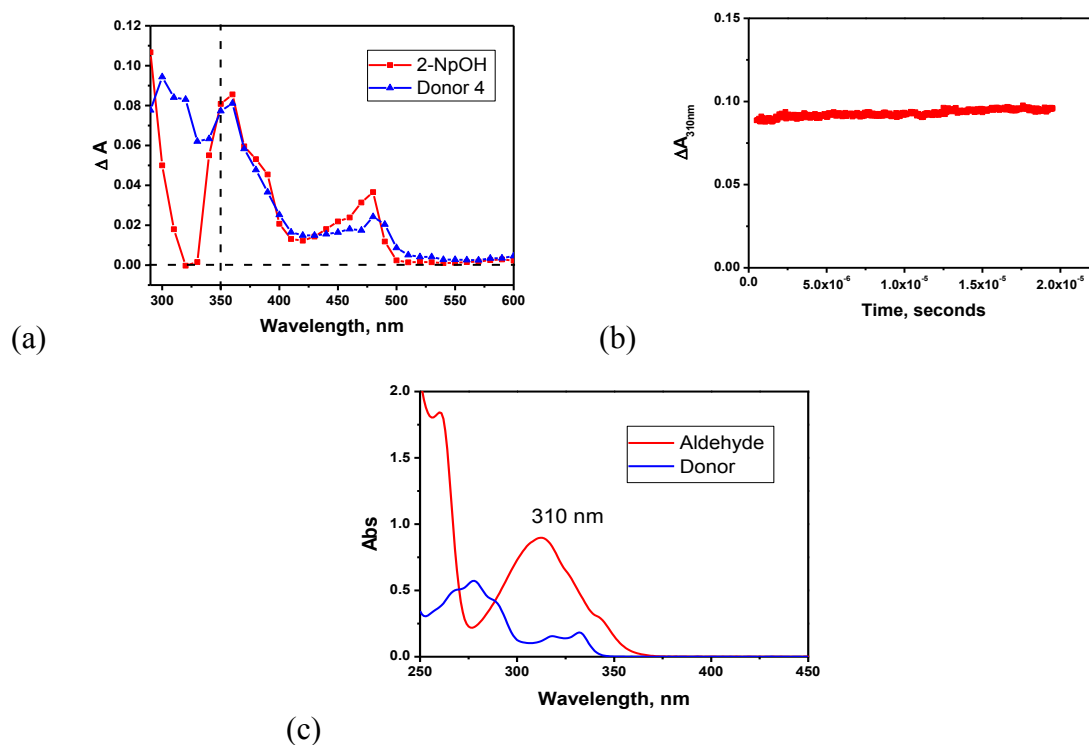


Figure 5.11. (a) Transient absorption spectra for 2-naphthol and **4** in oxygenated MeCN at 900 ns. The vertical dashed line indicates the approximate wavelength above which the ground state species does not absorb; hence at longer wavelengths, ground state bleach is not a concern. (b) Single wavelength kinetics at 310 nm. (c) UV-vis spectra for aldehyde **8** (75  $\mu\text{M}$ ) and **4** (80  $\mu\text{M}$ ) in MeCN.

ns (Figure 5.11(b)) and is not observed upon photolysis of 2-naphthol (Figure 5.11(a)). Notably, aldehyde **8** absorbs more strongly at 310 nm compared to donor **4** (Figure 5.11(c)). Based on this, the absorption band at 310 nm observed in the photolysis of donor **4** is assigned to product species aldehyde **8**. This implies that N-O bond cleavage occurs prior to 900 ns.

### 5.3.4 Femtosecond Transient Absorption of **4b** in MeCN

Femtosecond transient absorption spectra were recorded in order to probe the time-resolved spectroscopic characteristics of donor **4b**. The ns-LFP data indicated that aldehyde **8** was formed prior to 900 ns after excitation of donor **4b**. The fs-TA analysis of 2-naphthol was used to assist with identification of excited states attributable to photophysical or photochemical processes relating to the naphtholic structure (that is, not related to O-N bond cleavage; see Chapter 4, Section 4.4.3). The fs-TA experiments were performed during a research visit to the University of Hong Kong with assistance from the research group of Prof. David Lee Phillips.

Photolysis of donor **4b** in MeCN produced bands at 340 nm and 430 nm which arose within the first picosecond (Figure 5.12(a)). These are assigned to the  $S_1$  to  $S_n$  absorption. From  $\sim 1$  ps to 34 ps, donor **4b** shows a decrease in absorbance at 330 nm and increase in absorbance at 440 nm in MeCN (Figure 5.12(b)). This process is assigned to vibrational cooling of the  $S_1$  state losing heat to the solvent.<sup>151</sup> Bands at 340 and 420 nm (broad shoulder at 550 nm) then decrease within the next three nanoseconds (Figure 5.12(c)). This is assigned to the decay of donor **4b**'s  $S_1$  state. The triplet state decays slower at 430 nm compared with the  $S_1$  state, which is observed at 550 nm (Figure 5.12(d)). Donor **4b**'s and 2-naphthol's fs-TA spectra were compared to understand how the loss of leaving group affects ultrafast processes. Throughout the ultrafast photolysis studies, donor **4b** had strikingly similar spectra to model compound 2-naphthol (see Chapter 4, Section 4.4.3). Each species entered into an  $S_1$  state within  $\sim 1$  ps, underwent vibrational cooling as observed by narrowing of the absorption bands, and then decayed into the ground state or entered into a triplet state. This suggests that the loss of leaving group to form the sulfonamide and aldehyde **8** ( $\sim 310$  nm) is not observable in the experiment's spectroscopic window.

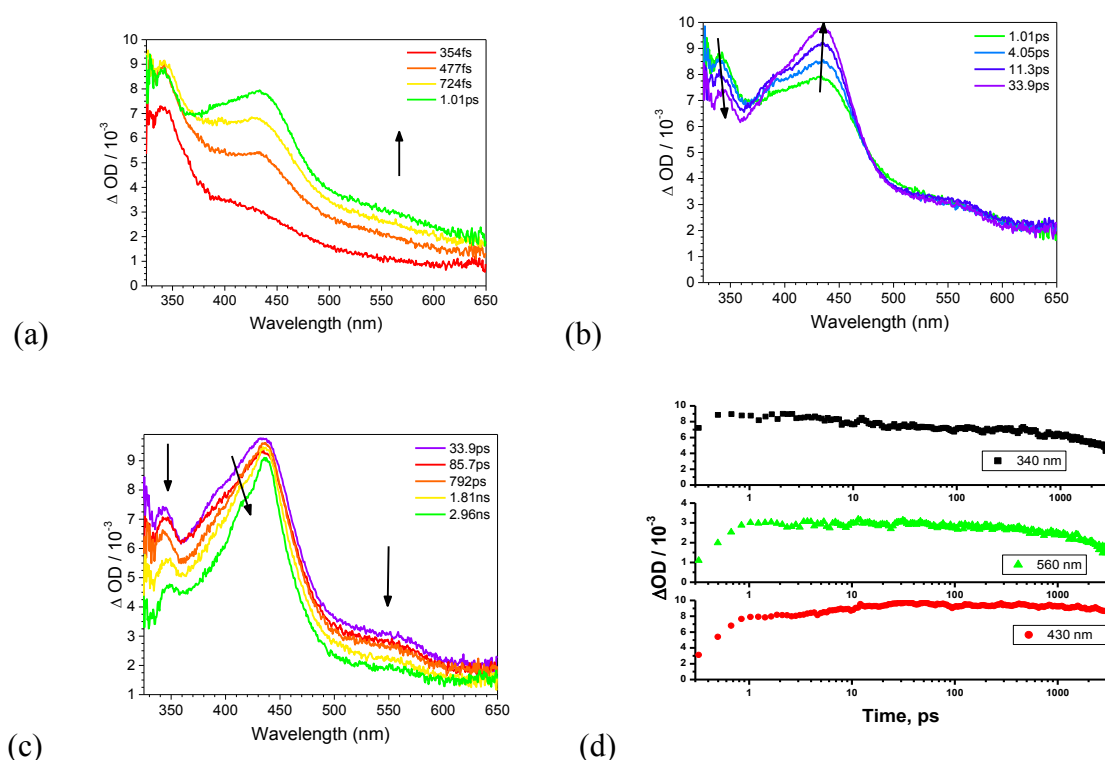


Figure 5.12. fs-TA of donor **4b** in aerobic MeCN achieved from 267 nm excitation.

## 5.4 STUDIES ON N-O BOND CLEAVAGE FROM EXCITATION OF THE NAPHTHOLATE ANALOGUE OF DONOR **4**

### 5.4.1 Homolytic versus Heterolytic Bond Cleavage

The aromatic photoproduct generated by **4b** was previously examined in MeCN and was observed to proceed via primarily heterolytic bond cleavage. The type of bond cleavage proceeding from **4c** was also investigated (Scheme 5.3). The steady state photolysis of **4c** (2.49 mM) was monitored in an anaerobic mixture of 60:40 v/v CD<sub>3</sub>CN to 0.1 M NaOH using <sup>19</sup>F NMR spectroscopy (Figure 5.13(a)). Photolysis of **4c** generated sulfonamide CF<sub>3</sub>SO<sub>2</sub>NH<sub>2</sub> (Figure 5.13(b)). The observed rate of photodecomposition was pseudo first-order ( $k_{\text{obs}} = 0.20 \pm 0.01 \text{ min}^{-1}$ ; Figure 5.13 (c)). To characterize the aromatic photoproducts, a partial conversion experiment was completed for photolysis of **4c** (2.49

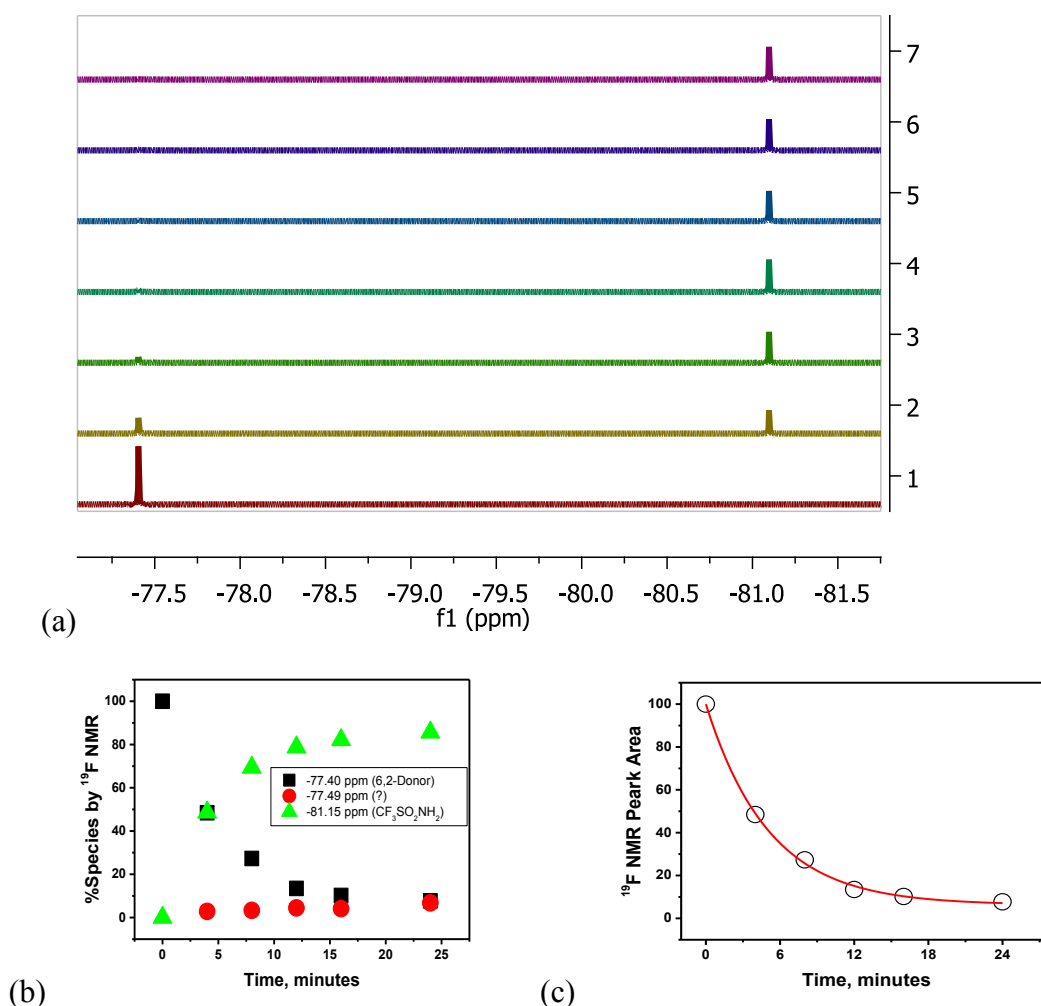


Figure 5.13. (a) <sup>19</sup>F NMR spectra as a function of irradiation time (8 x 350 nm bulbs, 4 W; 0, 4, 8, 12, 16, and 24 min) for the photodecomposition of **4** (2.49 mM) in anaerobic 60:40 v/v CD<sub>3</sub>CN to 0.1 M NaOH. (b) Plot of observed species as a function of irradiation time. (c) Best fit of donor **4** (-CF<sub>3</sub>) to a first-order rate equation, giving  $k_{\text{obs}} = 0.20 \pm 0.01 \text{ min}^{-1}$ .

mM) in an anaerobic mixture of 60:40 v/v CD<sub>3</sub>CN to 0.1 M NaOH using <sup>1</sup>H NMR spectroscopy (Figure 5.14(a)). By <sup>19</sup>F NMR spectroscopy, 50% of **4c** was converted to CF<sub>3</sub>SO<sub>2</sub>NH<sub>2</sub>. A 1:1 ratio of donor **4c** to aldehyde **8** was observed in the photoproduct mixture, indicating that aldehyde **8** is the primary aromatic photoproduct produced from N-O heterolytic bond cleavage.

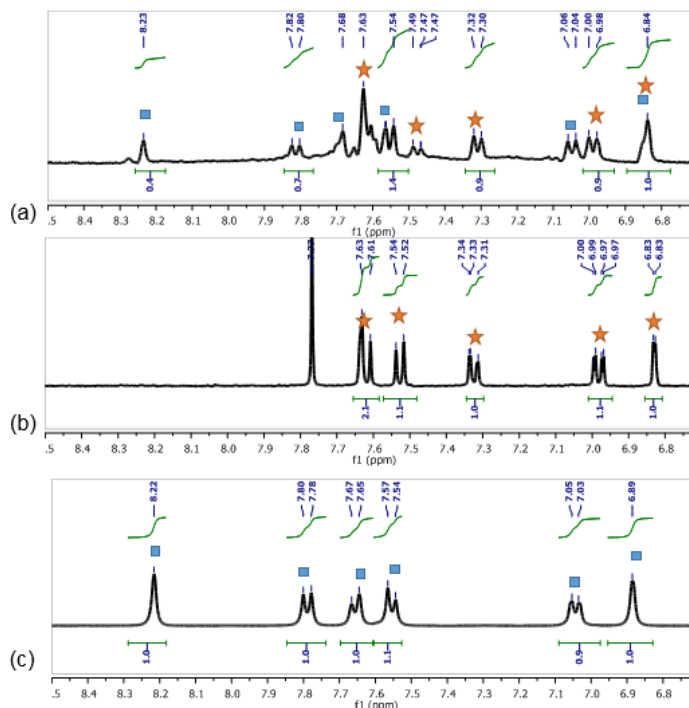


Figure 5.14. (a) <sup>1</sup>H NMR spectrum of **4** (2.49 mM) in 80:20 v/v CD<sub>3</sub>CN to 0.1 M NaOH upon total photolysis (50% conversion to CF<sub>3</sub>SO<sub>2</sub>NH<sub>2</sub>). (b) <sup>1</sup>H NMR spectrum of an authentic sample of **4** in 80:20 v/v CD<sub>3</sub>CN to 0.1 M NaOH.  $\delta = 7.63, 7.54, 7.33, 7.31, 7.00, 6.99, 6.97, 6.83$  ppm. (c) <sup>1</sup>H NMR spectrum of an authentic sample of aldehyde **8** in 80:20 v/v CD<sub>3</sub>CN to 0.1 M NaOH. Aldehyde **8**:  $\delta = 8.22, 7.80, 7.78, 7.67, 7.65, 7.57, 7.54, 7.05, 7.03, \text{ and } 6.89$  ppm.

#### 5.4.2 Photoproduct Quantum Yields

The efficiency of N-O bond cleavage of **4c** was investigated by determining the photoproduct quantum yields in alkaline conditions using azobenzene actinometry. As described previously, CF<sub>3</sub>SO<sub>2</sub>NH<sub>2</sub> was used as a chemical marker for the N-O bond cleavage pathway. In 60:40 v/v MeCN to 0.1 M NaOH, **4c** had a photoproduct quantum yield of  $\Phi_{PP} = 0.27 \pm 0.07$  (unaffected by oxygen; Table 5.2). Therefore, N-O bond cleavage proceeding from **4c** in alkaline conditions is slightly more favorable than N-O bond cleavage proceeding from **4b** in MeCN ( $0.18 \pm 0.04$ ; Table 5.2).

### 5.4.3 Formation of **4c** from Excitation of **4a** in Aqueous Solutions

The excited state  $pK_{a(OH)^*}$  of **4** was estimated to be  $pK_{a(OH)^*} \approx 3.4 \pm 0.4$  (Chapter 4, Section 4.3.1). Hence, excitation of **4a** in neutral solutions could potentially result in an excited state **4c** through excited state proton transfer to solvent (PTTS). However, previous work showed that PTTS does not readily occur for 2-naphthol or donor **4** at low aqueous concentrations of 5.0 mM phosphate buffer (pH 7.0; 20% by vol.) in MeCN (see Chapter 5, Section 4.4.2). Therefore, the ability of **4a** to generate **4c** from excitation in solvent mixtures with a higher percent of the aqueous component was examined and correlated with N-O bond cleavage pathway selectivity.

The naphtholate analogues have a spectroscopically distinguishable emission spectrum compared to that of their parent molecules; thus, fluorescence spectroscopy is a common technique used to determine when PTTS occurs from the OH to solvent.<sup>137</sup> Following additions of 5.0 mM phosphate buffer solution (pH 7.0), the fluorescence intensity of **4** increases, with bands observed from the parent structure ( $\lambda_{max} = 360$  nm), its conjugate base (**4c**,  $\lambda_{max} = 441$  nm), and a sideband (500-600 nm). Due to fluorescence quenching caused by HNO photorelease (see Chapter 4, Section 4.2), it is difficult to determine what percentage of 5.0 mM phosphate buffer (pH 7.0) in MeCN is required for PTTS to occur. Therefore, the model compound 2-naphthol was used as it has similar  $pK_a$  and  $pK_a^*$  values to donor **4** (Chapter 4, Section 4.3.1). The emission spectra of 2-naphthol was recorded upon additions of small and large amounts of 5.0 mM phosphate buffer (pH 7.0) in co-solvent MeCN. Following additions of 40% v/v of 5.0 mM phosphate buffer solution (pH 7.0), a band is observed with  $\lambda_{max} = 410$  nm (Figure 5.15). This is assigned

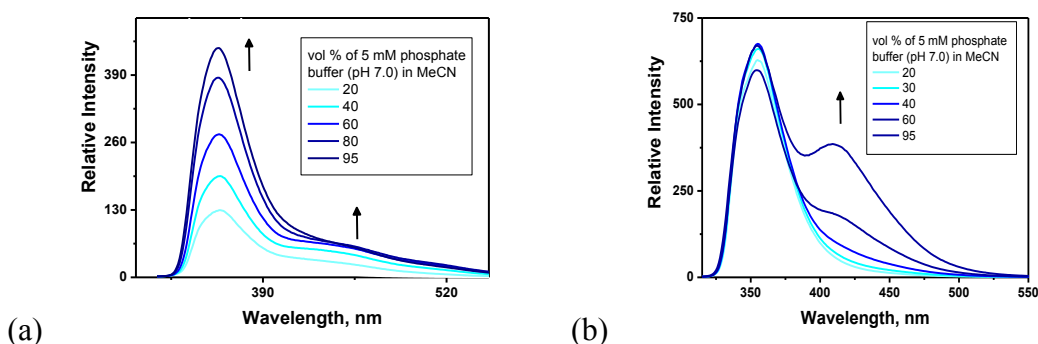


Figure 5.15. (a) Emission spectra of donor **4** ( $\mu\text{M}$ ) in MeCN upon addition of 20-95% by vol. of 5.0 mM phosphate buffer solution, pH 7.0. (b) Emission spectra of 2-naphthol ( $\mu\text{M}$ ) in MeCN upon addition of 20-95% vol. of 5.0 mM phosphate buffer solution, pH 7.0.

to emission from 2-naphtholate, which is formed from PTTS. At concentrations of water > 22 M (or 40% by vol), PTTS to solvent from the naphtholic OH can occur.

The solvent dependence of N-O bond cleavage from **4a** was investigated in CD<sub>3</sub>CN at varying concentrations of water (5.0 mM phosphate buffer solution, pH 7.0). Samples were prepared and irradiated until fully converted to photoproducts. Figure 5.16 shows that increasing additions of 5.0 mM phosphate buffer (pH 7.0) increases the selectivity towards N-O bond cleavage (as indicated by CF<sub>3</sub>SO<sub>2</sub>NH<sub>2</sub> rather than C-O and N-S bond cleavages to give CF<sub>3</sub>SO<sub>2</sub><sup>-</sup>). Donor **4** (mM) is not readily soluble in higher aqueous solvent conditions, and thus, photolysis could not be completed at concentrations above 80% by vol. H<sub>2</sub>O in CD<sub>3</sub>CN. These findings imply that PTTS enables formation of **4c** at concentrations > 40% by vol. of 5.0 mM phosphate buffer solution (pH 7.0) in MeCN; **4c** selectively undergoes N-O bond cleavage. Hence, PTTS decreases selectivity towards HNO generation from photolysis of donor **4**.

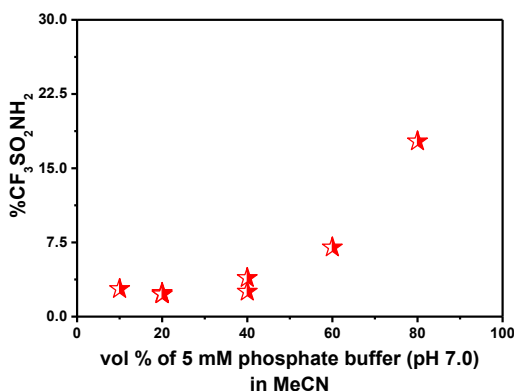


Figure 5.16. Effect of solvent composition on the percentage of N-O bond cleavage generated upon irradiation of HNO donor **4a** (0.500-2.00 mM; Rayonet photoreactor, 8 x 350 nm bulbs, 4 W) in mixtures of 5.0 mM phosphate buffer (pH 7.0) in CD<sub>3</sub>CN (v/v).

### 5.5 THE INFLUENCE OF EXCITED STATE INTRAMOLECULAR PROTON TRANSFER ON PATHWAY SELECTIVITY

The influence of excited state intramolecular interactions was investigated using donor **1**. Donor **1** is the structural analogue of donor **4**, but contains the 3,2-HNM photocage as opposed to the 6,2-HNM photocage. Donor **1** can achieve a maximum 70% selectivity for HNO photorelease as opposed to N-O bond cleavage (Scheme 5.1, Pathway (a) and (c)), whereas donor **4** can achieve stoichiometric (~98%) HNO generation (Scheme 5.2). These findings imply that intramolecular interactions can lead N-O bond cleavage.

### 5.5.1 Investigation of Excited State Intramolecular Interactions in MeCN

First, the excited state intramolecular reactions of donor **1** were investigated in MeCN. In MeCN, donor **1** is in the neutral form of the molecule (i.e. deprotonation does not occur). The photolysis of donor **1** in MeCN eliminates the possibility of excited state proton transfer (ESPT) occurring via a solvent bridge because MeCN is aprotic.<sup>153</sup> Hence, excited state proton transfer can only occur via an intramolecular proton transfer from the photoacidic site to the photobasic site.<sup>153</sup>

#### 5.5.1.1 Photoproduct Characterization in MeCN

Steady state photolysis of **1** (1.00 mM) was carried out in CD<sub>3</sub>CN. The photolytic product solution (100% conversion, 30 min irradiation) was analyzed by <sup>1</sup>H NMR and <sup>19</sup>F NMR spectroscopy. The <sup>19</sup>F NMR spectrum showed two major photoproducts ( $\delta$  -79.9 (CF<sub>3</sub>SO<sub>2</sub>NH<sup>-</sup>) and -81.2 ppm (CF<sub>3</sub>SO<sub>2</sub>NH<sub>2</sub>); Figure 5.17(a)). By comparison to authentic samples, aldehyde **6** (Figure 5.18(b);  $\delta$  8.43, 7.98 ppm) and diol **7** (Figure 5.18(c);  $\delta$  7.16 ppm) are observed in the photolytic mixture. The <sup>1</sup>H NMR integration (aldehyde **6**, 60%; diol **5**, 40%) shows that the main photoproduct is aldehyde **6** (Figure 5.18(a)). The ground state stability of aldehyde **6** was investigated separately by our collaborators and shown to be stable. This indicates that conversion of aldehyde **6** to diol **5** does not occur. Observation of two aromatic species (aldehyde **6** and diol **5**) suggests that at least two mechanisms lead to N-O bond cleavage. Based on the studies of donor **4**, one of these pathways is via N-O bond cleavage to form CF<sub>3</sub>SO<sub>2</sub>NH<sub>2</sub> and aldehyde **6**; the other pathway is proposed to occur from ES IPT between the photoacidic naphtholic OH and the oxygen atom in the leaving group, generating CF<sub>3</sub>SO<sub>2</sub>NH(H) and diol **5** (Scheme 5.4).

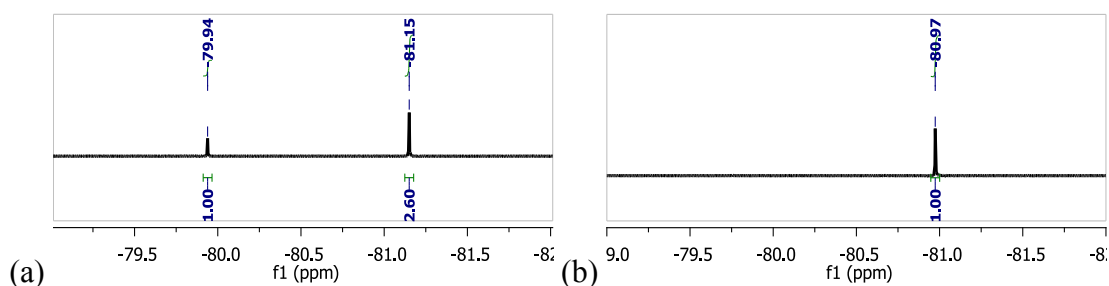


Figure 5.17. <sup>19</sup>F NMR of photolyzed donor **1** (1.00 mM; Rayonet photoreactor, 8 x 350 nm bulbs, 4 W) in (a) anaerobic CD<sub>3</sub>CN and (b) with addition of 20% by volume 5.0 mM phosphate buffer solution, pH 7.0.

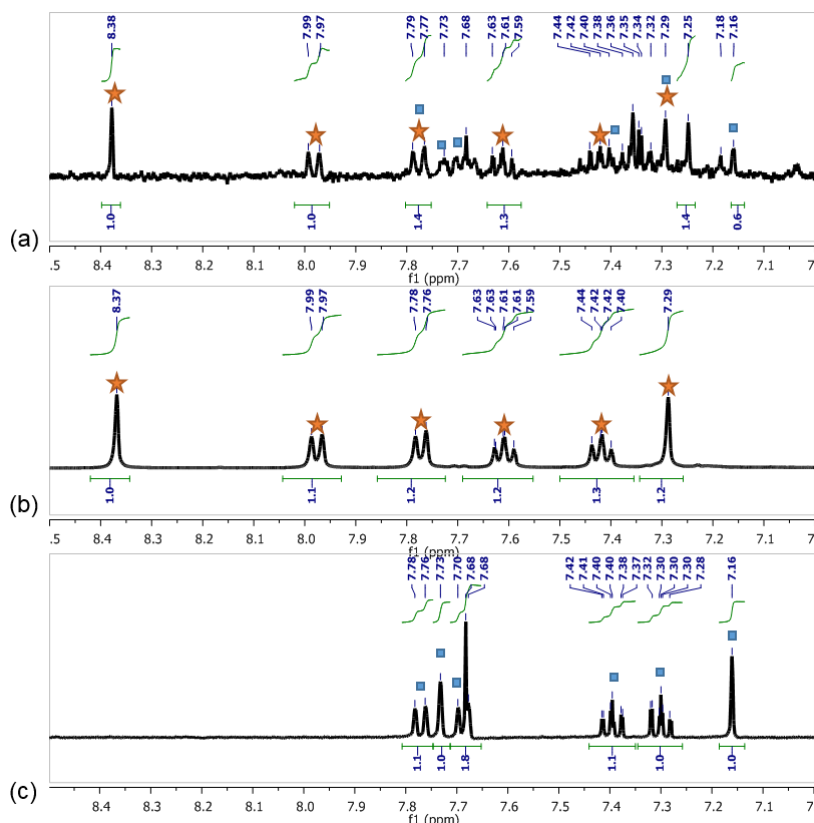
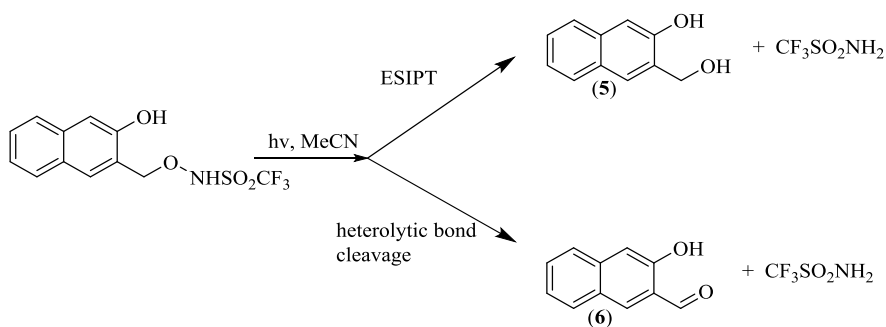


Figure 5.18. (a)  $^1\text{H}$  NMR spectra of photolyzed donor **1** (1.00 mM; Rayonet photoreactor, 8 x 350 nm bulbs, 4 W) in anaerobic  $\text{CD}_3\text{CN}$  (100% conversion to  $\text{CF}_3\text{SO}_2\text{NH}_2$ ). (b)  $^1\text{H}$  NMR spectrum of authentic aldehyde **6** in  $\text{CD}_3\text{CN}$ . Aldehyde **6**:  $\delta = 10.26, 10.12, 8.37, 7.99, 7.97, 7.78, 7.76, 7.63, 7.63, 7.61, 7.61, 7.59, 7.44, 7.42, 7.42, 7.40, 7.29$  ppm. (c)  $^1\text{H}$  NMR spectrum of authentic diol **7** in  $\text{CD}_3\text{CN}$ .  $\delta = 7.78, 7.76, 7.73, 7.70, 7.68, 7.42, 7.41, 7.40, 7.38, 7.37, 7.32, 7.32, 7.30, 7.30, 7.30, 7.28, 7.16, 4.79$  ppm. Residual chloroform is observed at 7.68 ppm.

Scheme 5.4. Proposed decomposition pathways observed upon photolysis of HNO donors **1** in MeCN.



### 5.5.1.2 Photoproduct Quantum Yields of N-O Bond Cleavage in MeCN

The influence of photoprotection using either the 6,2-HNM-PPG or 3,2-HNM-PPG was investigated further by determining photoproduct quantum yields for donors **4** and **1**,

using azobenzene actinometry. The photoproduct quantum yield for donors **4** and **1** in aerobic MeCN was  $\Phi_{pp} = 0.18$  and  $0.53$  (Table 5.4). The high quantum yield of donor **1** to yield  $\text{CF}_3\text{SO}_2\text{NH}_2$  shows that the 3,2-HNM photocage enables an additional process to occur (i.e. ES IPT leading to N-O bond cleavage).

Table 5.4. Photoproduct quantum yields for N-O bond cleavage (as indicated by chemical marker  $\text{CF}_3\text{SO}_2\text{NH}_2$ ) in MeCN.

Photoactive HNO Donor	MeCN
Donor <b>4</b>	$0.18 \pm 0.04$ (aerobic)
	$0.18 \pm 0.02$ (anaerobic)
Donor <b>1</b>	$0.53 \pm 0.06$ (aerobic)

## 5.5.2 Investigation of Excited State Intramolecular Interactions in Aqueous Solutions

### 5.5.2.1 Photoproduct Characterization in Aqueous Solutions

The products formed upon photodecomposition of donor **1** in a solvent mixture of 60:40 v/v  $\text{CD}_3\text{CN}$  to 0.10 M phosphate buffer (pH 7.0) were characterized using  $^{19}\text{F}$  NMR spectroscopy. The relocation of the OH group from the 6- to the 3- position on the

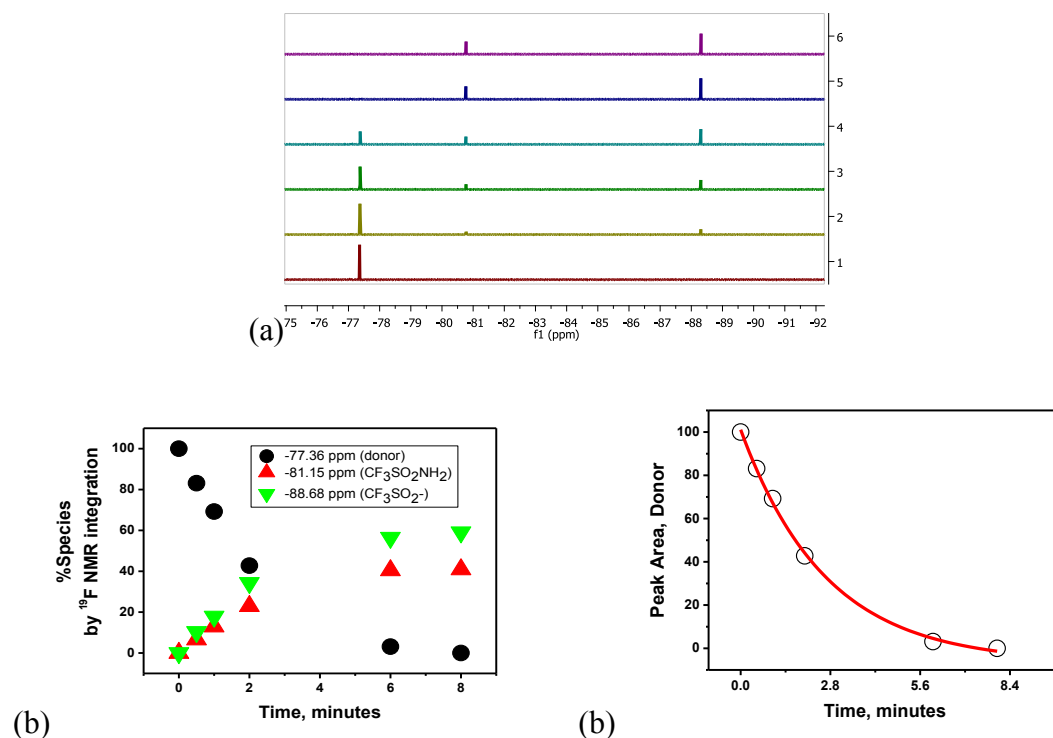
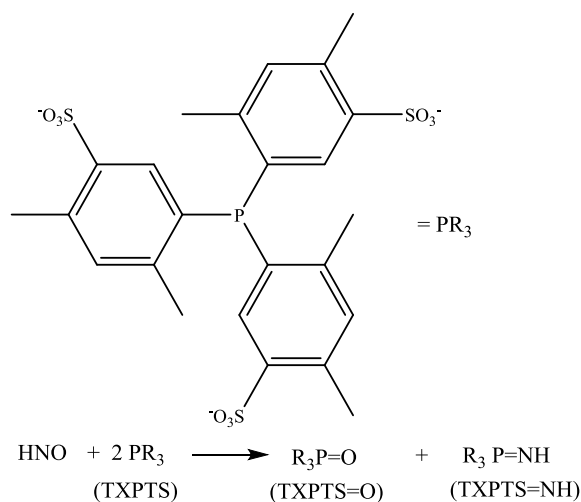


Figure 5.19. (a)  $^{19}\text{F}$  NMR spectra as a function of irradiation time (0, 0.5, 1.0, 2.0, 6.0, and 8.0 min) for the photodecomposition of HNO donor **1** (1.0 mM) in an anaerobic mixture of 60:40 v/v  $\text{CD}_3\text{CN}$  to 5 mM phosphate buffer solution, pH 7.0. (b) Plot of observed species as a function of irradiation time. Final composition:  $\text{CF}_3\text{SO}_2^-$  ( $\delta$  -88.7 ppm; 41%);  $\text{CF}_3\text{SO}_2\text{NH}_2$  ( $\delta$  -81.2 ppm; 59%). (c) Best fit of the peak area of donor **1** ( $-\text{CF}_3$ ) to a first-order rate equation, giving  $k_{\text{obs}} = 0.38 \pm 0.03 \text{ min}^{-1}$ .

aromatic is unlikely to significantly affect the  $pK_a$  values of the naphtholic OH or the NH on the leaving group. It is likely that the nitrogen atom of donor **1** is not protonated in this solvent mixture. Upon total photolysis, donor **1** generated a mixture of fluorinated species:  $\text{CF}_3\text{SO}_2\text{NH}_2$  (40%) and  $\text{CF}_3\text{SO}_2^-$  (60%; Figure 5.19).  $\text{CF}_3\text{SO}_2\text{NHOH}$  or its conjugate base were not observed during the photolysis of donor **1** by  $^{19}\text{F}$  NMR spectroscopy.

Evidence of HNO generation from photolysis of donor **1** in aqueous solutions was next investigated. It is well established by others that the sodium salt of *tris*-(4,6-dimethylphenyl)phosphine-3,3',3''-trisulfonate (TXPTS) efficiently traps HNO to form the corresponding phosphine oxide and aza-ylide (Scheme 5.5).<sup>263</sup> The reaction is not stoichiometric due to hydrolysis of the phosphine aza-ylide to the phosphine oxide.<sup>30</sup> Prior to using TXPTS in trapping experiments from photolysis of donor **1**, a series of control studies were performed.

Scheme 5.5. HNO reacts with the phosphine TXPTS to give the corresponding phosphine oxide and aza-ylide.



Typically, TXPTS is used in aqueous solutions;<sup>264-266</sup> however, donor **1** is not soluble in water and therefore requires mixed solvent conditions. The stability of TXPTS (5.00 mM) was investigated in an anaerobic mixture of 80:20 v/v MeCN to 5.0 mM carbonate buffer (pH 10.3). The sample showed no signs of decomposition after 48 hr as monitored by  $^{31}\text{P}$  and  $^1\text{H}$  NMR spectroscopy (data not shown). The photostability of TXPTS was also investigated. An anaerobic sample of TXPTS (2.30 mM) was prepared in 80:20 v/v  $\text{CD}_3\text{CN}$  to 5 mM phosphate buffer (pH 7.0) in an airtight NMR tube (J-Young cap). The sample was irradiated and  $^{31}\text{P}$  NMR spectra recorded at a range of time intervals. After

132 min irradiation, the  $^{31}\text{P}$  NMR peak for the TXPTS reactant at  $\delta$  -35.1 ppm was essentially negligible and two major photoproducts were observed at  $\delta$  -38.2 and -41.8 ppm (Figure 5.20). A plot of the  $^{31}\text{P}$  NMR peak area of TXPTS versus irradiation time is given in Figure 5.21. This data were fit to a first-order rate constant for decomposition of TXPTS, giving  $k_{\text{obs}} = 0.029 \pm 0.002 \text{ min}^{-1}$ ;  $t_{1/2} \sim 24 \text{ min}$ .

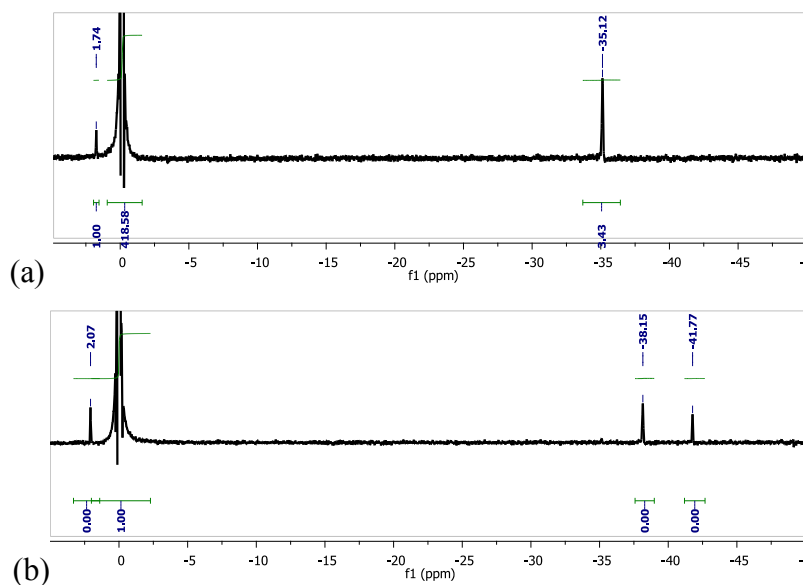


Figure 5.20. (a)  $^{31}\text{P}$  NMR spectra for an anaerobic solution of TXPTS (2.30 mM) in 80:20 v/v  $\text{CD}_3\text{CN}$  to phosphate buffer (5.0 mM, pH 7.0); (b) Sample (a) irradiated for 132 min (Rayonet photoreactor, 8 x 350 nm bulbs, 4 W). The peaks at  $\delta$  1.75 (a) and 2.07 ppm (b; note that the insufficient buffering capacity of the buffer is most likely responsible for the difference in chemical shift values) can be assigned to the phosphate buffer,  $\delta$  0.00 ppm to the external reference (phosphoric acid),  $\delta$  -35.12 ppm to TXPTS, and  $\delta$  -38.2 and -41.8 ppm to two major products of TXPTS photodecomposition. (No attempt was made to characterize these latter species.)

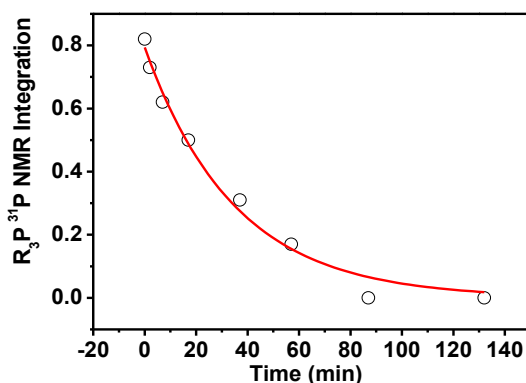


Figure 5.21. Plot of the  $^{31}\text{P}$  NMR peak area of TXPTS versus total irradiation time. The data has been fit to a first-order equation, giving  $k_{\text{obs}} = 0.029 \pm 0.002 \text{ min}^{-1}$ .

The ability of TXPTS to trap HNO in mixed solvent conditions was investigated using HNO donor, methylsulfonylhydroxylamine (MSHA;  $\text{CH}_3\text{SO}_2\text{NHOH}$ ). MSHA spontaneously decomposes in alkaline conditions to generate HNO and  $\text{MeSO}_2^-$ .<sup>212</sup> MSHA does not readily absorb in the wavelength region of irradiation ( $350 \pm 50$  nm) and hence is therefore ideal to test the ability of TXPTS to trap HNO while the solution is simultaneously exposed to irradiation. Two samples were prepared of TXPTS (5.00 mM) and MSHA (2.50 mM) in anaerobic mixtures of 80:20 v/v  $\text{CD}_3\text{CN}$  to 5.0 mM carbonate buffer (pH 10.3; 550  $\mu\text{L}$  total). One sample was photolyzed for 5 min immediately after sample preparation while the other was exposed to ambient light only. The samples were both analyzed using  $^{31}\text{P}$  NMR spectroscopy (Figure 5.22). Aza-ylide ( $\delta$  37.0 ppm) and phosphine oxide ( $\delta$  40.6 ppm) were observed in both samples, confirming HNO release from photolysis of donor **1**.

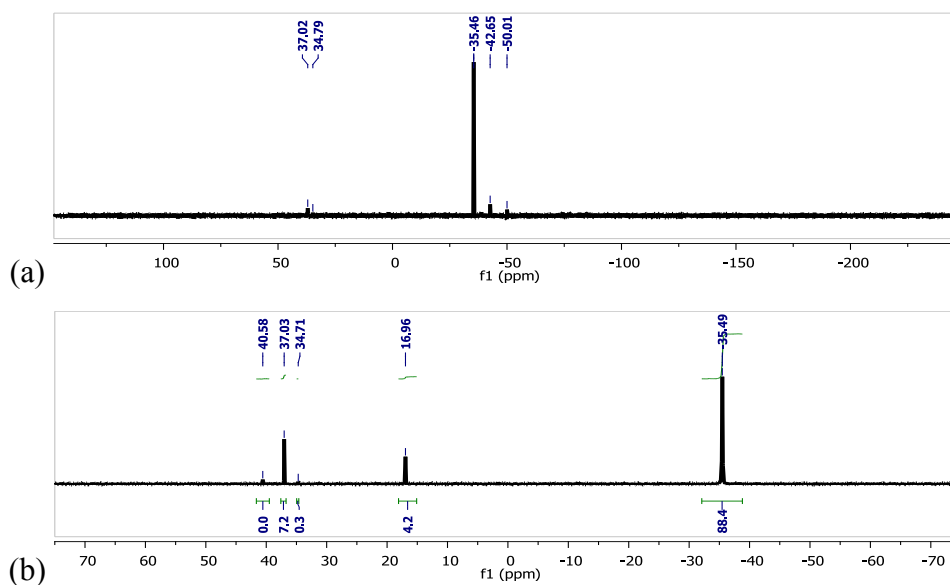


Figure 5.22. (a)  $^{31}\text{P}$  NMR spectra of a solution of TXPTS (5.00 mM) and  $\text{CH}_3\text{SO}_2\text{NHOH}$  (2.50 mM) in an anaerobic mixture of 80:20 v/v MeCN to 5 mM carbonate buffer (pH 10.3). (b)  $^{31}\text{P}$  NMR spectra of the same sample upon irradiation (5 min, 8 x 350 nm bulbs, 4 W).

Donor **1** was therefore irradiated in the presence of TXPTS to confirm that it releases HNO upon irradiation. A sample of TXPTS (20 mM) and donor **1** (5.0 mM) in an anaerobic mixture of 80:20 v/v  $\text{CD}_3\text{CN}$  to 5.0 mM phosphate buffer (pH 7.0) was prepared and transferred to a NMR tube fitted with a J-Young air-tight cap. The sample was irradiated for 12 min and analyzed by  $^1\text{H}$  NMR,  $^{19}\text{F}$  NMR, and  $^{31}\text{P}$  NMR spectroscopy. The  $^{19}\text{F}$  NMR spectrum showed  $\sim 85\%$  donor **1** decomposition to generate

the expected fluorinated photoproducts  $\text{CF}_3\text{SO}_2^-$  (14%) and  $\text{CF}_3\text{SO}_2\text{NH}_2$  (85%) ( $^{19}\text{F}$  NMR spectrum not shown). To establish the chemical shifts of the phosphine oxide and aza-ylide in this solvent system, an aliquot of the HNO donor Angeli's salt (final concentration 1.0 mM, 23  $\mu\text{L}$  of 37 mM stock solution, final volume 800  $\mu\text{L}$ ) dissolved in phosphate buffer (5 mM, pH 7.0) was subsequently added to the sample solution. Angeli's salt decomposes to form HNO and one equivalent of  $\text{NO}_2^-$  ( $4 < \text{pH} < 8$ ;  $k_{\text{obs}} = 6.8 \times 10^{-4} \text{ s}^{-1}$ ).<sup>74</sup> Angeli's salt was allowed to fully decompose (half-life  $\sim 20$  min) and  $^1\text{H}$  NMR,  $^{19}\text{F}$  NMR, and  $^{31}\text{P}$  NMR spectra recorded.

To determine which peaks in the spectra arise from photodecomposition of TXPTS, an anaerobic solution of TXPTS (20 mM) in the same solvent system was irradiated for 12 min and the product mixture analyzed by  $^1\text{H}$  NMR and  $^{31}\text{P}$  NMR spectroscopy.<sup>24</sup> An aliquot of Angeli's salt (final concentration 1.0 mM, 23  $\mu\text{L}$  of 37 mM stock solution, final volume 800  $\mu\text{L}$ ) dissolved in phosphate buffer (5 mM, pH 7.0) was subsequently added to this sample. The solution was allowed to react for 2 hr and NMR spectra recorded.

The  $^{31}\text{P}$  NMR spectra for all solutions are given in Figure 5.23. As expected, upon irradiation TXPTS decomposes in the absence of the donor **1** with the appearance of the phosphine oxide of TXPTS at  $\delta$  38.8 ppm and photoproducts at  $\delta$  19.2, -38.1 and -41.3 ppm. From the  $^1\text{H}$  NMR spectrum of the same solution, it was determined that  $\sim 34\%$  of the TXPTS decomposes (spectrum not shown). Upon the addition of the HNO donor Angeli's salt to this solution (no further irradiation), a new peak attributable to the phosphine aza-ylide of TXPTS appears at  $\delta$  35.7 ppm, and the peak arising from the phosphine oxide of TXPTS at  $\delta$  38.8 ppm increases in intensity (see Figure 5.23, spectrum 2). Comparison of the chemical shifts of the remaining species in these two spectra (the additional peaks upon the addition of Angeli's salt at  $\delta$  32.2 and 26.8 ppm) suggests that HNO may also react with the products of TXPTS photolysis. When a solution of HNO donor **1** (5 mM) and TXPTS (20 mM) is irradiated for 12 min under the same conditions (Figure 5.23, spectrum 3), a small peak attributable to the aza-ylide of TXPTS (TXPTS=NH) is observed at  $\delta$  36.3 ppm, in addition to the phosphine oxide ( $\delta$  38.78 ppm) and products arising from photodecomposition of TXPTS. Addition of Angeli's salt clearly shows an increase in the intensity of the aza-ylide ( $\delta$  36.4 ppm, TXPTS=NH) and phosphine oxide peaks ( $\delta$  38.8 ppm), as expected (Figure 5.23, spectrum 4). Hence, HNO is released from donor **1** upon irradiation.

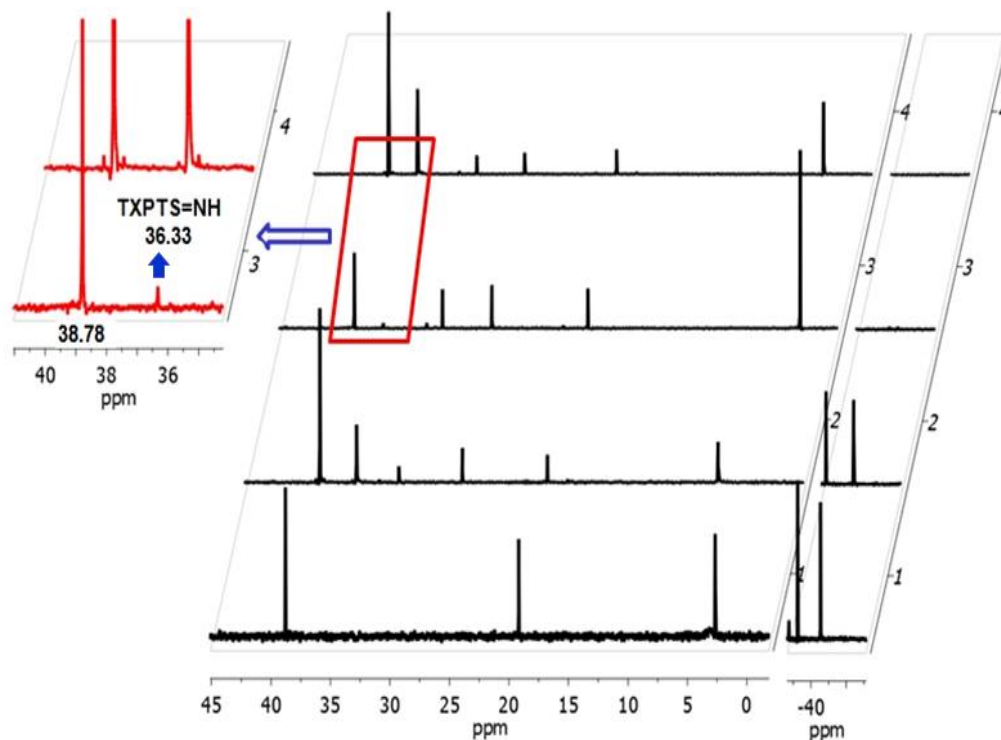


Figure 5.23.  $^{31}\text{P}$  NMR spectra for (1) the photodecomposition of TXPTS (20 mM; 350 nm, 4 W, 12 min irradiation) in an anaerobic mixture of 20:80 v/v  $\text{CD}_3\text{CN}$  to 5.0 mM phosphate buffer (pH 7.00), (2) solution 1 with addition of Angeli's salt (1 mM, no further irradiation), (3) a photolysis solution of donor **1** (5 mM) and TXPTS (20 mM) in an anaerobic mixture of 20:80 v/v  $\text{CD}_3\text{CN}$  to 5.0 mM phosphate buffer (pH 7.00; 350 nm, 4 W, 12 min irradiation) and (4) solution 3 with addition of Angeli's salt (1 mM, no further irradiation).

Another method was sought to confirm HNO release upon irradiation of donor **1**. Aquacobalamin ( $\text{H}_2\text{OCbl(III)}^+$ ) reacts stoichiometrically (1:1) with the HNO donor Angeli's salt to form bright orange nitroxylcobalamin,  $\text{NO}^- \text{-Cbl(III)}$  (also called nitrosylcobalamin<sup>213</sup>).<sup>78</sup> Importantly,  $\text{H}_2\text{OCbl(III)}^+$  reacts selectively with HNO as opposed to  $\text{NO}$ .<sup>227</sup>  $\text{H}_2\text{OCbl(III)}^+$  and  $\text{NO}^- \text{-Cbl(III)}$  have characteristic UV-vis spectra ( $\lambda_{\text{max}}(\text{H}_2\text{OCbl(III)}^+) = 317, 351, 411, 499, \text{ and } 527 \text{ nm}$ ;<sup>267</sup>  $\lambda_{\text{max}}(\text{NO}^- \text{-Cbl(III)}) = 256, 278$  (shoulder), 289, 315, 478 nm),<sup>78</sup> which allows for convenient monitoring of the reaction using the sharp isosbestic points occurring at 341, 370, and 498 nm upon conversion of  $\text{H}_2\text{OCbl(III)}^+$  to  $\text{NO}^- \text{-Cbl(III)}$  in aqueous solution.<sup>230,268</sup> A partial photolysis experiment was performed on a reaction mixture of  $\text{H}_2\text{OCbl(III)}^+$  and donor **1**. This experiment is not included in this thesis as it has been published in another research group member's thesis.<sup>209</sup> The ratio of  $\text{H}_2\text{OCbl(III)}^+$  conversion to  $\text{NO}^- \text{-Cbl(III)}$  corresponded to  $\text{CF}_3\text{SO}_2^-$  conversion in a 1:1 ratio.<sup>24</sup> Thus,  $\text{CF}_3\text{SO}_2^-$  serves as a useful chemical marker for HNO release from donor **1**, as observed for donor **4**.<sup>24</sup>

The aromatic products formed upon complete photodecomposition of donor **1** in a mixture of phosphate buffer (pH 7.0, 0.10 M) and CD<sub>3</sub>CN (40:60, v/v) were characterized by another member of our research group using <sup>19</sup>F and <sup>1</sup>H NMR spectroscopy.<sup>24</sup> It was found that diol **5** and aldehyde **6** were formed upon photolysis of donor **1** (Scheme 5.1, Pathway (a) and Pathway (c)).

### 5.5.2.2 Photoproduct Quantum Yields of HNO Generation and N-O Bond Cleavage in MeCN

The photoproduct quantum yields of pathway (a) and (c) were determined using azobenzene actinometry (Scheme 5.1). Donor **1** had a lower photoproduct quantum yield for HNO photorelease than donor **4** in 60:40 v/v MeCN to 5.0 mM phosphate buffer solution (pH 7.0) (as determined by CF<sub>3</sub>SO<sub>2</sub><sup>-</sup>;  $\Phi_{PP} = 0.50$  versus  $\Phi_{PP} = 0.38$  for **4** and **1**, respectively; Table 5.4). Notably, while donor **4** decomposes to release HNO only upon irradiation in 60:40 v/v MeCN to 5.0 mM phosphate buffer solution (pH 7.0), donor **1** can also undergo N-O bond cleavage ( $\Phi_{PP} = 0.33 \pm 0.07$ ). This suggests that an additional N-O bond cleavage pathway arises from ESIPT. Based on the observed photoproducts, ESIPT may occur from the naphtholic OH to the nitrogen atom on the leaving group (Figure 5.24).<sup>23</sup> Notably, this pathway has a similar photoproduct quantum yield to that of HNO generation ( $\Phi_{PP} = 0.41$  vs  $\Phi_{PP} = 0.33$ ; Table 5.4), which is reflected in the substoichiometric selectivity for donor **1** in these solvent conditions.

Table 5.5. Photoproduct quantum yields for HNO photorelease (as indicated by chemical marker CF<sub>3</sub>SO<sub>2</sub><sup>-</sup> for HNO generation or CF<sub>3</sub>SO<sub>2</sub>NH<sub>2</sub> for N-O bond cleavage) in 60:40 v/v MeCN to 5.0 mM phosphate buffer solution (pH 7.0).

Photoactive Donor	HNO Generation	N-O Bond Cleavage
<b>Donor 4</b>	0.48 ± 0.06 (aerobic) 0.51 ± 0.07 (anaerobic)	Not Observed
<b>Donor 1</b>	0.41 ± 0.05 (aerobic)	0.33 ± 0.07 (aerobic)

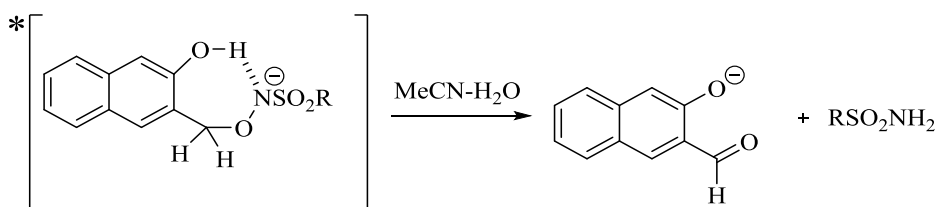


Figure 5.24. A proposed pathway for excited state intramolecular proton transfer to generate aldehyde **6** and the corresponding sulfonamide.<sup>23</sup>

## 5.6 CONCLUSIONS

In this chapter, the mechanisms of N-O bond cleavage were examined for two trifluoromethanesulfonamidoxy analogues of Piloty's acid bearing either a (6-hydroxynaphthalen-2-yl)methyl (6,2-HNM) or a (3-hydroxynaphthalen-2-yl)methyl (3,2-HNM) photocage. Less than stoichiometric HNO release is a common problem for photoprotected Piloty's acid analogues. These experiments indicate that the other undesired pathway of N-O bond cleavage proceeds via heterolytic bond cleavage and is promoted by conditions where ESPT can occur. N-O bond cleavage was observed to occur primarily via bond heterolysis upon excitation of **4b** and **4c**. Importantly, it is clear that deprotonation of the nitrogen atom on the leaving group enables HNO release to occur as the primary pathway, as evidenced by selective HNO release proceeding from **4a** in partially aqueous conditions (Chapters 3 and 4). However, excitation of **4a** in a solvent mixture where phosphate buffer is the main component of the mixture allows PTTS to occur from the naphtholic OH. Hence, an excited state of **4c** can be formed upon excitation of **4a** in highly aqueous conditions. A direct correlation was observed between formation of **4c** in the excited state (as observed by fluorescence spectroscopy) and an increased selectivity for N-O bond cleavage proceeding from donor **4**. Furthermore, use of the 3,2-HNM photocage enables ESIPT to occur to the leaving group on either the oxygen atom or the nitrogen atom and decreases selectivity for HNO generation. One possible means to prevent ESPTs is to methylate the photoacidic site.<sup>123,156,179</sup> Hence, future studies could investigate the impact of methylation of the naphtholic OH on the HNM protected trifluoromethanesulfonamidoxy analogue of Piloty's acid.

# CHAPTER 6: STUDIES ON THE REACTIONS OF HYDROXYCOBALAMIN AND NITROXYLCOBALAMIN WITH PILOTY'S ACID

---

## 6.1 INTRODUCTION

There is currently much interest in the triatomic species HNO. HNO functions as a biological signaling molecule, reacting primarily with protein thiols (cysteine), low molecular weight thiols, and metal centers of proteins.<sup>8,35,236,269</sup> The ability of mammals to produce HNO remains unclear, although several *in vitro* studies suggest endogenous production is likely.<sup>29,50,270,271</sup> HNO-releasing therapeutics also show considerable promise to treat congestive heart failure.<sup>222</sup> Kinetic and mechanistic studies between HNO and reactive biomolecules are challenging because HNO is unstable. HNO rapidly dimerizes and decomposes to form N<sub>2</sub>O and H<sub>2</sub>O ( $k = 8 \times 10^6 \text{ M}^{-1} \text{ s}^{-1}$ , 22 °C).<sup>6</sup> To circumvent these issues, HNO donor molecules are used in chemical and biological studies. The HNO donor molecules release HNO slowly ( $t_{1/2} \sim$  minutes to hours), making kinetic studies of HNO and relevant biomolecules particularly challenging.<sup>3,7,8</sup> HNO reacts with biomolecules on the order of  $10^3 - 10^7 \text{ M}^{-1} \text{ s}^{-1}$ .<sup>9</sup>

Vitamin B<sub>12</sub> derivatives (CbIs) are a class of redox active complexes that are cobalt-containing corrinoids. While multiple studies have been published on the chemistry of HNO donor molecules with structurally related porphyrin complexes,<sup>63,236,270,272</sup> only recently has the reactivity of HNO or HNO donor molecules with CbIs been investigated.<sup>67,78,240</sup> CbIs are essential coenzymes for mammals. In humans, there are two B<sub>12</sub>-dependent enzyme reactions, requiring either adenosylcobalamin (AdoCbl, X = 5' - deoxyadenosyl (Ado), Figure 6.1) or methylcobalamin (MeCbl X = CH<sub>3</sub>, Figure 6.1). Importantly, CbIs modulate NO-associated events in biological systems.<sup>273</sup> Hence, our research group became interested in understanding the mechanisms and kinetics of the reactions between HNO and CbIs.<sup>67,78,240,274</sup> In this chapter, the rate of reaction between HNO and HOCbl (X = OH, Figure 6.1) was investigated by kinetic modeling of

experimental data provided by Prof. Rudi van Eldik's research group at Friedrich Alexander University of Erlangen-Nürnberg in Germany. Kinetic studies were also carried out on the reaction between  $^1\text{HNO}/^3\text{NO}^-$  and nitroxylcobalamin ( $\text{NO}^-$ -Cbl(III);  $\text{X} = \text{NO}^-$ , also called nitrosylcobalamin<sup>213</sup>, Figure 6.1). A major motivation for these studies was to potentially use the reactions of  $\text{HOcbl}$  or  $\text{NO}^-$ -Cbl(III) with  $\text{HNO}$  to indirectly determine the  $\text{p}K_a$  of  $^1\text{HNO}/^3\text{NO}^-$ .

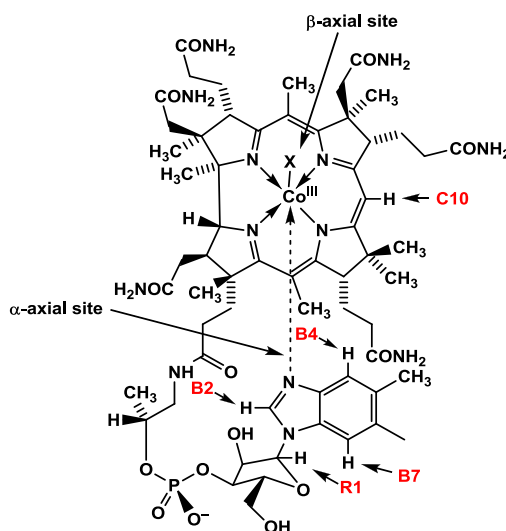


Figure 6.1. The structure of vitamin B<sub>12</sub>:  $\text{X} = \text{CN}^-$ ,  $\text{CH}_3$ , Ado,  $\text{H}_2\text{O}$ ,  $\text{NO}$  etc.

## 6.2 METHODS

Kinetic analyses and modeling were completed using Applied Photophysics – Pro-KIV. All solutions were prepared using buffers (0.20 M) with a constant ionic strength maintained using sodium triflate ( $\text{NaCF}_3\text{SO}_3$ ,  $I = 1.0$  M). Sodium hydroxide solutions (0.1-0.35 M,  $I = 1.0$  M sodium triflate) were prepared. Air free UV-vis spectrometric measurements were carried out in Schlenk cuvettes fitted with a J-Young stopcock on a Cary 100 spectrophotometer equipped with a thermostatted cuvette compartment ( $25.0 \pm 0.1$  °C). Microcal Origin version 8.0 software was used to process all the UV-vis data. Samples were prepared in a glove box by adding a concentrated stock solution of Piloty's acid (200.0  $\mu\text{L}$ , 0.24 M, in 5.0 mM phosphate buffer solution, pH 7.0; stirred vigorously for  $> 1$  hr until fully dissolved) into the cuvette's side bulb. The purity of Piloty's acid was checked using  $^1\text{H}$  NMR spectroscopy. Due to the high concentration of Piloty's acid, the stock solution was stirred continuously throughout the experiment. Buffer (3.000 mL) or sodium hydroxide (3.000 mL) and an aliquot of concentrated  $\text{NO}^-$ -Cbl(III) ( $\sim 7$  mM, in  $\text{H}_2\text{O}$ ) was pipetted into the cuvette. The cuvette was allowed to equilibrate in the cell

holder to achieve 25.0 °C. The solutions were mixed immediately prior to data collection. The pH of the solution was measured upon completion of the reaction. Note that shifts in pH were observed following addition of the concentrated Piloty's acid stock solution. The reported pH values are the pH of the solutions *after* the reactions have gone to completion.

### 6.3 STUDIES ON THE REACTIONS BETWEEN $^1\text{HNO}/^3\text{NO}^-$ AND HYDROXYCOB(III)ALAMIN

#### 6.3.1 Estimation of the Rate Constants for the Reactions between HNO and Hydroxycob(III)alamin

It was previously determined that HOCbl and  $^1\text{HNO}$  react in a 1:1 stoichiometric ratio to form  $\text{NO}^-$ -Cbl(III).<sup>274</sup> To confirm this, samples (550  $\mu\text{L}$  total volume) were prepared of HOCbl (6.00 mM) with a slight excess of Piloty's acid in anaerobic pD 10.0 carbonate buffer (0.5 M), anaerobic pD 12.5 phosphate buffer (0.5 M), and anaerobic 0.1 M NaOD (Figure 6.2). In alkaline solution, the commonly used HNO donor Piloty's acid ( $\text{p}K_{\text{a}} = 9.29$ ) decomposes to give HNO and benzenesulfinate.<sup>81</sup> The rate of decomposition of Piloty's acid to give HNO (and  $\text{C}_6\text{H}_5\text{SO}_2^-$ ) increases with increasing pH and is essentially pH independent at  $\text{pH} > 10$ .<sup>82</sup> After 1.5 hr, stoichiometric  $\text{NO}^-$ -Cbl(III) formation was observed via  $^1\text{H}$  NMR spectroscopy under all three experimental conditions. It is unclear whether  $^1\text{HNO}$  and/or  $^3\text{NO}^-$  react with HOCbl to form  $\text{NO}^-$ -Cbl(III), as  $^1\text{HNO}$  and  $^3\text{NO}^-$  are in equilibrium.<sup>2,9</sup>

Based on the observed stoichiometric reaction, a lower limit for the rate constant for the reaction of HNO and HOCbl could be estimated through kinetic modeling. In the reaction mixture, a number of reactions occur simultaneously (Table 6.1). Piloty's acid decomposes in alkaline solutions to form benzenesulfinate and HNO (Table 6.1; Eqn. 6.1). HNO is in equilibrium with  $\text{NO}^-$  (Table 6.1; Eqn. 6.2 and Eqn. 6.3). Notably, HNO rapidly dimerizes (Table 6.1; Eqn. 6.4 and Eqn. 6.5). Eqn. 6.5 can be ignored in the model as it has no effect on the concentration of HNO in solution.  $^1\text{HNO}$  will also react with  $^3\text{NO}^-$  (Table 6.1; Eqn. 6.6), although this reaction and its rate are not well established.<sup>25</sup> HNO can also react with HOCbl to give  $\text{NO}^-$ -Cbl(III) (Table 6.1; Eqn. 6.7). For this reaction to occur, it must outcompete dimerization (Eqn. 6.4). Therefore, to determine the lower limit for the rate constant of the reaction between HNO and HOCbl ( $8.5 \times 10^{-5}$  M), a reaction model using equations Eqn. 6.1, Eqn. 6.2, Eqn. 6.3, Eqn. 6.4, Eqn. 6.6, and Eqn. 6.7 was simulated in Pro-KIV. At pH 10.2, the rate of Eqn. 6.2 is  $7.7 \text{ s}^{-1}$ . The rate of

Eqn. 6.7 was varied and the percent of  $\text{NO}^-$ -Cbl(III) was determined (Figure 6.3). Using

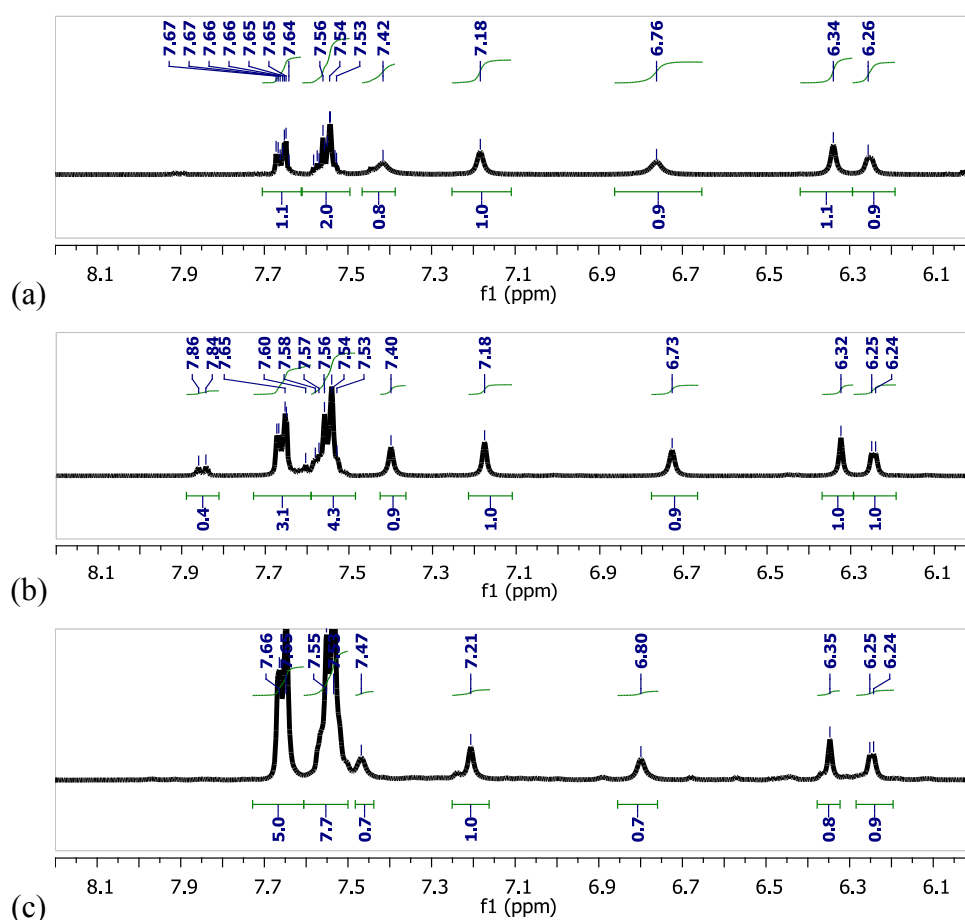


Figure 6.2. (a)  $^1\text{H}$  NMR spectra of an equilibrated solution of HOCbl (6.00 mM) with 1.0 molar equivalents of Piloty's acid in anaerobic 0.5 M carbonate buffer (pD 10.0). (b)  $^1\text{H}$  NMR spectra of HOCbl (6.00 mM) with 1.5 mol. equiv. of Piloty's acid in anaerobic 0.5 M phosphate buffer (pD 12.5; Spectrum 2); (c)  $^1\text{H}$  NMR spectra of HOCbl (6.00 mM) with 2.5 mol. equiv. on Piloty's acid in anaerobic 0.1 M NaOD (Spectrum 3).  $\text{NO}^-$ -Cbl(III):  $\delta \sim 7.42, 7.20, 6.80, 6.34, 6.25$  ppm. Piloty's acid: 8.43 ppm.  $\text{PhSO}_2^-$ : 7.67-7.65, 7.55-7.54 ppm.

Table 6.1. Reactions observed upon addition of excess Piloty's acid to HOCbl.

Reaction	Rate, $pK_a$	Eqn.
$\text{PA} \rightarrow \text{PhSO}_2^- + \text{HNO}$	$k = 3.8 \times 10^{-4} \text{ s}^{-1}$ ; $pK_a = 9.29$	Eqn. 6.1 <sup>82</sup>
$^1\text{HNO} + \text{OH}^- \rightarrow \text{H}_2\text{O} + ^3\text{NO}^-$	$k = 4.9 \times 10^4 \text{ M}^{-1}\text{s}^{-1}$	Eqn. 6.2 <sup>9</sup>
$^3\text{NO}^- + \text{H}_2\text{O} \rightarrow ^1\text{HNO} + \text{OH}^-$	$k = 1.38 \times 10^2 \text{ s}^{-1}$	Eqn. 6.3 <sup>1</sup>
$2\text{HNO} \rightarrow \text{HONNOH}$	$k = 8.0 \times 10^6 \text{ M}^{-1}\text{s}^{-1}$	Eqn. 6.4 <sup>1</sup>
$\text{HONNOH} \rightarrow \text{N}_2\text{O} + \text{H}_2\text{O}$	$k = 5.0 \times 10^{-4} \text{ s}^{-1}$	Eqn. 6.5 <sup>6</sup>
$^3\text{NO}^- + ^1\text{HNO} \rightarrow \text{N}_2\text{O} + \text{OH}^-$	$k = 6.6 \times 10^9 \text{ M}^{-1}\text{s}^{-1}$	Eqn. 6.6 <sup>25</sup>
$^1\text{HNO} + \text{HOCbl} \rightarrow \text{NO}^-$ -Cbl(III) + $\text{H}_2\text{O}$	$k = ?$	Eqn. 6.7
$^3\text{NO}^- + \text{HOCbl} \rightarrow \text{NO}^-$ -Cbl(III) + $\text{H}_2\text{O}$	$k = ?$	Eqn. 6.8

this model, the rate constant between HNO and HOCbl must be at least  $3 \times 10^5 \text{ M}^{-1}\text{s}^{-1}$  for  $\geq 90\%$  of HOCbl to react with HNO to form  $\text{NO}^-$ -Cbl(III).

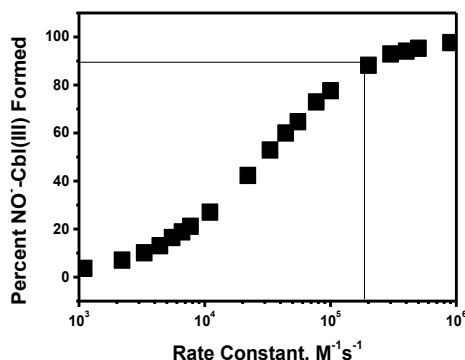


Figure 6.3. Percent  $\text{NO}^-$ -Cbl(III) formed as a function of the rate constant of reaction ( $\text{HNO} + \text{HOCbl} \rightarrow \text{NO}^-$ -Cbl(III);  $[\text{HOCbl}] = 8.5 \times 10^{-5} \text{ M}$ ) simulated from a model incorporating Eqn. 6.1, Eqn. 6.2, Eqn. 6.3, Eqn. 6.4, Eqn. 6.6, and Eqn. 6.7, at pH 10.2.

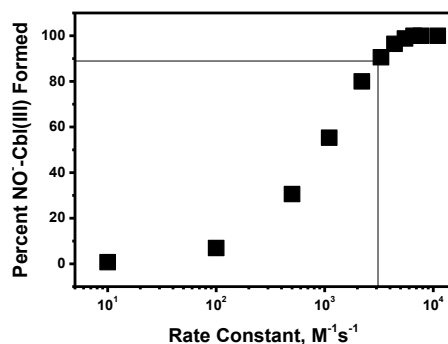


Figure 6.4. Percent product formed as a function of rate constant ( $\text{HNO} + \text{HOCbl} \rightarrow \text{NO}^-$ -Cbl(III);  $[\text{HOCbl}] = 8.5 \times 10^{-5} \text{ M}$ ) simulated by a model incorporating Eqn. 6.1, Eqn. 6.4, and Eqn. 6.7 at pH 9.5.

The reactions described in Eqn. 6.1, Eqn. 6.2, Eqn. 6.3, and Eqn. 6.4 are well established. Conversely, the rate constant for the reaction between  $^1\text{HNO}$  and  $^3\text{NO}^-$  (Eqn. 6.6) is abnormally fast for a reaction between a singlet and triplet molecule.<sup>25</sup> Subsequently, a simpler model was also applied assuming that only  $^1\text{HNO}$ , not  $^3\text{NO}^-$ , is present in solution. In other words, the model included Eqn. 6.1, Eqn. 6.4, and Eqn. 6.7. The rate constant of Eqn. 6.7 was varied and the concentration of product  $\text{NO}^-$ -Cbl(III) was recorded (Figure 6.4). Using this model, the rate constant between HNO and HOCbl must be  $\geq 3 \times 10^3 \text{ M}^{-1}\text{s}^{-1}$  for 90% of HOCbl to react with HNO to form  $\text{NO}^-$ -Cbl(III).

### 6.3.2 Fitting of Experimental Data for the Reaction of Hydroxycob(III)alamin and Piloty's Acid to a Simple Model

Work done by our collaborators (van Eldik group) showed that the initial rate of reaction of HNO with HOCbl was independent of the concentration of Piloty's acid upon addition of a large excess of Piloty's acid (Piloty's acid  $> 0.010$  M; data unpublished). Kinetic data for the reaction between excess Piloty's acid (0.013 M) and HOCbl ( $8.5 \times 10^{-5}$  M) was collected at a range of pH conditions by collaborators. The spectral changes and observation of isosbestic points were consistent with clean conversion of HOCbl to  $\text{NO}^-$ -Cbl(III) at all pH conditions.

The data collected at pH 10.05 and 10.12 were modeled using the model described in Table 6.2. Under these pH conditions, the rate constants for the reactions between  ${}^1\text{HNO}$  and  ${}^3\text{NO}^-$  ( $k_6$ ) and between  $\text{NO}^-$ -Cbl(III) and  ${}^3\text{NO}^-$  ( $k_8$ ) can be ignored due to the concentration of  ${}^3\text{NO}^-$  ( $\text{p}K_a({}^1\text{HNO}/{}^3\text{NO}^-) = 11.4$ ).<sup>1</sup> Figure 6.5 shows the best fit of the data to the model described in Table 6.2 superimposed on top of the experimental data

Table 6.2. Reaction model with rate constants.

Reaction	Rate	Notes
$\text{PA} \rightarrow \text{HNO}$	$k_1 = 3.8 \times 10^{-4}, \text{s}^{-1}$	Decomposition is slightly pH dependent
$\text{HNO} \rightarrow {}^3\text{NO}^-$	$k_2 = (4.9 \times 10^4) \times [\text{OH}^-], \text{s}^{-1}$	pH dependent
${}^3\text{NO}^- \rightarrow \text{HNO}$	$k_3 = 1.2 \times 10^2, \text{s}^{-1}$	
$\text{HNO} + \text{HNO} \rightarrow \text{N}_2\text{O} + \text{H}_2\text{O}$	$k_4 = 8.0 \times 10^6, \text{M}^{-1}\text{s}^{-1}$	
$\text{HNO} + \text{HOCbl} \rightarrow \text{NO}^-$ - $\text{Cbl(III)}$	$k_7 = \text{varied}, \text{M}^{-1}\text{s}^{-1}$	Reaction of interest

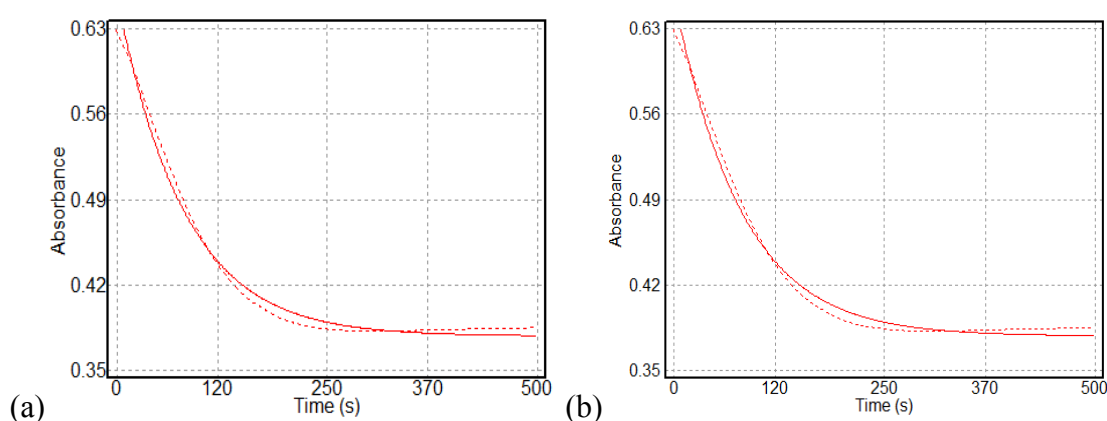


Figure 6.5. Overlaid best fit (solid line) of the reaction between HNO as generated by Piloty's acid (0.0128 M) and HOCbl ( $8.5 \times 10^{-5}$  M) monitored at 535 nm to the model described in Table 6.2 for data collected at pH 10.05 (a) and pH 10.12 (b) on the experimental data (dotted line). The rate constant between HNO and HOCbl was calculated to be  $(2.46 \pm 0.01) \times 10^4 \text{ M}^{-1}\text{s}^{-1}$ .

observed for the reaction between Piloty's acid (0.0128 M) and HOCbl ( $8.5 \times 10^{-5}$  M) using the model described in Table 6.2 for data collected under pH 10.05 (a) and pH 10.12 (b) conditions. The rate constant between HNO and HOCbl was calculated as  $(2.46 \pm 0.01) \times 10^4 \text{ M}^{-1}\text{s}^{-1}$ . The fits of the data indicated that an additional process may occur (such as reactions involving  ${}^3\text{NO}^-$ , Eqn. 6.6 or Eqn. 6.8 in Table 6.1); another possible explanation is that one or more rate constants used in the model are not accurate.

The calculated rate constant for the reaction between  ${}^1\text{HNO}$  and HOCbl decreased by nearly an order of magnitude as the pH conditions became more alkaline (pH > 10.2; data not shown). Hence, the model described in Table 6.2 could not be used for these pH conditions.

### 6.3.3 Observation of a Secondary Reaction between ${}^3\text{NO}^-$ and Hydroxycobalamin

An attempt was made to reproduce the results from the van Eldik group under slightly modified experimental conditions. Preliminary results suggested that an additional subsequent reaction occurred at pH 12.5. Therefore, the reactions of Piloty's acid (0.0150 M) and HOCbl ( $1 \times 10^{-4}$  M) in anaerobic 0.2 M phosphate buffers (pH 10.0-12.5) were monitored for 300 minutes (Figure 6.6). The product mixture was stable at pH 10.0 but showed additional reactions at pH 11.5 and pH 12.5. One possible explanation is that product species  $\text{NO}^-$ -Cbl(III) reacts with  ${}^3\text{NO}^-$ . Hence, a series of studies were carried out in Section 6.4 to directly investigate the reactivity of  ${}^3\text{NO}^-$  with  $\text{NO}^-$ -Cbl(III).

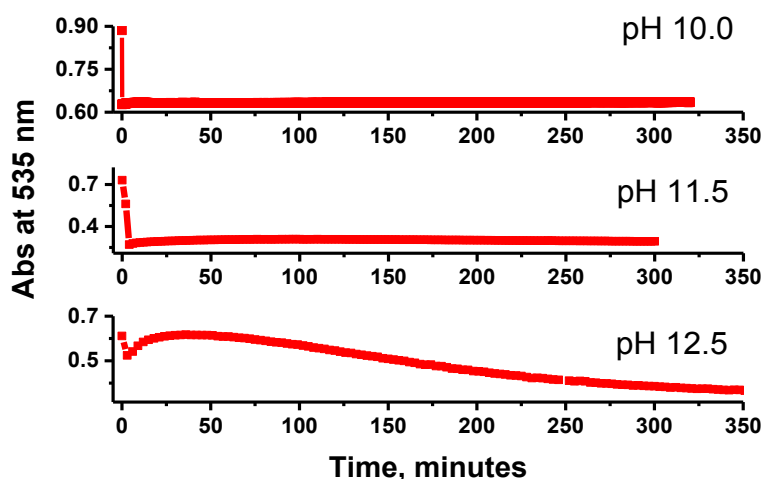


Figure 6.6. Absorbance at 535 nm for the reaction of Piloty's acid (0.0150 M) with HOCbl ( $\sim 1 \times 10^{-4}$  M) in anaerobic 0.2 M carbonate buffer (pH 10.0, 11.5, and 12.5).

6.4 STUDIES ON THE REACTIONS BETWEEN  ${}^1\text{HNO}/{}^3\text{NO}^-$  AND NITROXYLCOBALAMIN6.4.1 UV-Vis Spectrometric Investigation of the Reaction between  ${}^1\text{HNO}/{}^3\text{NO}^-$  and Nitroxylcobalamin

The reaction between  $\text{NO}^-$ -Cbl(III) and  ${}^1\text{HNO}/{}^3\text{NO}^-$  ( $\text{p}K_a$  11.4)<sup>1</sup> generated using excess HNO donor ( $[\text{PA}] \gg [\text{HOcbl}]$ ) was initially investigated using UV-vis spectroscopy at pH 12.5. A large excess of HNO donor to  $\text{NO}^-$ -Cbl(III) ( $\sim 150:1$ ) was used in order to determine whether  $\text{NO}^-$ -Cbl(III) reacts with  ${}^1\text{HNO}/{}^3\text{NO}^-$  (Figure 6.7). A fast reaction ( $\Delta A_{535\text{nm}} = 0.06$  a.u.;  $t_{1/2} \sim 6$  min) with a clean isosbestic point (502 nm) was observed for the reaction mixture of  $\text{NO}^-$ -Cbl(III) ( $6.5 \times 10^{-5}$  M) with Piloty's acid (0.0150 M) in anaerobic 0.2 M phosphate buffer (final pH 12.5,  $I = 1.0$  M ( $\text{NaCF}_3\text{SO}_3$ ); Figure 6.7). A slow absorbance change ( $\Delta A_{535\text{nm}} = 0.002$  a.u.;  $t_{1/2} > 20$  min) was observed between  $\text{NO}^-$ -Cbl(III) ( $7.0 \times 10^{-5}$  M) and benzenesulfinate (0.0150 M) in anaerobic 0.2 M phosphate buffer (pH 12.0,  $I = 1.0$  M ( $\text{NaCF}_3\text{SO}_3$ ); Figure 6.8). This absorbance change is negligible within the time frame of the studies of the reaction between  $\text{NO}^-$ -Cbl(III) and  ${}^1\text{HNO}/{}^3\text{NO}^-$ .

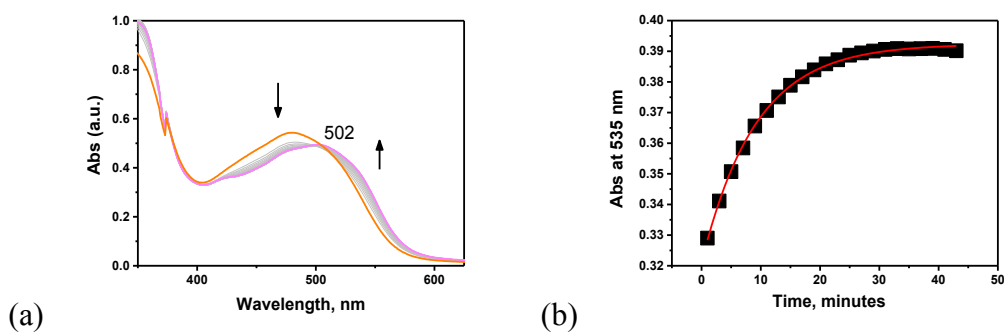


Figure 6.7. (a) UV-vis spectra of  $\text{NO}^-$ -Cbl(III) ( $7.2 \times 10^{-5}$  M) upon addition of Piloty's acid (0.015 M) in anaerobic 0.2 M phosphate buffer (final pH 12.5,  $I = 1.0$  M ( $\text{NaCF}_3\text{SO}_3$ )) monitored for 45 min. (b) Absorbance at 535 nm.

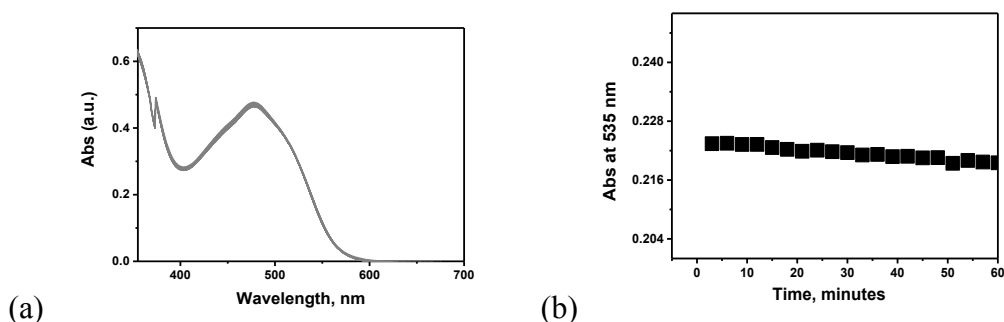


Figure 6.8. (a) UV-vis spectra for  $\text{NO}^-$ -Cbl(III) ( $7.0 \times 10^{-5}$  M) upon addition of benzenesulfinate, sodium salt (0.015 M) in anaerobic 0.2 M phosphate buffer (pH 12.0,  $I = 1.0$  M ( $\text{NaCF}_3\text{SO}_3$ )) as monitored for 60 min. (b) Absorbance at 535 nm.

Hence, the data indicates that the product of the reaction between HOCbl and HNO, namely  $\text{NO}^-$ -Cbl(III), is reactive with either  $^1\text{HNO}$  or  $^3\text{NO}^-$ .

#### 6.4.2 Investigation of the Products of the Reaction between $^1\text{HNO}/^3\text{NO}^-$ and Nitroxycobalamin

The pH of the reaction between  $\text{NO}^-$ -Cbl(III) and excess Piloty's acid was varied in order to further understand the reaction. A slow reaction ( $\Delta A_{535\text{nm}} = 0.02$  a.u.;  $t_{1/2} \sim 6$  min) was observed between  $\text{NO}^-$ -Cbl(III) ( $7 \times 10^{-5}$  M) and Piloty's acid (0.0150 M) at pH 10.0; Figure 6.9(a). At pH 13.1, a fast reaction ( $\Delta A_{535\text{nm}} = 0.18$  a.u.;  $t_{1/2} \sim 1$  min) was observed (Figure 6.9(b), inset). Isosbestic points at  $377 \pm 3$  nm and  $499 \pm 3$  nm were seen. Notably, the isosbestic points for the reaction of HOCbl and HNO to give  $\text{NO}^-$ -Cbl(III) are 375 and 500 nm. This, together with the spectral shape of the observed species (HOCbl  $\lambda_{\text{max}} = 357, 420, 509$  and  $536$  nm), indicates that  $\text{NO}^-$ -Cbl(III) is converted to HOCbl upon

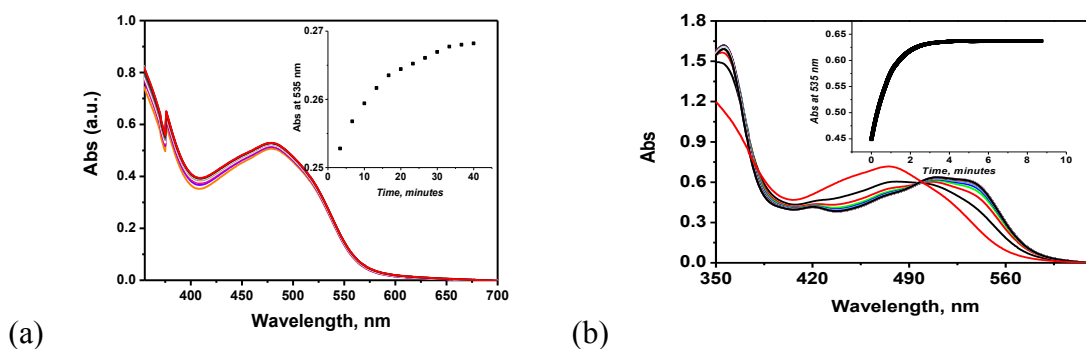


Figure 6.9. (a) UV-vis spectra for  $\text{NO}^-$ -Cbl(III) ( $7.0 \times 10^{-5}$  M) upon the addition of Piloty's acid (0.015 M) in anaerobic 0.20 M phosphate buffer (pH 10.0,  $I = 1.0$  M ( $\text{NaCF}_3\text{SO}_3$ )). The reaction was monitored for 40 min. Inset: Plot of absorbance at 535 nm versus time. (b) UV-vis spectra of  $\text{NO}^-$ -Cbl(III) ( $7.8 \times 10^{-5}$  M) upon the addition of Piloty's acid (0.0150 M) in 0.15 M NaOH ( $I = 1.0$  M ( $\text{NaCF}_3\text{SO}_3$ )). Inset: Absorbance at 535 nm as a function of time.  $\text{NO}^-$ -Cbl(III) partially reacts with Piloty's acid, isosbestic points are observed at 375 and 499 nm. Inset: Plot of absorbance at 535 nm versus time.

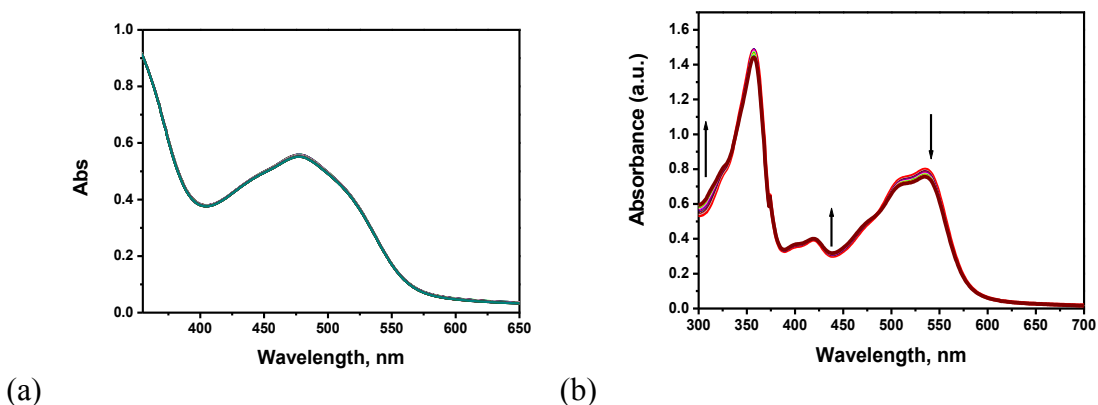


Figure 6.10. (a) UV-vis spectra of  $\text{NO}^-$ -Cbl(III) ( $\sim 7.0 \times 10^{-5}$  M) in anaerobic 0.1 M NaOH monitored every minute for 1 hr. (b) UV-vis absorption spectra of HOCbl ( $8.5 \times 10^{-5}$  M) in anaerobic 0.2 M phosphate buffer (pH 12.5) monitored for 8 hr.

addition of excess Piloty's acid. The unclear isosbestic points are probably due to HOcbl's instability in alkaline solutions (Figure 6.10(a));  $\text{NO}^-$ -Cbl(III) is stable in alkaline solutions for 1 hr (Figure 6.10(b)). Based on the observation that the reaction is much faster at pH 13.1 compared to pH 10.0, the reacting species is proposed to be  $^3\text{NO}^-$ , which is generated by the decomposition of Piloty's acid and subsequent deprotonation of  $^1\text{HNO}$ . Note that the observed rate constants for Piloty's acid decomposition to give HNO and benzenesulfinate at pH 10.0 and in 0.15 M NaOH are  $3.18 \times 10^{-4} \text{ s}^{-1}$  and  $3.80 \times 10^{-4} \text{ s}^{-1}$ , respectively.

The product of the reaction between  $\text{NO}^-$ -Cbl(III) and Piloty's acid was investigated using  $^1\text{H}$  NMR spectroscopy (Figure 6.11). It has been previously shown that the aromatic region of the  $^1\text{H}$  NMR spectrum for cobalamins is useful for following ligand substitution reactions involving the  $\beta$ -axial ligand.<sup>228</sup>  $\text{NO}^-$ -Cbl(III) (5.00 mM) and Piloty's acid (0.0, 0.3, 1.0, 1.5, or 3.0 molar equiv.) were allowed to react in anaerobic 0.15 M NaOD for 2-3 hr.  $\text{NO}^-$ -Cbl(III) was unstable for 2 hr in this solvent condition (~10-20% decomposition, new peaks observed at  $\delta$  7.89, 7.14, 7.02, 6.46, 6.20 ppm, from decomposition of the corrin macrocycle; Figure 6.11(a)). No additional species were observed upon addition of Piloty's acid to  $\text{NO}^-$ -Cbl(III) (Figure 6.11(b)-(e)).

The degradation of  $\text{NO}^-$ -Cbl(III) in 0.15 M NaOD was further investigated by adding sodium cyanide immediately after sample preparation and 2.5 hr after sample preparation. Cobalamins react readily with excess cyanide to form dicyanocobalamin.<sup>275</sup> Additional peaks were observed in the latter sample (Figure 6.12); therefore it is likely that additional peaks arise from corrin macrocycle decomposition in alkaline solution, as others have reported.<sup>276</sup> A similar experiment was completed at pD 12.5 with 10 mol equiv. Piloty's acid to  $\text{NO}^-$ -Cbl(III) (data not shown). No additional species were present.

The product of the reaction between  $\text{NO}^-$ -Cbl(III) and  $^3\text{NO}^-$  could not be confirmed by  $^1\text{H}$  NMR spectroscopy. The previously observed reactions in the UV-vis experiments were observed following addition of a large excess of Piloty's acid to  $\text{NO}^-$ -Cbl(III). In  $^1\text{H}$  NMR spectroscopy, these experimental conditions could not be replicated due to the protons of Piloty's acid, which would be of much greater intensity than those of the product cobalamin species in the spectra. Hence, it is likely that a large excess of Piloty's acid is required for the reaction to proceed and/or the product of the reaction is reactive with  $^3\text{NO}^-$ , reforming the starting material,  $\text{NO}^-$ -Cbl(III).

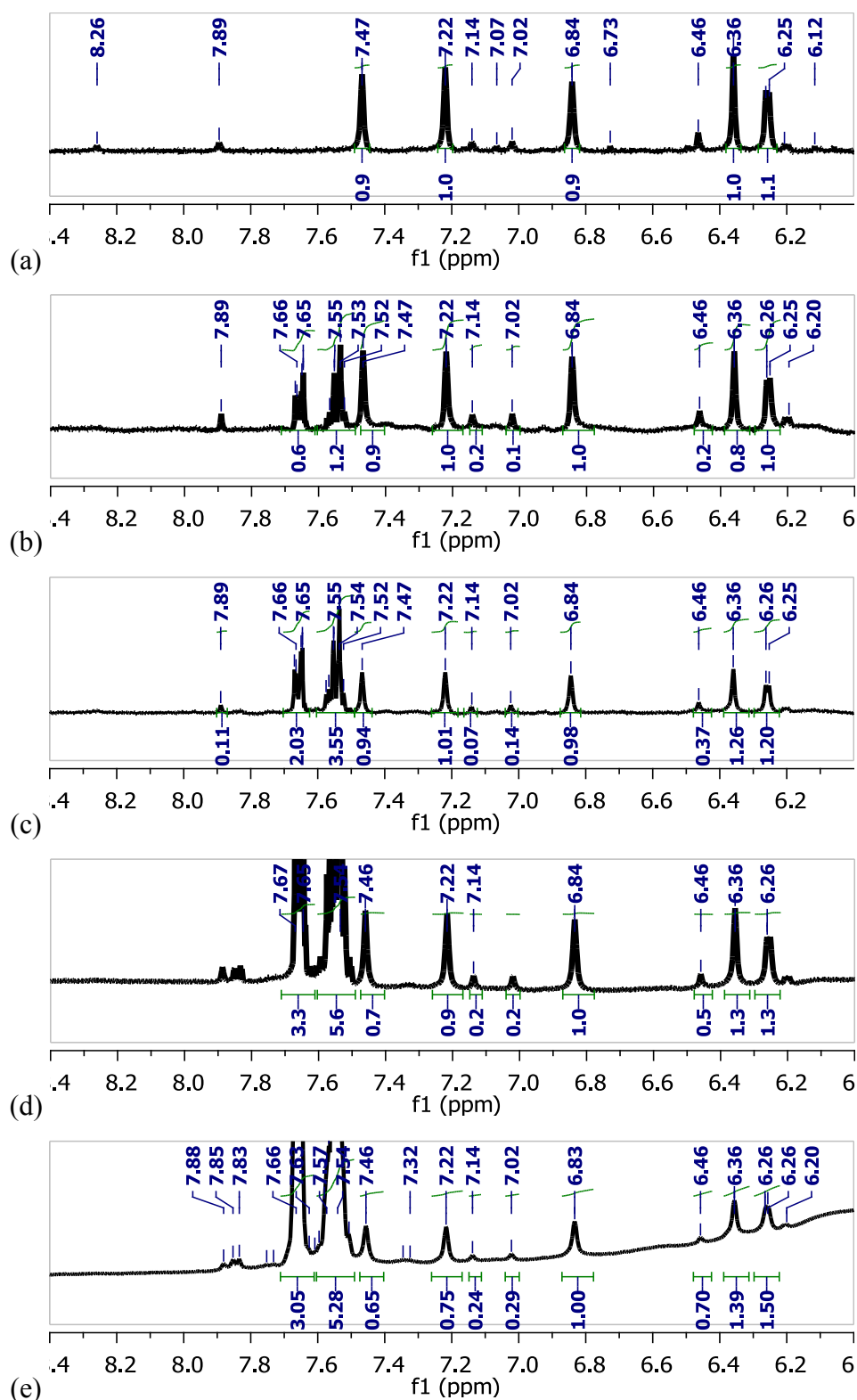


Figure 6.11.  ${}^1\text{H}$  NMR spectra of  $\text{NO-Cbl(III)}$  (5.0  $\times 10^{-4}$  M) in 0.15 M NaOD upon addition: (a) no Piloty's acid, (b) 0.3 mol. equiv. of Piloty's acid, (c) 1.0 mol. equiv. of Piloty's acid, (d) 1.5 mol. equiv. of Piloty's acid, and (e) 3.0 mol. equiv. of Piloty's acid. Spectra were recorded 2-3 hr after solution preparation. Decomposition of  $\text{NO-Cbl(III)}$  in 0.15 M NaOD is observed (10-20%; new peaks observed at  $\delta$  7.89, 7.14, 7.02, 6.46, 6.20 ppm).  $\text{NO-Cbl(III)}$ :  $\delta$  7.47, 7.22, 6.84, 6.36, 6.26 ppm. Unreacted Piloty's acid: 8.43 ppm.  $\text{PhSO}_2^-$ : 7.67-7.65, 7.55-7.54 ppm.

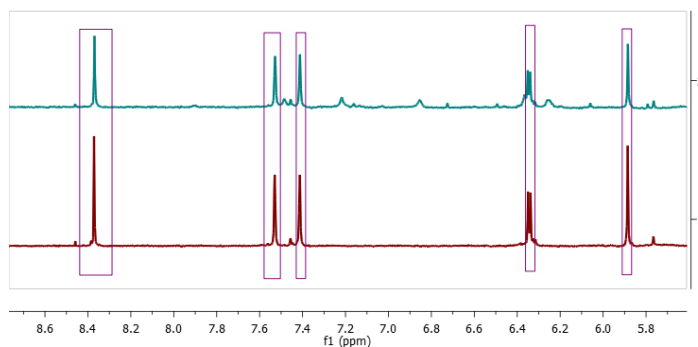


Figure 6.12.  ${}^1\text{H}$  NMR spectra of  $\text{NO}^-$ -Cbl(III) ( $5.0 \times 10^{-4}$  M) in anaerobic 0.15 M NaOD with the addition of sodium cyanide ( $\sim 10$  mol. equiv.) immediately upon sample preparation (Spectrum 1) and addition of sodium cyanide 2.5 hr following sample preparation (Spectrum 2). Dicyanocobalamin ( $\delta$  8.38, 7.51, 7.39, 6.35, 6.34, 5.87 ppm) highlighted with purple boxes.

### 6.4.3 Determination of the Initial Rates for the Reaction between ${}^1\text{HNO}/{}^3\text{NO}^-$ and Nitroxycobalamin

Kinetic measurements were carried out on the reaction between  $\text{NO}^-$ -Cbl(III) and excess Piloty's acid (0.015 M) as a function of pH (see Appendix E, Figure A16). As shown in the inset to Figure A16 (f) (pH 11.70), the data did not fit to an equation for a first-order reaction. This could be due to the reaction between the product  $\text{HO}^-\text{Cbl}$  and excess Piloty's acid, and/or due to a competing reaction between  ${}^3\text{NO}^-$  and  $\text{HNO}$ . Therefore, the initial rate data were obtained from the kinetic data. The spectra of the product mixture and the rate of reaction were observed to be pH-dependent (Figure 6.13). The initial reaction rate increased exponentially above pH  $\sim 11.7$  (Figure 6.13). A similar trend was observed for the absorbance change at 535 nm (Figure 6.14).

An additional set of experiments was completed in anaerobic 0.35 M NaOH to verify that the rate constant between  ${}^3\text{NO}^-$  and  $\text{NO}^-$ -Cbl(III) increases above pH  $> 12.5$  and the absorbance changes are not instead attributable to decomposition of the  $\text{NO}^-$ -Cbl(III) corrin macrocycle. First, the stabilities of  $\text{HO}^-\text{Cbl}$  and  $\text{NO}^-$ -Cbl(III) were examined upon immediate addition to anaerobic 0.35 M NaOH. A concentrated stock solution of  $\text{NO}^-$ -Cbl(III) was added to anaerobic 0.35 M NaOH using the side bulb on an anaerobic cuvette; see Figure 6.15. The absorbance at 535 nm did not change over 10 min; that is, the time frame of the kinetic experiments shown in Figure A16. Under the same conditions,  $\text{HO}^-\text{Cbl}$  showed an absorbance decrease ( $\Delta A_{535\text{nm}} < 0.02$  a.u.) over 10 min; see Figure 6.15. This indicates that  $\text{NO}^-$ -Cbl(III) is not degrading during the kinetic experiment. While  $\text{HO}^-\text{Cbl}$  is degrading during the experiments, it is degrading so slowly

that the initial rates reflect the reaction between  $\text{NO}^-$ -Cbl(III) and  ${}^1\text{HNO}/{}^3\text{NO}^-$  (Figure 6.15(b)). Thus,  $\text{NO}^-$ -Cbl(III) degradation is not responsible for the increase in initial rate of the reaction between  $\text{NO}^-$ -Cbl(III) and Piloty's acid for  $\text{pH} > 12.4$ .

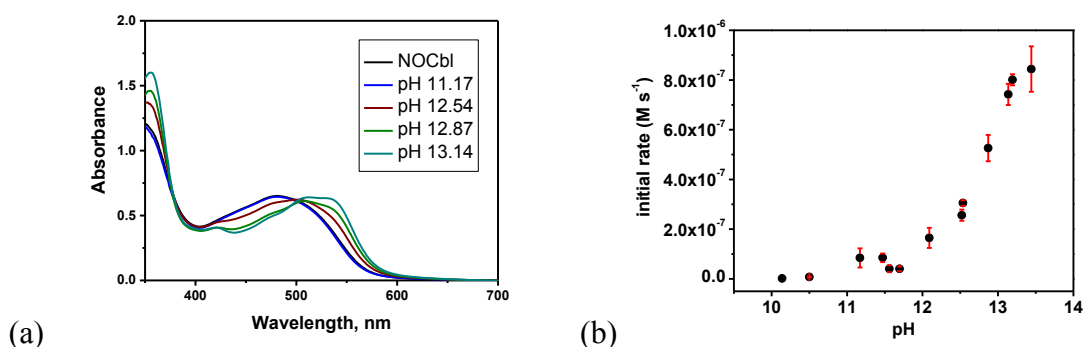


Figure 6.13. (a) Spectra taken after 20-30 min for the reaction between  $\text{NO}^-$ -Cbl(III) ( $\sim 7.0 \times 10^{-5}$ ) and Piloty's acid (0.015 M) in anaerobic 0.2 M buffered solutions (carbonate or phosphate,  $I = 1.0$  M ( $\text{NaCF}_3\text{SO}_3$ )) or sodium hydroxide solutions (0.15-0.35 M,  $I = 1.0$  M ( $\text{NaCF}_3\text{SO}_3$ )). (b) Plot of initial rate as a function of pH for the reaction between  $\text{NO}^-$ -Cbl(III) ( $\sim 7.0 \times 10^{-5}$ ) and Piloty's acid (0.015 M) in anaerobic 0.2 M buffered solutions (carbonate or phosphate,  $I = 1.0$  M ( $\text{NaCF}_3\text{SO}_3$ )) or sodium hydroxide solutions (0.15-0.35 M,  $I = 1.0$  M ( $\text{NaCF}_3\text{SO}_3$ )). Initial rates were calculated by determining the initial slope of plots of change in concentration versus time ( $\Delta c = \Delta \text{Abs} / (\epsilon(\text{HOcbl}) - \epsilon(\text{NO}^- \text{-Cbl(III)}))$ );  $\epsilon(\text{HOcbl}) = 8260 \text{ M}^{-1} \text{ cm}^{-1}$  and  $\epsilon(\text{NO}^- \text{-Cbl(III)}) = 4430 \text{ M}^{-1} \text{ cm}^{-1}$  at 535 nm; determined by experiment.

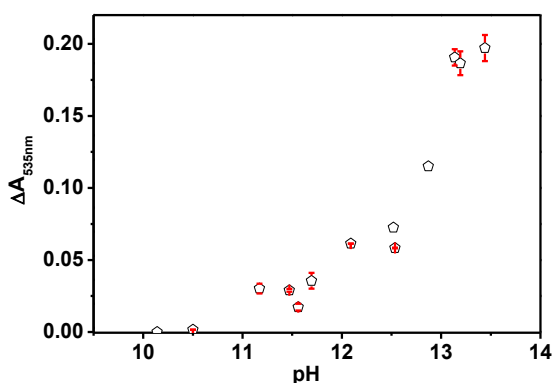


Figure 6.14. Change in absorbance at 535 nm as a function of pH for the reaction between  $\text{NO}^-$ -Cbl(III) ( $\sim 7.0 \times 10^{-5}$ ) and Piloty's acid (0.015 M) in anaerobic 0.2 M buffered solutions (carbonate or phosphate,  $I = 1.0$  M ( $\text{NaCF}_3\text{SO}_3$ )) or sodium hydroxide solutions (0.15-0.35 M,  $I = 1.0$  M ( $\text{NaCF}_3\text{SO}_3$ )).

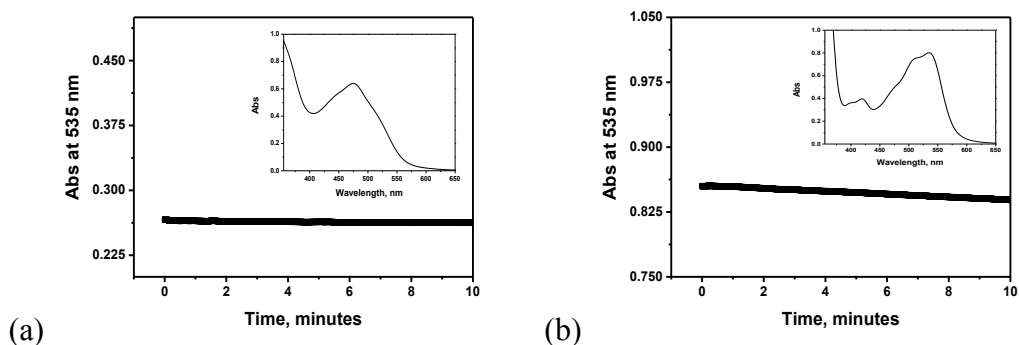


Figure 6.15. (a) Plot of absorbance at 535 nm versus time upon the addition of a concentrated stock solution of  $\text{NO}^-$ -Cbl(III) ( $\sim 7.0 \times 10^{-5} \text{ M}$ ) in anaerobic  $\text{H}_2\text{O}$  to anaerobic 0.35 M NaOH. Inset: Final spectrum. (b) Plot of absorbance at 535 nm versus time upon the addition of a concentrated stock solution of HOCbl ( $\sim 7.0 \times 10^{-5} \text{ M}$ ) in anaerobic  $\text{H}_2\text{O}$  to anaerobic 0.35 M NaOH. Inset: Final spectrum.

## 6.5 DISCUSSION AND CONCLUSIONS

The aim of this work was to obtain a better understanding of the mechanism for the reaction between HOCbl and HNO. Upon release of HNO from Piloty's acid at pH 10.0, HNO can either react with HOCbl or react with another molecule of HNO ( $k = 8 \times 10^6 \text{ M}^{-1}\text{s}^{-1}$ ) to give  $\text{N}_2\text{O}$  and  $\text{H}_2\text{O}$ . Given that the reaction of HOCbl with HNO is stoichiometric at pH 10.0, this means that under these conditions, the reaction of HOCbl with HNO must be at least five times faster than the dimerization of HNO. Based on this, a lower limit of the rate constant could be calculated by simulation. Assuming that the reactions between  ${}^3\text{NO}^-$  and HOCbl and between  ${}^3\text{NO}^-$  and  ${}^1\text{HNO}$  are unimportant, a lower limit of  $3 \times 10^3 \text{ M}^{-1}\text{s}^{-1}$  was obtained. Alternatively, allowing for the reaction between  ${}^3\text{NO}^-$  and  ${}^1\text{HNO}$ , a lower limit of  $3 \times 10^5 \text{ M}^{-1}\text{s}^{-1}$  was obtained.

Another kinetic model was also simulated using experimental data provided by the research group of Prof. Rudi van Eldik. In the experiments, the Piloty's acid concentration was high so that the reaction between HOCbl and HNO was the rate determining step rather than the decomposition of Piloty's acid to release HNO. The experimental data did not fit well to a first-order reaction. Using modeling software, a rate constant between HOCbl and HNO was estimated to be  $2.5 \times 10^4 \text{ M}^{-1}\text{s}^{-1}$  at pH 10.05-10.12. However, the model did not fit well to experimental data collected at higher pH conditions, where  ${}^3\text{NO}^-$  increases in concentration.

${}^3\text{NO}^-$  itself is a good reductant,<sup>277</sup> and therefore, experimental work was carried out to investigate the reaction between  ${}^1\text{HNO}$  and  ${}^3\text{NO}^-$  and  $\text{NO}^-$ -Cbl(III). Our collaborators

observed that the initial rate of reaction between HOCbl and an excess of Piloty's acid was pH-dependent. The sigmoidal shape of the plot of pH versus initial rates implied that the initial rate of the reaction was dependent on the concentration of  $^1\text{HNO}$  and  $^3\text{NO}^-$ . The initial rate approached  $0 \text{ M s}^{-1}$  at high pH conditions, suggesting that  $^3\text{NO}^-$  is not readily reactive with HOCbl. However, upon further investigation, a direct reaction was observed between  $^3\text{NO}^-$  and the product of the reaction between  $^1\text{HNO}/^3\text{NO}^-$  and HOCbl, namely  $\text{NO}^-$ -Cbl(III). The UV-vis spectroscopic characteristics of the product of the reaction between  $^3\text{NO}^-$  and  $\text{NO}^-$ -Cbl(III) suggested the product species is HOCbl. Unfortunately, the cobalamin product of the reaction reacted further with  $^1\text{HNO}/^3\text{NO}^-$  to form  $\text{NO}^-$ -Cbl(III); hence, further characterization of the product cobalamin species could not be achieved at this time. Overall, these experiments indicate that the data observed for the initial rates of reaction between HOCbl and an excess of Piloty's acid may be explained by a reaction between  $^1\text{HNO}$  and/or  $^3\text{NO}^-$  and HOCbl forming  $\text{NO}^-$ -Cbl(III) and a subsequent reaction between  $^3\text{NO}^-$  and  $\text{NO}^-$ -Cbl(III) to reform HOCbl. The combination of these two reactions is most likely responsible for the initial rate of the observed reaction to between HOCbl and Piloty's acid approaching  $0 \text{ M s}^{-1}$  at high pH conditions.

To the best of our knowledge, this is the second example of a reaction between  $^3\text{NO}^-$  and a coordination complex. Others have reported the reaction of  $^3\text{NO}^-$  with the high spin  $[\text{Fe}(\text{NO})(\text{N}_3\text{PyS})]\text{BF}_4$  complex.<sup>277</sup> Little mechanistic information is known at this time about the reaction between  $^3\text{NO}^-$  and  $\text{NO}^-$ -Cbl(III). However,  $\text{NO}^-$ -Cbl(III) reacts with  $^3\text{O}_2$ , which is isoelectronic with  $^3\text{NO}^-$ ; this reaction generates a mixture of HOCbl and  $\text{NO}_2\text{Cbl}$ .<sup>214</sup> A similar mechanism may be possible for the reaction between  $^3\text{NO}^-$  and  $\text{NO}^-$ -Cbl(III). Nonetheless, the mechanism of this system is challenging to study, due to not only the instability of the reactant and products in alkaline solutions for prolonged periods of time, but also that both HOCbl and  $\text{NO}^-$ -Cbl(III) are reactive with  $^1\text{HNO}$  and/or  $^3\text{NO}^-$ .

The research presented in this chapter clearly highlights the need for HNO donor molecules which release  $^1\text{HNO}$  on the ultrafast scale in order to enable kinetic and mechanistic studies for the reactivity between  $^1\text{HNO}$  and relevant biomolecules. In these experiments, a large excess of Piloty's acid was required to generate  $^1\text{HNO}$  as rapidly as possible. The initial rate of reaction between  $^1\text{HNO}/^3\text{NO}^-$  and HOCbl was independent of the concentration of Piloty's acid in a ratio of  $\sim 120:1$  Piloty's acid to HOCbl. However, the large excess of Piloty's acid ( $\text{p}K_a = 9.26$ ) enabled additional, undesired reactions (e.g.

$^3\text{NO}^-$  reacts with product species  $\text{NO}^-$ -Cbl(III)). The experiments were also costly in terms of materials. The use of donor molecules that release  $^1\text{HNO}$  selectively on the ultrafast timescale would enable the reaction of  $^1\text{HNO}$  and the biomolecule of interest to be the rate determining step without the need for a large excess of the  $^1\text{HNO}$  donor molecule, and hence avoid potentially additional chemistry involving reactions between  $^1\text{HNO}$  or  $^3\text{NO}^-$  and the reaction products.

# CHAPTER 7: SUMMARY AND FUTURE DIRECTIONS

In this thesis, the trifluoromethanesulfonamidoxy moiety tethered to a 6-hydroxynaphthalen-2-yl (6,2-HNM) photocage was shown to release  $^1\text{HNO}$  in a near stoichiometric amount (~98%). The high selectivity for  $^1\text{HNO}$  photorelease is unprecedented for photolysis of a photocaged Piloty's acid-based leaving group.<sup>23,24,114</sup> Importantly, as proposed for donor **1**,<sup>24</sup>  $^1\text{HNO}$  release from excitation of **4** occurs via concerted C-O and N-S heterolytic bond cleavages. Other photoactive derivatives of Piloty's acid release  $\text{RSO}_2\text{NHOH}$  upon activation.<sup>23,24,114</sup> However,  $\text{CF}_3\text{SO}_2\text{NH}_2\text{OH}$  was not observed in the photolysis of donor **4** even under conditions where  $\text{CF}_3\text{SO}_2\text{NH}_2\text{OH}$  is stable. Therefore, the trifluoromethanesulfonamidoxy moiety is a superior leaving group compared with currently available Piloty's acid-based leaving groups.<sup>23,24,114</sup>

$^1\text{H}$  NMR and UV-vis spectroscopic experiments showed that **4** exists in three protonation states ( $\text{p}K_{\text{a}(\text{NH})} = 4.39 \pm 0.06$  and  $\text{p}K_{\text{a}(\text{OH})} = 9.73 \pm 0.01$  as determined by UV-vis spectroscopic titrations). Excitation of donor **4** under conditions where the leaving group nitrogen atom is deprotonated and naphtholic OH is protonated selectively generated the desired pathway. Emission studies indicated that donor **4** contains both photoacidic and photobasic sites. However, selective photoactivation of the HNO-generating pathway was achieved by irradiating donor **4** either in a solvent mixture of 80:20 v/v MeCN to 5 mM phosphate buffer solution (pH 7.0) or in an aprotic solvent (DMSO or MeCN) upon the addition of one mol. equiv. carboxylate salt. In both cases, the nitrogen atom of donor **4** is deprotonated while the OH function remains protonated even upon excitation. Hence, excited state proton transfers (ESPTs) are not involved in the mechanism of  $^1\text{HNO}$  release from excitation of **4**. Importantly, the photoproduct quantum yields of donor **4** where  $^1\text{HNO}$  is generated were unaffected by oxygen. Therefore, donor **4** must release  $^1\text{NO}^-$  upon excitation, which rapidly protonates to form the desired product,  $^1\text{HNO}$  ( $\text{p}K_{\text{a}}(^1\text{HNO}/^1\text{NO}^-) \sim 23$ ).

Time-resolved spectroscopic studies indicate that  $^1\text{HNO}$  generation may occur on the picosecond timescale following excitation of donor **4**. Femtosecond transient absorption experiments indicate that  $^1\text{NO}^-$  is released directly from donor **4**'s singlet excited state

species (Figure 7.1). Notably, the resulting (6-hydroxynaphthalen-2-yl)methyl cation species can undergo nucleophilic attack from solvent water or from HNO in the absence of an effective HNO trap to form 6-(hydroxymethyl)naphthalen-2-ol or 6-[(*E*)-(hydroxyimino)methyl]naphthalen-2-ol, respectively (Figure 7.2). 6-[(*E*)-(hydroxyimino)methyl]naphthalen-2-ol is photosensitive, forming 6-hydroxy-2-naphthaldehyde and 6-hydroxy-2-naphthamide upon irradiation (Figure 7.3). The nanosecond transient absorption studies indicated that 6-[(*E*)-(hydroxyimino)methyl]naphthalen-2-ol is formed rapidly and then undergoes intersystem crossing to a triplet state species.

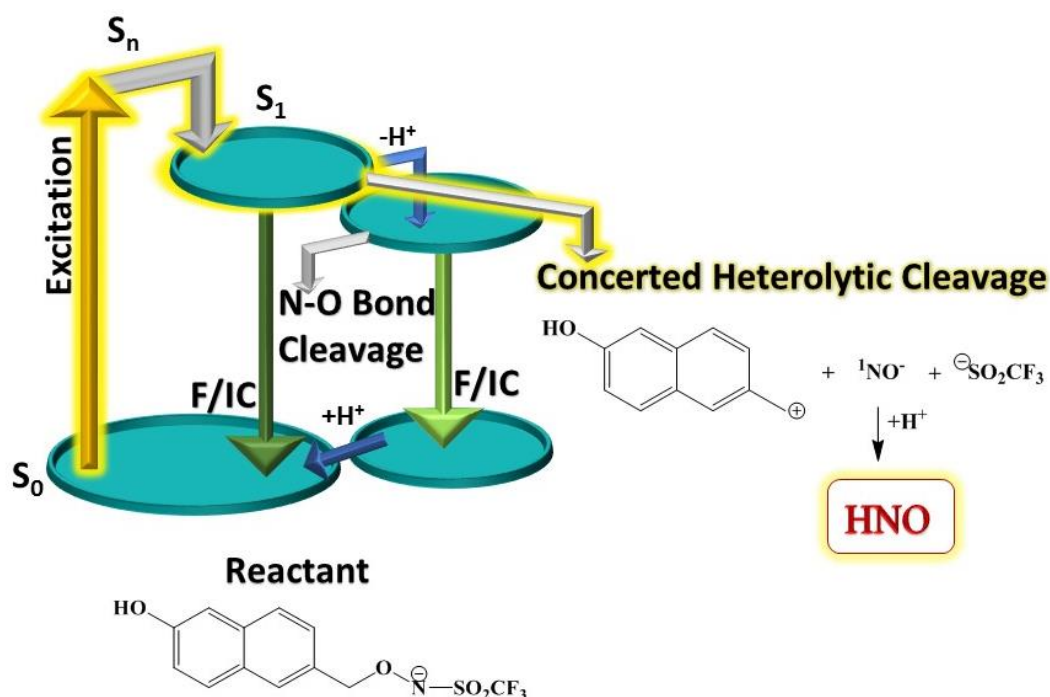


Figure 7.1. Simplified Jablonski diagram for donor **4**.  $S_0$ : Ground state;  $S_n$  ( $n \geq 1$ ): excited singlet states; F: fluorescence; IC: internal conversion. Not depicted: intersystem crossing (ISC).

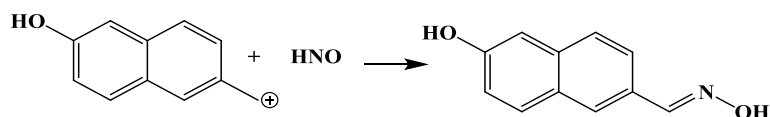


Figure 7.2. The proposed reaction of (6-hydroxynaphthalen-2-yl)methyl cation and HNO to form 6-[(*E*)-(hydroxyimino)methyl]naphthalen-2-ol.

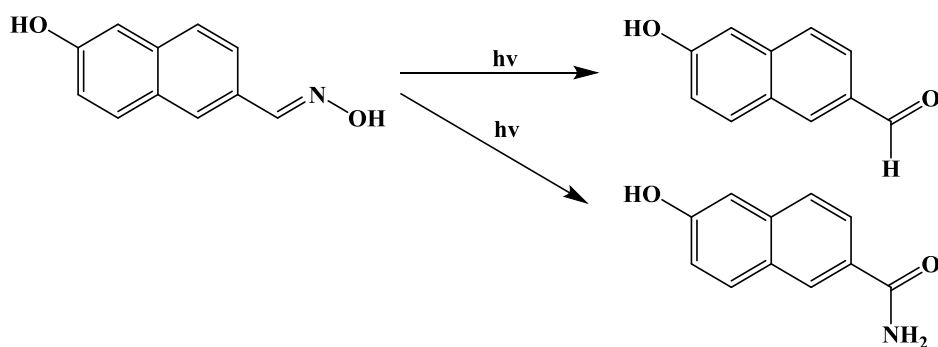


Figure 7.3. Photolysis of 6-[(*E*)-(hydroxyimino)methyl]naphthalen-2-ol.

While excitation of **4** has a high probability of undergoing the desired  $^1\text{HNO}$  photorelease pathway ( $\Phi_{\text{PP}} = 0.50$ ), donor **4** can undergo other photophysical or photochemical deactivation pathways.  $^1\text{HNO}$  release from the photolysis of donor **4** was shown to be highly dependent on solvent and pH conditions. Hence, the observed undesired pathways were examined in order to consider ways to limit competitive processes. As observed for donor **1**,<sup>24</sup> a solvent dependent N-O bond cleavage pathway was observed upon photolysis of **4** (Figure 7.1). Excited state proton transfers (ESPT) were shown to promote N-O bond cleavage upon photolysis of donor **1** and donor **4**. Additional spectroscopically observed deactivation pathways included fluorescence decay of the parent molecule and its conjugate base, intersystem crossing of the parent molecule to a triplet state, O-H bond homolysis, and photoejection of an electron to form a radical cation (Table 7.1). While all pathways were observed, not all pathways are competitive to  $^1\text{HNO}$  generation. Fluorescence was quenched under solvent conditions where only the desired  $^1\text{HNO}$  generation occurs. The products of O-H bond homolysis or photoejection of an electron were not observed via  $^1\text{H}$  NMR spectroscopy, indicating that these pathways are very minor. Overall, these findings show that  $^1\text{HNO}$  generation from the HNM photocage tethered to the trifluoromethanesulfonamidoxy moiety clearly does not require ESPT to occur. Indeed, ESPT even enables competitive undesired N-O bond cleavage pathways to occur. One possible means to prevent ESPTs is to methylate the photoacidic site.<sup>123,156,179</sup> Two structures are proposed as possible avenues of further work on the photoactive HNO donors using the trifluoromethanesulfonamidoxy leaving group, namely 1,1,1-trifluoro-*N*-[(6-methoxynaphthalen-2-yl)methoxy]methanesulfonamide or 1,1,1-trifluoro-*N*-[(3-methoxynaphthalen-2-yl)methoxy]methanesulfonamide (Figure 7.4).

Table 7.1. Interfering pathways to HNO photorelease following excitation of donor **1** or **4**.

Interfering Pathway	Evidence	Competitive with HNO Photorelease
Fluorescence Decay	Emission studies	No
ISC	Observation of triplet-triplet absorption in time-resolved absorption studies	No
ESIPT to form RSO <sub>2</sub> NH <sub>2</sub>	Photoproduct quantum yield studies of <b>1</b> and <b>4</b>	Prevented by 6,2-HNM-photoprotection
Heterolytic N-O bond cleavage following PTTS	Comparison of photoproduct quantum yields	Yes
O-H bond homolysis	Observation of naphthoxyl radical in LFP studies	No, minor pathway
Photoejection of an electron	Observation of a solvated electron in LFP studies	No, minor pathway

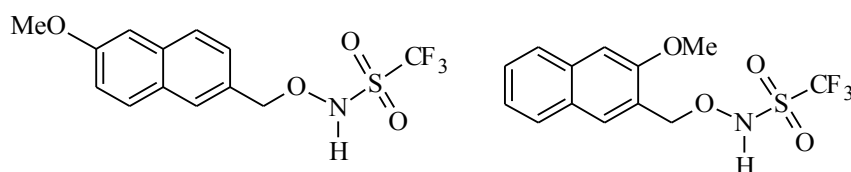


Figure 7.4. Proposed modifications to the HNM-photocage.

The HNM-photocage is a structurally simple photocage and is useful to illuminate the mechanism of release from caged substituents. Importantly, the results presented in this thesis indicate that the release of <sup>1</sup>HNO can be achieved from electron transfer upon excitation resulting in heterolytic bond cleavages. As ESPT is not essential for the desired pathway to occur, it is likely that other photocages tethered to the trifluoromethanesulfonamidoxy moiety will also release <sup>1</sup>HNO upon excitation. A limitation of donor **4** is that it is excited by UV light only. Hence, selective excitation of the photoactive donor **4** in kinetic and mechanistic studies of HNO with biomolecules is unlikely. However, visible excitation of photoactive HNO donors would enable selective excitation of the donor molecule only (i.e. not the biomolecule) and thus would be ideal for kinetic and mechanistic studies of photogenerated HNO with biomolecules. Furthermore, *in vitro* studies require a photocage that absorbs in the visible region of the spectrum and is soluble in water. One option is to tailor the HNM-photocage to absorb in the visible region by extension of conjugation in combination with methanolation of the naphtholic OH (e.g. use of anthracene derivatives). Other options include coumarin<sup>10,22,241</sup> or BODIPY<sup>114</sup> photoprotection, both of which absorb in the visible region. Indeed, (7-diethylaminocoumarin-4-yl)methyl group has already been shown to successfully release HNO when linked to Piloty's acid derivatives but with poor

selectivity for HNO release.<sup>114</sup> Based on the results presented in this thesis, tethering the (7-diethylaminocoumarin-4-yl)methyl group or another coumarin derivative to the trifluoromethanesulfonamidoxy moiety would likely enhance selectivity for HNO release. Another possibility is the use of BODIPY photoprotection, which has recently been explored as a photocage for release of small molecules in biological studies.<sup>278</sup> BODIPY photoprotection provides uncaging cross sections over  $10,000 \text{ M}^{-1} \text{ cm}^{-1}$  in the visible region.<sup>107</sup>

An intrinsic aspect of the development of HNO donor molecules is unambiguous HNO detection and quantification. Direct detection of HNO is inherently challenging due to its rapid dimerization ( $8.0 \times 10^6 \text{ M}^{-1} \text{ s}^{-1}$ ).<sup>9</sup> Many indirect detection methods were developed to characterize for HNO.<sup>24,31,64,65,234,264-266,270,279-282</sup> However, methods for HNO detection from photoactive HNO donors remain largely unexplored. Typically, HNO is quantified using GC-MS headspace analysis of the dimerization product,  $\text{N}_2\text{O}$ ,<sup>6</sup> and further confirmed using an additional trapping method. GC-MS headspace analysis was used to quantify HNO photorelease from a series of 1,2,4-oxadiazole-4-oxides,<sup>112</sup> from (7-diethylaminocoumarin-4-yl)methyl photocage tethered to Piloty's acid derivatives (bearing  $-\text{NO}_2$  or  $-\text{Br}$  at the ortho position),<sup>114</sup> and from hetero-Diels–Alder cycloadducts from acyl nitroso derivatives and 9,10-dimethylanthracene.<sup>109</sup> An HNO-specific fluorescence probe, P-Rhod, was used to qualitatively confirm the release of HNO from (7-diethylaminocoumarin-4-yl)methyl photocage tethered to Piloty's acid derivatives (bearing  $-\text{NO}_2$  or  $-\text{Br}$  at the ortho position) in cells.<sup>114</sup> EPR analysis of a ferrous nitroxyl complex further confirmed HNO release from photolysis of hetero-Diels–Alder cycloadducts from acyl nitroso derivatives.<sup>109</sup> HNO from photolysis of Angeli's salt and related diazeniumdiolates was confirmed through HNO's reaction with  $\text{NO}$ .<sup>25</sup> In this thesis, one method of HNO quantification ( $\text{H}_2\text{OCbl(III)}^+$  trapping) and of qualitative HNO detection (TXPTS trapping) were added to the growing library of HNO detection methods suitable for photoactive HNO donor molecules. Partial conversion experiments were used to show that donor **1** and **4** generate HNO upon photolysis (as indicated by UV-vis spectral changes for  $\text{H}_2\text{OCbl(III)}^+$  conversion to  $\text{NO}^-\text{Cbl(III)}$ ) in a 1:1 ratio to chemical marker  $\text{CF}_3\text{SO}_2^-$ .<sup>24</sup> HNO generation was confirmed using TXPTS or GC-MS headspace analysis of  $\text{N}_2\text{O}$ . Prior to the development of this method, GC-MS headspace analysis of  $\text{N}_2\text{O}$  has typically been used to quantify the amount of HNO generated from photoactive donors. GC-MS headspace analysis is not selective for HNO.<sup>265,283</sup>

Substoichiometric amounts of HNO were indicated for our system, as the photocage ejects electrons upon photoexcitation. Trapping of HNO by  $\text{H}_2\text{OCbl(III)}^+$  provides a powerful method to quantify HNO released from photoactive HNO donors that release HNO in the singlet excited state.

Simulations were also carried out to estimate the rate constant for the reaction between HNO and a cobalamin derivative, hydroxycobalamin (HOCbl); a series of experiments were carried out by our collaborator's research group. Rapid HNO release was achieved using a large excess of HNO donor Piloty's acid so that the rate-determining step was the reaction between HNO and HOCbl. The pH of the reaction was varied so that the ratio of HNO and its conjugate base ( $\text{p}K_{\text{a}} (^1\text{HNO}/^3\text{NO}^-) = 11.4$ )<sup>1</sup> would vary. The experimental data did not fit to a simple first-order reaction. Using modeling software, the rate constant for the reaction between HOCbl and HNO was calculated to be  $(2.46 \pm 0.01) \times 10^4 \text{ M}^{-1}\text{s}^{-1}$  at pH  $\sim 10.1$ . However, under highly alkaline conditions, a competing reaction between  $^3\text{NO}^-$  and product nitroxylcobalamin ( $\text{NO}^-$ -Cbl(III)) complicated the analysis. Hence, the rate constants for the reaction between HOCbl and  $^1\text{HNO}$  or  $^3\text{NO}^-$  could not be verified. Overall, it is likely that this method can be applied to select systems in order to accurately determine the rate of reaction between HNO and biomolecules. A compound is required that does not react with  $^3\text{NO}^-$  or has an established rate constant for this. The biomolecules of interest need to be carefully selected prior to investigation, especially because this method is costly in terms of materials and involves challenging experimental and analytical work.

The experiments with HOCbl and Piloty's acid indicate that direct release of  $^3\text{HNO}$  from a photocaged molecule will complicate kinetic and mechanistic studies with biomolecules. If  $^3\text{HNO}$  is released,  $^3\text{HNO}$  would rapidly deprotonate ( $\text{p}K_{\text{a}} (^3\text{HNO}/^3\text{NO}^-) \sim -1.8$ ) to form  $^3\text{NO}^-$ .<sup>1</sup> This species would protonate to form the desired product,  $^1\text{HNO}$  ( $\text{p}K_{\text{a}} (^1\text{HNO}/^3\text{NO}^-) = 11.4$ ).<sup>1</sup> However, the protonation of  $^3\text{NO}^-$  to form  $^1\text{HNO}$  is slow ( $1.38 \times 10^2 \text{ s}^{-1}$ ;  $t_{1/2} \sim 5.8 \text{ ms}$ ),<sup>2,9</sup> making  $^3\text{NO}^-$  a relatively long-lived species.<sup>26</sup>  $^3\text{NO}^-$  itself is a good reductant,<sup>277</sup> and reacts with transition metal complexes, including HOCbl and  $\text{NO}^-$ -Cbl(III) (as described in this thesis) in addition to  $[\text{Fe}(\text{NO})(\text{N}_3\text{PyS})]\text{BF}_4$ .<sup>277</sup> Therefore, if the photoactive HNO donor releases  $^3\text{HNO}$  from a triplet excited state, a reaction between  $^3\text{NO}^-$  and biomolecules may be observed instead of the desired reaction between  $^1\text{HNO}$  and the biomolecule. Hence, photorelease of  $^3\text{HNO}$  directly from a triplet

excited state is not ideal. Importantly, the HNM-photocages discussed in this thesis generate  $^1\text{HNO}$  upon irradiation.

Further research in the area of rapid and clean HNO release from photoactive molecules is required before in depth understanding of HNO's reactivity with biomolecules can be obtained. We believe that the development and understanding of HNO photorelease from HNM-protected  $\text{CF}_3\text{SO}_2\text{NHOH}$  is an important step towards this goal, as concerted C-O and N-S bond cleavages using the photocaged trifluoromethanesulfonamidoxy moiety ensures that HNO is rapidly generated, rather than the undesired  $\text{CF}_3\text{SO}_2\text{NHOH}$ .

# REFERENCES

- (1) Shafirovich, V.; Lyman, S. V. *Proc. Natl. Acad. Sci.* **2002**, *99* (11), 7340–7345.
- (2) Paolucci, N.; Jackson, M. I.; Lopez, B. E.; Miranda, K. M.; Tocchetti, C. G.; Wink, D. A.; Hobbs, A. J.; Fukuto, J. M. *Pharmacol. Ther.* **2007**, *113*, 442–458.
- (3) Miranda, K. M.; Nagasawa, H. T.; Toscano, J. P. *Curr. Top. Med. Chem.* **2005**, *5*, 649–664.
- (4) Shafirovich, V.; Lyman, S. V. *J. Am. Chem. Soc.* **2003**, *125* (21), 6547–6552.
- (5) Bartberger, M. D.; Liu, W.; Ford, E.; Miranda, K. M.; Switzer, C. H.; Fukuto, J. M.; Farmer, P. J.; Wink, D. A.; Houk, K. N. *Proc. Natl. Acad. Sci.* **2002**, *99* (17), 10958–10963.
- (6) Fehling, C.; Friedrichs, G. *J. Am. Chem. Soc.* **2011**, *133* (44), 17912–17922.
- (7) Basudhar, D.; Bharadwaj, G.; Salmon, D. J.; Miranda, K. M. In *The Chemistry and Biology of Nitroxyl (HNO)*; Doctorovich, F., Farmer, P. J., Marti, M. A., Eds.; Elsevier Inc.: Amsterdam, 2016; pp 11–36.
- (8) Fukuto, J. M. *Br. J. Pharmacol.* **2019**, *176* (2), 135–146.
- (9) Miranda, K. M. *Coord. Chem. Rev.* **2005**, *249*, 433–455.
- (10) Pelliccioli, A. P.; Wirz, J. *Photochem. Photobiol. Sci.* **2002**, *1* (7), 441–458.
- (11) Stensrud, K.; Noh, J.; Kandler, K.; Wirz, J.; Heger, D.; Givens, R. S. *J. Org. Chem.* **2009**, *74* (15), 5219–5227.
- (12) Adams, S. R.; Kao, J.; Grynkiewicz, G.; Minta, A.; Tsien, R. Y. *J. Am. Chem. Soc.* **1988**, *110* (10), 3212–3220.
- (13) Parthenopoulos, D. A.; McMorrow, D. P.; Kasha, M. *J. Phys. Chem.* **1991**, *95* (7), 2668–2674.
- (14) Filevich, O.; Carrone, G.; Pavlovsky, V. A.; Etchenique, R. *Anal. Chem.* **2012**, *84* (13), 5618–5624.
- (15) Ellis-Davies, G. C. R.; Matsuzaki, M.; Paukert, M.; Kasai, H.; Bergles, D. E. *J. Neurosci.* **2007**, *27* (25), 6601–6604.
- (16) del Mármol, J.; Filevich, O.; Etchenique, R. *Anal. Chem.* **2010**, *82* (14), 6259–6264.
- (17) Belov, V. N.; Wurm, C. A.; Boyarskiy, V. P.; Jakobs, S.; Hell, S. W. *Angew. Chem. Int. Ed.* **2010**, *49* (20), 3520–3523.
- (18) Young, D. D.; Deiters, A. *Angew. Chem. Int. Ed.* **2007**, *119* (23), 4368–4370.
- (19) Shestopalov, I. A.; Sinha, S.; Chen, J. K. *Nat. Chem. Biol.* **2007**, *3* (10), 650–651.
- (20) Chou, C.; Deiters, A. *Angew. Chem. Int. Ed.* **2011**, *50* (30), 6839–6842.
- (21) Mayer, G.; Heckel, A. *Angew. Chem. Int. Ed.* **2006**, *45* (30), 4900–4921.
- (22) Givens, R. S.; Conrad, G. P.; Yousef, A. L.; Lee, J.-I. In *CRE Handbook of Organic Photochemistry and Photobiology*; CRE Handbook of Organic Photochemistry and Photobiology, 2nd Edition; W. Horspool and F. Lenci, 2003.
- (23) Zhou, Y.; Cink, R.; Fejedelem, Z.; Simpson, M. C.; Seed, A.; Sampson, P.; Brasch, N. E. *Eur. J. Org. Chem.* **2018**, *2018* (15), 1745–1755.
- (24) Zhou, Y.; Cink, R.; Dassanayake, R. S.; Seed, A. J.; Brasch, N. E.; Sampson, P. *Angew. Chem. Int. Ed.* **2016**, *55* (42), 13229–13232.

## References

- (25) Lyman, S. V.; Shafirovich, V. *J. Phys. Chem. B* **2007**, *111* (24), 6861–6867.
- (26) Hamer, M.; Vásquez, M. A. M.; Doctorovich, F. In *The Chemistry and Biology of Nitroxyl (HNO)*; Doctorovich, F., Farmer, P. J., Marti, M. A., Eds.; Elsevier Inc., 2016; pp 1–10.
- (27) Sabbah, H. N.; Tocchetti, C. G.; Wang, M.; Daya, S.; Gupta, R. C.; Tunin, R. S.; Mazhari, R.; Takimoto, E.; Paolocci, N.; Cowart, D.; Colucci, W. S.; Kass, D. A. *Circ. Heart Fail.* **2013**, *6* (6), 1250–1258.
- (28) Wong, P. S. Y.; Hyun, J.; Fukuto, J. M.; Shirota, F. N.; DeMaster, E. G.; Shoeman, D. W.; Nagasawa, H. T. *Biochem.* **1998**, No. 37, 5362–5371.
- (29) Eberhardt, M.; Dux, M.; Namer, B.; Miljkovic, J. L.; Cordasic, N.; Will, C.; Kichko, T. I.; la Roche, de, J.; Fischer, M.; Suarez, S. A.; Bikiel, D. E.; Dorsch, K.; Leffler, A.; Babes, A.; Lampert, A.; Lennerz, J. K.; Jacobi, J.; Martí, M. A.; Doctorovich, F.; Hogerstatt, E. D.; Zygmunt, P. M.; Ivanović-Burmazović, I.; Messlinger, K.; Reeh, P.; Filipovic, M. R. *Nat. Comm.* **2014**, *5* (4381), 1–17.
- (30) Heinecke, J. L.; Khin, C.; Pereira, J. C. M.; Suárez, S. A.; Iretskii, A. V.; Doctorovich, F.; Ford, P. C. *J. Am. Chem. Soc.* **2013**, *135* (10), 4007–4017.
- (31) Cline, M. R.; Toscano, J. P. *J. Phys. Org. Chem.* **2011**, *24*, 993–998.
- (32) Irvine, J. C.; Ritchie, R. H.; Favalaro, J. L.; Andrews, K. L.; Widdop, R. E.; Kemp-Harper, B. K. *Trends Pharmacol. Sci.* **2008**, *29* (12), 601–608.
- (33) Tita, C.; Gilbert, E. M.; Van Bakel, A. B.; Grzybowski, J.; Haas, G. J.; Jarrah, M.; Dunlap, S. H.; Gottlieb, S. S.; Klapholz, M.; Patel, P. C.; Pfister, R.; Seidler, T.; Shah, K. B.; Zieliński, T.; Venuti, R. P.; Cowart, D.; Foo, S. Y.; Vishnevsky, A.; Mitrovic, V. *Eur. J. Heart Fail.* **2017**, *19* (10), 1321–1332.
- (34) Shoman, M. E.; DuMond, J. F.; Isbell, T. S.; Crawford, J. H.; Brandon, A.; Honovar, J.; Vitturi, D. A.; White, C. R.; Patel, R. P.; King, S. B. *J. Med. Chem.* **2011**, *54* (4), 1059–1070.
- (35) Bianco, C. L.; Toscano, J. P.; Bartberger, M. D.; Fukuto, J. M. *Arch. Biochem. Biophys.* **2017**, *617*, 129–136.
- (36) Braunersreuther, V.; Jaquet, V. *Curr. Pharm. Biotechnol.* **2012**, *13*, 97–114.
- (37) Kemp-Harper, B. K.; Horowitz, J. D.; Ritchie, R. H. *Drugs* **2016**, *76* (14), 1337–1348.
- (38) Cowart, D.; Venuti, R. P.; Lynch, K.; Guptill, J. T.; Noveck, R. J.; Foo, S. Y. *J. Clin. Pharmacol.* **2019**, *61* (4), 391–404.
- (39) Switzer, C. H.; Flores-Santana, W.; Mancardi, D.; Donzelli, S.; Basudhar, D.; Ridnour, L. A.; Miranda, K. M.; Fukuto, J. M.; Paolocci, N.; Wink, D. A. *Biochim. Biophys. Acta* **2009**, *1787* (7), 835–840.
- (40) Kim, W. K.; Choi, Y. B.; Rayudu, P. V.; Das, P.; Asaad, W.; Arnelle, D. R.; Stamler, J. S.; Lipton, S. A. *Neuron* **1999**, *24* (2), 461–469.
- (41) Choe, C.-U.; Lewerenz, J.; Gerloff, C.; Magnus, T.; Donzelli, S. *Antioxid. Redox Signal.* **2011**, *14* (9), 1699–1711.
- (42) Shoeman, D. W.; Shirota, F. N.; DeMaster, E. G.; Nagasawa, H. T. *Alcohol* **2000**, *20* (1), 55–59.
- (43) Reisz, J. A.; Bechtold, E.; King, S. B. *Dalton Trans.* **2010**, *39* (22), 5203–5212.
- (44) DeMaster, E. G.; Nagasawa, H. T.; Shirota, F. N. *Pharmacol. Biochem. Behav.* **1983**, *18* (1), 273–277.
- (45) DeMaster, E. G.; Shirota, F. N.; Nagasawa, H. T. *Biochem. Biophys. Res. Commun.* **1984**, *122* (1), 358–365.

## References

---

- (46) Fukuto, J. M.; Dutton, A. S.; Houk, K. N. *ChemBioChem* **2005**, *6* (4), 612–619.
- (47) Lopez, B. E.; Shinyashiki, M.; Han, T. H.; Fukuto, J. M. *Free Radic. Biol. Med.* **2007**, *42* (4), 482–491.
- (48) Miranda, K. M.; Espey, M. G.; Yamada, K.; Krishna, M.; Ludwick, N.; Kim, S.; Jourd'heuil, D.; Grisham, M. B.; Feelisch, M.; Fukuto, J. M.; Wink, D. A. *J. Biol. Chem.* **2001**, *276* (3), 1720–1727.
- (49) Miljkovic, J. L.; Kenkel, I.; Ivanović-Burmazović, I.; Filipovic, M. R. *Angew. Chem. Int. Ed.* **2013**, *52* (46), 12061–12064.
- (50) Suárez, S. A.; Muñoz, M.; Alvarez, L.; Venâncio, M. F.; Rocha, W. R.; Bikiel, D. E.; Martí, M. A.; Doctorovich, F. *J. Am. Chem. Soc.* **2017**, *139* (41), 14483–14487.
- (51) Fukuto, J. M.; Cisneros, C. J.; Kinkade, R. L. *J. Inorg. Biochem.* **2013**, *118*, 201–208.
- (52) Miranda, K. M.; Paolocci, N.; Katori, T.; Thomas, D. D.; Ford, E.; Bartberger, M. D.; Espey, M. G.; Kass, D. A.; Feelisch, M.; Fukuto, J. M.; Wink, D. A. *Proc. Natl. Acad. Sci.* **2003**, *100* (16), 9196–9201.
- (53) Jackson, M. I.; Han, T. H.; Serbulea, L.; Dutton, A.; Ford, E.; Miranda, K. M.; Houk, K. N.; Wink, D. A.; Fukuto, J. M. *Free Radic. Biol. Med.* **2009**, *47* (8), 1130–1139.
- (54) Kirsch, M.; de Groot, H. *J. Biol. Chem.* **2002**, *277* (16), 13379–13388.
- (55) Kawai, K.; Ieda, N.; Aizawa, K.; Suzuki, T.; Miyata, N.; Nakagawa, H. *J. Am. Chem. Soc.* **2013**, *135* (34), 12690–12696.
- (56) Filipovic, M. In *The Chemistry and Biology of Nitroxyl (HNO)*; Doctorovich, F., Farmer, P. J., Marti, M. A., Eds.; Elsevier Inc.: Amsterdam, 2016; pp 105–126.
- (57) Doyle, M. P.; Mahapatro, S. N.; Broene, R. D.; Guy, J. K. *J. Am. Chem. Soc.* **1988**, *110*, 593–599.
- (58) Bartberger, M. D.; Fukuto, J. M.; Houk, K. N. *Proc. Natl. Acad. Sci.* **2001**, *98* (5), 2194–2198.
- (59) Fukuto, J. M.; Bartberger, M. D.; Dutton, A. S.; Paolocci, N.; Wink, D. A.; Houk, K. N. *Chem. Res. Toxicol.* **2005**, *18* (5), 790–801.
- (60) Van Stappen, C.; Goodrich, L. E.; Lehnert, N. In *The Chemistry and Biology of Nitroxyl (HNO)*; Doctorovich, F., Farmer, P. J., Marti, M. A., Eds.; Elsevier Inc.: Amsterdam, 2016; pp 155–192.
- (61) Bazylinski, D. A.; Hollocher, T. C. *J. Am. Chem. Soc.* **1985**, *107*, 7982–7986.
- (62) Huang, J.; Sommers, E. M.; King, S. B. *J. Am. Chem. Soc.* **2002**, *124* (13), 3473–3480.
- (63) Doctorovich, F.; Bikiel, D. E.; Pellegrino, J.; Suárez, S. A.; Martí, M. A. In *Inorganic/Bioinorganic Reaction Mechanisms*; Elsevier Inc., 2012; Vol. 64, pp 97–139.
- (64) Bari, S. E.; Martí, M. A.; Amorebieta, V. T.; Estrin, D. A.; Doctorovich, F. *J. Am. Chem. Soc.* **2003**, *125* (50), 15272–15273.
- (65) Martí, M. A.; Bari, S. E.; Estrin, D. A.; Doctorovich, F. *J. Am. Chem. Soc.* **2005**, *127* (13), 4680–4684.
- (66) Bonner, F. T.; Akhtar, M. J. *Inorg. Chem.* **1981**, *20* (10), 3155–3160.
- (67) Subedi, H.; Brasch, N. E. *Eur. J. Inorg. Chem.* **2015**, *2015* (23), 3825–3834.
- (68) Bryukov, M. G.; Kachanov, A. A.; Timonnen, R.; Seetula, J.; Vanadoren, J.; Sarkisov, O. M. *Chem. Phys. Lett.* **208** (5-6), 392–398.

## References

---

- (69) Miranda, K. M.; Yamada, K.; Espey, M. G.; Thomas, D. D.; DeGraff, W.; Mitchell, J. B.; Krishna, M. C.; Colton, C. A.; Wink, D. A. *Arch. Biochem. Biophys.* **2002**, *401*, 134–144.
- (70) Aizawa, K.; Nakagawa, H.; Matsuo, K.; Kawai, K.; Ieda, N.; Suzuki, T.; Miyata, N. *Bioorganic Med. Chem. Lett.* **2013**, *23* (8), 2340–2343.
- (71) Lee, M. J. C.; Shoeman, D. W.; Goon, D. J. W.; Nagasawa, H. T. *Nitric Oxide* **2001**, *5* (3), 278–287.
- (72) Matsuo, K.; Nakagawa, H.; Adachi, Y.; Kameda, E.; Tsumoto, H.; Suzuki, T.; Miyata, N. *Chem. Commun.* **2010**, *46* (21), 3788–3790.
- (73) DuMond, J. F.; King, S. B. *Antioxid. Redox Signal.* **2011**, *14* (9), 1637–1648.
- (74) Hughes, M. N.; Wimbledon, P. E. *J. Chem. Soc., Dalton Trans.* **1976**, *0*, 703–705.
- (75) Bonner, F. T.; Ravid, B. *Inorg. Chem.* **1975**, *14* (3), 558–563.
- (76) Maragos, C. M.; Morley, D.; Wink, D. A.; Dunams, T. M.; Saavedra, J. E.; Hoffman, A.; Bove, A. A.; Isaac, L.; Hrabie, J. A.; Keefer, L. K. *J. Med. Chem.* **1991**, *34* (11), 3242–3247.
- (77) Miranda, K. M.; Dutton, A. S.; Ridnour, L. A.; Foreman, C. A.; Ford, E.; Paolocci, N.; Katori, T.; Tocchetti, C. G.; Mancardi, D.; Thomas, D. D.; Espey, M. G.; Houk, K. N.; Fukuto, J. M.; Wink, D. A. *J. Am. Chem. Soc.* **2005**, *127* (2), 722–731.
- (78) Subedi, H.; Hassanin, H. A.; Brasch, N. E. *Inorg. Chem.* **2014**, *53* (3), 1570–1577.
- (79) Akhtar, M. J.; Bonner, F. T.; Hughes, M. N.; Humphreys, E. J.; Lu, C. S. *Inorg. Chem.* **1986**, *25* (26), 4635–4639.
- (80) Miranda, K. M.; Katori, T.; Torres de Holding, C. L.; Thomas, L.; Ridnour, L. A.; McLendon, W. J.; Cologna, S. M.; Dutton, A. S.; Champion, H. C.; Mancardi, D.; Tocchetti, C. G.; Saavedra, J. E.; Keefer, L. K.; Houk, K. N.; Kass, D. A.; Fukuto, J. M.; Paolocci, N.; Wink, D. A. *J. Med. Chem.* **2005**, *48* (26), 8220–8228.
- (81) Zamora, R.; Grzesiok, A.; Weber, H.; Feelisch, M. *Biochem. J.* **1995**, *312*, 333–339.
- (82) Hughes, M. N.; Cammack, R. *Methods Enzymol.* **1999**, *301*, 279–287.
- (83) Fukuto, J. M.; Hszieh, R.; Gulati, P.; Chiang, K. T.; Nagasawa, H. T. *Biochem. Biophys. Res. Commun.* **1992**, *187* (3), 1367–1373.
- (84) Pennington, R. L.; Sha, X.; King, S. B. *Bioorganic Med. Chem. Lett.* **2005**, *15* (9), 2331–2334.
- (85) Sirsalmath, K.; Suarez, S. A.; Bikiel, D. E.; Doctorovich, F. *J. Inorg. Biochem.* **2013**, *118*, 134–139.
- (86) Conway, T. T.; DeMaster, E. G.; Lee, M. J.; Nagasawa, H. T. *J. Med. Chem.* **1998**, *41* (15), 2903–2909.
- (87) Lee, M. J.; Nagasawa, H. T.; Elberling, J. A.; DeMaster, E. G. *J. Med. Chem.* **1992**, *35* (20), 3648–3652.
- (88) Shirota, F. N.; DeMaster, E. G.; Lee, M.; Nagasawa, H. T. *Nitric Oxide* **1999**, *3* (6), 445–453.
- (89) Toscano, J. P.; Brookfield, F. A.; Cohen, A. D.; Courtney, S. M.; Frost, L. M.; Kalish, V. No. 8,030,356. J. US Patent Office 2011.
- (90) Adas, S. K.; Bharadwaj, V.; Zhou, Y.; Zhang, J.; Seed, A. J.; Brasch, N. E.; Sampson, P. *Chem. Eur. J.* **2018**, *24*, 7330–7334.
- (91) Sha, X.; Isbell, S.; Patel, R. P.; Day, C. S.; King, S. B. *J. Am. Chem. Soc.* **2006**, *128* (30), 9687–9692.

## References

---

- (92) Guthrie, D. A.; Kim, N. Y.; Siegler, M. A.; Moore, C. D.; Toscano, J. P. *J. Am. Chem. Soc.* **2012**, *134* (4), 1962–1965.
- (93) Nagasawa, H. T.; DeMaster, E. G.; Redfern, B.; Shirota, F. N.; Goon, D. J. *W. J. Med. Chem.* **1990**, *33*, 3122–3124.
- (94) Sutton, A. D.; Williamson, M.; Weismiller, H.; Toscano, J. P. *Org. Lett.* **2012**, *14* (2), 472–475.
- (95) Cohen, A. D.; Zeng, B.-B.; King, S. B.; Toscano, J. P. *J. Am. Chem. Soc.* **2003**, *125* (6), 1444–1445.
- (96) Nakagawa, H. *J. Inorg. Biochem.* **2013**, *118*, 187–190.
- (97) Zeng, B.-B.; Huang, J.; Wright, M. W.; King, S. B. *Bioorganic Med. Chem. Lett.* **2004**, *14* (22), 5565–5568.
- (98) Truzzi, D. R.; Franco, D. W. *Inorganica Chim. Acta* **2014**, *421*, 74–79.
- (99) Rhine, M. A.; Rodrigues, A. V.; Bieber Urbauer, R. J.; Urbauer, J. L.; Stemmler, T. L.; Harrop, T. C. *J. Am. Chem. Soc.* **2014**, *136* (36), 12560–12563.
- (100) Ackermann, M. N.; Powell, R. E. *Inorg. Chem.* **1966**, *5* (8), 1334–1337.
- (101) Carrone, G.; Pellegrino, J.; Doctorovich, F. *Chem. Commun.* **2017**, *53*, 5314–5317.
- (102) Turro, N. J.; Ramamurthy, V.; Scaiano, J. C. *Principles of Molecular Photochemistry: An Introduction*; University Science Books, 2009.
- (103) Atkins, P.; de Paula, J. *Physical Chemistry*, Seventh. W. H. Freeman and Company: New York, 2002.
- (104) Ma, C.; Kwok, W. M.; Chan, W. S.; Du, Y.; Kan, J. T. W.; Toy, P. H.; Phillips, D. L. *J. Am. Chem. Soc.* **2006**, *128* (8), 2558–2570.
- (105) Il'ichev, Y. V.; Schwörer, M. A.; Wirz, J. *J. Am. Chem. Soc.* **2004**, *126* (14), 4581–4595.
- (106) Franco, L. P.; Cicillini, S. A.; Biazotto, J. C.; Schiavon, M. A.; Mikhailovsky, A.; Burks, P.; Garcia, J.; Ford, P. C.; Santana da Silva, R. *J. Phys. Chem. A* **2014**, *118* (51), 12184–12191.
- (107) Slanina, T.; Shrestha, P.; Palao, E.; Kand, D.; Peterson, J. A.; Dutton, A. S.; Rubinstein, N.; Weinstain, R.; Winter, A. H.; Klán, P. *J. Am. Chem. Soc.* **2017**, *139* (42), 15168–15175.
- (108) da Rocha, Z. N.; Marchesi, M. S. P.; Molin, J. C.; Lunardi, C. N.; Miranda, K. M.; Bendhack, L. M.; Ford, P. C.; da Silva, R. S. *Dalton Trans.* **2008**, No. 32, 4282–4287.
- (109) Adachi, Y.; Nakagawa, H.; Matsuo, K.; Suzuki, T.; Miyata, N. *Chem. Commun.* **2008**, No. 41, 5149–5151.
- (110) Matsuo, K.; Nakagawa, H.; Adachi, Y.; Kameda, E.; Aizawa, K.; Tsumoto, H.; Suzuki, T.; Miyata, N. *Chem. Pharm. Bull.* **2012**, *60* (8), 1055–1062.
- (111) Evans, A. S.; Cohen, A. D.; Gurard-Levin, Z. A.; Kebede, N.; Celius, T. C.; Miceli, A. P.; Toscano, J. P. *Can. J. Chem.* **2011**, *89* (2), 130–138.
- (112) Memeo, M. G.; Dondi, D.; Mannucci, B.; Corana, F.; Quadrelli, P. *Tetrahedron* **2013**, *69* (35), 7387–7394.
- (113) Grither, W. R.; Korang, J.; Sauer, J. P.; Sherman, M. P.; Vanegas, P. L.; Zhang, M.; McCulla, R. D. *J. Photochem. Photobiol. A* **2012**, *227* (1), 1–10.
- (114) Kawaguchi, M.; Tani, T.; Hombu, R.; Ieda, N.; Nakagawa, H. *Chem. Commun.* **2018**, *54* (73), 10371–10374.
- (115) Eckardt, T.; Hagen, V.; Schade, B.; Schmidt, R.; Schweitzer, C.; Bendig, J. *J. Org. Chem.* **2002**, *67* (3), 703–710.
- (116) Agmon, N. *J. Phys. Chem. A* **2005**, *109* (1), 13–35.

## References

---

- (117) Arumugam, S.; Popik, V. V. *J. Am. Chem. Soc.* **2012**, *134* (20), 8408–8411.
- (118) Westlake, B. C.; Paul, J. J.; Bettis, S. E.; Hampton, S. D.; Mehl, B. P.; Meyer, T. J.; Papanikolas, J. M. *J. Phys. Chem. B* **2012**, *116* (51), 14886–14891.
- (119) Chou, P.; McMorrow, D.; Aartsma, T. J.; Kasha, M. *J. Phys. Chem.* **1984**, *88* (20), 4596–4599.
- (120) Arumugam, S.; Popik, V. V. *J. Am. Chem. Soc.* **2009**, *131* (33), 11892–11899.
- (121) Chiang, Y.; Kresge, A. J.; Zhu, Y. *J. Am. Chem. Soc.* **2000**, *122*, 9854–9855.
- (122) Veljković, J.; Uzelac, L.; Molčanov, K.; Mlinarić-Majerski, K.; Kralj, M.; Wan, P.; Basarić, N. *J. Org. Chem.* **2012**, *77* (10), 4596–4610.
- (123) Basarić, N.; Cindro, N.; Bobinac, D.; Uzelac, L.; Mlinarić-Majerski, K.; Kralj, M.; Wan, P. *Photochem. Photobiol. Sci.* **2012**, *11* (2), 381–396.
- (124) Kulikov, A.; Arumugam, S.; Popik, V. V. *J. Org. Chem.* **2008**, *73* (19), 7611–7615.
- (125) Arumugam, S.; Popik, V. V. *Photochem. Photobiol. Sci.* **2012**, *11* (3), 518–521.
- (126) Rosenberg, M.; Dahlstrand, C.; Kilså, K.; Ottosson, H. *Chem. Rev.* **2014**, *114* (10), 5379–5425.
- (127) Simkovitch, R.; Huppert, D. *J. Phys. Chem. B* **2015**, *119* (46), 14683–14696.
- (128) Lee, Y.-S.; Yu, H.; Kwon, O.-H.; Jang, D.-J. *Phys. Chem. Chem. Phys.* **2008**, *10* (1), 153–158.
- (129) Simkovitch, R.; Akulov, K.; Shomer, S.; Roth, M. E.; Shabat, D.; Schwartz, T.; Huppert, D. *J. Phys. Chem. A* **2014**, *118* (25), 4425–4443.
- (130) Kang, B.; Shi, H.; Yan, S.; Lee, J. Y. *RSC Adv.* **2014**, *4*, 38551–38557.
- (131) Kuss-Petermann, M.; Wenger, O. S. *J. Phys. Chem. A* **2013**, *117* (28), 5726–5733.
- (132) Rosspeintner, A.; Lang, B.; Vauthey, E. *Annu. Rev. Phys. Chem.* **2013**, *64* (1), 247–271.
- (133) Pérez-Lustres, J. L.; Rodriguez-Prieto, F.; Mosquera, M.; Senyushkina, T. A.; Ernsting, N. P.; Kovalenko, S. A. *J. Am. Chem. Soc.* **2007**, *129* (17), 5408–5418.
- (134) Solntsev, K. M.; Cohen, B.; Huppert, D.; Hayashi, Y.; Feldman, Y. *J. Am. Chem. Soc.* **2002**, *124* (31), 9046–9047.
- (135) Solntsev, K. M.; Al-Ainain, S. A.; Il'ichev, Y. V.; Kuzmin, M. G. *J. Photochem. Photobiol. A* **2005**, *175*, 178–191.
- (136) Kumpulainen, T.; Rosspeintner, A.; Dereka, B.; Vauthey, E. *J. Phys. Chem. Lett.* **2017**, *8* (18), 4516–4521.
- (137) Tolbert, L.; Harvey, L. C.; Lum, R. C. *J. Phys. Chem.* **1993**, *97*, 13335–13340.
- (138) Prémont-Schwarz, M.; Barak, T.; Pines, D.; Nibbering, E. T. J.; Pines, E. *J. Phys. Chem. B* **2013**, *117* (16), 4594–4603.
- (139) Pines, D.; Pines, E. In *Handbook of Hydrogen Transfer*; Schowen, R. L., Ed.; Hydrogen-Transfer Reactions: Weinheim, 2006; pp 377–415.
- (140) Tolbert, L.; Solntsev, K. M. In *Hydrogen-Transfer Reactions*; Hynes, J. T., Kliman, J. P., Limbach, H. H., Schowen, R. L., Eds.; Wiley Online Library: Weinheim, 2007; pp 417–439.
- (141) Suzuki, S.; Fujii, T.; Ishikawa, T. *J. Mol. Spectrosc.* **1975**, *57*, 490–499.
- (142) Driscoll, E. W.; Hunt, J. R.; Dawlaty, J. M. *J. Phys. Chem. Lett.* **2016**, *7* (11), 2093–2099.
- (143) Shirai, M.; Tsunooka, M. *Prog. Polym. Sci.* **1996**, *21*, 1–45.
- (144) Flegel, M.; Lukeman, M.; Wan, P. *Can. J. Chem.* **2008**, *86* (2), 161–169.

## References

- (145) Arnaut, L. G.; Formosinho, S. J. *J. Photochem. Photobiol. A: Chem.* **1993**, *75* (1), 1–20.
- (146) Green, O.; Simkovitch, R.; Pinto da Silva, L.; Esteves da Silva, J. C. G.; Shabat, D.; Huppert, D. *J. Phys. Chem. A* **2016**, *120* (31), 6184–6199.
- (147) Wan, P.; Yates, K. *J. Org. Chem.* **1983**, *48* (6), 869–876.
- (148) Sinha, H. K.; Thomson, P. C. P.; Yates, K. *Can. J. Chem.* **1990**, *68*, 1507–1513.
- (149) Lukeman, M.; Veale, D.; Wan, P.; Munasinghe, V. R. N.; Corrie, J. E. *Can. J. Chem.* **2004**, *82* (2), 240–253.
- (150) Wan, P.; Yates, K.; Boyd, M. K. *J. Org. Chem.* **1985**, *50* (16), 2881–2886.
- (151) Du, L.; Zhang, X.; Xue, J.; Tang, W.-J.; Li, M.-D.; Lan, X.; Zhu, J.; Zhu, R.; Weng, Y.; Li, Y.-L.; Phillips, D. L. *J. Phys. Chem. B* **2016**, *120* (43), 11132–11141.
- (152) Ditkovich, J.; Mukra, T.; Pines, D.; Huppert, D.; Pines, E. *J. Phys. Chem. B* **2015**, *119* (6), 2690–2701.
- (153) Kasha, M. *J. Chem. Soc., Faraday Trans. 2* **1986**, *82*, 2379–2392.
- (154) Fischer, M.; Wan, P. *J. Am. Chem. Soc.* **1999**, *121* (19), 4555–4562.
- (155) Isaks, M.; Yates, K.; Kalanderopoulos, P. *J. Am. Chem. Soc.* **1984**, *106*, 2728–2730.
- (156) Diao, L.; Yang, C.; Wan, P. *J. Am. Chem. Soc.* **1995**, *117*, 5369–5370.
- (157) Percivalle, C.; La Rosa, A.; Verga, D.; Doria, F.; Mella, M.; Palumbo, M.; Di Antonio, M.; Freccero, M. *J. Org. Chem.* **2011**, *76* (9), 3096–3106.
- (158) Toteva, M. M.; Moran, M.; Amyes, T. L.; Richard, J. P. *J. Am. Chem. Soc.* **2003**, *125* (29), 8814–8819.
- (159) Foster, K. L.; Baker, S.; Brousmiche, D. W.; Wan, P. *J. Photochem. Photobiol. A* **1999**, *129*, 157–163.
- (160) Richter, S. N.; Maggi, S.; Mels, S. C.; Palumbo, M.; Freccero, M. *J. Am. Chem. Soc.* **2004**, *126* (43), 13973–13979.
- (161) Škalamera, Đ.; Mlinarić-Majerski, K.; Martin-Kleiner, I.; Kralj, M.; Wan, P.; Basarić, N. *J. Org. Chem.* **2014**, *79*, 4390–4397.
- (162) Brousmiche, D. W.; Wan, P. *J. Photochem. Photobiol. A* **2002**, *149*, 71–81.
- (163) Doria, F.; Lena, A.; Bargiggia, R.; Freccero, M. *J. Org. Chem.* **2016**, *81* (9), 3665–3673.
- (164) Arumugam, S.; Popik, V. V. *J. Org. Chem.* **2010**, *75* (21), 7338–7346.
- (165) Colloredo-Mels, S.; Doria, F.; Verga, D.; Freccero, M. *J. Org. Chem.* **2006**, *71* (10), 3889–3895.
- (166) Basarić, N.; Žabčić, I.; Mlinarić-Majerski, K.; Wan, P. *J. Org. Chem.* **2010**, *75* (1), 102–116.
- (167) Lukeman, M. In *ChemInform*; ChemInform, 2009; pp 1–32.
- (168) Chiang, Y.; Kresge, A. J.; Zhu, Y. *J. Am. Chem. Soc.* **2002**, *124* (22), 6349–6356.
- (169) Chiang, Y.; Kresge, A. J.; Zhu, Y. *J. Am. Chem. Soc.* **2002**, *124* (4), 717–722.
- (170) Verga, D.; Nadai, M.; Doria, F.; Percivalle, C.; Di Antonio, M.; Palumbo, M.; Richter, S. N.; Freccero, M. *J. Am. Chem. Soc.* **2010**, *132* (41), 14625–14637.
- (171) Wan, P.; Barker, B.; Diao, L.; Fischer, M. *Can. J. Chem.* **1996**.
- (172) Diao, L.; Wan, P. *Can. J. Chem.* **2008**, *86* (2), 105–118.
- (173) Ma, J.; Zhang, X.; Basarić, N.; Wan, P.; Phillips, D. L. *Phys. Chem. Chem. Phys.* **2015**, *17* (14), 9205–9211.
- (174) Lukeman, M.; Simon, H.; Wan, P.; Wang, Y.-H. *J. Org. Chem.* **2015**, *80* (22), 11281–11293.

## References

---

- (175) Ma, J.; Zhang, X.; Basarić, N.; Phillips, D. L. *J. Am. Chem. Soc.* **2017**, *139* (50), 18349–18357.
- (176) Klíčová, L.; Šebej, P.; Šolomek, T.; Hellrung, B.; Slavíček, P.; Klán, P.; Heger, D.; Wirz, J. *J. Phys. Chem. A* **2012**, *116* (11), 2935–2944.
- (177) Chang, J. A.; Kresge, A. J.; Zhan, H. Q.; Zhu, Y. *J. Phys. Org. Chem.* **2004**, *17* (6-7), 579–585.
- (178) Chiang, Y.; Kresge, A. J.; Zhu, Y. *Phys. Chem. Chem. Phys.* **2003**, *5*, 1039–1042.
- (179) Škalamera, Đ.; Mlinarić-Majerski, K.; Martin Kleiner, I.; Kralj, M.; Oake, J.; Wan, P.; Bohne, C.; Basarić, N. *J. Org. Chem.* **2017**, *82* (12), 6006–6021.
- (180) Lukeman, M.; Wan, P. *J. Am. Chem. Soc.* **2002**, *124* (32), 9458–9464.
- (181) Basarić, N.; Cindro, N.; Hou, Y.; Žabčić, I.; Mlinarić-Majerski, K.; Wan, P. *Can. J. Chem.* **2011**, *89* (2), 221–234.
- (182) Basarić, N.; Došlić, N.; Ivković, J.; Wang, Y.-H.; Veljković, J.; Mlinarić-Majerski, K.; Wan, P. *J. Org. Chem.* **2013**, *78* (5), 1811–1823.
- (183) Basarić, N.; Cindro, N.; Bobinac, D.; Mlinarić-Majerski, K.; Uzelac, L.; Kralj, M.; Wan, P. *Photochem. Photobiol. Sci.* **2011**, *10* (12), 1910–1925.
- (184) Škalamera, Đ.; Bohne, C.; Landgraf, S.; Basarić, N. *J. Org. Chem.* **2015**, *80* (21), 10817–10828.
- (185) Brousmiche, D. W.; Xu, M.; Lukeman, M.; Wan, P. *J. Am. Chem. Soc.* **2003**, *125* (42), 12961–12970.
- (187) Yan, Z.; Du, L.; Lan, X.; Zhang, X.; Phillips, D. L. *J. Mol. Struct.* **2018**, *1172*, 102–107.
- (188) Modica, E.; Zanaletti, R.; Freccero, M.; Mella, M. *J. Org. Chem.* **2001**, *66*, 41–42.
- (189) Basarić, N.; Došlić, N.; Ivković, J.; Wang, Y.-H.; Mališ, M.; Wan, P. *Chem. Eur. J.* **2012**, *18* (34), 10617–10623.
- (190) Škalamera, Đ.; Mlinarić-Majerski, K.; Uzelac, L.; Kralj, M.; Wan, P.; Basarić, N. *Photochem. Photobiol. Sci.* **2013**, *12* (11), 2043–2056.
- (191) McClelland, R. A.; Cozens, F. L.; Steenken, S.; Amyes, T. L.; Richard, J. P. *J. Chem. Soc., Perkin Trans. 2* **1993**, *10*, 1717–1722.
- (192) Doria, F.; Percivalle, C.; Freccero, M. *J. Org. Chem.* **2012**, *77* (7), 3615–3619.
- (193) Lukeman, M.; Wan, P. *Chem. Commun.* **2001**, No. 11, 1004–1005.
- (194) Gadosy, T. A.; Shukla, D.; Johnston, L. J. *J. Phys. Chem. A* **1999**, *103*, 8834–8839.
- (195) Vialaton, D.; Richard, C.; Baglio, D.; Paya-Perez, A.-B. *J. Photochem. Photobiol. A* **1999**, *123*, 15–19.
- (196) Mohan, H.; Hermann, R.; Naumov, S.; Mittal, J. P.; Brede, O. *J. Phys. Chem. A* **1998**, *102*, 5754–5762.
- (197) Dixon, W. T.; Murphy, D. *J. Chem. Soc., Faraday Trans. 2* **1976**, *72*, 1221–1230.
- (198) Bordwell, F. G.; Cheng, J. *J. Am. Chem. Soc.* **1991**, *113* (5), 1736–1743.
- (199) Land, E. J.; Porter, G.; Strachan, E. *J. Chem. Soc. Faraday Trans.* **1961**, *57*, 1885–1893.
- (200) McClelland, R. A.; Mathivanan, N.; Steenken, S. *J. Am. Chem. Soc.* **1990**, *112* (12), 4857–4861.
- (201) Mialocq, J. C.; Sutton, J.; Goujon, P. *J. Chem. Phys.* **1980**, *72* (12), 6338–6345.

## References

---

- (202) Joschek, H.-I.; Grossweiner, L. I. *J. Am. Chem. Soc.* **1966**, *88* (14), 3261–3268.
- (203) Shukla, D.; Schepp, N. P.; Mathivanan, N.; Johnston, L. J. *Can. J. Chem.* **1997**, *75* (12), 1820–1829.
- (204) Foti, M.; Ingold, K. U.; Luszyk, J. *J. Am. Chem. Soc.* **1994**, *116*, 9440–9447.
- (205) Zhou, C.-W.; Kislov, V. V.; Mebel, A. M. *J. Phys. Chem. A* **2012**, *116* (6), 1571–1585.
- (206) Pincock, J. A. *Acc. Chem. Res.* **1997**, *30* (1), 43–49.
- (207) Slocum, G. H.; Schuster, G. B. *J. Org. Chem.* **1984**, *49* (12), 2177–2185.
- (208) Givens, R. S.; Athey, P. S.; Matuszewski, B.; Kueper, L. W. I.; Xue, J.-Y.; Fister, T. *J. Am. Chem. Soc.* **1993**, *115*, 6001–6012.
- (209) Zhou, Y. Development of Photolabile Nitroxyl (HNO) Donor Molecules Using Photolabile Protecting Groups, Kent State University, 2017, pp 1–288.
- (210) Douheret, G. *Bulletin de la Societe Chimique de France* **1968**, *7*, 3122–3131.
- (211) Jordan, F. *J. Phys. Chem.* **1973**, *77* (22), 2681–2683.
- (212) Adas, S. K. Synthesis and Kinetic Studies of N-Hydroxysulfonamide Nitrosyl Hydride Donor Molecules and their Reactions with Cob (III) alamin, Kent State University, 2016.
- (213) Polaczek, J.; Orzeł, Ł.; Stochel, G.; van Eldik, R. *J. Biol. Inorg. Chem.* **2019**, *24*, 311–313.
- (214) Subedi, H.; Brasch, N. E. *Inorg. Chem.* **2013**, *52* (19), 11608–11617.
- (215) Georghiou, P. E.; Ashram, M.; Clase, H. J.; Bridson, J. N. *J. Org. Chem.* **1998**, *63* (6), 1819–1826.
- (216) Tang, C.; Tan, J.; Fan, R.; Zhao, B.; Tang, C.; Ou, W.; Jin, J.; Peng, X. *J. Chromatogr. A* **2016**, *1461*, 59–69.
- (217) Rahn, R. O.; Stefan, M. I.; Bolton, J. R.; Goren, E.; Shaw, P.-S.; Lykke, K. R. *Photochem. Photobiol.* **2003**, *78* (2), 146–152.
- (218) Marafatto, F. F.; Strader, M. L.; Gonzalez-Holguera, J.; Schwartzberg, A.; Gilbert, B.; Peña, J. *Proc. Natl. Acad. Sci.* **2015**, *112* (15), 4600–4605.
- (219) Kuhn, H. J.; Braslavsky, S. E.; Schmidt, R. *Chemical Actinometry (IUPAC Technical Report)*; 2004; pp 1–47.
- (220) Siampiringue, N.; Guyot, G.; Monti, S.; Bortolus, P. *J. Photochem.* **1987**, *37*, 185–188.
- (221) Kuhn, H. J.; Braslavsky, S. E.; Schmidt, R. *Pure Appl. Chem.* **2004**, *76* (12), 2105–2146.
- (222) Parissis, J.; Bistola, V.; Ikonomidis, I.; Triposkiadis, F. *Eur. J. Heart Fail.* **2017**, *19* (10), 1333–1334.
- (223) Zhang, C.-P.; Wang, Z.-L.; Chen, Q.-Y.; Zhang, C.-T.; Gu, Y.-C.; Xiao, J.-C. *J. Fluorine Chem.* **2010**, *131* (7), 761–766.
- (224) Trepka, R. D.; Harrington, J. K.; Belisle, J. W. *J. Org. Chem.* **1974**, *39* (8), 1094–1098.
- (225) Bonner, F. T.; Ko, Y. *Inorg. Chem.* **1992**, *31* (12), 2514–2519.
- (226) Valeur, B.; Berberan-Santos, M. N. *Molecular fluorescence: principles and applications*; 2012.
- (227) Roncaroli, F.; Shubina, T. E.; Clark, T.; van Eldik, R. *Inorg. Chem.* **2006**, *45* (19), 7869–7876.
- (228) Brasch, N. E.; Finke, R. G. *J. Inorg. Biochem.* **1999**, *73* (4), 215–219.
- (229) Cregan, A. G.; Brasch, N. E.; van Eldik, R. *Inorg. Chem.* **2001**, *40* (7), 1430–1438.

## References

---

- (230) Wolak, M.; Zahl, A.; Schnepfenseieper, T.; Stochel, G.; van Eldik, R. *J. Am. Chem. Soc.* **2001**, *123* (40), 9780–9791.
- (231) Fukuto, J. M.; Carrington, S. J. *Antioxid. Redox Signal.* **2011**, *14* (9), 1649–1657.
- (232) Nourian, S.; Zilber, Z. A.; Toscano, J. P. *J. Org. Chem.* **2016**, *81* (19), 9138–9146.
- (233) Walter, M. R.; Dzul, S. P.; Rodrigues, A. V.; Stemmler, T. L.; Telser, J.; Conradie, J.; Ghosh, A.; Harrop, T. C. *J. Am. Chem. Soc.* **2016**, *138* (38), 12459–12471.
- (234) Miao, Z.; King, S. B. *Nitric Oxide* **2016**, *57*, 1–14.
- (235) Kalish, V. J.; Brookfield, F. A.; Courtney, S. M.; Frost, L. M. US Patent Office 2015.
- (236) Doctorovich, F.; Bikiel, D. E.; Pellegrino, J.; Suárez, S. A.; Martí, M. A. *Acc. Chem. Res.* **2014**, *47* (10), 2907–2916.
- (237) Ishimura, Y.; Gao, Y. T.; Panda, S. P.; Roman, L. J.; Masters, B. S. S.; Weintraub, S. T. *Biochem. Biophys. Res. Commun.* **2005**, *338* (1), 543–549.
- (238) Sreekanth, R.; Prasanthkumar, K. P.; Sunil Paul, M. M.; Aravind, U. K.; Aravindakumar, C. T. *J. Phys. Chem. A* **2013**, *117* (44), 11261–11270.
- (239) Misra, R. N.; Hopewell, N. J. *United States Patent*. 1990.
- (240) Subedi, H.; Brasch, N. E. *Dalton Trans.* **2016**, *45* (1), 352–360.
- (241) van Wilderen, L. J. G. W.; Neumann, C.; Rodrigues-Correia, A.; Kern-Michler, D.; Mielke, N.; Reinfelds, M.; Heckel, A.; Bredenbeck, J. *Phys. Chem. Chem. Phys.* **2017**, *19*, 6487–6496.
- (242) Gurzadyan, G.; Steenken, S. *Chem. Eur. J.* **2001**, *7* (8), 1808–1815.
- (243) Tagawa, S.; Nagahara, S.; Iwamoto, T.; Wakita, M.; Kozawa, T.; Yamamoto, Y.; Werst, D.; Trifunac, A. D. Houlihan, F. M., Ed.; SPIE, 2000; Vol. 3999, pp 204–211.
- (244) Marciniak, B.; Kozubek, H.; Paszyc, S. *J. Chem. Educ.* **1992**, *69* (3), 247–249.
- (245) Shizuka, H. *Acc. Chem. Res.* **1985**, *18*, 141–147.
- (246) Solntsev, K. M.; Huppert, D.; Agmon, N. *J. Phys. Chem. A* **1998**, *102* (47), 9599–9606.
- (247) Shizuka, H.; Tobita, S. *J. Am. Chem. Soc.* **1982**, *104* (25), 6919–6927.
- (248) Moyle, M. P.; Tyner, M. *Ind. Eng. Chem.* **1953**, *45* (8), 1794–1797.
- (249) Taft, R. W.; Abboud, J.-L. M.; Kamlet, M. J.; Abraham, M. H. *J. Solution Chem.* **1985**, *14* (3), 153–186.
- (250) Jackson, G.; Porter, G. *Proc. R. Soc. Lond. A* **1961**, *260*, 13–30.
- (251) Webb, S. P.; Phillips, L. A.; Yeh, S. W.; Tolbert, L.; Clark, J. H. *J. Phys. Chem.* **1986**, *90*, 5154–5164.
- (252) Losi, A.; Viappiani, C. *Chem. Phys. Lett.* **1998**, *289*, 500–506.
- (253) Gottlieb, H. E.; Kotlyar, V.; Nudelman, A. *J. Org. Chem.* **1997**, *62* (21), 7512–7515.
- (254) Oscar, B. G.; Liu, W.; Rozanov, N. D.; Fang, C. *PCCP* **2018**, *18*, 26151–26160.
- (255) Mondal, S. K.; Ghosh, S.; Sahu, K.; Sen, P.; Bhattacharyya, K. *J. Chem. Sci.* **2007**, *119* (2), 71–76.
- (256) Brouwer, A. M. *Pure Appl. Chem.* **2011**, *83* (12), 2213–2228.
- (257) Wasylenko, W. A.; Kebede, N.; Showalter, B. M.; Matsunaga, N.; Miceli, A. P.; Liu, Y.; Ryzhkov, L. R.; Hadad, C. M.; Toscano, J. P. *J. Am. Chem. Soc.* **2006**, *128* (40), 13142–13150.

## References

---

- (258) Langan, J. G.; Sitzmann, E. V.; Eisenthal, K. B. *Chem. Phys. Lett.* **1986**, *124* (1), 59–62.
- (259) Gajst, O.; Pinto da Silva, L.; Esteves da Silva, J. C. G.; Huppert, D. *J. Phys. Chem. A* **2018**, *122* (20), 4704–4716.
- (260) Goldberg, S. Y.; Pines, E.; Huppert, D. *Chem. Phys. Lett.* **1992**, *192* (1), 77–81.
- (261) Wudl, F.; Lightner, D. A.; Cram, D. J. *J. Am. Chem. Soc.* **1967**, *89* (16), 4099–4101.
- (262) Braverman, S.; Pechenick, T.; Zafrani, Y. *ARKIVOC* **2004**, *2*, 51–63.
- (263) Chavez, T. A.; Toscano, J. P. In *The Chemistry and Biology of Nitroxyl (HNO)*; Doctorovich, F., Farmer, P. J., Marti, M. A., Eds.; Elsevier Inc., 2016; pp 255–268.
- (264) Miao, Z.; King, S. B. In *The Chemistry and Biology of Nitroxyl (HNO)*; Doctorovich, F., Farmer, P. J., Marti, M. A., Eds.; Elsevier Inc.: Amsterdam, 2016; pp 225–238.
- (265) Reisz, J. A.; Zink, C. N.; King, S. B. *J. Am. Chem. Soc.* **2011**, *133* (30), 11675–11685.
- (266) Reisz, J. A.; Klorig, E. B.; Wright, M. W.; King, S. B. *Org. Lett.* **2009**, *11* (13), 2719–2721.
- (267) Xia, L.; Cregan, A. G.; Berben, L. A.; Brasch, N. E. *Inorg. Chem.* **2004**, *43* (21), 6848–6857.
- (268) Zheng, D.; Birke, R. L. *J. Am. Chem. Soc.* **2001**, *123* (19), 4637–4638.
- (269) Khade, R. L.; Yang, Y.; Shi, Y.; Zhang, Y. *Angew. Chem. Int. Ed.* **2016**, *55*, 15058–15061.
- (270) Doctorovich, F.; Bikiel, D. E.; Pellegrino, J.; Suárez, S. A.; Larsen, A.; Martí, M. A. *Coord. Chem. Rev.* **2011**, *255*, 2764–2784.
- (271) Li, H.; Yao, Q.; Xu, F.; Xu, N.; Ma, X.; Fan, J.; Long, S.; Du, J.; Wang, J.; Peng, X. *Anal. Chem.* **2018**, *90* (7), 4641–4648.
- (272) Goodrich, L. E.; Roy, S.; Alp, E. E.; Zhao, J.; Hu, M. Y.; Lehnert, N. *Inorg. Chem.* **2013**, *52* (13), 7766–7780.
- (273) Brouwer, M.; Chamulitrat, W.; Ferruzzi, G.; Sauls, D. L.; Weinberg, B. J. *Blood* **1996**, *88* (5), 1857–1864.
- (274) Subedi, H. Mechanistic studies on the reactions of Vitamin B12 complexes with the nitroxyl (HNO) donors: Angeli's salt and Piloty's acid, Kent State University, 2014, pp 1–235.
- (275) Reenstra, W. W.; Jencks, W. P. *J. Am. Chem. Soc.* **1979**, *101* (19), 5780–5791.
- (276) Pratt, J. M. *Inorganic Chemistry of Vitamin B12*; London, UK, Academic Press Inc. (London) Ltd., 1972.
- (277) Confer, A. M.; McQuilken, A. C.; Matsumura, H.; Moëne-Loccoz, P.; Goldberg, D. P. *J. Am. Chem. Soc.* **2017**, *139* (31), 10621–10624.
- (278) Palao, E.; Slanina, T.; Muchová, L.; Šolomek, T.; Vítek, L.; Klán, P. *J. Am. Chem. Soc.* **2016**, *138* (1), 126–133.
- (279) Miao, Z.; King, S. B. *ChemistryOpen* **2016**, *5* (2), 110–114.
- (280) Suárez, S. A.; Martí, M. A.; De Biase, P. M.; Estrin, D. A.; Bari, S. E.; Doctorovich, F. *Polyhedron* **2007**, *26* (16), 4673–4679.
- (281) Ren, M.; Dong, B.; Lin, W. In *The Chemistry and Biology of Nitroxyl (HNO)*; Doctorovich, F., Farmer, P. J., Marti, M. A., Eds.; Elsevier Inc.: Amsterdam, 2016; pp 207–224.

## References

---

- (282) Doctorovich, F.; Bikiel, D. E.; Pellegrino, J.; Suárez, S. A.; Martí, M. A. *Prog. Inorg. Chem.* **2014**, *58*, 145–183.
- (283) Bobko, A. A.; Ivanov, A.; Khramtsov, V. V. *Free Radic. Res.* **2013**, *47* (2), 74–81.

# GLOSSARY

---

Abs	Absorbance
AS	Angeli's Salt
DMSO	Dimethyl sulfoxide
EtOAc	Ethyl acetate
EtOH	Ethanol
ESIPT	Excited State Intramolecular Proton Transfer
ESPT	Excited State Proton Transfer
fs	Femtosecond
fs-TA	Femtosecond Transient Absorption
GC-MS	Gas Chromatography-Mass Spectrometry
HFIP	1,1,1,3,3,3-Hexafluoro-2-propanol
HNM	Hydroxynaphthenyl methyl
HOMO	Highest Occupied Molecular Orbital
IC	Internal Conversion
ISC	Intersystem Crossing
LC-HRMS	Liquid Chromatography-High Resolution Mass Spectrometry
LFP	Laser Flash Photolysis
LUMO	Lowest Unoccupied Molecular Orbital
MeCN	Acetonitrile
MeOH	Methanol
MO	Molecular Orbital
MS	Mass Spectrum

## Glossary

---

Nd:YAG	Neodymium-Doped Yttrium Aluminium Garnet
NMR	Nuclear Magnetic Resonance
ns	Nanosecond
ns-TA	Nanosecond Transient Absorption
OD	Optical Density
PA	Piloly's Acid
PTTS	Excited State Proton Transfer to Solvent
ps	Picosecond
QM	Quinone Methide
ROS	Reactive Oxygen Species
S	Singlet State
T	Triplet State
THF	Tetrahydrofuran
TFE	2,2,2-Trifluoroethanol
TMS	Tetramethylsilane
TSP	3-(Trimethylsilyl)propionic-2,2,3,3-d <sub>4</sub> acid sodium salt
UV/Vis	Ultraviolet/Visible
YAG	Yttrium Aluminum Garnet
$\epsilon$	Molar Absorption Coefficient
$\lambda_{\max}$	Wavelength at Maximum Amplitude
$\mu\text{s}$	microsecond
$\Phi$	Photoproduct Quantum Yield

# APPENDICES

## Appendix A. NMR from Syntheses

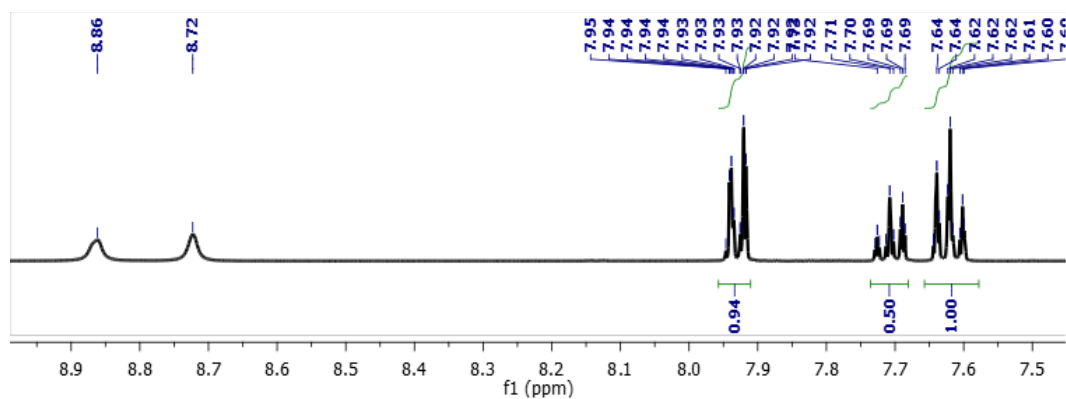


Figure A1.  $^1\text{H}$  NMR spectrum of Piloty's Acid in  $d_6$ -acetone.

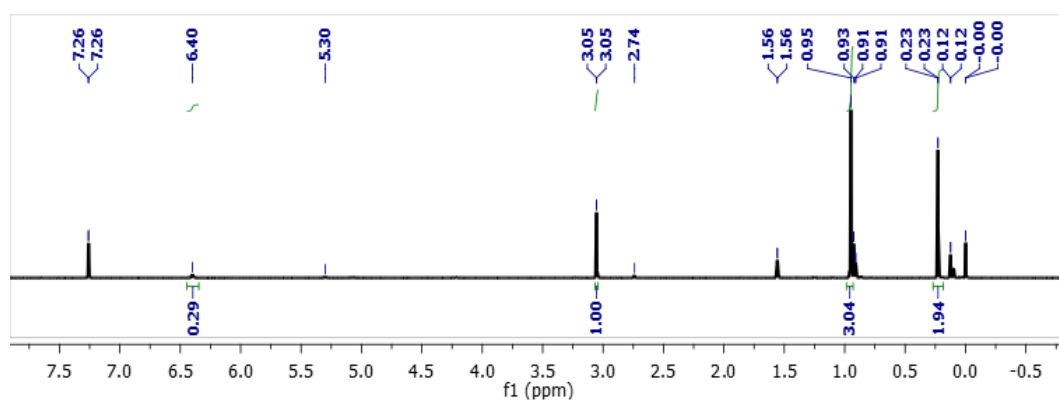


Figure A2.  $^1\text{H}$  NMR of MSHA-TBS in  $\text{CDCl}_3$ .

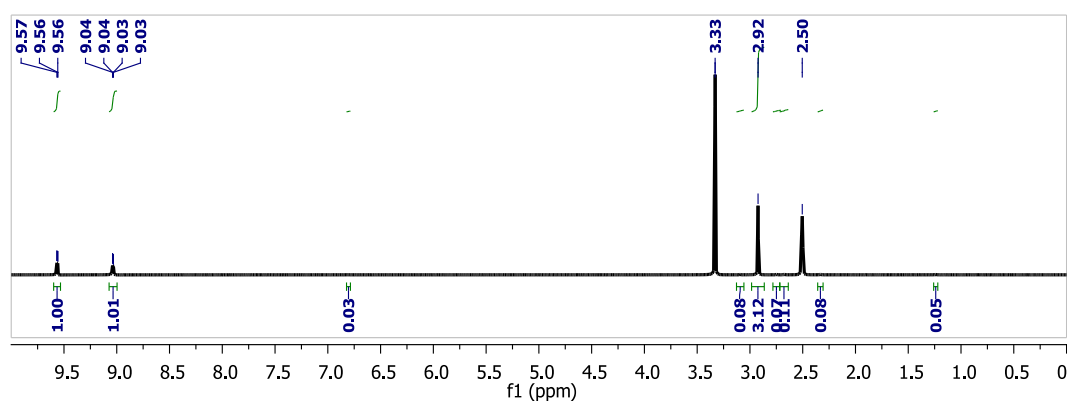


Figure A3.  $^1\text{H}$  NMR spectrum of MSHA in DMSO.

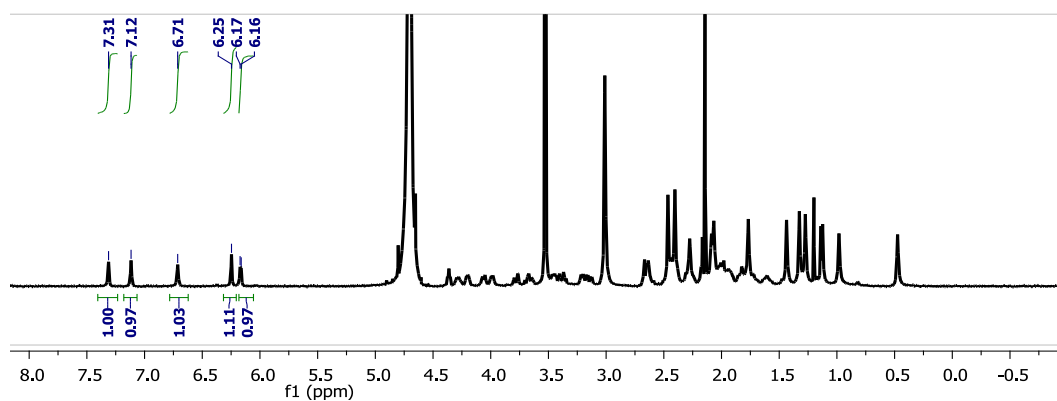


Figure A4.  $^1\text{H}$  NMR spectrum of NO-Cbl(III) in anaerobic  $\text{D}_2\text{O}$ .

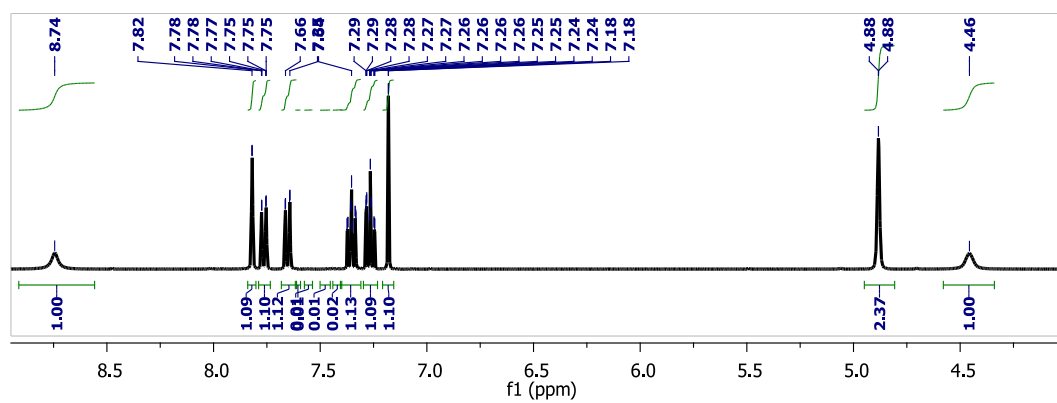


Figure A5.  $^1\text{H}$  NMR spectrum of diol **10** in  $\text{d}_6$ -acetone.

## Appendix B. Equilibrium Constant Calculation from Spectrophotometric Titration

Mole fractions:

$$X_{A^-} = \frac{[A^-]}{[HA] + [A^-]}$$

$$X_{HA} = 1 - X_{A^-}$$

Observed absorbance relation to ratio of acid and conjugate base:

$$A_{obs} = \frac{[HA]}{[HA] + [A^-]} A_{[HA]} + \frac{[A^-]}{[HA] + [A^-]} A_{[A^-]}$$

$$A_{obs} = (1 - X_{A^-}) A_{[HA]} + (X_{A^-}) A_{[A^-]}$$

$$\frac{A_{obs} - A_{[HA]}}{A_{[A^-]} - A_{obs}} = \frac{X_{A^-}}{1 - X_{A^-}} = \frac{[A^-]}{[HA]}$$

Substitution into Henderson-Hasselbalch equation:

$$pH = pK_a + \log \frac{[A^-]}{[HA]}$$

$$pH = pK_a + \log \frac{A_{obs} - A_{[HA]}}{A_{[A^-]} - A_{obs}}$$

$$A_{obs} = \frac{A_{HA} + A_{A^-} \times 10^{pH - pK_a}}{1 + 10^{pH - pK_a}}$$

Initial and final absorbance are the acid and conjugate base, respectively:

$$A_{obs} = \frac{A_i + A_f \times 10^{pH - pK_a}}{1 + 10^{pH - pK_a}}$$

A.6. Equilibrium constant calculation for spectrophotometric titration.

## Appendix C. Examples of Data Used to Calculate Photoproduct Quantum Yields

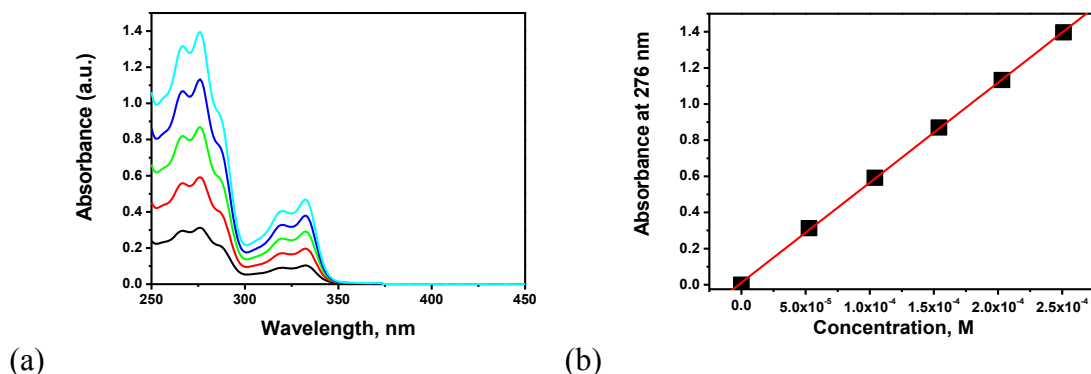


Figure A6. Example of method used to determine molar attenuation coefficients. a) Plot of donor **4**'s absorption (53, 104, 154, 203, and 251  $\mu\text{M}$ ) in 60:40 v/v MeCN to 5.0 mM phosphate buffer. (b) Plot of absorbance at 276 nm as a function of concentration. The molar extinction coefficient (slope) is  $(5.54 \pm 0.06) \times 10^3 \text{ M}^{-1} \text{ cm}^{-1}$ .

Table A2. Molar extinction coefficients at 313 nm. See Chapter 2, Section 2.3.1 for details.

Compound	Solvent	$\epsilon_{313}$ ( $\text{M}^{-1}\text{cm}^{-1}$ )
<b>4</b>	MeCN	$1.17 \times 10^3$
<b>4</b>	DMSO	$1.16 \times 10^3$
<b>4</b>	60:40 v/v MeCN to 5 mM phosphate buffer solution (pH 7.0)	$1.22 \times 10^3$
<b>4</b>	20:80 v/v MeCN to 5 mM phosphate buffer solution (pH 7.0)	$1.27 \times 10^3$
<b>4</b>	60:40 v/v MeCN to 0.1 M NaOH	$2.40 \times 10^3$
<b>3</b>	MeCN	$1.23 \times 10^3$
<b>1</b>	MeCN	$1.20 \times 10^3$
<b>1</b>	60:40 v/v MeCN to 5 mM phosphate buffer solution (pH 7.0)	$1.35 \times 10^3$
<b>1</b>	60:40 v/v MeCN to 0.1 M NaOH	$8.19 \times 10^3$
<b>2</b>	MeCN	$1.21 \times 10^3$

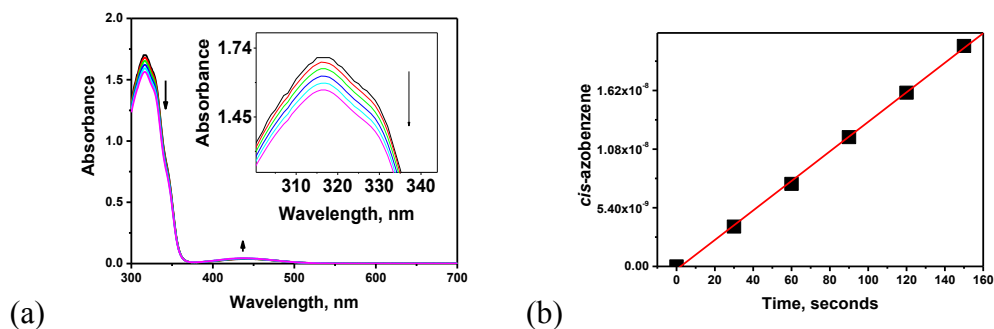


Figure A7. (a) Typical UV-vis spectra of solutions of azobenzene ( $67 \mu\text{M}$ , in MeOH) irradiated for 0 – 150 s using a Xe lamp ( $313 \pm 2 \text{ nm}$ , monochromator slit width = 2.0 mm). The initial absorbance at  $A_{313} = 1.670 \text{ a.u.}$  The photon flux was  $\varphi = (1.08 \pm 0.12) \times 10^{-9} \text{ einsteins s}^{-1}$ . (b) Moles of *cis*-azobenzene photoproduct calculated from the absorbance change at 313 nm as a function of total irradiation time. Maximum conversion = 8.9%.

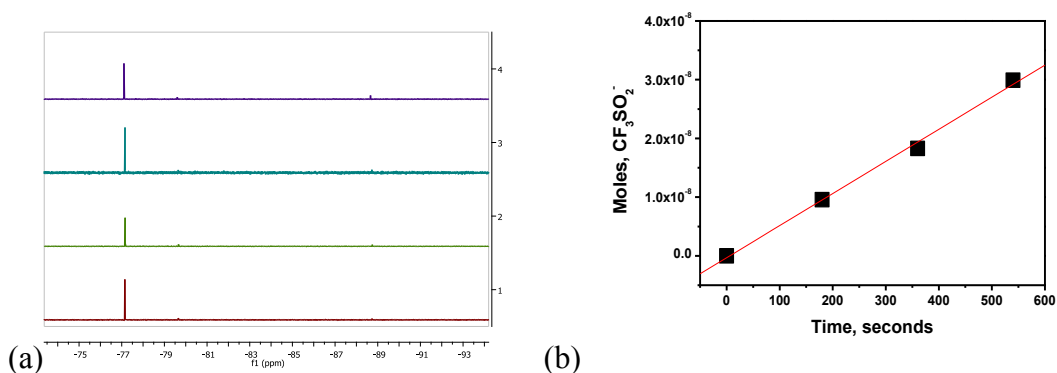


Figure A8. (a)  $^{19}\text{F}$  NMR spectra following photolysis of donor **4** ( $224 \mu\text{M}$ ) in anaerobic 60:40 v/v MeCN : 5.0 mM phosphate buffer solution, pH 7.0, as of function of irradiation time (1: 0 min, 2: 3.00 min, 3: 6.00 min, and 4: 9.00 min; no more than 6.1% conversion). NMR samples were prepared as a 1:1 ratio of photolysis solution with MeOD, and  $\alpha,\alpha,\alpha$ -trifluorotoluene was used as an internal standard ( $\alpha,\alpha,\alpha$ -trifluorotoluene impurity observed at  $\delta -79.94 \text{ ppm}$ ).  $A_{313} = 0.273 \text{ a.u.}$  (b) Plot of moles  $\text{CF}_3\text{SO}_2^-$  generated from the photolysis of compound **4** as a function of time. Using azobenzene as the actinometer,  $\Phi_{\text{PP}} = 0.51 \pm 0.07$

## Appendix D. Global Analysis Fittings

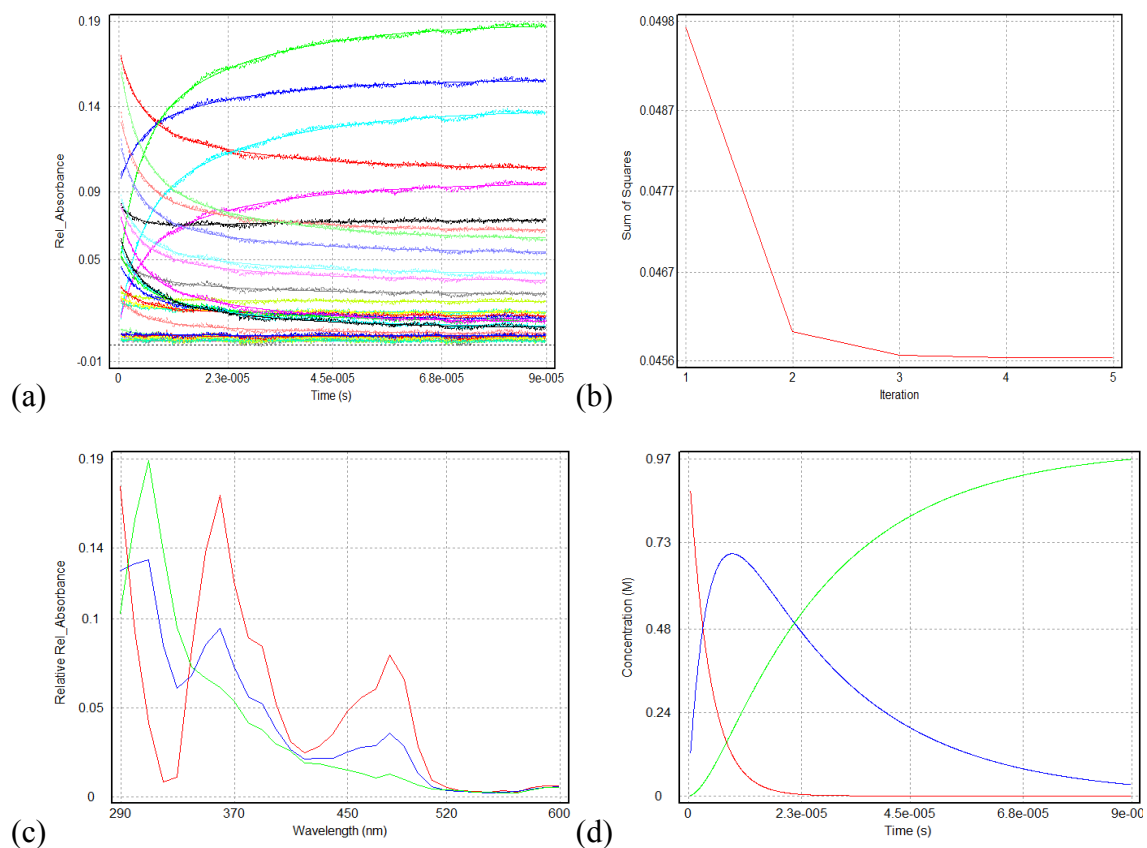


Figure A9. Global analysis of 2-naphthol in oxygenated 80:20 v/v MeCN to 5.0 mM phosphate buffer solution (pH 7.0): (a) fitted data with two processes; (b) residual sum square progression of the fit; (c) component spectra; (d) lifetime of three components on a linear time scale.

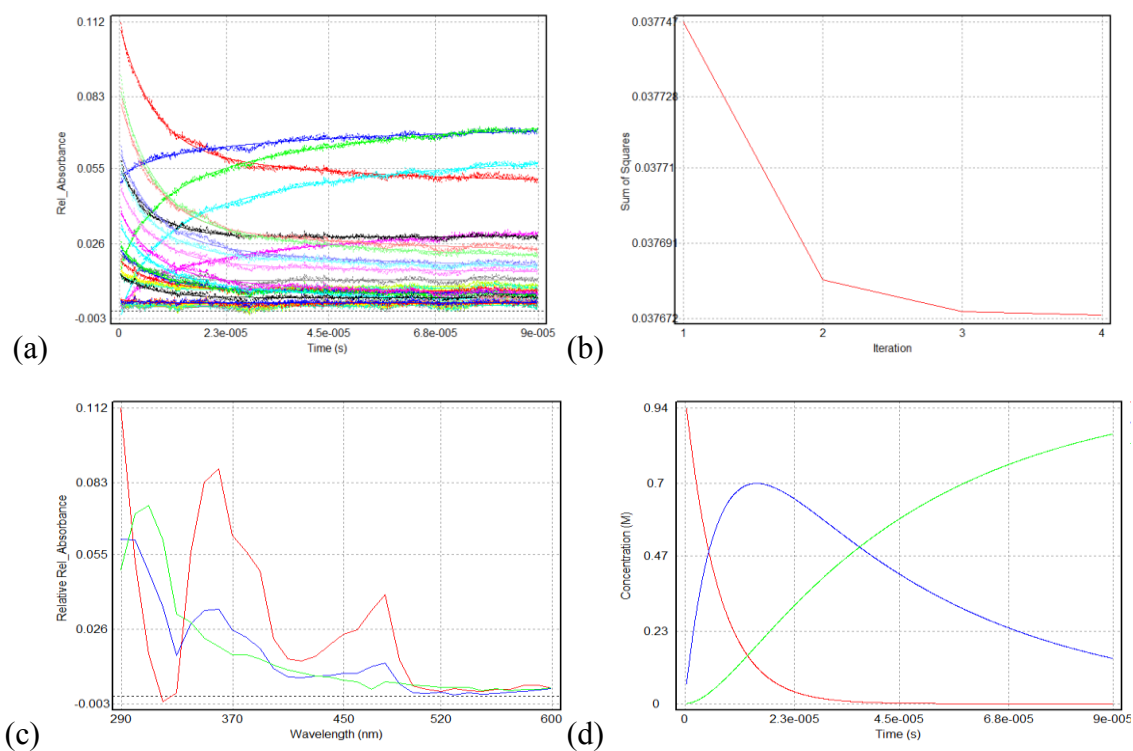


Figure A10. Global analysis of 2-naphthol in oxygenated MeCN: (a) fitted data with two processes; (b) residual sum square progression of the fit; (c) component spectra; (d) lifetime of three components on a linear time scale.

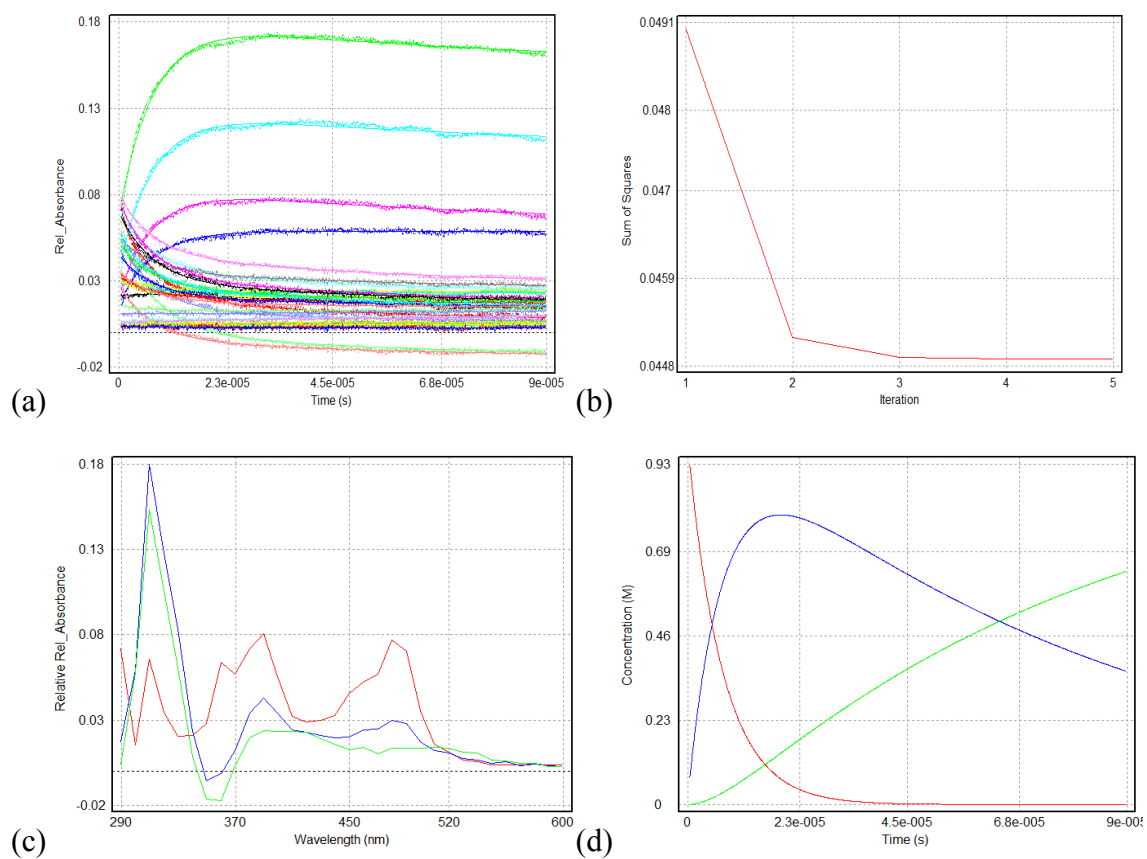


Figure A11. Global analysis of 2-naphtholate in oxygenated 80:20 v/v MeCN to 0.1 M NaOH: (a) fitted data with two processes shown; (b) residual sum square progression of the fit; (c) component spectra; (d) lifetime of three components on a linear time scale.

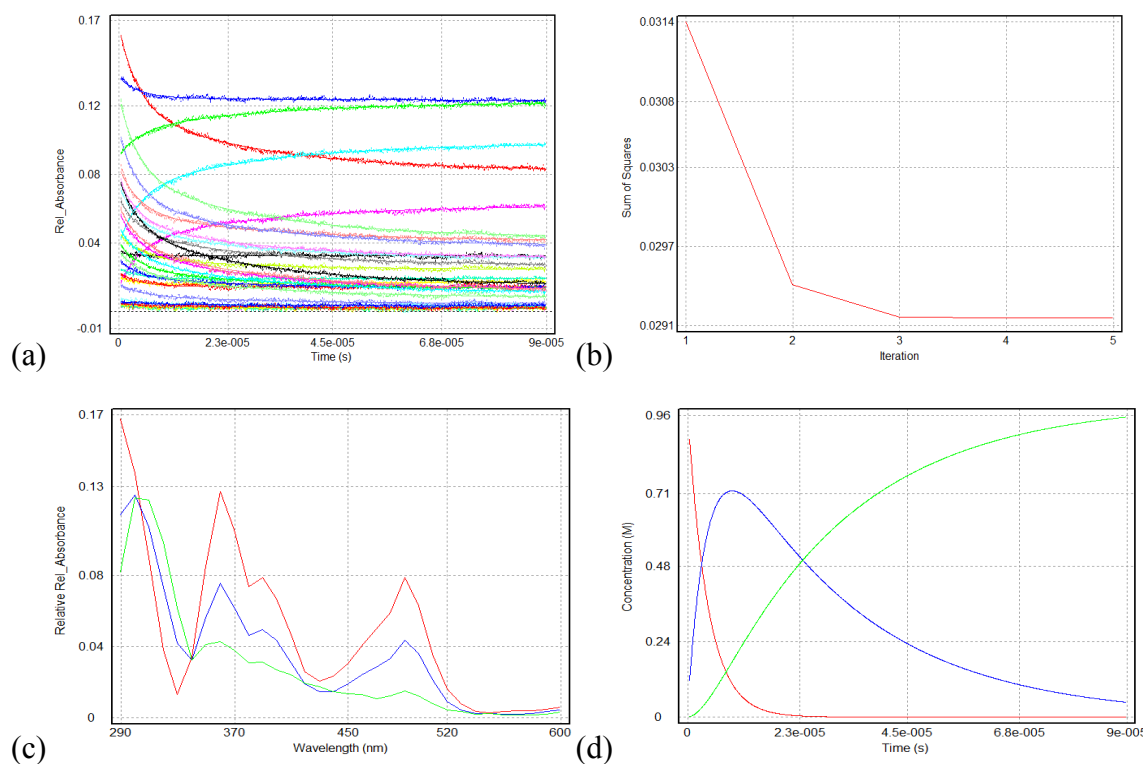


Figure A12. Global analysis of diol **7** in oxygenated 80:20 v/v MeCN to 5.0 mM phosphate buffer solution (pH 7.0): (a) fitted data with two processes; (b) residual sum square progression of the fit; (c) component spectra; (d) lifetime of three components on a linear time scale.

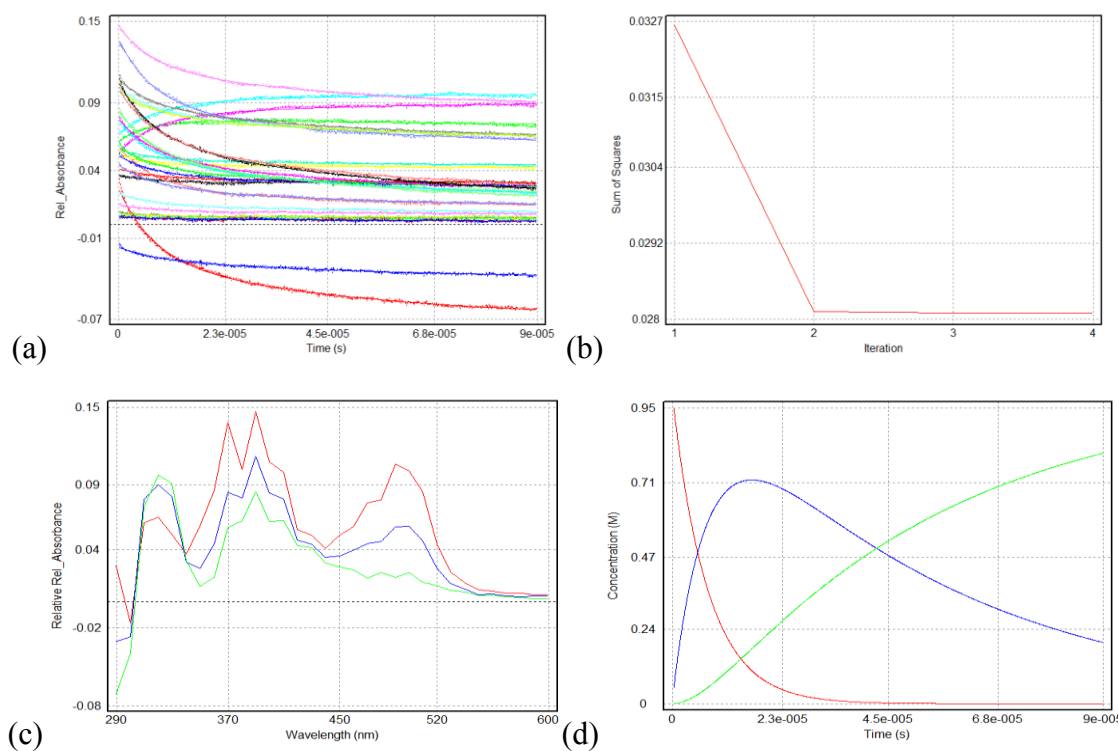


Figure A13. Global analysis of **4** in oxygenated 80:20 v/v MeCN to 0.1 M NaOH: (a) fitted data with two processes shown; (b) residual sum square progression of the fit; (c) component spectra; (d) lifetime of three components on a linear time scale.

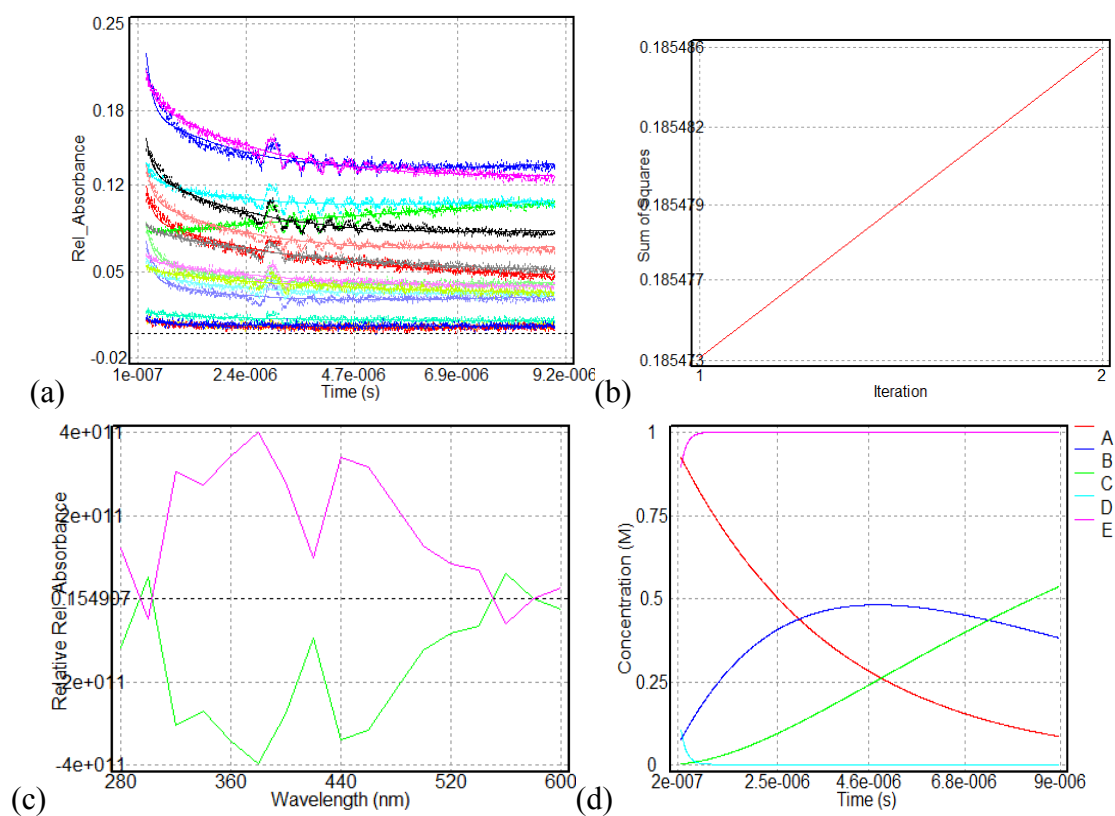


Figure A14. Global analysis of donor **4** in oxygenated 80:20 v/v MeCN to 5.0 mM phosphate buffer solution (pH 7.0): (a) fitted data with two processes; (b) residual sum square progression of the fit; (c) component spectra; (d) lifetime of three components on a linear time scale.

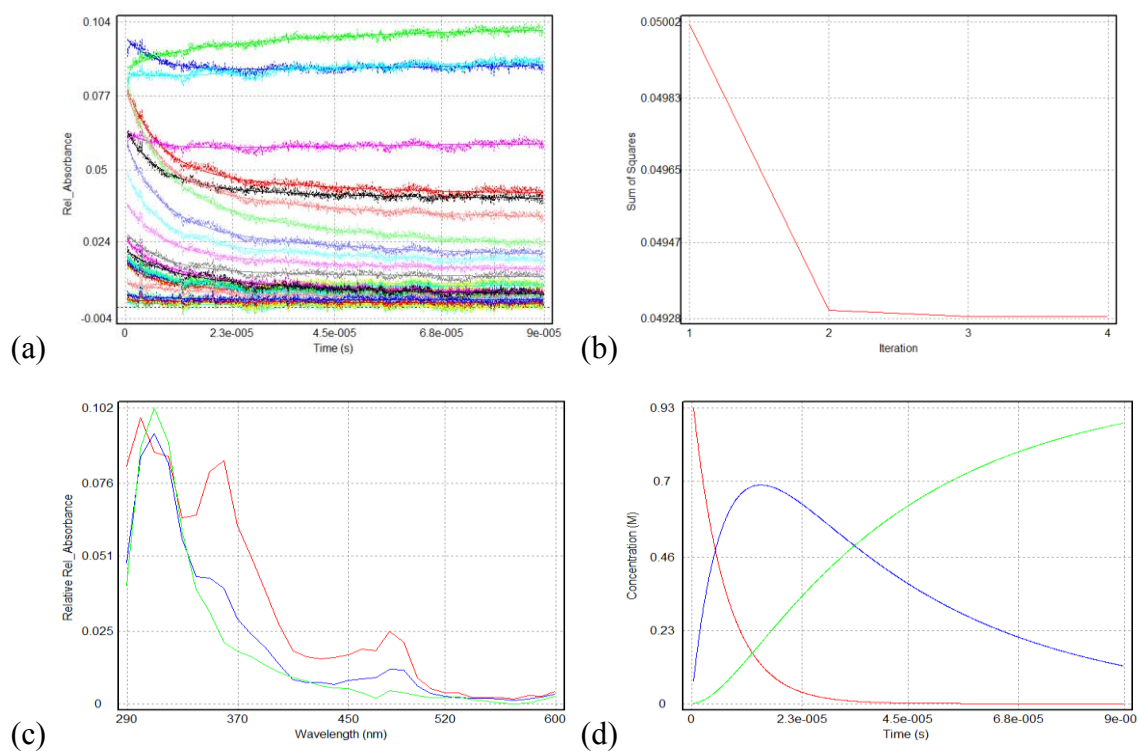
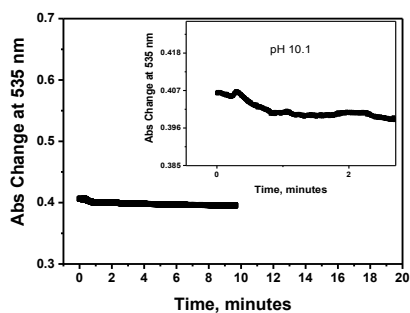
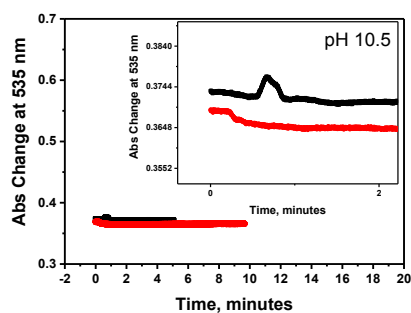


Figure A15. Global analysis of donor **4** in oxygenated MeCN: (a) fitted data with two processes; (b) residual sum square progression of the fit; (c) component spectra; (d) lifetime of three components on a linear time scale.

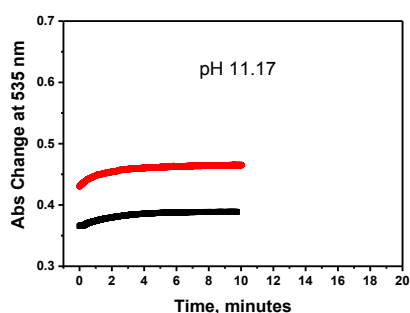
**Appendix E. Kinetic traces for the reaction between NO<sup>-</sup>-Cbl(III) (~7.0 x 10<sup>-5</sup> M) and Piloxy's acid (0.015 M)**



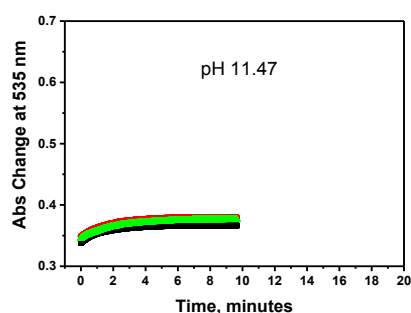
(a)



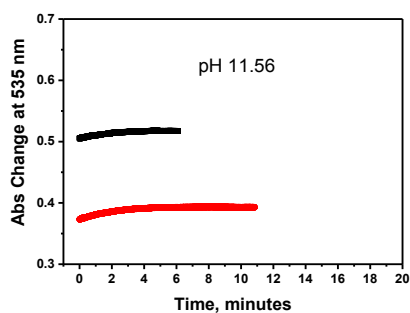
(b)



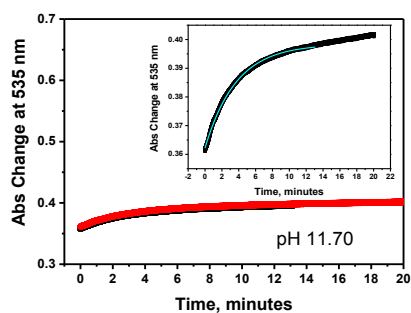
(c)



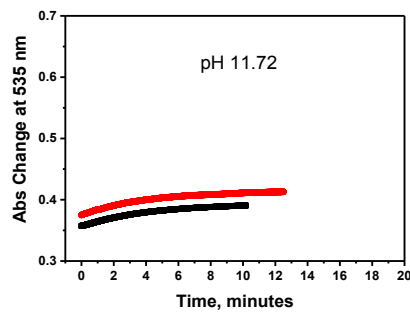
(d)



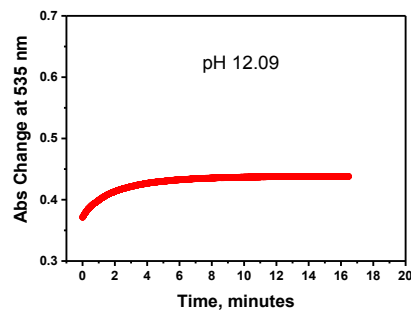
(e)



(f)



(g)



(h)

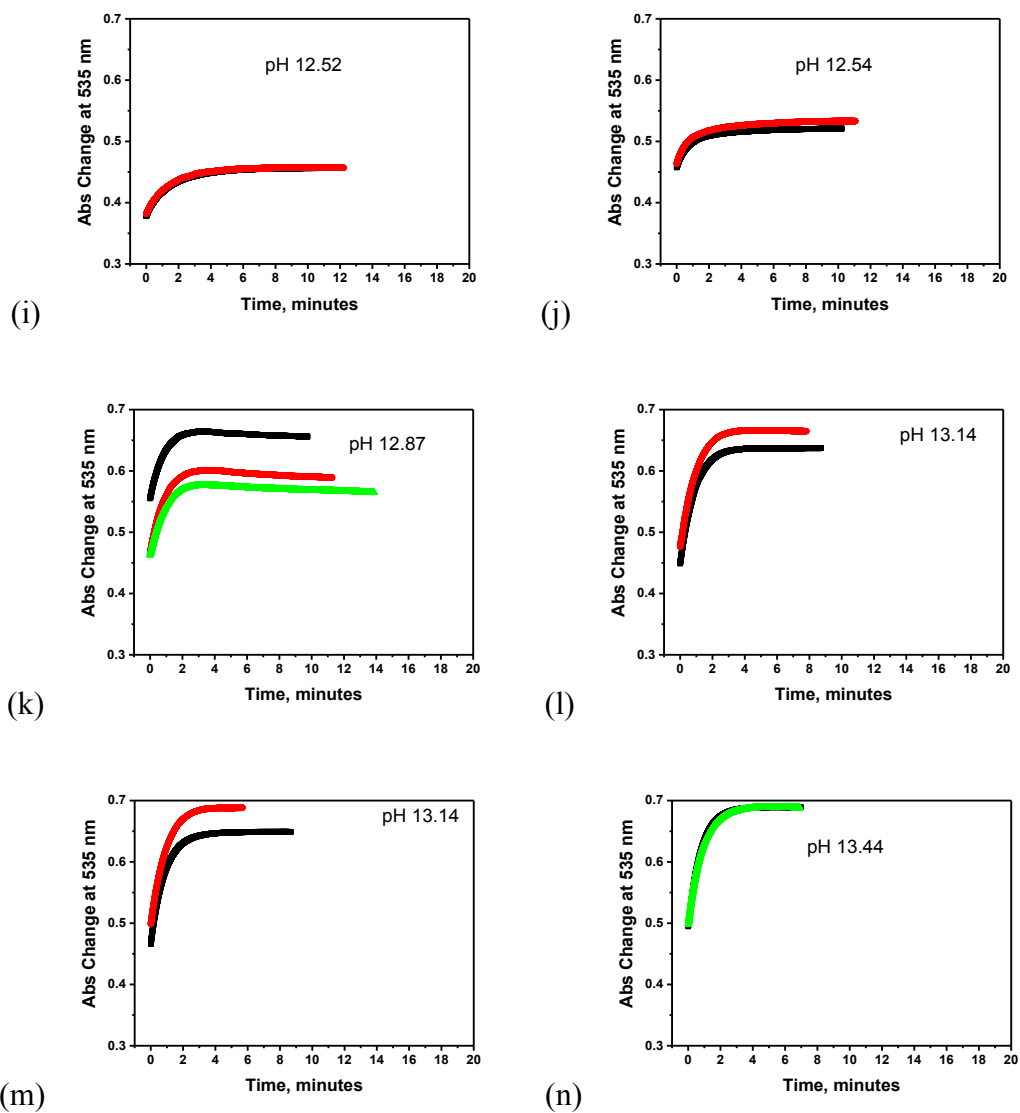


Figure A16. Kinetic traces for the reaction between NO<sup>-</sup>-Cbl(III) ( $\sim 7.0 \times 10^{-5}$  M) and Piloxy's acid (0.015 M) in anaerobic 0.2 M buffered solutions (carbonate or phosphate,  $I = 1.0$  M (NaCF<sub>3</sub>SO<sub>3</sub>)) or sodium hydroxide solutions (0.15-0.35 M,  $I = 1.0$  M (NaCF<sub>3</sub>SO<sub>3</sub>)) taken at 535 nm.